Mílton Jorge Santos Cordeiro
Mestre em Biotecnologia

Gold NanoBeacons for Spectral Codification – Application as a DNA Sensor

Dissertação para obtenção do Grau de Doutor em Biotecnologia

Orientador: João Carlos Lima, Professor Associado com agregação, FCT-UNL
Co-orientador: Pedro Viana Baptista, Professor Associado com agregação, FCT-UNL

Júri:

Presidente: Prof. Doutor Maria João Lobo de Reis Madeira Crispim Romão.

Arguentes: Prof. Doutor Manuel José Estevez Prieto.
Prof. Doutor Jorge Miguel de Ascenção Oliveira.

Vogais: Prof. Doutor Nuno Correia dos Santos.
Prof. Doutor Maria João Lobo de Reis Madeira Crispim Romão.

FACULDADE DE CIÊNCIAS E TECNOLOGIA
UNIVERSIDADE NOVA DE LISBOA

Janeiro 2018

Universidade Nova de Lisboa

Faculdade de Ciências e Tecnologia

Gold NanoBeacons for Spectral Codification - Application as a DNA Sensor

Mílton Jorge Santos Cordeiro

supervised by

Prof. João Carlos Lima

Prof. Pedro Viana Baptista

January 2018

“Gold NanoBeacons for Spectral Codification – application as a DNA sensor“

The work presented in this Thesis was funded by the Doctoral Fellowship SFRH/BD/87836/2012 financed by the Portuguese Foundation for Science and Technology – Ministry of Science, Technology and Higher Education.

The research performed during this fellowship was published in International Peer-Reviewed Scientific Journals.

1. **Cordeiro M.**; Carvalho L.; Silva J.; Saúde L.; Fernandes A.R.; Baptista P.V. Gold Nanobeacons for Tracking Gene Silencing in Zebrafish. *Nanomaterials* **2017**,*7*, 10.

2. Vinhas R.; **Cordeiro M.**; Pedrosa P.; Fernandes A.R.; Baptista P.V. Current trends in molecular diagnostics of Chronic Myeloid Leukemia. *Leukemia lymphoma* **2016**, 0,0, 1-14.

3. **Cordeiro M.**; Carlos F.F.; Pedrosa P.; Lopez A.; Baptista P.V. Gold Nanoparticles for Diagnostics: Advances Towards Point-of-Care. *Diagnostics* **2016**, 6, 43.

4. **Cordeiro M.**; Giestas L.; Lima J.C.; Baptista P.M.V. BioCode gold-nanobeacon for the detection of fusion transcripts causing chronic myeloid leukemia. *Journal of Nanobiotechnology* **2016**, 14, 38.

5. Larguinho M.; Canto R.; **Cordeiro M.**, Pedrosa P., Fortuna A., Vinhas R., Baptista P.V. Gold nanoprobe-based non-crosslinking hybridization for molecular diagnostics. *Expert Rev. Mol. Diagn.* **2015**, 15, 10,1355–1368.

6. **Cordeiro M.**; Vinhas R.; Carlos F.F.; Mendo S.; Fernandes A.R.; Figueiredo S.; Baptista P.V. Gold nanoparticle-based theranostics: disease diagnostics and treatment using a single nanomaterial, *Nanobiosensors in Disease Diagnosis* **2015**, 4, 11–23.

7. **Cordeiro M.**; Giestas L.; Lima, J.C.; Baptista, P.V. Coupling an universal primer to SBE combined spectral codification strategy for single nucleotide polymorphism analysis. *J. Biotechnol.* **2013**, 168, 1, 90–94

Agradecimentos

Esta tese é dedicada à Rita. Porque só tu sabes de que foi feito este percurso. Só te posso agradecer pela força, motivação e constante presença. Fazes de mim uma pessoa melhor. E mais importante que tudo, pelo Vasco.

Vasco, fizeste-me perceber o que de facto é importante.

Pai e Mãe. Não há palavras que possam transmitir a minha gratidão por tudo o que vocês fizeram por mim. Vocês são o melhor que alguém pode desejar.

Bruno. Apesar da distância, continuas a ser o 'Mamajero'.

Aos Meus Orientadores, João Carlos Lima e Pedro Viana Baptista. Espero ter adquirido uma fracção do conhecimento com que me presentearam todos os dias. São um exemplo que vou para sempre recordar.

Letícia. Não sabes o quanto fizeste por mim.

Rosa, Larguinho, Fábio, Raquel, Sara. Rita 'tu é que és', Veigas, Gonçalo, Conde, Pedrosa e Sofia. Porque aprendi com vocês o que significa ser parte de uma equipa. Nenhum grupo chega perto do 315.

André, Pekas, Lois, Kebra, Bana, Toni, … O tempo passa, mas aqui estamos.

Eu não sou de grandes palavras. Mas se somos a soma das nossas experiências vocês fizeram de mim o que sou hoje.

Abstract

The use of gold nanoparticles (AuNPs) to develop sensing platforms for the detection of nucleic acids has gained momentum for the past decade. This is due to unique physical properties of AuNPs, such as intense optical modulation, coupled to the possibility of tailoring their reactivity through surface modification.

The main objective of this thesis was to develop a biosensor based on the gold nanobeacons technology coupled to wavelength shift mediated by Förster resonance energy transfer (FRET). As a proof-of-concept, the molecular hallmark of Chronic Myeloid Leukemia (CML) - the BCR-ABL fusion gene - was chosen as target. The detection is based on a spectral shift of the donor signal to the acceptor, which allows the corroboration of the hybridization event. The Au-nanobeacon acts as a scaffold for detection of the target in a homogenous format whose output capability (i.e. additional layers of information/NP) is potentiated via the specific FRET signal. To do so, the design of the conventional molecular beacon was changed into a two-component system comprising 1) a donor labeled single-strand DNA with a hairpin structure and 2) an acceptor labeled oligonucleotide that hybridizes to the open state of the hairpin. This system was optimized to allow the specific detection of the fusion sequences and not be triggered by the partial non-fused sequence and, subsequently, hybridize to an acceptor-labeled oligo that identifies which hairpin was triggered in solution. The spectral coded Au-nanobeacons (BioCode) allowed the detection of synthetic pathogenic fusion sequences (with high specificity towards partial complementary sequences), using two distinct fluorescence signals (FRET signal and a partial recovery of the donor emission) over the same hybridization event.

Translation of this BioCode strategy to intracellular signaling was also attempted in a theranostic approach. Here, the specific gene silencing and tracking the silencing events via the beacon's emission. Conceptually, silencing of the enhanced green fluorescence protein (EGFP) mRNA in zebrafish embryos, followed by application to CML cell lines.

Keywords: Gold nanoparticles, Förster resonance energy transfer, Biosensor, Chronic Myeloid Leukemia, BCR-ABL fusion, Au-nanobeacon, Zebrafish.

Resumo

O uso de nanopartículas de ouro para o desenvolvimento de plataformas de deteção de ácidos nucleicos baseado em fluorescência tem sido alvo de investigação intensa nas ultimas décadas. Isto deve-se às suas propriedades físicas únicas, como a modulação da fluorescência de fluoróforos vizinhos, acoplada à possibilidade de modificar a sua reatividade através da alteração/funcionalização da sua superfície.

Esta tese teve como objetivo principal, o desenvolvimento de um biossensor baseado na tecnologia de *nanobeacons* (faróis moleculares) de ouro e acoplar um mecanismo de transição de sinal mediado por FRET (Transferência de energia por ressonância de Förster). Como prova de conceito, esta plataforma foi otimizada para a deteção das sequências de fusão BCR-ABL associadas ao desenvolvimento de Leucemia Mielóide Crónica (CML). O princípio de deteção é baseado na mudança espectral devido à transferência de energia entre o fluoróforo doador e o fluoróforo aceitante, o que permite a corroboração da ocorrência de hibridação. O Au-*nanobeacon* atua como uma matriz de deteção do alvo em meio homogéneo em que o sinal de deteção é potenciado através do sinal FRET específico gerado. Para tal, o design de faróis moleculares convencional foi transformado num sistema de dois componentes: 1) uma molécula de DNA em cadeia simples marcada com o fluoróforo dador com uma estrutura de *hairpin*; e 2) um oligonucleótido marcado com aceitador que apenas é capaz de hibridar com o estado aberto do *hairpin*. Este sistema foi otimizado para: a) permitir a deteção específica das sequências de fusão e não ser desencadeado pelas sequências parciais não fundidas; b) permitir a hibridação de um oligonucleótido marcado com o fluoróforo aceitante. O sinal de fluorescência gerado pela ocorrência de transferência de energia identificará qual sequência está presente em solução. O Au-*nanobeacons* com esta codificação espectral (BioCode) permitiu a deteção de cada uma das sequências de fusão patogénicas sintéticas, usando dois sinais de fluorescência distintos (sinal FRET e recuperação parcial da emissão do doador) para o mesmo evento de hibridação.

A utilização dos nanoconstructos desenvolvidos foi aplicada numa abordagem de teragnóstico, em que o silenciamento de mRNA da uma *green fluorescence protein* (EGFP) em embriões de uma linha transgénica de peixe zebra fli-EGFP foi visualizada e rastreada via a sinalização do farol (nano)molecular. A mesma abordagem foi aplicada em linhagens humana de CML.

Palavras-chave: Nanopartículas de ouro, Transferência de energia por ressonância de Förster, Biossensor, Leucemia Mielóide Crónica, BCR-ABL, Au-*nanobeacon*; Peixe zebra.

Table of contents

Table of Figures

Table index

Abbreviations and symbols

ABL	Abelson murine leukemia
ASO	Anti-sense oligonucleotide
AuNP	Gold nanoparticle
AuNP@citrate	Citrate-capped gold nanoparticle
AuNP@PEG	Gold nanoparticle functionalized with polyethylene glycol
BCR	Breakpoint Cluster Region
bp	Base pair
DEPC	Diethyl pyrocarbonate
DLS	Dynamic light scattering
DMEM	Dulbecco's Modified Eagle's medium
DTNB	5,5'-dithio-bis-[2-nitrobenzoic acid]
DTT	Dithiothreitol
EGFP	Enhanced green fluorescence protein
EMSA	Electrophoretic mobility shift assay
FBS	Fetal bovine serum
FRET	Förster resonance energy transfer
ITC	Isothermal titration calorimetry
LSPR	Localized surface plasmon resonance
MST	Microscale thermophoresis
NC	Non-complementary
NSET	Nano surface energy transfer
NTP	Nucleoside triphosphate
PEG	Polyethylene glycol
PMT	Photomultiplier
POS	Positive reaction
RPMI	Roswell Park Memorial Institute
RT	Room temperature
SAXS	Small-Angle X-Ray Scattering
TAE	Tris-acetate-EDTA
tcMB	Two component molecular beacon
TEM	Transmission electron microscopy
UV-Vis	Ultraviolet and visible light range

Φ_{ET}	Energy transfer efficiency
R_0	Förster critical radius

1 General Introduction

Some of the literature review presented within this Chapter was derived from the following publications:

1. Vinhas R.; **Cordeiro M.**; Pedrosa P.; Fernandes A.R.; Baptista P.V. Current trends in molecular diagnostics of Chronic Myeloid Leukemia. *Leukemia lymphoma* **2016**, 0,0, 1-14.

2. **Cordeiro M.**; Carlos F.F.; Pedrosa P.; Lopez A.; Baptista P.V. Gold Nanoparticles for Diagnostics: Advances Towards Point-of-Care. *Diagnostics* **2016**, 6, 43.

3. Larguinho M.; Canto R.; **Cordeiro M.**, Pedrosa P., Fortuna A., Vinhas R., Baptista P.V. Gold nanoprobe-based non-crosslinking hybridization for molecular diagnostics. *Expert Rev. Mol. Diagn.* **2015**, 15, 10,1355–1368.

4. **Cordeiro M.**; Vinhas R.; Carlos F.F.; Mendo S.; Fernandes A.R.; Figueiredo S.; Baptista P.V. Gold nanoparticle-based theranostics: disease diagnostics and treatment using a single nanomaterial, *Nanobiosensors in Disease Diagnosis* **2015**, 4, 11–23.

1.1 **Light**

The electromagnetic radiation (ER) can be viewed as oscillating electric and magnetic field in perpendicular planes that radiates perpendicularly from the direction of the wave propagation – see Figure 1.1. These fields are generated by electric charges in non-uniform movement. This type of oscillations are self-perpetuating considering that the electric oscillation generates the magnetic moment which in turns regenerates the electric field ER (1).

The type of ER is defined by its wavelength (separation of consecutive maxima of one complete revolution - λ) and the full ER spectrum is comprised of distinct types of radiation (gamma ray, X-ray, ultraviolet light (UV), visible light (Vis), infra-red (IR), microwave and radio waves).

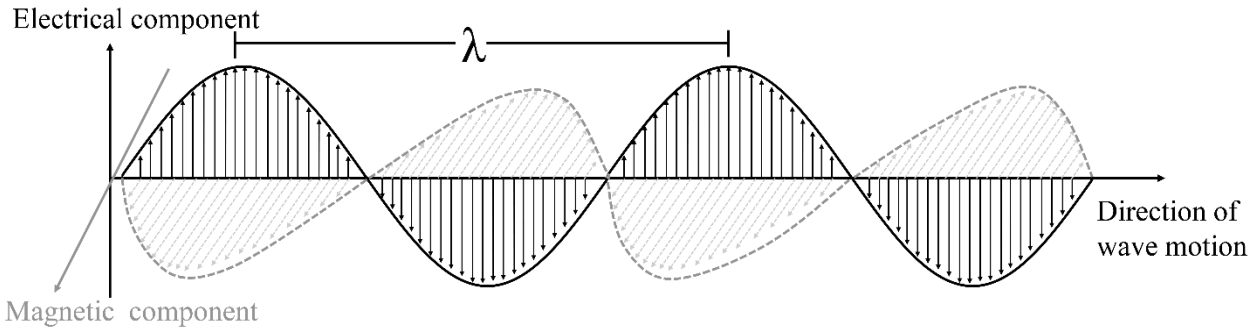

Figure 1. Representation of a monochromatic, plane polarized electromagnetic wave. Black arrows represent the electrical vector (electric component) and the gray arrows represent the magnetic vectors (magnetic component).

Considering a constant velocity for light propagation ($c \approx 3.00 \times 10^8$ m/s), the energy (E) of each type of radiation is inversely proportional to its frequency (ν) as shown in Equation 1.1 and 1.2, where h denotes the Plank constant (6.626×10^{-34} J.s) (1)

$$\nu = \frac{c}{\lambda} \qquad \text{Equation 1.1}$$

$$E = h \times \nu \qquad \text{Equation 1.2}$$

1.1.1 **Light absorption**

Photophysics and photochemistry is a result from the interaction of an electromagnetic field (light) and matter. This interaction can occur via different processes, each governed by specific laws and principles. When a light beam with a given, wavelength passes through a sample, the incident light can be absorbed, scattered or induce the emission of light by the sample (Photoluminescence) – see Figure 1.1. (2)

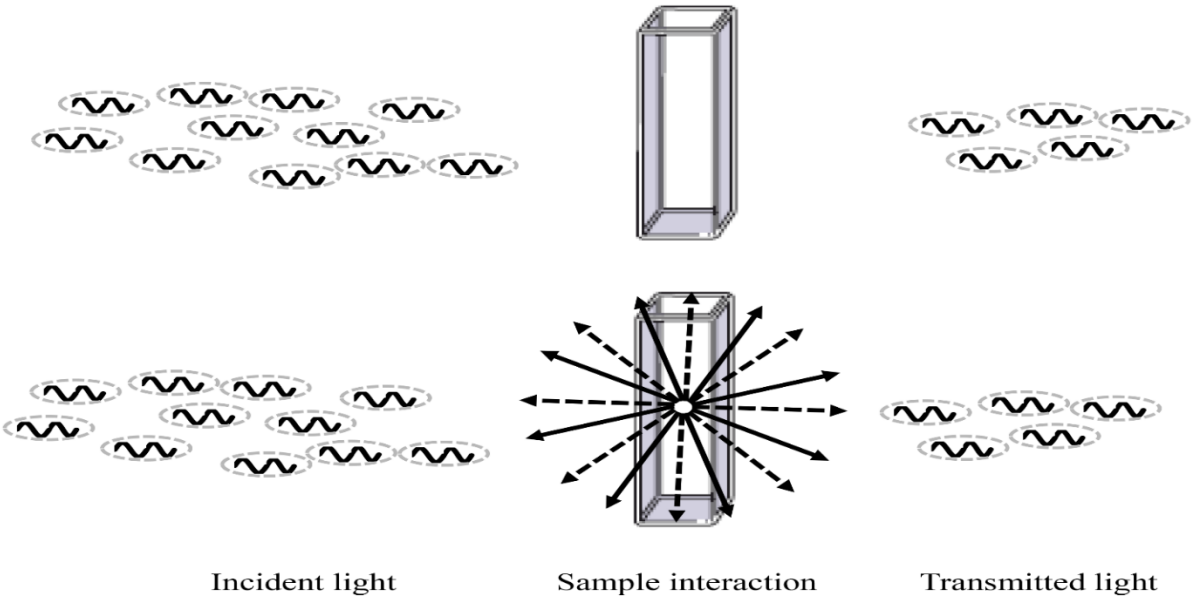

Figure 1.1. Schematic representation of the possible ways non-ionizing electromagnetic radiation interacts with matter. Top panel represents the absorption processes, where the incident light was more photons than the transmitted light, Solid arrows and dashed arrows in bottom panel represents the isotropic scattering and photoluminescent processes.

The absorbed light is converted into chemical energy, since the molecules that absorbed this light beam are promoted into higher levels of energy. The system can return to a basal energy level either by the occurrence of photochemistry (excited state chemistry), by the emission of this energy in the form of a photon or through non-radiative processes in the form of heat. Assuming a defined path in which light travels, the photoluminescence and scattering processes are always isotropic (i.e the same intensity in all directions) (3).

The mechanism by which the EM is absorbed by a molecule depends on the frequency of the incident EM (ionizing radiation (such as gamma rays), X-Ray UV-Vis, IR or microwave) but the fundamental process is that the energy of the incident light is incorporated into the molecule (i.e absorption of a discrete amount of

energy). In all situations, the energy that is required to promote a molecule from its ground state to its energized (excited) state must be equal to the energy separation between the two energy levels – Figure 1.2 represents the electronic transition of a given absorbing molecule. The absorption of UV-Vis radiation (200-800 nm), induces the electronic transition between the electronic ground state to an excited state. In the ground state, the orbitals of a given molecule are filled in order of increasing energy, respecting the Pauli principle of exclusion. This principle postulates that any given orbital can only contain two electrons with opposite spins. Upon absorption of a photon with this type of radiation, electrons from the **h**ighest **o**ccupied **m**olecular **o**rbital (HOMO) are promoted to a higher empty energy orbital. The organic molecules that absorb EM in this region (200-800 nm) contains electrons from π- or non-bonding orbitals (conjugated unsaturation, aromatic compounds, etc). The absorption of IR radiation is associated with the vibration of the molecular bonds (stretching, compression, scissoring, etc) and rotation of the overall molecule. The absorption of microwaves is associated with the rotational movement of the molecules (1). Considering that work within this thesis revolves around fluorescence, the process of the UV-Vis absorption and emission will be described in greater detail in the next section.

As described previously, an optically active molecule absorbs the EM field that corresponds to the energy difference between the HOMO and higher energy orbitals with vacant positions (or from the ground state configuration to higher energy configurations or electronic excited states). As the energy levels between these two states are fixed, the absorption spectrum (i.e. the absorption of the EM field by an electronic state) should be composed of sharp vertical lines that correspond to the energy separation between the before mentioned states. Experimentally, this is rarely the case, as most analytes optically active in the UV-Vis have absorption spectrum that are broader than a single transitional line. Multiple factors contribute to the broadening of the absorption spectra, such as 1) the existence of various vibrational and rotational levels within a given electronic state and that the transition can occur from any vibrational state of the ground state to any vibrational level of the excited state – Figure 1.2; 2) Doppler broadening, where the motion of the absorbing analyte towards the optical detector, generates a change of the absorption frequency in a velocity-dependent manner (4).

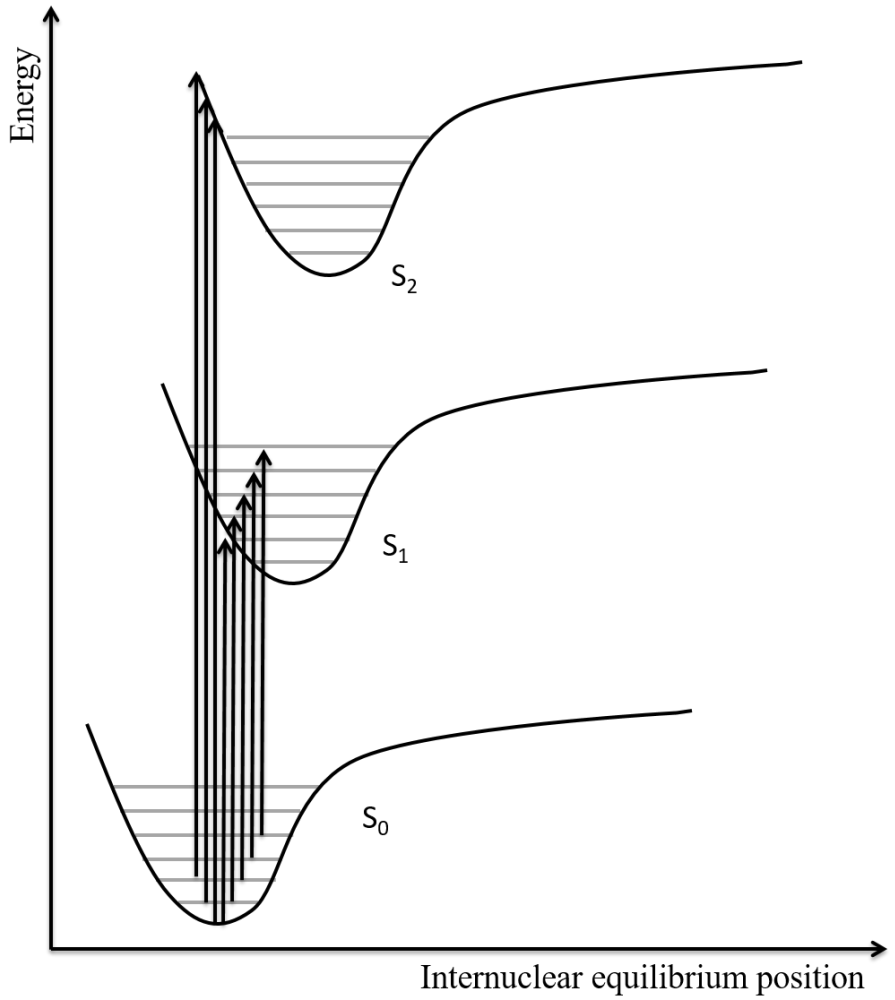

Figure 1.2. Schematic representation of vertical electronic transitions generated from absorption of photons with wavelengths in the UV-Vis range. Solid black line represents different electronic levels; Horizontal gray lines within each electronic level corresponds to vibrational levels; Vertical arrows represents the electronic transitions.

From a practical viewpoint, the absorption spectrum of a given solution is determined by the attenuation of a variable monochromatic light beam, after interaction with a given solution. This attenuation is determined by the fraction of the light beam that reaches an optical detector – Transmittance (%T) – Equation 1.3. The relationship between the transmittance and the absorbance is given by Equation 1.4. (2)

$$\%T = \frac{I}{I_0} \times 100 \qquad \text{Equation 1.3}$$

$$Abs = -\log(T) = \log(\frac{I_0}{I}) \qquad \text{Equation 1.4}$$

Where I and I_0 correspond to the monochromatic light that reaches the detector in the presence and absence of the absorbing species, respectively. This means that for any given wavelength that passes through the solution, containing the analyte of interest, with a given intensity (I), must be divided by the intensity of light of the same wavelength that passes through the same solution in the absence of the analyte (I_0) – reference solution – in order to evaluate the attenuation of light imposed by the analyte. This allows the correction for the residual absorption of the solvent and possible interaction of the EM with the sample holder (i.e possible reflection and scattering events).

When the attenuation of the light beam follows a proportional relationship with the concentration of the absorbing species, the degree of the light attenuation is independent of the incident light intensity and each layer of the medium absorbs an equal fraction of the incident light, the absorbing species is said to follow the Lambert-Beer Law (2, 5). The degree of light attenuation dependents on 1) the number of absorbing molecules in solution - concentration (C - usually in molar (M) - moles per liter) -a higher number of absorbing molecules generates a higher absorption peak intensity in the absorption spectrum; 2) the length of the path that the beam of light has to travel (l - optical path usually in cm) – the increase of the optical path also increases intensity of absorption; 3) the molar absorptivity of the chemical under study (ε – usually in $M^{-1}.cm^{-1}$). It is a constant for specific absorbing molecules and specific for a given wavelength and solvent. The relationship of these parameters and the absorbance of a chemical is given by Equation 1.5.

$$Abs = \varepsilon \, . \, l . \, C \qquad \text{Equation 1.5}$$

Normally, the absorbance can range from 0 to 2 (99 % of absorption) or even higher, depending on the apparatus digital resolution, but the application of the Lambert beer Law for quantification purposes should be applied using values of absorbance under 1, as above this value the linearity between the Abs and concentration can be lost. Another consideration must be considered when applying this expression, such as 1) Avoid electrostatic interactions between the absorbing species (only valid for attractive forces), 2) Minimize changes of the refractive index in comparison to the reference cell; 3) emitting species - fluorescence or phosphorescence can disrupt the linearity between Abs and concentration; 4) presence of particulates that can greatly enhance scattering; 4) stray light. As such, it is of the utmost importance to use well-dispersed solutions with the lowest concentration of analyte possible to perform these measurements (2).

1.2 **Fluorescence**

After the absorption of a photon that promotes a molecule to an electronic excited state, the decay to the ground state can occur through several pathways, such as 1) radiative decay, i.e. the emission of photons (via spin allowed fluorescence or spin forbidden phosphorescence pathways) or via non-radiate decay mechanism, such as: excited state energy transfer, vibration relaxation, solvent collision and others (5). For the radiative decay, when the electron in the excited state is paired (spin wise) with the ground state orbital, i.e. both electron present an opposite spin state, the return to the ground state is 'spin allowed' and occurs in rapidly through the emission of a photon (typically around 10^{-9} seconds) – Fluorescence. On the other hand, if the electron in the excited state orbital has the same spin orientation than the electron in the ground state, this transition is forbidden and the decay to the ground level occurs slowly (typically in the order of the 10^{0} to 10^{-3} seconds) - Phosphorescence (3).

The transition to an electronic excited state and the decay to the ground state is usually represented by the simplified Jablonsky diagram presented in Figure 1.3.

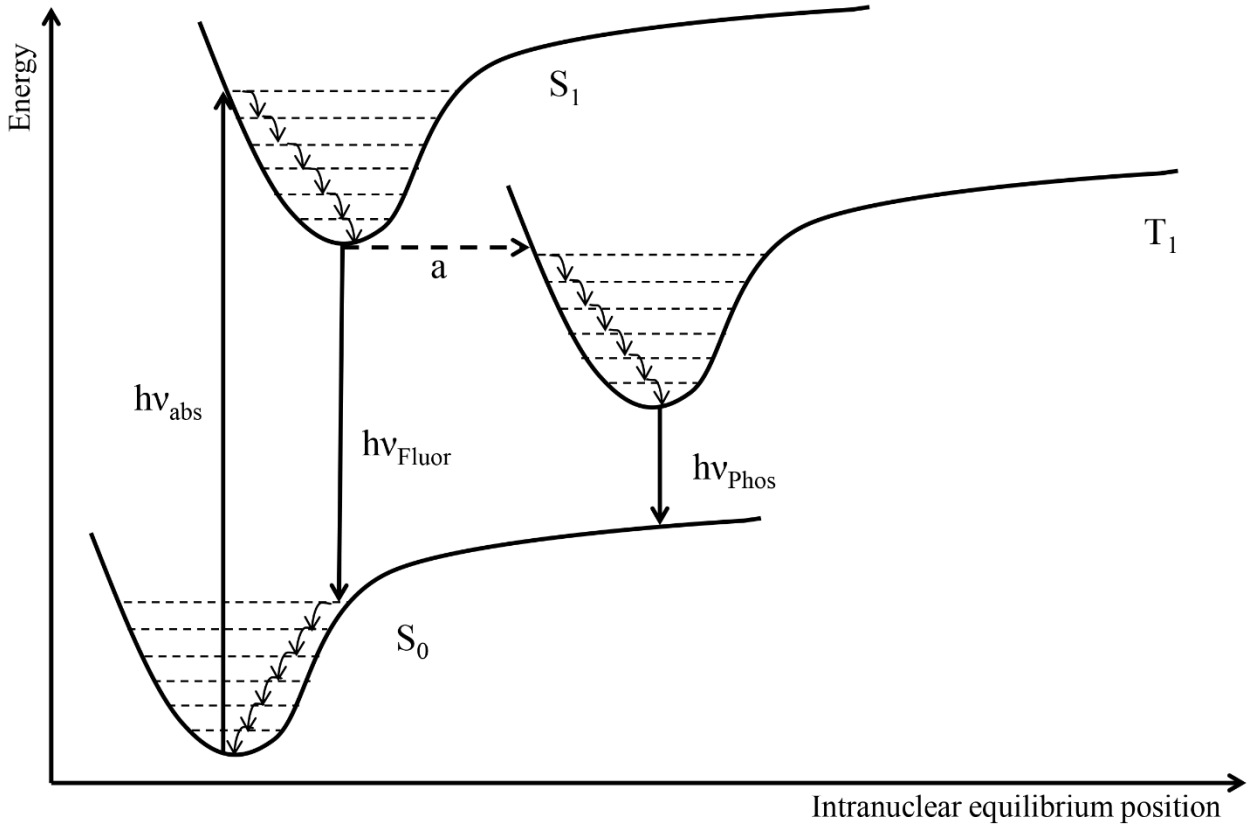

Figure 1.3. Jablonski diagram. Upward facing straight arrows represents the electronic excitation of electrons to higher energy orbitals. Downward facing straight arrows represents the electronic decay of an electron from high-energy orbital to the ground state orbitals. Curved arrows represent the vibrational relaxation within each electronic state. The horizontal line represents intersystem crossing. $h\nu_{abs}$ - Energy of the absorbed light. $h\nu_{Fluor}$ - Energy of the emitted light via fluorescence; $h\nu_{Phos}$ - Energy of the emitted light via phosphorescence.

The absorption process typically takes around 10^{-15} seconds, which is too fast for nuclear rearrangement. As such, upon electronic excitation (S_1), the molecule is at the same vibrational level (intramolecular distance distribution) as the ground state (S_0) – Frank Codon principle (3), that states that the electronic transitions occur vertically. The excited molecule then decays to the lower vibrational level of the electronic excited state (internal conversion), which leads to the new intramolecular distance distribution of equilibrium of the excited state. This intramolecular rearrangement usually occurs in the 10^{-12} second-time range. Considering that the typical fluorescence timescale is within the 10^{-9} seconds, the decay from the electronic excited state to the ground level occurs from the lower vibrational level of the excited state. This loss of energy in the form of heat, coupled with the solvent relaxation process (solvent molecules reorientation around the excited-state dipole) is responsible for the Stokes Shift (3, 6, 7) – separation between the maximum of absorption and maximum of emission – Figure 1.4. This loss of energy to the environment is the reason why the fluorescence emission occurs at higher wavelengths (i.e. lower frequencies) than the absorbed light. The process of intersystem crossing can also occur when a molecule

is in its excited state and can reach lower energy levels by unpairing the excited electron spin with the partially occupied orbital in the ground level (3).

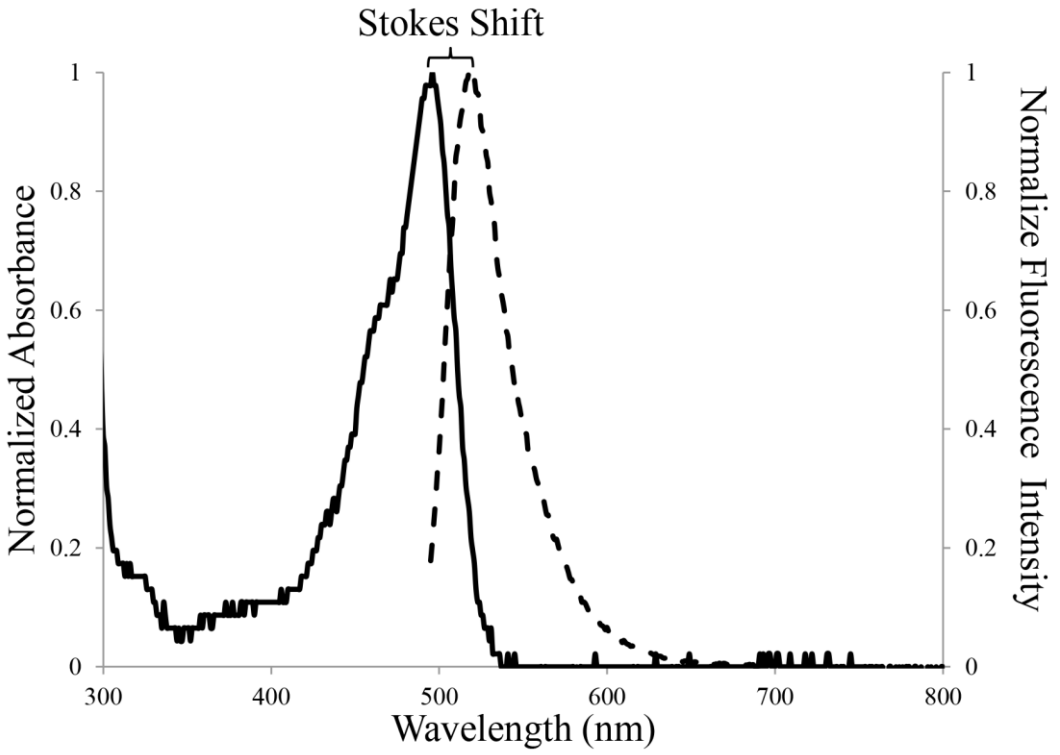

Figure 1.4. Absorption and emission spectra of 6-carboxyfluorescein with ~25 nm Stokes shift. Solid black line represents the normalized absorption spectrum and the dashed black line represents the normalized emission spectrum.

The decay to the ground state is accompanied by the emission of a photon with a frequency that corresponds to the energy gap between the lowest excited and the ground state (minus the energy loss by internal conversion), because the non-radiative relaxation of the higher excited states to the lowest excited state is usually faster than the radiative process. As such, the frequency of emission of a given fluorophore is independent of its excitation energy – Kashas Rule – given that the excitation occurs within the molecule absorption spectrum (3).The excitation at the absorption peak (that corresponds to the transition from the ground state to the lowest excited state) will populate this excited state more efficiently and, will ultimately lead to a higher emission intensity.

The efficiency of the fluorescence process can be measured by the fluorescence quantum yield (ϕ). This parameter describes the proportion of excited molecules that decays to the ground state via emission of photons. Generally, it is the ratio between the number of emitted photons and absorbed photons – Equation 1.6.

$$\phi = \frac{\text{Emitted photons}}{\text{Absorbed Photons}}$$ Equation 1.6

As such, this parameter can be related to the emissive pathways (k_r – decay to the ground state via fluorescence emission) and the non-emissive pathways (8) (k_{nr} – processes that depopulate the excited state of a given fluorophore without the emission of a photon, i.e. internal conversion, intersystem crossing, and energy transfer can be combined with a single parameter) using the relationship presented in Equation 1.7:

$$\phi = \frac{k_r}{k_r + k_{nr}}$$ Equation 1.7

Due to the loss of energy via excited state internal conversion, the quantum yield will always be under 1. In fact, only perfect emitters will have a quantum yield of 1 (as well as perfect scatterers, however these are not technically fluorophores). Nonetheless, fluorophores that exhibit a ϕ near 1 will be brighter than the ones having a ϕ near 0. In this last case (ϕ=0), the absorbing species will not emit and will decay to the ground state exclusively by non-radiative means. Another important parameter for the characterization of a fluorophore is their fluorescence lifetime (τ_f). This parameter is defined as the inverse of the emissive rate in the absence of non-emissive pathways that depopulate the excited state – theoretical situation. In practice, it is usually measured the via the fluorescence decay time instead, which is defined by the inverse of the overall rate of excited state relaxation, as presented in Equation 1.8. The quantum yield and the fluorescence decay time can be used to calculate the fluorescence lifetime, which is the reciprocal of the radiative rate constant, k_r.

$$\tau = \frac{1}{k_r + k_{nr}}$$ Equation 1.8

The fluorescence decay time is considered the average time that the molecule stays in the excited state before decaying to the ground state. This decay time is characteristic for each type of fluorophore in a given environment and is of paramount importance for photophysics/chemistry, as it determines the time that a molecule has for internal conversion, determines the available time for excited state chemical reactions and can be used for the determination of excited state interactions (such as energy transfer).

1.2.1 Steady-state and Time-resolved fluorescence

There are two main approaches for fluorescence measurements: steady-state and time-resolved measurements. In the steady state approach, the sample is continuously irradiated with a light beam, and the frequency and intensity of the light leaving the sample are measured. Due to the velocity of absorption and emission processes, the steady state is virtually reached instantaneously. Due to the nature of the measurement, the emission detection is usually detected at 90° or 173° to minimize the excitation light contamination in the recorded spectrum. For the time-resolved measurements, the sample is exposed to a flash of light whose duration should be below the fluorescence decay time of the fluorophore, otherwise, deconvolution methods must be used to retrieve the fluorophores decay from the convolution of the lamp flash and the fluorophore decay. This requires high-speed detection systems that can operate within the nanosecond and even picoseconds time scale to be useful in the determination of the fluorescence lifetime (9, 10). The steady-state measurements are an average of the time-resolved measurements, and some information is lost during the averaging process (for example, probes under different conformations or suffering different degrees of quenching will present different fluorescence decay times – one for each situation – while in a steady state approach all the mentioned situations would contribute to the same emission band, and the different populations would not be distinguishable). There are other types of information that are lost during the averaging processes, such as the mechanism behind fluorescence variation (energy transfer, diffusion, complex formation), the shape of macromolecules via anisotropy decay, among others (3). Although allowing a multitude of analysis that is impossible via steady-state approach, the time-resolved measurements require more complex and expensive instrumentation to be able to accumulate all the data necessary to unveil the mentioned details. These measurements also require a longer acquisition time and the lack of multi-sample analysis hinder the widespread use of these approaches, in comparison to steady state approaches.

1.2.2 Fluorescence intensity variation

The decrease in the emission of a given fluorophore via the inter-molecular interactions or due to environmental conditions is usually referred as quenching (a process that decreases the overall emission intensity or the decrease the time of permanence in the excited state) or enhancement (processes that increase the overall emission intensity and fluorescence decay time). There are two main quenching

processes: static and dynamic (or collisional) quenching (11–13). Both mechanisms require an interaction between a fluorophore and a quencher (molecular species responsible for quenching). In the static quenching, the quencher and the fluorophore react with each other in the ground state and form a non-emissive complex. A key feature for the identification of static quenching is the alteration of the absorption spectrum of the emissive molecule (14), due to the formation of a complex with its own absorption profile. For the dynamic quenching process, the fluorophore and the quencher must diffuse to the vicinity of each other during the duration of the excited state, and upon reaching a minimum threshold distance, the fluorophores decays to the ground state without the emission of photons. The mechanism behind the dynamic quenching depends on the fluorophore-quencher pairs and can occur via electron deficient molecules requiring a contact between the intervening molecules, such as oxygen, chlorine, acrylamide, or by energy transfer processes, where the contact is not required but a close distance is paramount (7). Energy transfer processes can also be responsible for the enhancement of a fluorophore emission (this type of process will be described in the next section). A fluorophore emission can also vary depending on the environmental conditions such as temperature, pH, concentration, hydrophobicity, and presence of other absorbing molecules. The temperature effect on fluorophores emission is well known (15, 16). Usually, the emission intensity is inversely proportional to the temperature of the sample. This occurs because the non-radiative processes that depopulate the excited state increase with temperature, such as collision with the solvent and molecules present in solution (17, 18). A high concentration of the fluorophore follows this trend, where the quenching can occur due to collisional self-deactivation (19). The pH can also have a great impact on the emission of a fluorophore, especially if the fluorophore has different ionization states that differ in fluorescence quantum yield. For instance, 6-carboxyfluorescein has at least 4 ionizable groups, and the overall emission spectra intensity is highly dependent on the ionization form of fluorescein, where the cation has a lower overall emission followed by the neutral form as finally the di-anion (higher overall emission) (20). The environment hydrophobicity also has a major impact on the emission of fluorophores (3). This situation is clearly demonstrated by the green fluorescent protein, isolated and cloned from *Aequorea Victoria.* Here, the naturally fluorescent amino acids are arranged within a hydrophobic pocket that greatly increases their emissive properties. This enhancement of emission is lost when the protein is denatured and this pocket is exposed to water (21).The same effect is observed in intercalation dyes, where the hydrophobic environment of the nucleobases greatly increases the quantum yield and fluorescence decay times (22, 23). There are other mechanisms that will decrease the overall emission of a fluorophore that is not based on molecular interaction, such as excitation light competition by other absorbing species (24, 25).

1.2.3 **Energy transfer systems**

The emission of fluorophores can be modulated via the process of energy transfer. The energy transfer process is a bimolecular event, involving the transfer of energy from one donor fluorophore to an acceptor molecule. The Förster resonance energy transfer (FRET) is one of the most widely used energy transfer approaches in life sciences, to probe biomolecular interactions. It was first described by Theodore Förster in 1948 (26, 27). FRET is a non-radiative, distance dependent, energy transfer process between an excited donor to a suitable acceptor in the ground state. This means that the donor molecule returns to the ground state without the emission of a photon while promoting an acceptor to the excited state, via interaction of the transition dipoles of both molecules. The acceptor may be another fluorophore, and the energy transfer will make the acceptor fluorophore emit, or the acceptor can be a non-emissive molecule. In this last case, the acceptor will decay to the ground state via heat generation (3, 7). The occurrence and efficiency of this energy transfer is highly dependent on three factors: 1) the overlap between the emission spectra of the donor fluorophore and the acceptor fluorophore – Figure 1.5; 2) the transitional dipole moment of the donor emission should be correctly aligned with the transition dipole moment of absorption of the acceptor – this parameter can have a massive impact on the energy transfer efficiency, where a perpendicular orientation will hinder the energy transfer efficiency and a collinear orientation will maximize it; 3) the distance between the donor and the acceptor – Equation 1.9 (3), where R corresponds to the distance between the donor and the acceptor and R_0 corresponds to the Förster critical radius. This R_0 corresponds to the distance where the energy transfer is equal to 50 %, where half of the donor molecules decay via the non-radiative energy transfer and the other half decay via the average of the emissive and non-emissive pathways, that occur in the absence of energy transfer) – Figure 1.6 for visual representation of the distance-dependent energy transfer, and its association with R_0. This parameter is used to evaluate if a given donor-acceptor pairs can be used to determine the occurrence of an interaction that occurs over a given distance. The R_0 can be calculated based on the spectral properties of the donor-acceptor pair and their respective architecture – Equation 1.10 (3). Where R_0 is determined in angstroms (Å), k^2 is a geometrical factor describing the relative orientation between the transition dipoles of the donor and acceptor, n represents the refractive index of the medium, ϕ_D is the quantum yield of the donor, $I_D(\lambda)$ is the normalized donor emission spectrum, $\varepsilon_A(\lambda)$ the absorption spectra of the acceptor in molar absorptivity ($M^{-1}cm^{-1}$) and the integral quantifies the overlap between the donor emission and acceptor absorption (with the wavelength expressed in nanometers). The correct determination of the k^2 is not easily achievable and usually, a value of 0.666 is used and corresponds to the orientation value of free rotating molecule in solution (and might not be most correct approximation when the fluorophores are used as labels, considering that the rotation is not free).

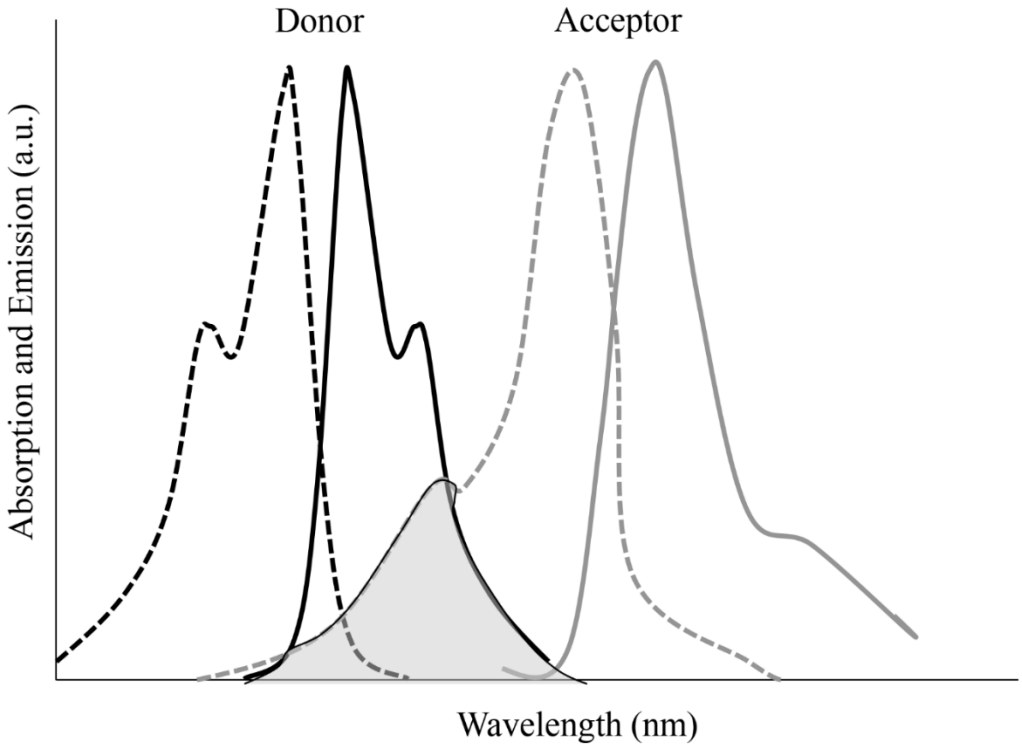

Figure 1.5. Schematic representation of the overlap between the donor emission spectrum and the acceptors absorption spectra. The dashed black line represents the donor absorption spectrum, Solid black line represents the emission spectrum of the donor; dashed gray line represents the acceptors absorption spectrum; solid gray line represents the acceptors emission.

$$\Phi = \frac{R^6}{R^6 + R_0^6} \qquad \text{Equation 1.9}$$

$$R_0 = 0.02 \cdot \left(\frac{k^2 \Phi_D \int^{\infty} I_D(\lambda) \Sigma_A(\lambda) \lambda^4 d\lambda}{n^4} \right)^{\frac{1}{6}} \qquad \text{Equation 1.10}$$

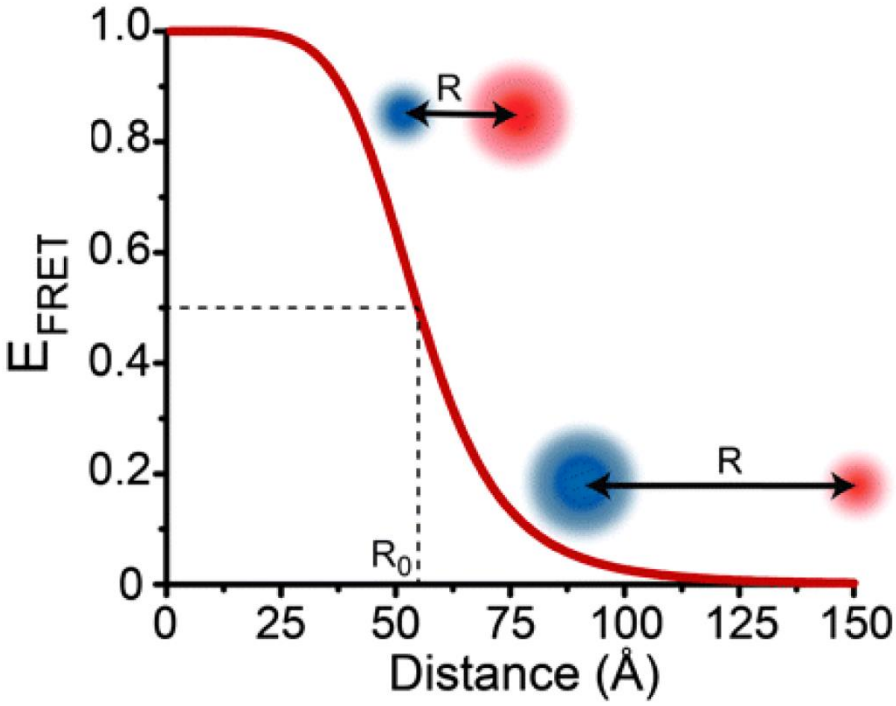

Figure 1.6. Graphical representation of the distance-dependent energy transfer efficiency and its relation to R_0. The diameter of the blue and red circles represents the donor and acceptors emission, respectively. R_0 is the Förster distance, where the energy efficiency is equal to 50%. The length of the double-sided arrow represents the distance (R) separating the donor and acceptor molecule.

As shown in Equation 1.9, the Förster energy transfer efficiency depends on the inverse of the sixth power of the distance separating the donor and acceptor. As such, the energy transfer efficiency decreases as the distance between the donor and acceptor increases. As the distances approach R_0, the energy transfer variation greatly increases and tends to zero (for distances greater than R_0, or to 1 for distances below R_0). This steep variation makes the energy transfer efficiency very susceptible to minute distance changes around R_0. This, coupled with the fact that R_0 for most donor-acceptor pair occurs between 10 and 100 Å, within the scale of biomolecular interaction, makes FRET a versatile phenomenon to be used for the study of these interactions (3, 28, 29). There is a wide range of applications where this phenomenon was used, from the development of several biosensors for nucleic acid, protein, and small molecule sensing(30, 31).

In practice, the occurrence of energy transfer (in steady-state spectroscopy) is determined using the donor emission in the absence of the acceptor (F_D) and in the presence of the acceptor (F_{DA}). Or by the donor and acceptors emission in a situation where the two fluorophores are in an incompatible distance for FRET and in a compatible distance for FRET (3), assuming a constant separation of the donor and acceptor molecule.

In the occurrence of FRET, the emission of the donor will decrease accompanied by the concomitant increase in the acceptor emission. The efficiency of energy transfer can be obtained from Equation 1.11.

$$\Phi_{ET} = 1 - \frac{F_{DA}}{F_D} \qquad \text{Equation 1.11}$$

Another energy transfer mechanism occurs at distances below 10 Å, a much shorter distance than that of the FRET process – Dexter Energy transfer. It was proposed by David Dexter in 1953, and the mechanism behind the energy transfer is based on electron transfer between the donor and acceptor molecules (32). The overlap between the donor emission spectrum and the acceptor absorption spectrum is also required for Dexter mechanism. Briefly, the electron that is in the acceptors highest occupied molecular orbital (HOMO) is transferred to the singly occupied HOMO of the excited donor, while the electron in the lowest unoccupied molecular orbital (LUMO) of the excited donor is transferred to the LUMO of the acceptor. The electrons transferred must be coupled spin wise as stated by the Pauli principle of exclusion (1, 3, 4). Upon this electron exchange, the previously excited donor is now at the ground level and the acceptor is electronically excited and may return to the ground state via emissive process. Due to the longer range of the FRET, this process usually is more preponderant than the Dexter mechanism at longer distances (above 10 Å). To be noted that the donor and acceptor fluorophore are unchanged after the energy transfer process.

1.2.4 **Spectral codification**

As discussed above, the occurrence of FRET in steady-state spectroscopy is determined by the decrease of the donor emission in the presence of the acceptor with the concomitant increase of the acceptor emission. Using this natural occurring signal variation upon FRET, Letícia *et al*. developed a spectral codification tool to unequivocally identify the spectral signatures generated by the hybridization of specific donor and acceptor labeled oligonucleotide. This tool allowed the determination of the Donor – acceptor (D/A) pairs formed in solution, allowing the assessment of multiple hybridization events. The isolated spectra were used as emission base set for a given excitation wavelength and were used to fit the mixture emission spectra, to determine the weight of each individual spectrum in the final spectra. This was first demonstrated using 2 donors and 4 acceptors (33) and was then adjusted for the presence of 3 donors and 4 acceptors (34). To do so, three oligonucleotide strands were labeled with three different donors (the 3 strands had the same sequence but each was labeled with a different donor fluorophore), and the complementary sequences

to the donor labeled oligonucleotides were labeled with 4 different acceptors fluorophores. The emission spectrum of each probe was addressed individually. The spectra for all the possible combinations of the donor and acceptor were tested (64 possible situations). The determination of sample composition was performed via the linear combination of the weighted emission spectrum of each flurophore, using the Equations 1.12 to 1.14.

$$F^{ex_1} = d_1^{ex_1}.f_{D_1}^{ex_1} + d_2^{ex_2}.f_{D_2}^{ex_1} + d_3^{ex_1}.f_{D_3}^{ex_1} + a_1^{ex_1}.f_{A_1}^{ex_1} + a_2^{ex_1}.f_{A_2}^{ex_1} + a_3^{ex_1}.f_{A_3}^{ex_1} + a_4^{ex_1}.f_{A_2}^{ex_1} \quad \text{Equation 1.12}$$

$$F^{ex_2} = d_1^{ex_2}.f_{D_1}^{ex_2} + d_2^{ex_2}.f_{D_2}^{ex_2} + d_3^{ex_2}.f_{D_3}^{ex_2} + a_1^{ex_2}.f_{A_1}^{ex_2} + a_2^{ex_2}.f_{A_2}^{ex_2} + a_3^{ex_2}.f_{A_3}^{ex_2} + a_4^{ex_2}.f_{A_2}^{ex_2} \quad \text{Equation 1.13}$$

$$F^{ex_3} = d_1^{ex_3}.f_{D_1}^{ex_3} + d_2^{ex_3}.f_{D_2}^{ex_3} + d_3^{ex_3}.f_{D_3}^{ex_3} + a_1^{ex_3}.f_{A_1}^{ex_3} + a_2^{ex_3}.f_{A_2}^{ex_3} + a_3^{ex_3}.f_{A_3}^{ex_3} + a_4^{ex_3}.f_{A_2}^{ex_3} \quad \text{Equation 1.14}$$

In Equation 1.12 to 1.14, the $f_{D_J}^{ex_*}$ and $f_{A_i}^{ex_*}$corresponds to the emission spectra of the donors (j - one to three) and acceptors (i - one to four) in the absence of FRET at excitation wavelength * (maximum of absorption of donor one to three). The value of the coefficient $d_j^{ex_*}$ and $a_i^{ex_*}$, were iterated to minimize the sum of the squared difference between the theoretical spectra derived from Equations 1.12 to 1.14 and the experimental spectra of the mixtures. These coefficients allow the determination of FRET through their variation. For the acceptors, they represent the degree of enhancement resulting from the donor direct excitation (FRET will result in values superior to 1). For the donors, the coefficient represents the degree of the quenching due to the energy transfer (FRET will result in coefficient values inferior to 1). The donor/acceptor coefficient values can be 0, when a given fluorophore is absence from solution, or 1 when no FRET occurs(33, 34).

In the presence of FRET, the acceptors coefficient can be decomposed in the ratio of the extinction coefficient of the donor and acceptor at the excitation wavelength multiplied by the FRET efficiency in the pair, and in the case of non-equimolar situation, the ratio of both concentration – Equation 1.15. Here, X_{D_j/A_i} corresponds to the molar fraction of the donor that is hybridized to the acceptor (1 for a equimolar reaction, 0 for an unhybridized pair), $\varepsilon_{D_j}^{ex_\lambda}$ and $\varepsilon_{A_i}^{ex_\lambda}$ are excitation coefficients of the donor j (one to three) and acceptor i (one to four) at the excitation wavelength and $\Phi_{ET_{D_J}A_i}$corresponds to the energy transfer efficiency (or FRET quantum yield) within the considered donor-acceptor pair.

$$a_i^{ex_\lambda} = n + X_{D_1/A_i}.\frac{\varepsilon_{D_1}^{ex_\lambda}}{\varepsilon_{A_i}^{ex_\lambda}}.\Phi_{ET_{D_1}A_i} + X_{D_2/A_i}.\frac{\varepsilon_{D_2}^{ex_\lambda}}{\varepsilon_{A_i}^{ex_\lambda}}.\Phi_{ET_{D_2}A_i} + X_{D_3/A_i}.\frac{\varepsilon_{D_3}^{ex_\lambda}}{\varepsilon_{A_i}^{ex_\lambda}}.\Phi_{ET_{D_3}A_i} \quad \text{Equation 1.15}$$

Considering that the coefficients can be mathematically estimated using the well-defined parameters, they can be compared to the ones obtained experimentally. Some difference exists between them, due to small differences between the real concentrations and the assumed concentrations, slight variations in the hybridization efficiencies and small variations in light intensity. The experimental coefficients and the theoretical coefficients can be organized into matrixes. When applying the minimal square difference between these matrixes, the surface plot, represented in Figure 1.7, arises.

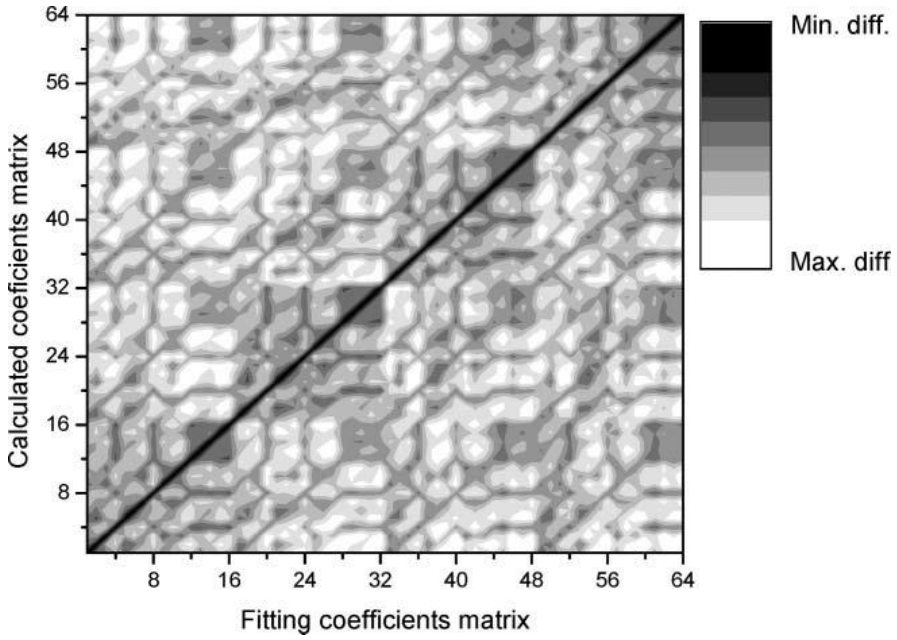

Figure 1.7. Surface plot of the square difference between the theoretical and fitting coefficients for all the possible combination. Black corresponds to the minimal difference. White corresponds to the maximum difference. From (34)

The lowest difference between the theoretical and experimental coefficient is represented by the darker colors, and the absolute minimum can be observed in the diagonal of the plot due to the perfect match between the calculated and experimental coefficient. Note that the coefficients are not matched in absolute value but in minimal difference. The presence of dark and light gray regions denote that some sample compositions generate similar coefficients (local minimal regions). These local minima occur due to cross-excitation of the fluorophores, i.e. because all of them present a non-negligible absorption at the excitation wavelength – Figure 1.8. This cross-excitation leads to excitation of other donor-acceptor pairs and therefore complicate the output signal, or by the increase of fluorescence due to direct excitation.

This tool was coupled to single base extension (SBE) reaction, using donor labeled oligonucleotides and acceptor labeled dideoxynucleotides (ddNTPs - a nucleotide that lacks the 3'-OH, therefore hindering

further polymerization). Each type of ddNTP was labeled with a different acceptor (i.e. different acceptors for the thymine, cytosine, guanine and uracil).

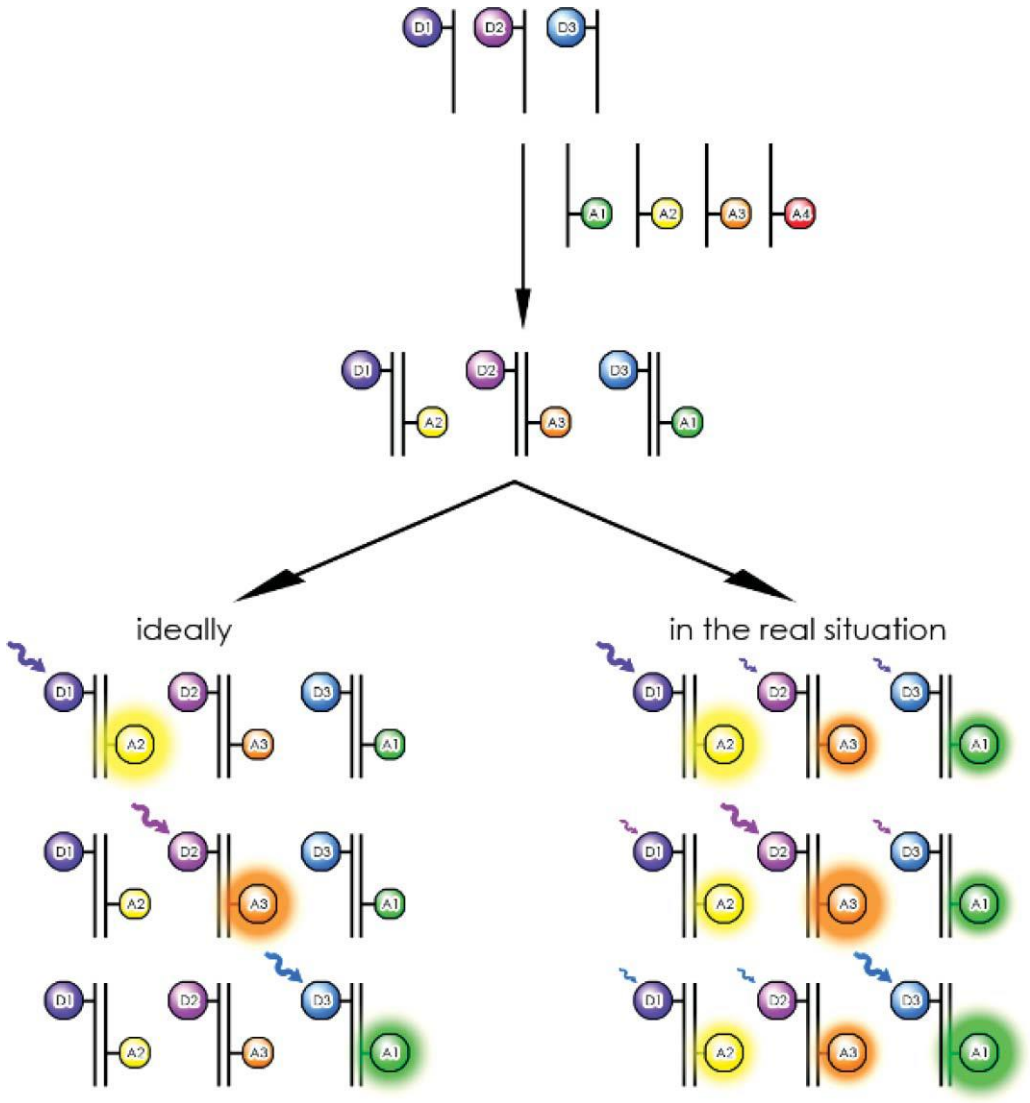

Figure 1.8. Representation of ideal direct excitation versus the occurrence of cross-excitation of the several fluorophores in solution at the excitation wavelengths. From (34)

The SBE relies on the hybridization of an oligonucleotide primer to the sequence adjacent to the nucleobase to be identified. Upon hybridization, the ddNTPs complementary to the nucleobase that occupies the position to be questioned is incorporated into the oligonucleotide primer, allowing the identification of the nucleobase. This a technique that is used for the identification of single nucleotide polymorphisms (SNP). For the coupling of the spectral codification tool to the SBE reactions, the incorporation of the acceptor-

labeled ddNTP puts the acceptor and donor within a FRET compatible distance, allowing the identification of the incorporated ddNTP via FRET signals. In this study, the results demonstrated that the direct excitation of the donor upon SBE, allowed for the unequivocal identification of the incorporation of the four possible nucleotides, corresponding to 4 distinct allele variants to be detected in a single reaction. This SBE procedure coupled with FRET output signal was further modified to allow the use of the donor labeled in a universal approach, using a SBE primer with two portions: one for the hybridization to the sequence adjacent to the nucleobase to be questioned where an acceptor-labeled ddNTP is incorporated and the other portion of the primer that allows the hybridization of the donor labeled oligonucleotide. In this configuration, the same tag oligonucleotide can be used, theoretically, to any SBE reaction with a FRET output signal (35).

1.3 **NanoBiotechnology**

Nanotechnology has brought forth new materials suitable for application in biotechnology, and biomedicine, in particular, that greatly boost current methodologies for clinic diagnostics, including gene expression profiling, biomarker quantification and imaging (36–38). Amongst the plethora of nanoscale structures, devices and particulates, nanoparticles have been mostly studied and characterized for biotechnology use.

Nanoparticles are entities that contain at least one dimension below 100 nanometers. Nanoparticles can be synthesized in a multitude of shapes, such as spherical, rod, stars, triangles, among others. They can be composed by a wide variety of different materials, including: metals, such as noble metals (gold (39) silver (40–42), copper (43), platinum (44), palladium (45)), non-noble metals (iron (46), nickel (47), cadmium-selenium (48) and others (49, 50)), and nonmetallic such as carbon-based nanoparticles including pure carbon (51), polymer-based and lipids (such as liposomes(52)). The properties of the nanoparticles depend on their composition, size, shape and surface modification. Some examples of nanoscale properties include surface plasmon resonance (SPR) (53, 54) and quantum confinement in some types of metal nanoparticles (55), superparamagnetism in magnetic nanoparticles (46), alteration in conductivity in carbon nanotubes (56), among others.

In particular, gold nanoparticles (AuNP) have been extensively studied, due to their ease of synthesis and a wide variety of nanoscale properties such as optical (SPR) (57, 58), electrical (high charge storage and conductivity) (59), catalytic(60), and low cytotoxicity(61).

AuNP can be fabricated essentially by two distinct concepts: top-down and bottom-up. Top-down approaches comprise techniques such as lithography and its variations (62), laser ablation (63, 64) and focused ion beam (65, 66), where the bulk material is removed (etched away) until achieving the desired shape and size for the nanomaterial. Despite having the potential to achieve narrow size dispersions, these methods tend to be slow and depend on the use of high-end, expensive equipment (49). On the other hand, bottom-up approaches have shown to be relatively simpler and faster. In bottom-up approaches, the nanomaterials are built from their precursors via self-assembly, depending on their molecular and atomic physicochemical properties, in a rather simple laboratory setup (67, 68). The reaction conditions must be thoroughly controlled to synthesize nanomaterials with a low dispersion of sizes and shape. Either top-down, bottom-up or a combination of the two concepts (69) has been used to produce nanomaterials with relatively narrow size dispersions, suitable for downstream biomedical applications.

1.3.1 Synthesis and functionalization

One of the most common methods for the production of spherical NPs with a narrow distribution of size in aqueous medium is the citrate reduction method developed and employed by Turkevich *et al*.(70) and later optimized by Frens (71) and Lee and Meisel (72). This method produces hydrophilic spherical AuNPs (10–30 nm) compatible with subsequent functionalization steps. For this synthesis approach, the citrate molecule acts as both a reducer and a capping agent.

The diameter of the produced AuNPs may be tailored, to an extent, by varying the relative ratio of citrate to gold salts. Higher concentrations of citrate yield smaller particles, while lower concentrations of citrate tend to favor the formation of larger particles (73, 74). This method yields rather stable particles with a negative charge due to the weak, electrostatic adsorption of citrate on the surface of the NP, which constitutes an advantage for subsequent surface modification. Another common chemical synthesis procedure that allows the production of AuNPs with a narrow size distribution is the Brust–Schiffrin method (75). This method involves a two-phase scheme: the synthesis is performed in an organic phase, commonly toluene, using sodium borohydride as a reduction agent and alkanethiols as capping agents. AuNPs produced by this method are usually insoluble in water; they require a subsequent ligand exchange to increase their hydrophilicity and/or a molecule to facilitate AuNP transfer to an aqueous phase(76). Nevertheless, ligand exchange can be troublesome, making this approach complicated for downstream biological applications (77). Some variations to this method combine sodium borohydride with sodium hydroxide, allowing the synthesis to occur in aqueous media (78). Furthermore, these routes typically yield

particles with a diameter between 2 and 5 nm (78–80), which imposes some limits to subsequent applications: their diminished size renders the AuNP more difficult to be concentrated via centrifugation; decreases the loading of different molecule at the surface and their extinction coefficient can be two to three orders of magnitude lower in comparison to 12–15 nm (81) AuNPs. A different method for the chemical synthesis of AuNPs is the seeding growth method (82, 83), which is particularly relevant when a stricter control oversize distribution is required (84). This method relies on the formation of a seed, that acts as nucleation spots, upon which additional layers of metal are deposited. The reaction conditions are particularly important as they define the predominant sizes and shapes of the NPs that are obtained. This method has proven to be more cumbersome and time-consuming than the previously discussed methods and bears an increased risk of additional nucleation that may lead to the formation of undesired shapes during synthesis (82, 85). Considering all these, the citrate reduction method is a simpler and straightforward approach for the synthesis of hydrophilic AuNPs in large quantities, with relatively low size dispersion, for subsequent modification and use, for instance in, sensing application. Also, the surface of NPs produced by this method is easily modified due to the loose interaction between citrate and the AuNP, in comparison to the borohydride route that requires a phase transfer.

AuNPs in aqueous solution, synthesized via citrate reduction have negatively charged citrate ions adsorbed on their surface. This citrate adsorption stabilizes the colloidal suspensions by electrostatic repulsions. Such colloids may be stable for years, but they aggregate easily following radical changes to pH or an increase in ionic strength, i.e. the presence of salts. To improve its stability, ligand molecules on its surface can be exchanged with others that provide new functionalities (86). One of the most used protocols is thiol ligand exchange: thiol groups are considered to have a higher affinity to gold than citrate, thus promoting an exchange on its surface. This binding is often termed chemisorption or quasi-covalent bond (approximately 200 kJ/mol) (87) and renders the particles more stable against aggregation induced by an acidic pH or high salt concentrations (86). Early studies by Alivisatos *et al*.(88) and Mirkin *et al* (89). report the use of thiol-modified oligonucleotides functionalized to the surface of AuNPs, showing the potential of DNA hybridization in the macroscopic assembly of an AuNP– DNA network.

The use of this thiol-gold chemistry allows the chemical functionality and reactivity of AuNPs to be customized through surface functionalization, which modulates the solubility, stability, charge effect of the nanocomplex, and interaction with other molecules (90–95) Such plasticity allows the modification and design of the AuNPs' surface chemistry, allowing the control of the AuNP stability and reactivity. There is a wide range of stabilizers available, such as thiolated biomolecules, polymers, dendrimers, phosphine, that may simultaneously act as therapeutic moieties (eg, microRNA, DNA, peptides, and antibodies) – Figure 1.9.

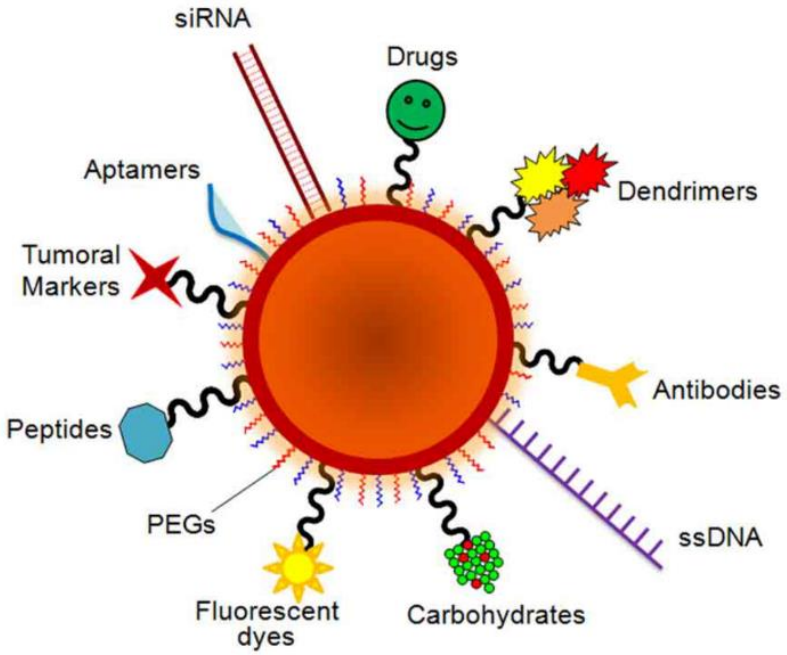

Figure 1.9. Schematic representation of the biomolecules that can be functionalized on the surface of AuNP. From (96).

The surface of an AuNP can also be modified via ionic coupling methods, in which the ligand exhibits an opposite charge to that of the AuNP or of the capping agent (97, 98). Ionic coupling procedures are quicker and do not require pre-activation of molecules. However, this originates more unstable constructs, and control over the biomolecule orientation is hindered (99). The widely-known biotin–streptavidin interaction can also be used for the surface modification of AuNPs. Although noncovalent, the functionalization of the AuNP with avidin or biotin usually requires a covalent immobilization of these molecules (either by direct functionalization using a thiolated molecule or through EDC coupling). Hydrophobic interactions, while not being covalent interactions, usually require a quasi-covalent attachment using a thiol coupling (100).

Polyethylene glycol (PEG) is one of the most widely used stabilizer molecules able to increase AuNPs' stability (101).The modification of the surface of AuNP with PEG not only increases the stability of AuNP against ionic strength induced aggregation (102), it also decreases the adsorption of molecules in the surface (103, 104), decreases the antigenicity of AuNPs (105, 106) and increases their circulation time (96). Bifunctional PEGs with a thiol molecule in one extremity and a different functional group on the other extremity (eg, amine, carboxylic, biotin, azide) have also been used to allow further functionalization with other biomolecules (Table 1.1).

Table 1.1. Common covalent immobilization strategies for AuNP functionalization.

Coupling reaction	Functional group at AuNP surface	Functional group on ligand	Linkers/spacers	Examples
Thiol	Direct coupling	Thiol	-	DNA [28,64] PEG[116] Fluorophores
EDC/NHS[a]	Carboxylic/phosphate or amine	Amine or carboxylic/ phosphate	Bifunctional PEG/DNA chain harboring a thiol and a(n) amine/ carboxylic group	Proteins[117] Antibodies14 Fluorophores[118]
Maleimide	Thiol/maleimide	Maleimide/thiol	Homo-bifunctional thiolated PEG or hetero-bifunctional PEG harboring maleimide	Peptides119 DNA120 Chemotherapeutic agents121

[a] EDC, 1-ethyl-3-(3-dimethylaminopropyl)carbodiimide; NHS, *N*-hydroxysuccinimide;.

1.4 **Optical properties**

Colloidal AuNPs have been extensively used for diagnostic platforms, due to their optical properties, ease of synthesis and surface functionalization. A very important optical property of AuNPs is the presence of a localized surface plasmon resonance (LSPR), which can be described as the collective oscillation of the conductive electrons of the gold atoms that is triggered through the interaction with an incident electromagnetic wave (i.e. light) – Figure 1.10. This collective oscillation generates a polarization of the AuNP (and the charge difference act as restoration force) inducing the formation of dipole moments that leads to the extinction of the electromagnetic wave with the appropriate frequency (107). The frequency at which the SPR occurs is greatly dependent on the size of the particle, with small particles favoring the extinction of high-frequency light and large particles favoring the extinction of low-frequency light.

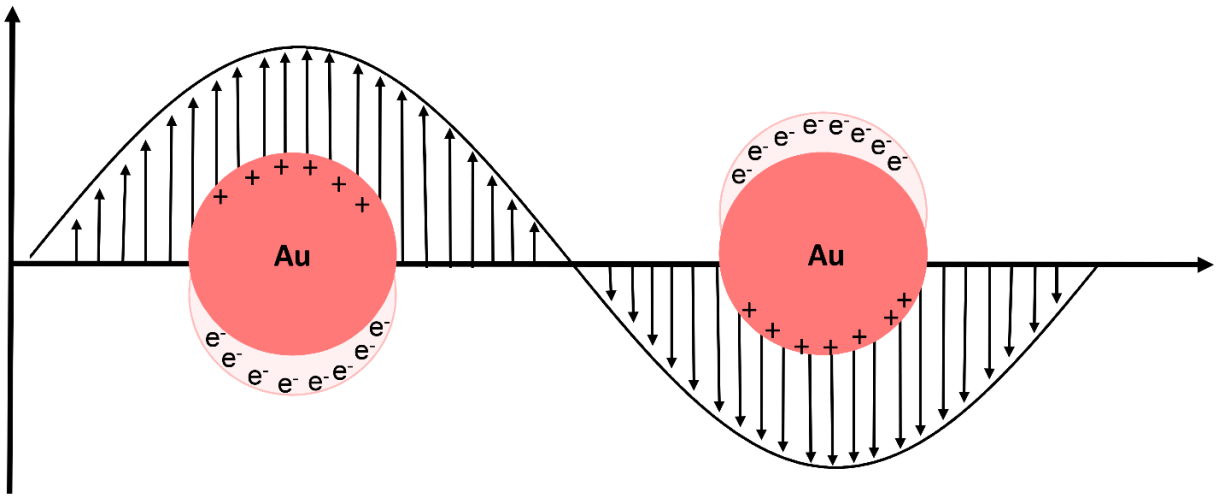

Figure 1.10. Schematic representation of metal nanoparticles in localized surface plasmon resonance (LSPR). Interaction of the electromagnetic waves with the metal nanoparticle (NP) surface electrons (e-) induces a surface plasmon resonance. From (108)

Localized surface plasmon resonance is not only highly dependent on size, but also shape, elemental composition, interparticle distance and dielectric surroundings. Therefore, it can be finely-tuned through the manipulation of these variable using various synthesis routes (109) or dispersion media (58). LSPR results in the absorption and the scattering of the AuNPs, and the relative weight of each to the overall LSPR can be controlled through the size and shape of the AuNP. For instance, small and regular AuNPs tend to favor the absorption component while larger and more irregular AuNPs tend to favor the scattering component (58). The LSPR extinction of incident light is so strong that the extinction coefficient associated with AuNP is usually three orders of magnitude higher than in conventional dyes (110), making them suitable agents for optical sensing applications. Usually, a solution of AuNP will present a deep red color due to the LSPR (absorption in the green regions of the UV-Vis Spectrum). As the diameter increases, the extinction band suffers a red-shift, yielding a bluish/purple solution. This red-shift of the LSPR is also observable when monodispersed particles couple their dipole moment either through proximity effects (aggregation) or by a designed controlled interaction. The surface chemistry also impacts the LSPR. For instance, by increasing the functionalization corona, the LSPR peak shifts to higher wavelengths as on would expect for bigger particles (111, 112). The high extinction coefficient allows for higher sensitivity and lower limits of detection (LOD) of sensing platforms that use this optical property of AuNP (113). The colloidal stability of the AuNP, i.e. the red-to-blue color shift (spectral redshift) is a convenient output signal that has been exploited for the development of several visual colorimetric biosensors.

1.4.1 **Interaction of AuNP with fluorophores**

One of the first evidence that suggested that metallic surface could have an impact in the emission of fluorophore was proposed in 1970 by Karl-Heinz Drexhage (114). In this study, it was demonstrated that the fluorescence decay time varies due to the presence of an interface between two dielectrics of different refractive indices. Recently, metal nanoparticles such as gold and silver, have been used for the modulation of the emission of fluorophores that are in the vicinity of the nanoparticles. Although a lot of work has been presented on the quenching properties AuNP (115–119), some authors reported the enhancement. Parak *et al* (120) showed that the fluorescence of the fluorophore Cy5 emission decreases in close proximity to the AuNP and that the decrease in the observable emission was dependent on the decrease of the radiative decay rate. In this approach, the distance of the fluorophore from the surface of the AuNP was controlled using a fluorescently labeled thiolated DNA molecule in single strand (ssDNA). Anger *et al* (121) reported that AuNP can simultaneously lead to the suppression or enhancement of a fluorophore emission. This was executed, using a substrate immobilized fluorophore and an 80 nm AuNP that was immobilized in an atomic force microscopy (AFM) tip. The use of AFM allowed the precise positioning of the fluorophore in relation to the fluorophore while keeping the same transitional dipole orientation, ensuring that the observed effect is a solely dependent on the distance separating the AuNP and the fluorophore. Here, both enhancement and quenching could be observed depending on the separation distance. Kuhn *et al* (122) reported similar results using AuNPs of 100 nm and terylene molecules as emitters. Kang *et al* (123), reported the similar observation, but in a solution (where the transitional dipole orientation is not as stationary as in the AFM measurements), using smaller AuNPs (8 and 16 nm). The occurrence of either enhancement or quenching is dependent on degree of separation between the interacting parties as demonstrated by Anger *et al* (121), Kuhn *et al* (122), among others (124) , nanoparticle size (125), the electronic properties of nanoparticle, emission frequencies of the fluorophore and the excitation wavelength (126, 127).

How AuNPs impact the emission of fluorophores may be due to several mechanisms, such as excitation decay rate changes and quantum yield changes; The latter one can be further divided in a) radiative decay change rates; b) Absorption rate; c) intrinsic non-radiative decay rate. The excitation decay rate and radiative decay rate can occur due to the interaction of the dipolar oscillation of the fluorophore with the plasmon field generated upon exposure to excitation light source. This is highly dependent on AuNP size and, of course, the excitation wavelength. The absorption rate highly depends on the emission of the fluorophore, as this process is the strongest at the LSPR peak. In this last situation, a higher overlap between the LSPR and the emission spectra of the donor reroutes the emissive pathways to non-emissive pathways – damping of the dipole oscillators by the nearby metal – leading to the decrease of the overall emission of

the system (i.e. energy transfer to the nanoparticle). The mechanism by which the energy is transferred from the fluorophore is transferred to the AuNP can occur via FRET with an efficiency that is inversely proportional to the sixth power of the distance between them, or via nano surface energy transfer (NSET (128)), with an efficiency that is inversely proportional to the fourth power of the distance between them. The absorption rate can also be influenced due to the metal amplifying the incident field, concentrating the local excitation intensity, leading to a higher observable emission (129). Fluorophores that have high non-radiative decay rates (low quantum yields - ± 1%) are more prone to emission enhancement by AuNPs (127).

1.4.2 **Other properties**

As stated before, the LSPR of the AuNP can be separated into an absorption and scattering component. When an AuNP absorbs light, the excited electron must return to the ground level by either the emission of a photon or through the generation of heat. The non-emissive decay, i.e. heat generation, occur via a three-step process: 1) the excitation of the AuNP sample using a monochromatic, coherent and collimated light (laser) at the LSPR peak, generates the before mentioned oscillation of the conductive electrons; 2) The collision of the electron with the nanocrystal lattice leads to the increase of the overall vibration of the lattice, a ~1ps process that is denominated as electron-phonon relaxation; 3) This leads to the increase of temperature of the crystalline lattice, that is followed by the cooling of the crystalline structure via a vibrational transfer of the energy to the surrounding media (denominated as phonon-phonon interaction), taking around 100 ps (130, 131). This property, coupled to their lack of toxicity and ease of surface functionalization, has been used for the development of nanoparticle-mediated photothermal therapy strategies for malignant solid cancerous tumors (131).

The high surface-to-volume, high conductivity and catalytic properties of AuNPs make them interesting platforms to use in electrochemistry. Considering their ease of synthesis and functionalization and lack of toxicity makes them good candidates for the development of electrochemical sensors for a wide array of biomolecules, from the detection DNA sequences and proteins with clinical relevance (94, 95) to small molecules such as estradiol (132). The electronic properties of AuNPs can be controlled through size, particle separation and surface modification (133). AuNPs can decrease the redox over-potential of redox reactions (134) and sustain the reversibility of redox reactions (135, 136). As such, AuNPs have been extensively used as electrochemical labels and carriers of biomolecules for detection of clinically relevant analytes, such as DNA (137), cancer-associated proteins (95, 138) and circulating cancer cells (139).

Additionally, AuNPs have been used to modify the electrode surface in order to increase the redox surface area, allow the immobilization of biomolecules and improve direct electron transfer which allows for electrochemical signal amplification (140).

AuNP can also be used to enhance the signal of Raman scattering spectroscopy. Raman scattering is a vibrational spectroscopic technique relying on the inelastic collision between an incoming source of light and an analyte of interest. This inelastic collision is responsible for the scatter of a lower energy radiation that serves as a fingerprint and provides information regarding structure, interaction or environment of the analyte (141). The probability of Raman scattering can suffer a 10^6 amplification increase of the Raman signal is possible by means of noble metal surfaces and structures, such as gold and silver. This signal amplification is known as surface-enhanced Raman scattering (SERS) and allows the development of sensitive procedures for characterization of target molecules. This signal amplification can occur, either by the interaction of the incident and scattered photons with the SPR of the metal surface, or a charge transfer between the metal surface and the target molecule (142).

1.5 Fluorescence-based nanodiagnostics

Due to the ease of synthesis, functionalization and remarkable nanoscale properties, a wide range of biosensing platforms have been developed using AuNPs. Methodologies for the detection of nucleic acids, proteins, antibodies, enzymes and other biological molecules have been developed using the optical, fluorescence modulation, or electrochemical properties. Here, emphasis will be given to optical approach, with a special focus on fluorescence-based AuNP biosensors. However, a brief introduction to the basis of biomolecular detection using AuNP will be performed.

A key aspect in the development of a biosensor is its ability to specifically detect the target molecule from a pool of non- or closely-related molecules. As such, the choice of biorecognition element—bioreceptor—is paramount (108). Given that the surface chemistry of AuNPs can be tailored through the incorporation of different functional moieties (96), it is possible to modulate the affinity of an AuNP towards a wide range of analytes.

Due to the ease of functionalization coupled to their nanoscale properties, AuNPs are a very versatile scaffold for the development of sensing platforms. Herein, the most prevalently used bioreceptors that allow AuNPs to have specific biomolecular recognition abilities will be described.

1.5.1 **Nucleic acids sensing**

Nucleic acids (DNA or RNA) are widely used in sequence dependent interactions of many hybridization assays, such as fluorescence in situ hybridization (FISH) (143, 144), DNA amplification techniques, such as PCR (145), loop-mediated isothermal amplification (LAMP) (146), hybridization chain reactions (HCR) (147) and microarray technology (148). Also, there are chemical analogues of nucleic acids that can be used as bioreceptors, such as locked nucleic acids (LNA) and peptide nucleic acids (PNA). For LNA, the ribose of the nucleotide contains a methylene bridge between the 4′ carbon and 2′ oxygen, yielding in a less flexible conformation due to a more pronounced base stacking (149), which leads to higher affinity towards the complementary strand as demonstrated by higher melting point of the duplexes (150, 151). For PNA, the phosphate backbone is replaced with *N*-(2-aminoethyl)- glycine molecules linked by peptide bonds, which removes the electrostatic repulsion between strands, allowing for more efficient hybridization. PNAs and LNAs are also more resistant to nucleases (152, 153) adding to the stability of the bioreceptor in complex media. These characteristics make both LNA and PNA suitable for biosensing. As mentioned before, Mirkin *et al* (154), where the first to report the use of thiol-modified ssDNA functionalized AuNP, using a two-probe approach, for the detection of a complementary target sequence – Figure 1.11. Here, one probe is complementary to the 5' and the other to the 3' of the target.

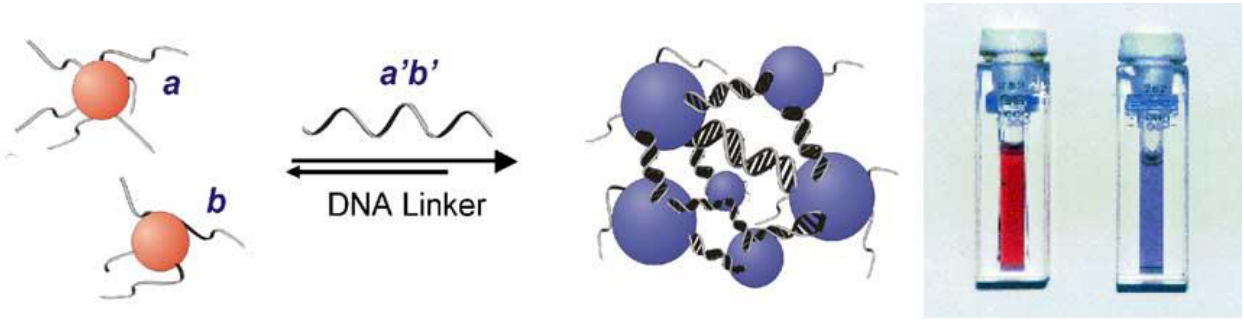

Figure 1.11. Representation of the cross-link method developed by Mirkin *et al*. Two population of AuNP, functionalized with different oligonucleotides (a and b) are dispersed, presenting a red color. In the presence of a complementary target, the interparticle distance decreases due to the hybridization of the AuNP to the target sequence, causing a red-shift in the LSPR (blue color). From (154)

The presence of the complementary target to the ssDNA immobilized onto the surface of the AuNP leads to the coupling of the LSPR of both probes, due to the target mediated cross-link. The cross-linked network causes a red shift of the LSPR to 578 nm. This approach allowed the identification of single nucleotide

polymorphisms (SNP) using a tight control of the temperature. In this situation, the presence of the SNP leads to a sharp melting transition of the cross-linked network.

Non-cross link approaches have been also developed. Baptista *et al*, devised a methodology where only one probe was necessary to attain SNP sensibility. Here, the increased electrostatic repulsion mediated by the hybridization of the target sequence increases the stability against salt mediated aggregation – Figure 1.12. This has been successfully applied in the detection of human pathogens, detection of biomarkers for chronic myeloid leukemia (CML) (155) and gene expression analysis (156), both without the need of retrotranscription or using isothermal amplification techniques (157).

Nucleic acids as bioreceptors are not limited to hybridization based detections. Aptamers are a special class of nucleic acids that have an affinity towards a wide range of analytes. These are short sequences of nucleic acids which have a secondary structure with a structural affinity towards a given analyte or which acquire a three-dimensional structure upon analyte binding (158). These interactions are ruled by a combination of pi bond stacking, London dispersion forces and hydrogen bonding (159, 160). Some aptamers have been developed to bind to a wide range of analytes such as metal ions (161), proteins (162, 163) and whole cells (164). As such, they are versatile as bio-recognition molecules for sensing applications due to their antibody-like specificity coupled with their ease of synthesis, higher thermal stability, cost-effective production, a wide range of analytes that can be targeted, lower batch to batch variation and simple modification with different chemical moieties (165).

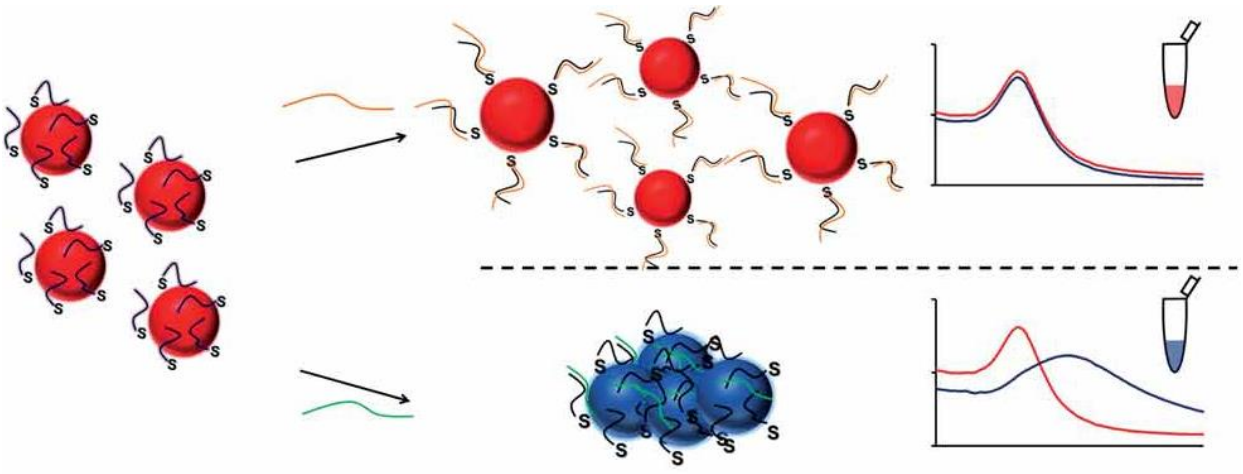

Figure 1.12. Representation of the non-cross link method developed by Baptista *et al*. Hybridization to a complementary target stabilizes the nanoprobe, and no salt-induced aggregation is observed. Presence of a non-complementary target does not stabilize the nanoprobes against salt-induced aggregation. Differences in particle size illustrate that depth and spatial organization (particles closer or further away). Adapted from (166)

1.5.2 **Protein sensing**

Proteins are another class of biopolymers that can be used as biorecognition agents in biosensing platforms. Antibodies (Ab) are one of the most used protein bioreceptors for biosensing due to their specificity towards their respective antigen. The specificity between the Ab paratope and antigen epitope has been applied in several immunoassays for clinical diagnosis through the well-established ELISA (167) and their use has been extended to point of care (POC) suitable testing such as lateral flow assays (LFA), i.e., pregnancy tests (168). Peptides and enzymes are also versatile bioreceptors for AuNP-based sensing as they can be functionalized to the surface of AuNP without losing their biorecognition capabilities. For instance, the high local concentration of immobilized enzymes at the surface of AuNP coupled to their catalytic specificity can be used for signal enhancement. Peptides, on the other hand, can serve as binding partners of an interaction event or be a substrate for specific reactions (108, 169).

1.5.3 **AuNP based fluorescence biosensors**

The occurrence of fluorescence quenching at the proximity of AuNPs can occur either by NSET or by FRET (170, 171) These two phenomena have been used for the development of biosensing platforms that detects the nucleic acids interaction, enzymatic interactions, antibody/antigen interactions.

Since nucleic acid biosensors typically function through a hybridization and/or coordination events(172), the manipulation of the sequence and the secondary structure of this biomolecule can be used for the detection of a plethora of nucleic acid targets as well as different analytes. Dubertret *et al* (124) presented a variation of a molecular beacon (173), where the DABCYL quencher (174) is replaced by a AuNP. In this system, a ssDNA hairpin structure was used to functionalized a 1.4 nm AuNP, generating a Au-nanobeacon, that was devised to detect single base mismatches. In the presence of the target nucleic acid, the hybridization to the loop portion of the molecular beacon, leads to the separation of the fluorophore from the quencher, restoring its fluorescence. The Au-nanobeacon allowed the discrimination between a fully complementary target and a target harboring a single nucleotide mismatch with a 100-fold enhanced sensitivity when compared to the conventional molecular beacon. Rosa *et al* (175) and Beni *et al* (176) applied the same principle, using 13 nm AuNP, for the real-time quantification of cMYC RNA (10.3 fmole of RNA per minute) and for the detection of mutations associated with cystic fibrosis (up to 1 nmolar), respectively. Pan *et al* (177), developed a gold nanobeacon with four different molecular hairpins, each one

labeled with a different fluorophore and specific for different mRNA sequences (c-MYC (178), TK1 (179), GalNac-t (180), GAPDH (181)) important for cancer diagnostics. This system could detect each target down to 50 nM.

The AuNP can also serve as a transfection agent, allowing the internalization of the functionalized molecules on the surface of the AuNP. This, coupled to the Au-nanobeacon technology was used for the development of platforms that could signalize the occurrence of hybridization via an increase of emission within the cell. This was demonstrated by Mirkin *et al* (182), where the oligo functionalized AuNP was previously hybridized to a fluorophore-labeled oligonucleotide (reporter probe). In this conformation, the emission of the fluorophore is residual due to the proximity to the AuNP surface. This construct was then transfected into cancerous derived breast cells. The hybridization of the complementary mRNA to the functionalized ssDNA, displace the reporter probe leading to the increase of its emission. Conde *et al* a similar approach using Au-nanobeacons and demonstrated that the hybridization of the complementary mRNA not only generates a positive detection signal, but also leads to the decrease of the complementary mRNA levels. This is of paramount importance for cancer therapy and has been used for the development of several cancer therapeutical approaches (98, 117, 183–185).

Besides the molecular beacons, nucleic acid aptamers can be used for fluorescence biosensing, since aptamers can be modified with fluorescence dyes and have a highly ordered tertiary structure that allows these molecules to coordinate, in a stable manner, with different targets such as proteins, nucleic acids and small ligands (186–188).

Chen *et al* (189) develop an aptamer conjugated AuNP that could not only recognize, but also, measure the distance between two binding sites on a membrane receptor (PTK7) in live leukemia T-cells, in a homogenous format. Briefly, an aptamer with a high affinity for a domain of PTK7 receptor was functionalized on AuNP (aptamer-AuNP) and an AlexaFluor®488 labeled antibody (anti PTK7) were used. In the presence of the PTK7 receptor, the aptamer-AuNP and the AlexaFluor®488 labeled antibody binds to their respective binding sites, leaving the fluorophore and the AuNP within energy transfer distance, leading to a decrease in the Alexa®Fluor488 fluorescence. Therefore, the distance between the two domains could be inferred through the variation of the quenching efficiency through the use of nanoparticle with different sizes.

Wang *et al* (190), presented a system using an aptamer-AuNP for the detection of proteins, using thrombin as a model. These authors tested different strategies for maximizing the detection of this protein. First, the functionalized aptamer is hybridized with a fluorophore-labeled ssDNA. Since the fluorophore is in the vicinity of the AuNP, its fluorescence is quenched and upon addition of thrombin, the fluorophore-labeled ssDNA is displaced, and hence its fluorescence is restored. In the other two strategies, the aptamer is labeled

with the fluorophore (limit if detection of 0.46 ± 0.18 nM). The other case, the aptamer is hybridized with a ssDNA (that is functionalized in the AuNP), and in the presence of thrombin, the aptamer is displaced from the surface of AuNP, restoring the fluorescence of the fluorophore (limit of detection 3.78 ± 0.33 nM). The third strategy is very similar to the previous, but the aptamer is electrostatically adsorbed to the surface of the AuNP (limit of detection 3.50 ± 1.40 nM). Zhang *et al* (191) presented a similar system, as a proof of concept, where three different aptamers specific for adenosine, potassium and cocaine, were labeled with different fluorophores and hybridized to the ssDNA functionalized at the AuNP surface. In the presence of one of these analytes, the respective aptamer is displaced from the surface of the AuNP and therefore, the fluorescence of each dye-labeled aptamer is restored. Chung *et al* (192), demonstrated a method for the simultaneous detection of Pb^{2+} and Hg^{2+} in human serum. In this method, two different aptamers (one for Pb^{2+} an another for Hg^{2+}) are hybridized to a fluorophore-labeled ssDNA (each ssDNA is labeled with different fluorophores), and in the presence of either Pb^{2+} or Hg^{2+} the ssDNA was displaced from the aptamer, and consequently, the fluorescence of each dye, recovered. With these AuNP conjugated AuNP complex it was possible to detect 121 pM and 128 pM of Hg^{2+} and Pb^{2+}, respectively, in human sera.

AuNP quenching can also be used for the detection of DNA cleavage by specific nucleases. Ray *et al* (193), demonstrated that the cleavage of a dye-labeled dsDNA mediated by an S1 nuclease, leads to a recovery of the fluorescence signal by 120 times, comparing to its quenched state. This approach is more sensitive than the usual techniques, such as HPLC and UV-Vis assays. Park *et al* (194), applied the same principle for the detection of specific activity of the protease MM-732. A dye-labeled peptide was used for the functionalization of an AuNP, leading to the quenching of the said dye. In the presence of the specific protease, the peptide is hydrolyzed promoting the separation of the dye from the AuNP surface, restoring the fluorescence of the dye. With this system, it was possible to detect the protease down to 10 ng/ml.

Yang *et al* (195), developed an indirect immunoassay based on FRET, using Bovine Serum Albumin as a model antigen. AuNP were used as quenchers (acceptors) and a fluorophore (Fluorescein isothiocyanate) labeled anti-BSA antibody as a donor. The BSA was functionalized on the surface of the AuNP, and the formation of the complex anti-BSA@BSA@AuNP resulted in a decrease in the fluorescence of Fluorescein isothiocyanate, due to the occurrence of FRET between the dye and the AuNP. The linear range of this system was 2.9 - 43.5 nM, with a detection limit of 0,5 nM. Mayilo *et al.* (196) proposed a similar system for the detection cardiac troponin T (cTnT), using homogenous sandwich immunoassay. In this approach, the cTnT interacts with two different antibodies, one functionalized on the surface of a AuNP and the other labeled with a fluorophore. In the presence of cTnT, both antibodies interact with it, bringing the fluorophore to the vicinity of the AuNP, thus quenching it. The degree of quenching depends on the number of complexes formed in solution, and this system presented a detection limit of 0.02 nM. Guirgis *et al* (197), presented a AuNP quenching immunoassay for malaria antigen detection. Here, a Cy3 labeled Plasmodium

falciparum heat shock protein 70 (PHsp70) forms an immune complex with an AuNP functionalized with an anti-PHsp70 Antibody. As such, the AuNP quenches the cy3 fluorescence. When the free PHsp70 antigen is present, the Cy3 labeled PHsp70 is displaced from the surface of the AuNP, leading to an increase in the Cy3 fluorescence. The authors tested two different approaches: a covalent bonding between the antibody and the AuNP, and an electrostatic adsorption. It was concluded that the adsorption method yielded a higher quenching efficiency, with a limit of detection of 2.4 µg/ml and a linear range of 8.2 to 23.8 µg/ml of antigen.

1.6 **Chronic Myeloid Leukemia**

Chronic myeloid leukemia (CML) is a myeloproliferative disorder with an annual incidence of 1–2 cases per 100,000 adults, accounting for 15–20% of newly diagnosed cases of leukemia in adults (198, 199). There has been a steady evolution of the strategies for laboratory diagnostics of CML, from cytogenetics to molecular characterization that supports therapeutic decisions, which ought to be tailored to the patient for improved therapy success.

The molecular hallmark of CML is the Philadelphia chromosome (Ph) – a shortened and truncated version of chromosome 22 present in at least 90% of patients (200). This abnormality occurs in the myeloid lineage of hematopoiesis and results in the reciprocal translocation of genetic material between the long arms of chromosomes 9 and 22 – t(9;22)(q34;11) – Figure 1.13.

The resulting fusion gene – the BCR-ABL1 oncogene – shows unregulated activity that triggers malignant cell transformation (200, 201). Constitutive expression of the active protein kinase leads to phosphorylation of a series of intracellular substrates, perturbing multiple signaling pathways, including the RAS/mitogen-activated protein kinases (RAS/MAPK), phosphatidylinositol-3- kinase/protein kinase B (PI3K/AKT), and Janus kinase 2/signal transducer and activator of transcription 5 (JAK2/STAT5) pathways. This phosphorylation cascade promotes cell growth, survival advantage, cytokine independence, protection against apoptosis, and cause the clonal expansion of fully differentiated myeloid cells (202–204) Chromosome instability due to three well-defined breakpoint regions in the breakpoint cluster region (BCR) gene (m-bcr, M-bcr, and l-bcr), originates a range of BCR-ABL1 variants of molecular weight: 190, 210, and 230 kD, containing the same region of the Abelson oncogene (ABL1) tyrosine kinase at the C-terminal but including different portions of BCR sequence at the N-terminal (205, 206). This reciprocal translocation during hematopoiesis combined with alternative splicing events may result in at least eight different reported BCR-ABL1 transcripts, all encoding proteins with high tyrosine kinase activity (205).

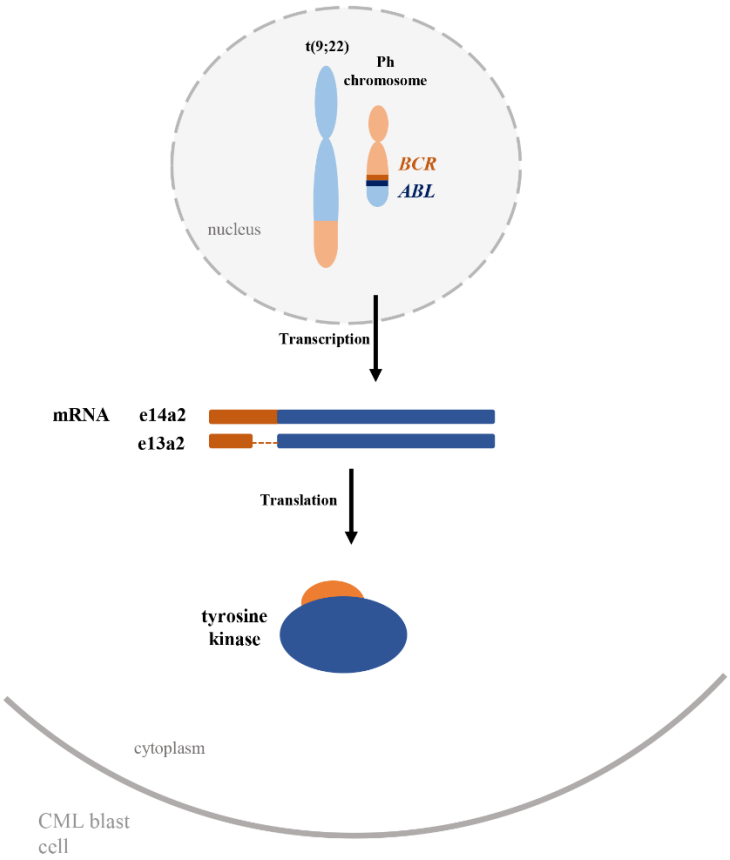

Figure 1.13. Schematic representation of the BCR-ABL translocation. The disease-causing translocation results in a shortened chromosome 9, the Philadelphia chromosome. The two most frequent BCR-ABL1 splicing variants (accounting for 95% of Ph+ cases) are represented, as well as the encoded enzyme.

Nevertheless, most Ph-positive (Ph+) CML patients (~95%), harbor the 210 kDa protein (p210BCR-ABL1) translated from either the e13a2 (b2a2) or e14a2 (b3a2) fusion transcripts. Less frequent in CML is the 190 kDa fusion protein (p190BCR-ABL1) translated from an e1a2 junction (<5%). ABL1 breakpoints can occur anywhere over a larger area at its 50 end but occur invariably between exon 1a and exon 2 (205, 207). Additional rare BCR-ABL1 fusion transcripts (<1%) have been described, such as e14a3, e13a3, e1a3, e19a3, e6a2, e8a2, and e18a2 (208, 209) Throughout the literature, there is plenty of discussion concerning the position of the breakpoint within the M-bcr region (5' M-bcr versus 3' M-bcr), or the type of fusion transcript (e.g. e13a2 versus e14a2) and the influence in CML phenotype (205, 210). The success of precise therapy for CML depends greatly on the diagnosis, whether in the early stages of the disease or through treatment. Three key parameters should be considered when monitoring CML patients' response to therapeutics: hematologic response or normalization of blood counts; cytogenetic response, which relates to the percentage of Ph+ cells in the bone marrow; and molecular response, defined by the expression level of BCR-ABL1 transcript in a bone marrow or blood sample. Currently, two PCR-based modalities can be

performed to detect the BCR-ABL1 transcript: nested reverse transcriptase polymerase chain reaction (RT-PCR), a qualitative approach; or real-time quantitative reverse transcriptase polymerase chain reaction (RT-qPCR), a quantitative assay. Nested RT-PCR provides a characterization of the transcript allowing the identification of the most frequent transcripts: e13a2 or e14a2, and, additionally, the atypical fusion transcripts, e1a2 (211). Recently, the ELN (European LeukemiaNet) expert panel acknowledged that the transcript type (e13a2 versus e14a2 or other more atypical variants) may influence response to therapy and disease outcome, which demonstrates the relevance of performing such molecular screening (212). RT-qPCR has a strong correlation between the results obtained from peripheral blood and bone marrow, allowing molecular monitoring without the necessity of obtaining bone marrow aspirations (212, 213). RT-qPCR is the current method of choice for CML molecular characterization and should be performed before initiation of specific therapy to establish a baseline for BCR-ABL1 RNA levels for each individual patient (212). RT-qPCR is the only tool capable of monitoring responses after patients reach complete cytogenetic response (CCyR-defined as absence of Ph+ chromosomes (213)). Information on the type of transcript and its expression levels can only be provided at the messenger RNA (mRNA) level, due to alternative splicing events and consequent genetic heterogeneity. Compared with cytogenetic testing, PCR-based molecular monitoring offers an analytical sensitivity 100–1000 times greater than FISH or bone marrow cytogenetic analysis (213), but strongly dependent on the quality and efficiency of RNA extraction and/or reverse transcription. Nevertheless, these approaches are performed separately for each of the BCR-ABL fusion sequences as a one pot platform capable of detecting the both fusion sequence in a single test tube is still lacking. Here, the development of a single platform that is able to detect both fusion sequence will be devised.

1.7 Scope of the Thesis

Biosensors using nanomaterials for diagnostics purposes is a research field that has expanded greatly in recent years. There is a growing need for the development of cheaper sensors with an increased performance that could use as an alternative for the current diagnosis technologies.

Gold nanoparticles are a widely-used nanomaterial for the development of optical biosensors, due to their ease of surface modification coupled to their unique nanoscale optical properties. One of the most appealing optical properties of AuNPs is their strong surface plasmon resonance, that is known by the ability to modulate the fluorescence of nearby fluorophores. The work developed in this thesis aims to integrate the spectral codification tool developed by Giestas *et al* with Gold nanobeacon technology developed by Dubertret and further optimized by Rosa and Conde *et al.* With this integration, it is expected the

development of a AuNP molecular beacon based biosensor coupled to a wavelength shift mediated by FRET. This platform will be optimized for the detection of the most common CML biomarkers, the e13a2 and e14a2 BCR-ABL fusion sequences. This model was chosen because its specific detection is complex, considering that the detection platform should not be triggered by the partial complementary targets; the isolated BCR and ABL sequences, and must be able to differentiate between both fusion sequences. To do so, the design of the conventional molecular beacons was modified into a two-component molecular beacon, where the donor labeled palindromic sequence acts as a secondary target for an acceptor-labeled oligonucleotide. Several techniques were employed in this characterization, such as steady-state fluorescence spectroscopy (the main technique used in the course of this work), Isothermal Titration Calorimetry, MicroScale Thermophoresis, Small-Angle X-ray Scattering and Differential Electrophoretic Mobility Assay. With this approach, the emission of the donor can be used as a signal for the occurrence of hybridization between the target sequence and the gold nanobeacon, and the secondary hybridization of the acceptor-labeled oligonucleotide can be used to identify which sequence is in solution, creating a double channel (Donor and acceptor) confirmation over the detection of a BCR-ABL fusion sequence - BioCode. The application of this technology was also attempted in the *in vitro* visualization of the expression of the fusion transcripts.

2 Materials and Methods

2.1 General information

All reagents used were purchased in the highest purity available from Sigma Aldrich, unless stated otherwise. All aqueous solutions were prepared using distilled (DI) water (18.3 MΩ · cm at room temperature). Aqueous solutions were sterilized by autoclave or filtered through a 0.2 μm sterile filter (Pall Life Sciences). All oligonucleotides were purchased from STAB Vida, and used without further purification unless stated otherwise. The oligonucleotides were suspended in TE buffer (10 mM Tris, pH 7.6 and 0.1 mM EDTA). The concentration of all oligonucleotides was confirmed by UV-Vis Spectroscopy, using the extinction coefficient provided by the manufacturer.

All absorption spectra were collected on a Thermo Scientific ™ 300 UV-Vis Spectrophotometer, using quartz cuvettes with reference number:119.004F-QS and 105.202-QS both with an optical length of 10 mm (Hellma Analytics). During the functionalization procedures, the oligonucleotide concentration was determined in a Nanodrop ND-1000 (Thermofisher). The fluorescence spectra were collected on a Cary Eclipse Fluorescence Spectrophotometer with a peltier accessory for temperature control (Agilent Technologies) using quartz micro cuvettes of reference: 105.251-QS, with an internal chamber of 3 × 3 mm. Fluorescence spectra presented on chapter 3 and chapter 4 were collected using an excitation and emission bandwidth slit of 5 nm, except for the double-labeled BioCode, that were collected using an excitation and emission bandwidth slit of 10 nm. Aqueous solutions used for RNA manipulation were pre-treated with diethylpyrocarbonate (DEPC, 0.1 % (*V*/*V*) for at least 16 hours and then autoclaved to sterilize and degrade the DEPC.

2.2 Fluorophore selection

The fluorophores were chosen based on their absorption and emission wavelengths to ensure the formation of a FRET pair. From the commercially available fluorophores, 6-carboxifluorescein (FAM) and sulfoindo cyanine (Cy3) were selected as donors and used to label the hairpin molecules; 5-carboxy-X-rhodamine (ROX), Dy-520XL Mega Stokes (Dy) and Tetramethyl-6-Carboxyrhodamine (TAMRA) were selected as acceptors and used to label a short oligonucleotide (revelator) with sizes of 8, 10 and 12 bp. The fluorophores were used to label the oligonucleotides via a 6 carbon alkine linker on the 3'-OH extremity.

2.3 Oligonucleotides

The sequence of the used oligonucleotides are presented in Table 2.1 and Table 2.2. Their sequence were chosen using the Basic Local Alignment tools (214), and the hybridization between strands was predicted and optimized using the software NUPACK (215). The hybridization was simulated using a 1 µM concentration of each strand in 100 mM of NaCl at 20 °C, limiting the number possible ensembles to 4.

Table 2.1. Unmodified oligonucleotides.

Name	Sequence (5'-3')	Σ_{260} ($M^{-1}cm^{-1}$)	Mw (g/mol)
Complementary e14a2_21bp (AJ131466.1)	cagagttcaaaagcccttcag	236400	6401
Complementary e14a2_22bp (AJ131466.1)	agagttcaaaagcccttcagcg	215800	6728.4
Complementary e13a2_22bp (AJ131467.1)	ataaggaagaagcccttcagcg	258500	6774
Non-Related	taccagacatgcgtggtccca	224800	6395
BCR-e13a2 (NM_004327.3)	tccgctgaccatcaataaggaagaa	228500	7041.6
BCR-e14a2 (NM_004327.3)	actcagccactggatttaagcagagttcaaaa	321300	9825.5
ABL (NM_005157.5)	gcccttcagcggccagtagcatctgacttt	376500	12257
ABL_out_Rv	gtttgggcttcacaccattcc	257800	6348.2
ABL_in_Rv	ttccccattgtgattatagccta	281300	6964.6
BCR_in_Fwd	cagatgctgaccaactcgtgt	270300	6406.2
BCR_out_Fwd	gaagtgtttcagaagcttctcc	276700	6725.4

Table 2.2. Sequences of donor labeled hairpins and revelator accessed experimentally.

Pair	Name	Hairpin sequence	Hairpin modification	Revelator sequence	Revelator modification
1	37bp_e14a2_hairpin	cacctcgtctgaagggcttttgaactctgacgaggtg	6-FAM (3')	cacctcgt	TAMRA (3')
2	43bp_e14a2_FAM[a]	cacctcgaaatctgaagggcttttgaactctgttttcgaggtg	6-FAM (3')	cacctcgaaa	TAMRA (3')
3	43bp_e13a2_FAM[a]	ccacgccaaacgctgaagggcttcttccttatttttggcgtgg	6-FAM (3')	ccacgccaaa	ROX (3')
4	43bp_e14a2_FAM[a]	cacctcgaaatctgaagggcttttgaactctgttttcgaggtg	6-FAM (3')	cacctcgaaa	Dy-520 Xl MegaStokes (3')
5	43bp_e14a2_cy3[a]	cacctcgaaatctgaagggcttttgaactctgttttcgaggtg	Cy3 (3')	cacctcgaaa	Dy-520 Xl MegaStokes (3')
6	47bp_e13a2_FAM[a]	ttccacgccaaacgctgaagggcttcttccttatttttggcgtggaa	6-FAM (3')	ttccacgccaaa	ROX (3')
7	47bp_e14a2_Cy3[a]	ttcacctcgaaacgctgaagggcttttgaactctttttcgaggtgaa	Cy3 (3')	ttcacctcgaaa	Dy-520 Xl MegaStokes (3')
8	47bp_e14a2_FAM[a]	ttcacctcgaaacgctgaagggcttttgaactctttttcgaggtgaa	6-FAM (5')	ttcacctcgaaa	Dy-520 Xl MegaStokes (3')

a After specific hybridization assessment, these oligonucleotides sequences were also modified with a C_6 thiol functional group at the 5' end for AuNP functionalization

2.4 Hairpin Characterization

2.4.1 Fluorescence spectroscopy

The assembly of the two-component molecular beacon (tcMB), triggered by the presence the desired target sequence was experimentally accessed using fluorescence spectroscopy. An equimolar concentration of donor labeled hairpins and revelator as used - see Table 2.2 for the sequences. The assembly of the desired structure was performed in several buffers, presented on table 2.3. On a first approach, the assembly of pair 1 was tested using a 2.5-fold excess of the complementary target (sequence e14a2) and non-complementary target, as a negative control, in the buffers A, B, C, D – see Table 2.3. The remaining pairs were accessed using an equimolar concentration of donor labeled hairpin, revelator and targets (or a 25% target excess).

Table 2.3. Condition used to evaluate the formation of the desired structure.

	Buffer
A	10 mM Tris-HCl pH 7.5; 100 mM NaCl
B	10 mM Tris-HCl pH 8.0; 100 mM NaCl
C	10 mM Tris-HCl pH 8.0; 50 mM KCl; 3.5 mM $MgCl_2$
D	10 mM Phosphate buffer pH 8.0; 100 mM NaCl
E	10 mM Phosphate buffer pH 8.0; 154 mM NaCl
F	TBE 0.5× pH 8.3; 154 mM NaCl

The formation of pair 2 was accessed in buffer D and E and pair 3 was performed in E and F. Pairs 4 to 8) were performed in F. The specificity of the pairs 2 to 9 was accessed towards the partial complementary targets (ABL, BCR sequence (BCR sequence derived from exon 13 or exon 14) and both – See Table 2.1 for sequences). The emission spectra at 20 °C, either at the hybridization end-point or upon target addition and collected over-time. For the end-point analysis, the reactional mixtures were heated to 95 °C for 30 seconds and allowed to cool down to 20 °C for 20 minutes.

The excitation wavelength depended on the donor used (λ=495 nm for FAM or λ=550 nm for Cy3) and emission was registered between 500 to 800 nm and between 550 nm to 800 nm for 6-FAM and Cy3

respectively. The photomultiplier (PMT) was set at 600 V, and the spectra were collected using a scan rate of 600 nm/min.

2.4.1.1 Fluorescence Melting Assay

A solution containing an equimolar concentration of donor labeled hairpin and revelator (pairs 2, 3 and 4) was prepared in buffer F (Table 2.3) using a 25% of target excess. The solution was then subjected to the thermal program presented in the previous section (used for the end-point analysis), before the increment of temperatures. For pair 2, the melting profile of the donor and acceptor was registered in the presence and absence of the complementary target. For the remaining pairs, the inherent thermal induced emission variation of the fluorophores was in the absence of target and in the presence of 1) a complementary, 2) non-complementary, and 3) a partially complementary target.

The emission spectra were collected using 495 nm as excitation wavelength. Spectra were collected at several temperatures, with a 5-minutes hold before measurement for temperature homogenization. The PMT was set at 600 V, and the spectra were collected using a scan rate of 600 nm/min.

2.4.2 Electrophoretic Mobility Shift Assay

The products of the hybridization reactions using pairs 4 and 5, were separated by gel electrophoresis (5% agarose in 1x TAE (40 mM Tris-HCl, 20 mM acetic acid, 1 mM EDTA, pH 8.0), and in a native 20% polyacrylamide in 1×TBE stained with GelRed™. This staining was performed by submerging the gel in a solution of the dye at 3.5× in the presence of 100 mM of NaCl. The mobility of each fragment was determined using the FIGI (ImageJ) software package (216).

2.4.3 Isothermal Titration Calorimetry

Isothermal titration calorimetry (ITC) was performed in a NanoITC (TA instruments) at 20 °C. The lyophilized DNA strands (sequence of pairs 2 and 3) were hydrated and suspended in the hybridization buffer (buffer F – Table 2.3). All oligonucleotide solutions were degassed prior to use. The sample chamber

was filled with the hairpin solution (0.964 ml) with a concentration ranging from 15 to 50 µM. The reference chamber was filled with the same volume of hybridization buffer. After thermal equilibrium (baseline stabilization) at 20 °C, the hairpin solution was titrated with the complementary target through the injection of aliquots of 3 to 5 µl of the complementary target at a concentration 10× the hairpin concentration in the sample chamber. The injections were performed at a minimum interval of 3 minutes (up to 5 minutes per injection) pass the point of hairpin saturation (equimolar concentrations). When possible, the titration continued beyond equimolar concentration to determine the heat of dilution. Upon the target and hairpin complex formation, the volume of the reaction chamber was corrected and the revelator was used to titrate the previously formed complex using the same setting as presented above.

2.4.4 **MicroScale Thermophoresis**

For the MicroScale Thermophoresis (MST) experiments, a solution of FAM-labeled hairpin (pair 2) was prepared at 30 nM in buffer F. The binding affinity for the hairpin/target hybridization was determined by the titration of the unlabeled complementary target against the fixed concentration of the hairpin. The target was titrated in 1:1 serial dilutions with an upper limit of 10 µM and a lower limit of 0.03 nM. For the binding affinity of the revelator hybridization, 30 nM of the FAM-labeled hairpin was pre-hybridized, for at least one hour at 20-23 °C (room temperature - RT), with 240 nM of complementary target. The hybridized hairpins were titrated with the unlabeled revelator sequence in 1:1 serial dilutions with an upper limit of 30 µM and a lower limit of 0.92 nM. The measurements were performed on a NanoTemper Monolith NT.115, using the blue LED at 60% power, and medium power of the 1480 nm infrared laser (manufacturer settings). The laser-on time was 20 seconds and laser-off was 5 seconds. The samples were measured in the standards capillaries produced by NanoTemper.

2.4.5 **Small-Angle X-ray Scattering**

The Small-Angle X-ray Scattering (SAXS) experiments were performed at EMBL P12 beamline, Petra III, Hamburg, Germany and at BM29 beamline, European Synchrotron Radiation Facility (ESRF), Grenoble, France. The scattering profile for each component (43bp_e13a2_hairpin, 43bp_e14a2_hairpin, e13a2 target sequence, e14a2 target sequence, e13a2-revelator and e14a2-revelator) was recorded as well as each hybridization step. The e13a2 components were measured at 4 °C, the e14a2 components and each

hybridization step were measured at 10 °C. Each condition was measured at different concentrations, from 2 mg/ml to 0.25 mg/ml in buffer F (prepared in a 1:1 serial dilution). Data of each condition were collected at different concentrations, from 2.0 to 0.25 mg/ml in buffer F (prepared in a 1:1 serial dilution). The primary data reduction was done automatically by the pipeline software (EDNA for the ESRF (217), and SASFLOW for Petra III (218)). The data was processed with the ATSAS package (219) using standard procedures, corrected for buffer contribution, and extrapolated to infinite dilution using the PRIMUS software (220) from the ATSAS package.

Using GNOM from the ATSAS package (221) a distance distribution function (p(r)) was determined based on the maximum intraparticle distance, D_{max}, pre-established by the program AutoGNOM. The radius of gyration (R_g), the intensity at zero angle ($I_{(0)}$) and the hydrated particle volume or Porod volume (Vp) were also determined.

The overall shape of each component and each hybridization step were calculated ab initio from its scattering profile using the program DAMMIF (222). The most typical model out of 20 independent reconstructions was determined by DAMAVER (223) and SUPCOMB (224).

2.5 Gold nanoparticles synthesis

Gold nanoparticles were synthesized via citrate reduction described by Turkevich (70), refined by Lee and Miesel (72), and widely used within the Nanomedicine@FCT research group.

All glassware used were previously treated with Aqua Regia (1 HNO_3:3 HCl) for a minimum of 12 hours. The glassware was then thoroughly washed, using at least 15 volumes of DI water per recipient. The appropriate amount of tetrachloroauric salt was handled with Teflon covered spatulas and dispersed in DI water in a clean, dust free and sterile recipient. In a 500 ml, round bottom flask equipped with a Liebig condenser, 250 ml of the tetrachloroauric at 1 mM was heated until boil with vigorous stirring. Upon stable reflux, 25 ml of a citrate tribasic solution at 38.8 mM (at 75 °C) was quickly injected into the tetrachloroauric solution. Upon successful color change (from pale yellow to dark black and finally ruby red), the reaction was kept for at least 20 minutes with vigorous stirring, yielding citrate-capped AuNP (AuNP@citrate). After 20 minutes, the heat was turned off and the agitation was kept until the AuNP@citrate solution reached RT. The AuNP@citrate were filtrated using membranes with 0.2 µm pore (Acrodisc) and kept in the dark at 4 °C until further use. The AuNP@citrate were characterized by UV-Vis, Transmission Electron Microscopy (TEM) and Dynamic Light Scattering (DLS). A $\varepsilon_{520\ nm}$ of 2.33×10^8 (225, 226) was used to quantify the AuNP@citrate.

2.6 Gold nanoparticle functionalization

2.6.1 AuNP functionalization with PEG - Ellman saturation curve

The AuNP synthetize on section 2.5 were further functionalized using a commercial hetero-functional polyethylene glycol (PEG) modified with a thiol group O-(2-mercaptoethyl)-O'-methylhexa(ethylene glycol), $C_{15}H_{32}O_7S$, 356.48 g/mol. To determine the appropriate PEG coverage, solutions containing 10 nM of the AuNP and 0.028% of SDS were incubated with a variable amount of PEG (0.003 mg/ml; 0.0045 mg/ml; 0.006 mg/ml, corresponding to 30 %, 45 % and 60 % surface coverage respectively) and were allowed to rest for 16 h, generating PEGylated AuNP (AuNP@PEG). These AuNP@PEG were purified through centrifugation at 14000 ×g for 45 minutes at 4 °C (Sartorius 2-16K). The oily pellet was washed three times and dispersed in MilliQ water. The AuNP@PEG was filtered through a 0.2 µm membrane, stored in the dark at 4 °C until further use.

2.6.2 PEGylated AuNP functionalization with hairpins

The thiolated donor labeled ssDNA with a hairpin structure were hydrated in an appropriate amount of DI water and a small fraction of this solution (5 µl at ≈ 1 mM) was aliquoted and kept in the dark at -20 °C until further use. The remaining solution was incubated for at least 2 hours at RT with 0.5 M DL-dithiothreitol (DTT). After this incubation, the DTT was brought to a final concentration of 0.1 M using DI water. The ssDNA was then extracted with 2 volumes of ethyl acetate and centrifuged at 9000 ×g for 5 minutes at RT. This was repeated 2 additional times. The thiolated oligonucleotide was then desalted with a NAP-5 column (GE Healthcare), following the manufacturer protocol, using 10 mM of phosphate buffer pH 8.0 as eluent. UV-Vis spectroscopy was used to quantify the nanomoles of purified double labeled ssDNA. The appropriate amount of nanomoles of AuNP@PEG (either with 30%, 45% or 60% of PEG coverage) was added to the purified double labeled ssDNA for a final ratio oligo:AuNP@PEG of 100:1 (based on the proportion of OD_{260} to nanomole of donor labeled oligonucleotide). Age I (10 mM phosphate buffer pH 8.0, 2% SDS (w/v)) was added to the solution for a final concentration of SDS of 0.01 % (w/v), and allowed to rest for 20 minutes at RT. The NaCl concentration was increased in 50 mM NaCl steps by adding the appropriate volume of AGE II (10 mM phosphate buffer, 1.5 M NaCl, pH 8.0) up to a final concentration of 100 mM NaCl. Then, the NaCl concentration was increased in 100 mM steps, up to a final

concentration of 300 mM. After each NaCl increment, the AuNP solution was sonicated for 20 s (Ultrasonic bath Elmasonic S10H) and stabilized for 20 minutes at RT. After the last addition of AGE II, the solution was left to rest for at least 16 hours at RT with mild agitation (avoiding foam formation) and protected from light. The mixture was centrifuged for 40 minutes at 14000 ×g at 4°C, and the oily pellet washed with 10 mM phosphate buffer at least three times. All supernatants were saved for subsequent analysis at 4 °C protected from light.

2.6.3 PEGylated AuNP dual functionalization with hairpins

The methodology described in section 2.5.2 was performed, with slight modifications. Upon quantification by UV-Vis of both thiolated hairpin sequences (either against variant e13a2 and variant e14a2) after the Nap-5 desalting procedure, the limiting hairpin was used as a reference and an equimolar solution of both hairpins was used for the functionalization of AuNP@PEG, using the same 100:1 ratio of oligo mixture to AuNP@45%PEG.

2.7 Au-nanobeacon characterization

2.7.1 Quantification of PEG molecules per NP

The AuNP synthesized on section 2.5 were functionalized using PEG-modified with a thiol group. To determine the appropriate coverage of PEG, solutions containing 10 nM of AuNP and 0.028% of SDS were incubated with a variable amount of PEG (0 mg/ml; 0.006 mg/ml; 0.008 mg/ml; 0.01 mg/ml; 0.035 mg/ml; 0.1 mg/ml) for 16 h with mild agitation. The PEGylated AuNP (AuNP@PEG) were purified by centrifugation at 14000 ×g for 45 minutes at 4 °C. The oily pellet was washed three times and dispersed in DI water. All supernatants fractions were collected and kept at 4 °C for subsequent analysis. The excess thiolated PEG chains was quantified by mixing 200 µl of each supernatant with 100 µl of 0.5 M phosphate buffer pH 7.5 and reacting with 7 µl of 5,5'-dithio-bis(2-nitrobenzoic) acid (DTNB) at 2 mg/mL (prepared in the 0.5 M phosphate buffer pH 7.5) for 5 minutes. After the incubation, the absorbance at 412 nm was measured. The Abs_{412} were then interpolated in a calibration curve prepared with the known concentration of thiolated PEG in the same conditions as the supernatants. The amount of PEG-functionalized was

determined by the difference of the PEG used for functionalization and the amount of removed PEG in every fraction collected during centrifugation. The AuNP were incubated with 0.003 mg/ml, 0.0045 mg/ml and 0.006 mg/ml, corresponding to 30 %, 45 % and 60 % surface coverage, respectively.

2.7.2 Quantification of Oligonucleotides per NP

The AuNP@PEG with 45% coverage generated in section 2.6.1 were further functionalized with the donor (either FAM or Cy3) labeled single strand oligonucleotides with a hairpin structure (herein denoted as a hairpin). The number of hairpins per particle was determined through the difference between the added oligonucleotides and those present on the supernatant collected during centrifugation. Direct excitation of the donor was performed for each fraction collected after each centrifugation step. The collected spectra were integrated and the value interpolated into a calibration curve with known concentration (with the signal integration plotted against concentration) in the same conditions as the supernatant. All emission spectra were integrated to minimize background noise.

2.7.3 Transmission Electron Microscopy

(Outsourced to IST microtechnology lab)

The synthesized AuNP@citrate and Au-nanobeacons were characterized by TEM in the MicroLab (IST-Lisboa) by Isabel Nogueira. The goal was to determine the morphology and diameter of the AuNP core. The AuNP were measured at the post-synthesis concentration (ranging from ≈11 nM to ≈14 nM). An appropriate volume was deposited to cover the surface area of the carbon-copper grids and air dried. The TEM was performed in a HITACHI H-8100 microscope. The average size and size dispersion was determined by measuring 250 to 500 particles per condition using the FIGI (image J) software package (216).

2.7.4 Dynamic Light Scattering

The hydrodynamic diameter of the AuNP@citrate, AuNP@PEG and Au-nanobeacons were determined by DLS using a SZ-100 Nanopartica Analyzer (Horiba) equipped with a peltier temperature control

(Horiba). A volume of at least 500 µl at 2 nM of AuNP@citrate, AuNP@PEG or Au-nanobeacon was measured with a prior thermal stabilization of at least 5 minutes. Each sample was measured at least 3 times, using a scattering angle of 90 °. For the melting assays, prior to each measurement and after each temperature increment, the solution was allowed to stabilize for 10 minutes. The measurements were performed at several temperatures: 20 °C, 25 °C, 40 °C, 50 °C and 60°C.

2.7.5 Zeta Potential

The zeta potential of AuNP@citrate and Au-nanobeacons were measured in an SZ-100 Nanopartica Analyzer (Horiba) using zeta potential cell with carbon coated electrodes (Horiba). A volume of at least 200 µl at 2 nM (in MilliQ water) of AuNP@citrate, AuNP@PEG or Au-nanobeacon was measured using an electrode voltage of 3.4 V. The viscosity of the medium ranged from 0.891 to 0.896 mPa.s with a conductivity between 0.173 and 0.196 mS/cm, using the Smoluchowski approximation (227).

2.8 BioCode synthetic target detection

The PMT was set to 800 V and a scan rate of 120 nm/min was used in the following section.

2.8.1 Target detection using BioCode with one acceptor

All detection/hybridization assays were performed with 1 nM of Au-nanobeacon in buffer F (Table 2.3). For the positive sample (POS), 500 nM of e13a2or e14a2 target sequence and 50 nM of the respective acceptor; for the Negative (NEG), 500 nM of non-complementary target and 50 nM of the respective acceptor; for Donor blank, 500 nM of complementary target and with 50 nM of the respective acceptor; for the reaction blank, water was added in the presence of 50 nM of the respective acceptor. To control and fully characterize the detection events, hybridizations were performed by (1) pre-hybridize the respective targets before collecting the emission spectra; (2) collecting several emission spectra before and after of addition of the respective targets and follow hybridization over time.

2.8.2 Acceptor titration against double labeled BioCode

The revelator titration was performed in buffer F against 1 nM of double-labeled BioCode. To ensure a target excess in each situation, 1 µM of each target was used. An increasing concentration of each revelator was added to each reaction assay (0.001; 0.01; 0.05; 0.1 µM). In parallel, reactions with the same final concentration of revelator in the absence of complementary targets were prepared and used as fluorescence baseline.

2.8.3 Target detection using double labeled BioCode and one acceptor

All detection/hybridization assays were performed with 1 nM of Au-nanobeacon in buffer F. For the POS, 500 nM of e13a2 and/or e14a2 target sequence was used with 50 nM of the respective acceptor; for the NEG, 500 nM of NC target and 50 nM of the respective acceptor; for Donor blank, 500 nM of each complementary target; for the reaction blank, water was added in the presence of 50 nM of the respective acceptor. The specificity of the double-labeled BioCode was assessed in the presence of the partially complementary targets ABL and BCR. The detection of the hybridization events was performed by collecting several emission spectra before and after of addition of the respective targets and follow hybridization over time.

2.8.4 Target detection using double labeled BioCode and two acceptors

The hybridization assays were performed with 1 nM of the double-labeled Au-nanobeacon in buffer F in the absence and in the presence of 50 nM of both acceptors (ROX and Dy-520Xl MegaStokes) labeled oligonucleotides. The fluorescence baseline was determined in the absence of target. The spectral response of the double-labeled BioCode was collected in the presence of 1 µM of either the e13a2 or e14a2 and in the presence of both targets. The hybridizations were performed at 20 °C for one hour at RT and the emission spectra were collected.

2.9 Biological relevance target

2.9.1 Human lymphoblastic cell culture maintenance

Immortalized cell lines derived from patients with Chronic Myeloid Leukemia (CML) in blast crisis, K562 (228) (BCR-ABL e14a2 fusion transcript positive, e13a2 negative) and BV173 (229) (BCR-ABL e13a2 fusion transcript positive; e14a2 negative) were cultured in DMEM and RPMI with 10 % FBS, respectively, at 37 °C with 5 % CO_2. Human monocytic leukemia cell line (THP1) (230), negative for BCR-ABL, was cultured in RPMI with 10% FBS, at 37 °C with 5% CO_2. As such, the k562 cell line provided the e14a2 target, BV173 provided the e13a2 target and THP1 provided a non-related template (negative control) for both cell lines (K562 and BV173).

2.9.2 Total RNA extraction

Total RNA was extracted from K562, BV173, and THP1 cell lines. The cells were counted using a hemocytometer, and aliquots of 5×10^6 cells were harvested by centrifugation at 200 ×g for 5 minutes at RT. The cell pellets were lysed through the incubation with 1 ml of TRIsure™ (Bioline), for 5 minutes at RT. After incubation, 200 µl of chloroform (4 °C) was added. These aliquots were hand shaken for around 15 seconds and allowed to rest for 3 minutes at RT. Samples were centrifuged at 12000 ×g at 4 °C for 15 minutes. The upper transparent aqueous phase was transferred to a new tube and the bottom, pale green organic phase as well as the white interphase, were discarded. To the aqueous phase, 500 µl of cold isopropyl alcohol (4 °C) was added and allowed to rest for 10 minutes at RT. The samples were centrifuged at 12000 ×g for 10 minutes at 4 °C. The supernatant was discarded and the pellet washed with 1 ml of 75% ethanol (prepared in DEPC treated water), vortexed for 5 seconds and centrifuged at 5000 ×g for 5 minutes at 4 °C. The washing step was repeated. The supernatant was removed and the pellet was air dried. The dried pellet was hydrated in DEPC treated water. Unless used right away, the extracted RNA was stored at – 80 °C. The purity and concentration of the extracted RNA were determined by UV-Vis spectroscopy.

2.9.3 **Reverse transcription**

The extracted RNA, described in the previous section, was used in reverse transcription (RT-PCR) for cDNA synthesis, using the NZY M-MuLV First-Strand cDNA Synthesis kit (Nzytech, Lisbon, Portugal). Random sequence hexamers and oligo$(dT)_{18}$ were used as primers. The RT-PCR-reactions were prepared following the manufacturer's protocol, using 100 ng of the extracted RNA. The samples were subjected to 37 °C for 50 minutes, to synthesize the complementary DNA strand, and then to 85 °C for 5 minutes to reverse transcriptase inactivation. The RNA was hydrolyzed by the addition of 1 µl of the NZY RNAse H from *Escherichia coli* (Nzytech) and incubation at 37 °C for 20 minutes. The cDNA was used right away or stored at -20 °C.

2.9.4 **PCR from cDNA**

Gene-specific primers (BCR_out_Fwd and ABL_out_Rv – Table 2.2) were used to amplify the cDNA in a nested-PCR scheme. The first round of the nested amplification was performed using 1 µl of the cDNA prepared in the previous section, 0.2 mM of each dNTPs, 0.2 µM of the outer primers, 1× *Dream Taq*™ buffer (Fermentas), and 1 unit of *Dream Taq*™ (Fermentas). The following thermal cycling program was used:

1.	95 °C	5 minutes		
2.	95 °C	30 seconds		
3.	55 °C	30 seconds	30 cycles	Thermal cycle 1
4.	72 °C	1 minute		
5.	72 °C	10 minutes		

The second round of the nested PCR amplification was performed using 1 µl of the product generated in the first round of the nested PCR, 0.2 mM of each dNTPs, 0.2 µM of the inner primers (BCR_in_Fwd and ABL_in_Rv) and 1unit of *Dream Taq*™, using the following thermal cycling program:

1. 95 °C 5 minutes
2. 95 °C 30 seconds
3. 55 °C 30 seconds — 30 cycles — Thermal cycle 2
4. 72 °C 1 minute
5. 72 °C 10 minutes

The PCR product length (in bp) confirmation was performed by agarose gel electrophoresis at 1 % in TAE 1x (40 mM Tris, 20mM acetic acid, 1 mM EDTA), 70 V for 1 hour.

2.9.5 **Asymmetric PCR**

The asymmetrical PCR was carried out using the product from the thermal cycle 2 (previous section). Here, 1 µl of the product of the first round was used as a template for the asymmetric PCR in the presence of 0.2 mM of each dNTPs, 0.2 µM of the BCR_out_Fwd and 1 unit of Dream Taq™. The reactional mixtures were subjected to the thermal cycle 1. The confirmation of amplification of product with desired length (bp) was performed by agarose gel electrophoresis at 1% with TAE 1x, 70 V for 1 hour. The resulting amplicons were stored at – 20 °C until use.

2.10 **Detection of fusion sequences**

The detection of the fusion sequences was attempted directly in a pool of total extracted RNA from the cell lines (described in section 2.9.2) after the RT-PCR performed in section 2.9.3 and using the PCR products generated in section 2.9.4 and 2.9.5.

3 Design of two-component molecular beacon as bioreceptor for fusion sequence biomarker for Chronic Myeloid Leukemia

Milton Cordeiro was responsible for the oligonucleotide design, FRET analysis, electrophoretic mobility shift assay, MicroScale Thermophoresis and data analysis of the state techniques. Milton was also responsible for the sample preparation for the SAXS technique and article drafting.

The work described in section 3.6 results from a collaboration with the Structural Biology group at UCIBIO@REQUIMTE, FCT/UNL, Portugal and European Molecular Biology Laboratory-Hamburg Outstation, Germany. Small Angle X-ray scattering (SAXS) data acquisition and processing were performed by Ana Rita Otrelo-Cardoso (UCIBIO@REQUIMTE, FCT/UNL) and Dr Peter Konarev (EMBL, Shubnikov Institute of Crystallography, National Research Centre "Kurchatov Institute").

3.1 Introduction

The use of fluorescence molecules as cellular labeling agents and their use in sensing/detection technologies (Sanger sequencing for example) has revolutionized modern day Biology. Several DNA sensing technologies heavily relies on fluorescence for the indication of the presence/absence of a given target sequence (231–234). Amongst the plethora of detection schemes, the use of molecular beacons provides simultaneously enhanced sequence discrimination and a signal output via FRET (35, 235–238). Conventional MBs are composed by a single strand DNA molecule (ssDNA) in loop configuration – recognition element – labeled with a fluorophore and a quencher in each end, and flanked by palindromic sequences (auto-complementary sequences). This linear ssDNA will exhibit a hairpin structure due to the hybridization of the palindromic sequences, forming a double strand on the extremities of the DNA molecule – stem portion – while the recognition element remains in a single strand and ready to hybridize to its target sequence – left panel of Figure 3.1. Upon positive recognition, the hairpin is disrupted and separates the fluorophore and quencher, allowing for a partial recovery of emission from the fluorophore, generating a positive detection signal (Right panel of Figure 3.1) (233, 239–241).

The concept of MB has been further applied in various systems (242, 243) including gold nanoparticle-based molecular beacons (Au-nanobeacons) (116, 175). As such, there is a wide range of sensors platforms whose output signals are dependent on a dynamic structure that responds to the presence/absence of a given analyte.

In this chapter, the development of a two-component molecular beacon (tcMB) based on specific FRET signals will be presented. This tcMB will be then used for the functionalization of AuNPs, generating a BioCode Au-nanobeacon, with a dual output signal: 1) Recovery of donor emission due to target hybridization; 2) Specific FRET signal for increased specificity and target recognition.

The optimization of the designed was mainly performed using FRET-based spectral codification and the validation of the design was performed using Isothermal Titration Calorimetry, MicroScale Thermophoresis, Small-Angle X-Ray Scattering, differential electrophoresis migration profiles and fluorescence melting profiles. The developed tcMB were designed to detect CML associated BCR-ABL fusion sequences, e13a2and e14a2, arising from gene translocation.

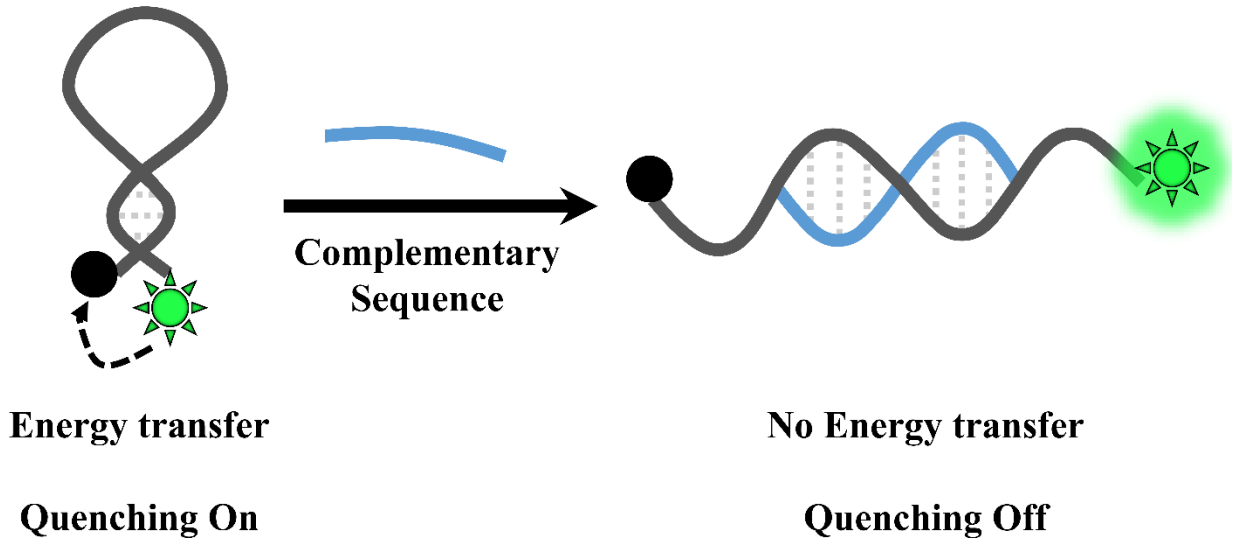

Figure 3.1. Working principle of conventional molecular beacon. Left panel: Hairpin in the close conformation. Right Panel: Upon hybridization to complementary fusion sequence, the hairpin structure is disrupted, leading to the separation between the fluorophore and the quencher

3.2 Fluorophore selection

The fluorophores were chosen based on their absorption and emission wavelengths to ensure the formation of an efficient FRET pair. As such, a spectral overlap between the donor's emission band and the acceptor's absorption band must exist and the final distance between both fluorophores should be between 1 and 10 nm, the typical distance for FRET (3). Considering the design of the BioCode Au-nanobeacon, the fluorophores should also respect the following conditions: 1) the emission band of the donor(s) should occur within the LSPR band of AuNP to maximize the quenching of the donor(s) emitted light; 2) the emission maxima of the acceptors should occur at distinct wavelengths; 3) the acceptor emission band should minimize the overlap with the LSPR band to allow a successful signal wavelength shift; 4) the fluorophores should be commercially available and suitable for oligonucleotide labeling. The donors must be suitable for oligonucleotide dual labeling with thiol modifications. From commercially available fluorophores, the pairs FAM/TAMRA, FAM/ROX, Cy3/Dy-520XL Mega Stokes and FAM/Dy-520XL Mega Stokes were chosen. See Figure 3.2 for full emission and absorption spectra of fluorophores and the LSPR of AuNP.

The software PhotoChemCad (244) was used to calculate the critical Förster radius (R_0) of the different pairs, using: 1) a refractive index of 1.333; 2) an orientation factor k^2=0.6666 (245) and a fluorescence quantum yield of 0.77 for FAM (246) and 0.04 for Cy3 (247). For the acceptors, an extinction coefficient at 555 nm of 65000 M^{-1} cm^{-1} (248) was used for TAMRA, and the experimentally assessed 70712 M^{-1} cm^{-1} for ROX at 583 nm and 44924 M^{-1} cm^{-1} at 542 nm for Dy-520 Xl Mega Stokes – See Figure I.1 and I.2

from Appendix I. This software was also used to estimate the energy transfer efficiency (Φ_{ET}) for each pair for a given distance (27.2 Å, 34 Å and 40.8 Å, for the theoretical separation between the donor and acceptor considering a base separation 3.4 Å (249) for strands with 8, 10 and 12 bp, respectively). See Table 3.1.

Sample excitation was performed at the absorption maximum of each donor fluorophore. The absorption spectra of the acceptors (solid gray line in Figure 3.2) reveals a residual absorption at these wavelengths, which results in the cross-excitation of the acceptors. This cross-excitation is not desirable but inevitable since the overlap between the emission spectrum of the donor and the absorption spectra of the acceptors is required. Moreover, these fluorophores have relatively wide emission/absorption spectra and the donors present a small Stokes shift. As such, the fluorescence baseline of the acceptors must be determined and compared to the situation where the formation of the complex is promoted.

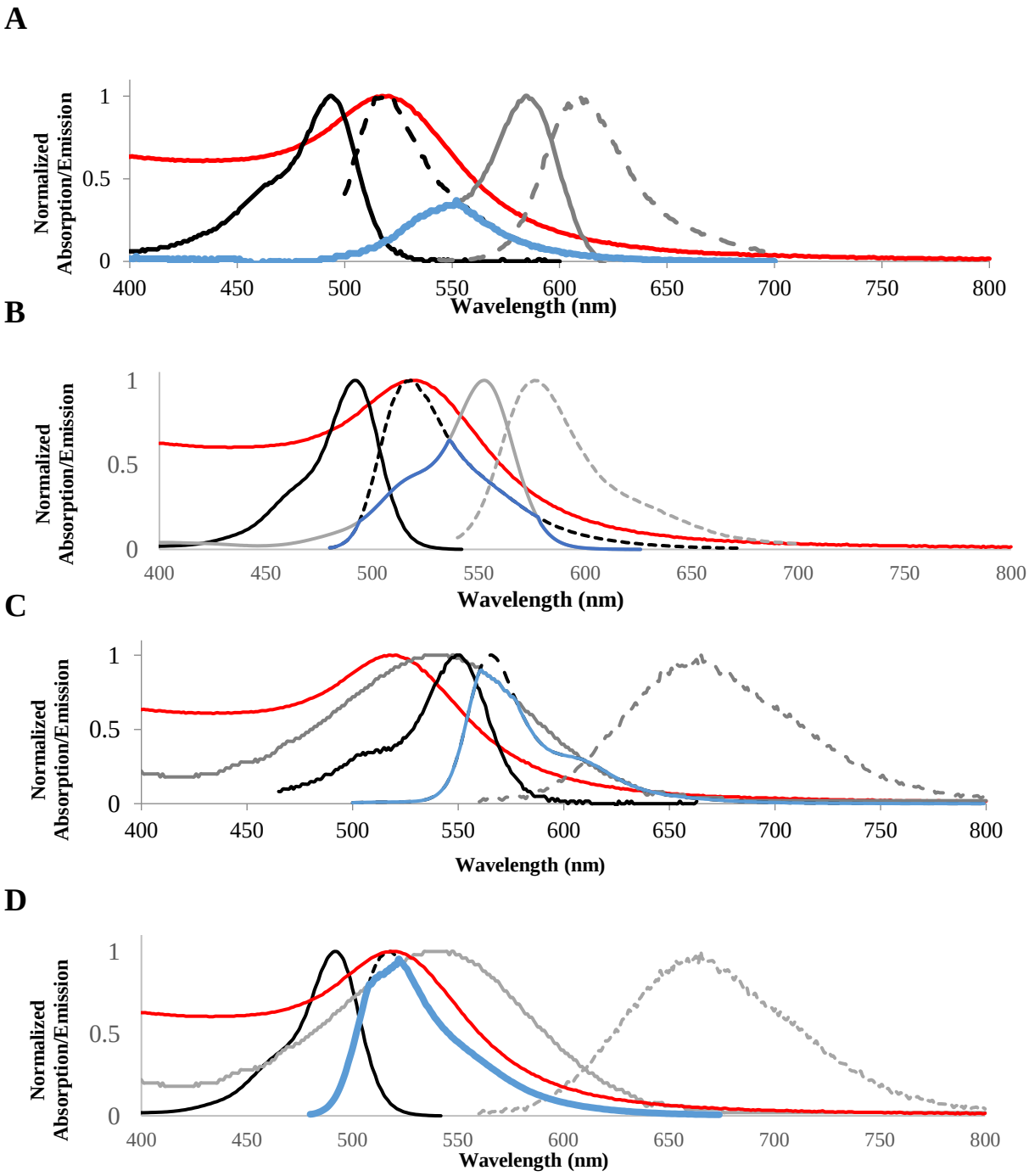

Figure 3.2. Normalized absorption and emission spectra of the used fluorophores and absorption spectra of AuNP. A) FAM/ TAMRA pair: Solid black line - FAM Absorption; dashed black line - FAM Emission; Solid gray line - TAMRA Absorption; Dashed gray line - TAMRA Emission; Solid red line - AuNP Absorption; Solid blue line – Overlap between emission spectra of FAM and absorption spectra of ROX; B) FAM/ROX pair: Solid black line – FAM Absorption; Dashed black line - FAM emission; Solid gray line – ROX Absorption; Dashed gray line – ROX Emission; Solid red line - AuNP absorption; Solid blue line – Overlap between emission spectra of FAM and absorption spectra of ROX; C) Cy3/Dy-520XL Mega Stokes pair: Solid black line – Cy3 absorption; Dashed black line – Cy3 Emission; Solid gray line – Dy-520XL MegaStokes Absorption; Dashed gray line – Dy-520XL MegaStokes emission; Solid red line - AuNP absorption; Solid blue line – overlap between emission spectra of Cy3 and absorption spectra of Dy-520XL MegaStokes; D) FAM/Dy-520XL MegaStokes pair: Solid black line – FAM Absorption; Dashed black line - FAM emission; Solid gray line – Dy-520XL MegaStokes absorption; Dashed gray line – Dy-520XL MegaStokes Emission; Solid red line- AuNP absorption; solid blue line – Overlap between emission spectra of FAM and absorption spectra of ROX.

Table 3.1. Förster distance of FRET pairs used and theoretical Φ_{ET} at different distances.

Fluorophore Pair	R_0 (Å)	Φ_{ET} (27.2 / 34 / 40.8 Å)
FAM/TAMRA	57.8	98.9/96/ 89
FAM/ROX	56.3	98.75/95.34/87.35
Cy3/Dy-520XL MegaStockes	36.4	85.3/60.3/ 33.7
FAM/Dy-520XL MegaStockes	59.4	99.1 /96.6/90.5

3.3 **Oligonucleotide *in silico* design**

The biorecognition element of the proposed biosensor – ssDNA with a hairpin structure labeled with a donor fluorophore – was designed to detect the two most common sequences associated with the development of CML, the fusion sequences e13a2 and e14a2. These fusion sequences are generated by the reciprocal translocation between chromosome 9 and 22. Due to the nature of the model, where the non-fused sequences are also present, the hybridization of the partially complementary sequence is not desirable. To ensure a specific detection, a ssDNA with hairpin structure was used considering that these structures are described as presenting higher specificity than the linear ssDNA, although with slower hybridization rates (250). This hairpin structure is also paramount due to its dynamic nature which lies at the core of the Au-nanobeacon technology. The hairpin conformation has the added benefit of a lower unspecific interaction with the gold surface (251) due to the repulsion of the phosphate groups of the less flexible secondary structure. While for a linear ssDNA (a more flexible conformation), the minimization of the electrostatic repulsion between the backbone and AuNP surface leads to the exposition of the nucleobase that, by Van der Waals interaction, leads to the unspecific adsorption of the AuNP (251, 252). The designed hairpin and revelator sequences presented in Table 2.2 of section 2.3 was guided using the secondary structural predictor software NUPACK (215). This software performs a thermodynamic analysis and simulates the possible nucleic acid ensembles based on the hybridization of putative interacting nucleic acid strands. NUPACK also predicts the equilibrium concentration of the final ensemble and each interacting strand. This prediction is based on the free energy of each base pair interaction using the nearest neighbor model (253), which can be calculated through oligonucleotide sequences, temperatures, and ionic strength (253, 254).

The loop portion of the hairpins was designed to be complementary to the target sequences – see Figure 3.3 A and B for the location of the recognition probe for fusion sequence e13a2 and e14a2, respectively.

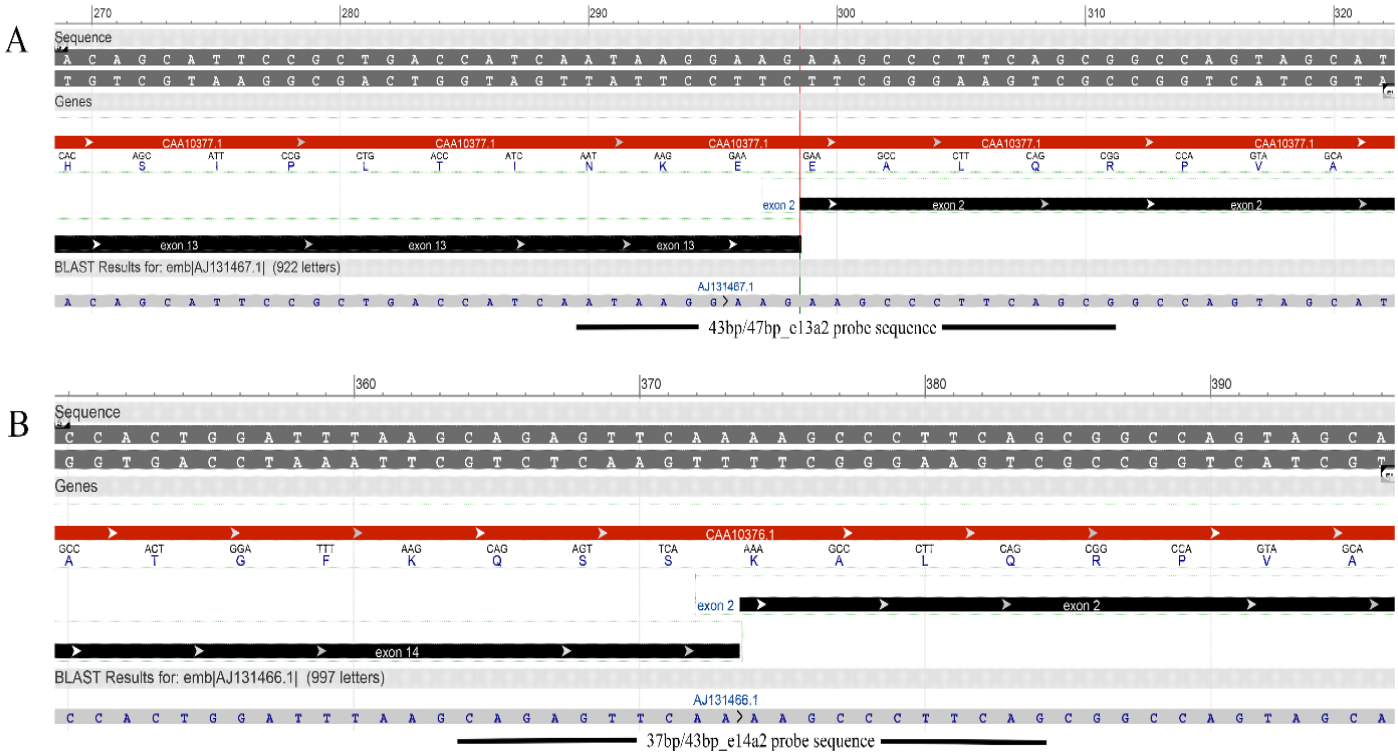

Figure 3.3. Schematic representation of fusion region of the most common BCR-ABL fusion sequences and localization of detection probe. A) Fusion sequence e13a2; B) Fusion sequence e14a2.

The hairpin conformation was achieved by flanking the loop sequence (complementary to either e13a2 or e14a2 sequences) with self-complementary sequences (palindromic sequences) of varying lengths at the 5' and 3' ends, forming the stem portion of the hairpin. This hairpin structure (Figure 3.4 A) must be disrupted when the loop portion hybridizes to a target sequence – Figure 3.4 B – exposing the palindromic sequence. An acceptor labeled oligonucleotide (revelator) can then hybridize to this region – Figure 3.4 C. This hybridization brings the donor and acceptor close together allowing energy transfer between the two fluorophores - tcMB.

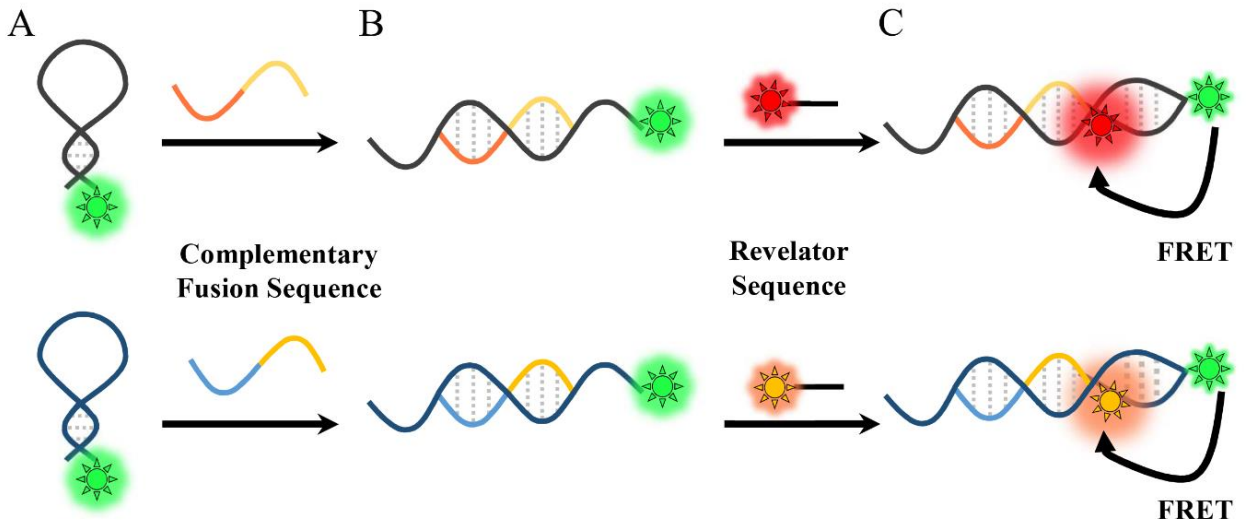

Figure 3.4. Schematic representation of the recognition principle used in the tcMB. A) Hairpin in the closed conformation; B) Secondary structure disruption due to hybridization to the target sequence; C) Hybridization of acceptor labeled oligonucleotide to exposed hairpin sequence renders a positive FRET signal.

The palindrome sequence was designed to: 1) allow the formation of a hairpin structure with a lower stability (i.e. lower free energy) than the hybridized form, to ensure the disruption of the secondary structure in the presence of the complementary target; 2) should have the highest melting temperature possible to maximize the probability of the closed conformation and increase the specificity of the hairpin – to achieve this longer stem sequences were used (250, 255, 256) (8, 10 and 12bp sequences were tested in comparison with the conventional 5 to 7 bp for the stem portion (257); 3) the composition of the palindromic sequences should be unique to allow specific targeting; 4) the palindromic sequence should allow the hybridization of the revelator, paramount for the generation of the FRET signal. As an example, Figure 3.5 represents the output of the NUPACK simulation for the hairpin/revelator pair 2 for the probe sequence: in the absence of target (Figure 3.5 A); when hybridized to the target sequence (Figure 3.5 B), and the hybridization of the revelator to the exposed palindromic sequence (Figure 3.5 C). As shown in Figure 3.5 A, the formation of the hairpin structure is a spontaneous reaction, with a free energy of -13.84 kcal/mol at 20 °C. This is necessary to keep the donor fluorophore near the surface of the AuNP in the absence of target. The hybridization of the target sequence to the loop portion of the hairpin and the sequential hybridization of the revelator to the palindromic are also spontaneous reactions at 20 °C, considering the free energy of -36.27 (Figure 3.5 B) and -52.79 kcal/mol (Figure 3.5 C), respectively. The hairpin secondary structure disruption was also theoretically assessed considering the presence of 1) revelator sequence; 2) non-complementary target; 3) partial complementary targets, such as 3.1) sequence derived from exon 2 of ABL and 3.2) sequence derived from exon 13 of BCR, not being expected a hybridization between these targets and the hairpins – see Figure 3.6. The same procedure was performed for all the hairpin-revelator pairs

presented in Table 2.2. (see Figure II.1 to Figure II.8 from Appendix II. After the *in silico* design of these sequences, the experimental assessment the hybridization of these pairs was performed.

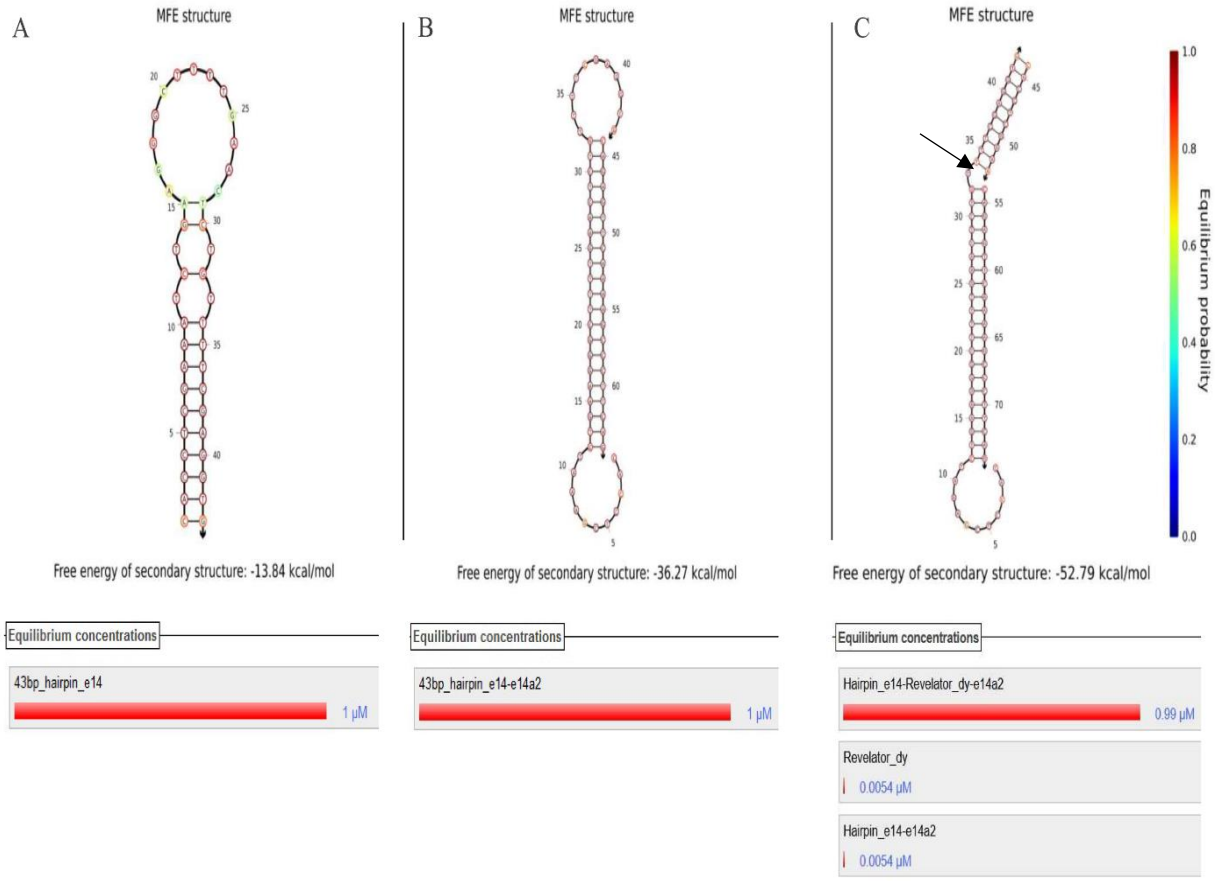

Figure 3.5. *In silico* assessment of hybridization for the sequences of pair 2. The prediction was performed with the NUPACK software. A) 43bp_Hairpin_e14 in absence of target and equilibrium concentration; B) 43bp_hairpin_e14 in the presence of complementary target and equilibrium concentration; C) 43bp_Hairpin_e14 in presence of complementary target and respective revelator; Black arrow shows a 1 nt spacer. This simulation was performed using 1 µM of each component, 20 °C, 100 mM of NaCl.

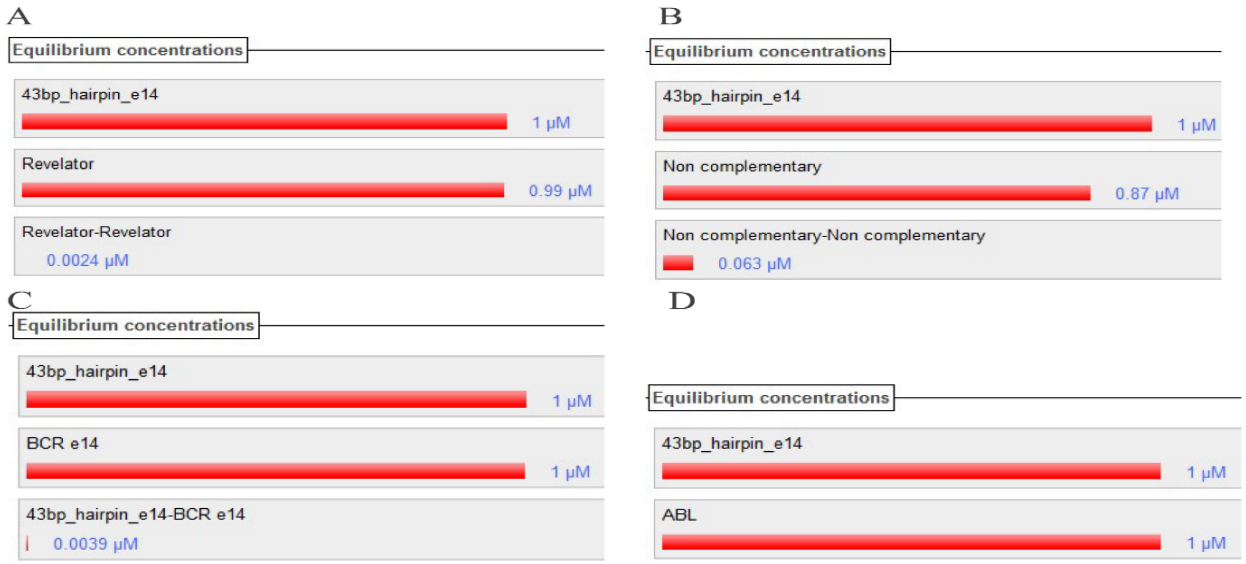

Figure 3.6. *In silico* simulation of equilibrium concentrations for the hairpin/revelator pair 2 and different targets. A) 43bp_hairpin_e14 and respective revelator; 43bp_hairpin_e14 and non-complementary target, C) 43bp_hairpin_e14 and BCR-e14 sequence; D) 43bp_hairpin_e14 and ABL sequence. This simulation was performed using 1 µM of each component, 20 °C, 100 mM of NaCl.

3.4 Fluorescence assessment of the designed hairpins

3.4.1 Design optimization

The assembly of the tcMB, was inferred through the generation of the specific FRET signature, i.e. the decrease of the donor emission with the concomitant enhancement of the acceptor emission. The occurrence of FRET was inferred by comparing the fluorescence emission of the donor and acceptor, in different scenarios: 1) hairpin in the presence of a complementary target and non labeled sequence of revelator – determination of the donor emission in the absence of FRET but in the same configuration as the final structure – donor blank; 2) tcMB in the presence of a non-complementary target or absence of target – determination of the specificity of the hairpin and the basal fluorescence of the system in the absence of FRET. The determination of the basal fluorescence must be performed due to direct excitation of the donor and cross-excitation of the acceptors, and serves as the fluorescence baseline; 3) Hairpin and revelator in the presence of a fully complementary target – generation of a FRET signal indicates the formation of the desired structure; 4) nonlabeled hairpin in the presence of a fully complementary target and labeled revelator – acceptor intrinsic signal variation upon hybridization.

The assembly of hairpin/revelator pair 1 (with a hairpin composed by 39 nucleotides (nts) with a palindromic sequence of 8 nts, designed to recognize the e14a2 fusion sequence, with its respective revelator sequence with a length of 8 nts) was not successful in the tested conditions. This because the presence of the complementary target induced the identical signal variation obtained for the presence of the non-complementary target – See Figure IV.1 of Appendix IV for the evolution of the emission of the donor and acceptor channels in the tested buffers. Table 3.2 summarizes the end-point variation of both channels for the tested conditions.

The absence of the FRET signal using the hairpin/revelator pair 1 can be due to: 1) either the hairpin failed to hybridize to the target sequence and the palindromic sequence was not accessible for hybridization with the revelator, or 2) the revelator was not able to hybridize to the exposed palindromic sequence. The loop sequence of the hairpin is composed by 21 nts which align with the conventional nucleic acids probe length described in the literature (225, 258, 259). Considering that 10 bp are involved in one complete turn of the DNA double helix (for the B-DNA form (260), the expected for these reactional conditions), the duplex formation between the palindromic sequence and the 8 bp revelator may be unstable enough (261) to prevent a measurable FRET signal. As such, the palindromic sequence was increased from 8 bp to 10 bp, and the loop portion was kept the same. A spacer of one unpaired nucleotide was inserted between the loop portion of the hairpin and the palindromic sequence (black arrow in Figure 3.2 C).

Table 3.2. Fold change in the emission of the donor and acceptor fluorophores after 2 hours of incubation in the tested conditions. Data expressed as the mean ± standard deviation of normalized values for $I_{t=0}$ for at least 3 independent assays.

	Donor Blank	**Negative**	**Positive**	**Acceptor Control**
a) 10 mM Tris-HCl pH 7.5, 100 mM NaCl (34)				
Donor	0.968 ± 0.03	0.958 ± 0.017	1.076 ± 0.04	-
Acceptor	-	0.977 ± 0.07	1.104 ± 0.05	0.992 ± 0.013
b) 10 mM Tris-HCl pH 8.0, 100 mM NaCl				
Donor	1.167 ± 0.015	1.003 ± 0.024	1.214 ± 0.036	-
Acceptor	-	0.891 ± 0.023	1.163 ± 0.021	0.981 ± 0.055
c) 10 mM Tris-HCl pH 8.0, 50 mM KCl 3.5 mM $MgCl_2$ (14)				
Donor	1.005 ± 0.01	0.963 ± 0.012	1.006 ± 0.021	-
Acceptor	-	0.861 ± 0.04	0.924 ± 0.039	0.985 ± 0.034
d) 10 mM Phosphate buffer pH 8.0, 100 mM NaCl				
Donor	1.126 ± 0.033	0.965 ± 0.012	1.102 ± 0.018	-
Acceptor	-	0.85 ± 0.03	1.055 ± 0.072	0.988 ± 0.015

These alterations were made to increase the stability of the duplex at the extremity of the hairpin, by increasing the number of base pairs and base stacking effect (261),while minimizing possible steric hindrance for the revelator hybridization. This alteration yielded a 43 bp hairpin and its respective 10 bp revelator (pair 2). The response of the pair 2 was recorded over time, in the presence of a non-complementary – Figure 3.7 A – and in presence of a complementary target – Figure 3.7 B. These spectra were compared and the formation of the donor/acceptor pair solution was revealed through the FRET signature. In the presence of a non-complementary target, there is no signal variation in both the donor and acceptor emission bands – Figure 3.7 A. Here, the background emission at 580 nm results from the direct excitation of the acceptor, due to the residual absorption of the acceptor at the donor absorption maximum (cross-excitation). In the presence of a complementary target, the quenching of the donor and enhancement of the acceptor is evident and occurs over time (black arrows in Figure 3.7 B), due to the hybridization of the target and revelator strand to the hairpin molecule that shifts the majority of the tcMB from the unbound state to the bound state. The kinetic profile of both situations is clearly distinguishable in both the donor and acceptor bands – gray triangles for the absence of target and gray circles for the non-complementary

target – Figure 3.7 C (for donor variation) and Figure 3.7 D (for acceptor variation). Through this profile, a decrease of ≈30 % is observable in the donor channel – black circles in Figure 3.7 C – with an increase of ≈ 50 % on the acceptor channel – black circles in Figure 3.7 D. An additional control was performed, absence of target, to ensure that the non-complementary target was not able to disrupt the hairpin structure. In this situation, the kinetic profile is identical to the non-complementary target, as in neither condition the hairpin was disrupted.

To access the thermal stability of the final complex, the emission of both fluorophores was recorded at different temperatures and the melting profile was obtained for the positive and negative reaction – Figure 3.7 E for donor variation and Figure 3.7 F for acceptor variation. The negative reaction allows for the determination of the intrinsic fluorescence variation of both the donor and acceptor as a function of temperature in the absence of FRET. In the positive reaction, the increase of temperature results in an abrupt increase of the donor channel signal (in comparison to the negative reaction) and a sharp decrease in the signal of the acceptor channel (the signal of the acceptor channel in negative reaction did not vary across the tested temperatures), which is concordant with the disassembly of the tcMB due to the melting of the revelator (separation of the donor and acceptor fluorophores). This separation interrupts the energy transfer, hence the quenching of the donor stops occurring (leading to a sharper increase of the donor emission in the positive reaction in comparison to the negative reaction). At high temperatures (above 50 °C), the signal of the donor and acceptor in both situation (positive and negative) reach the same plateau, which is expected considering that beyond this temperature the revelator cannot hybridize to the hairpin – rendering the same signal in both situations. The first derivative of the melting curves is presented in the inset of both Figure 3.7 E and F and turns the sigmoidal curve into a peak that is the widely used approach to determine the melting temperature (Tm - the temperature at which 50% of the oligonucleotide is double stranded with its complementary strand) of interacting DNA strands (262). The melting of the revelator starts at around 30 °C, with a melting peak at around 40 °C. To maximize the thermal stability of the complex, all the subsequent assays were performed at below 30 °C and maintained at 20 °C.

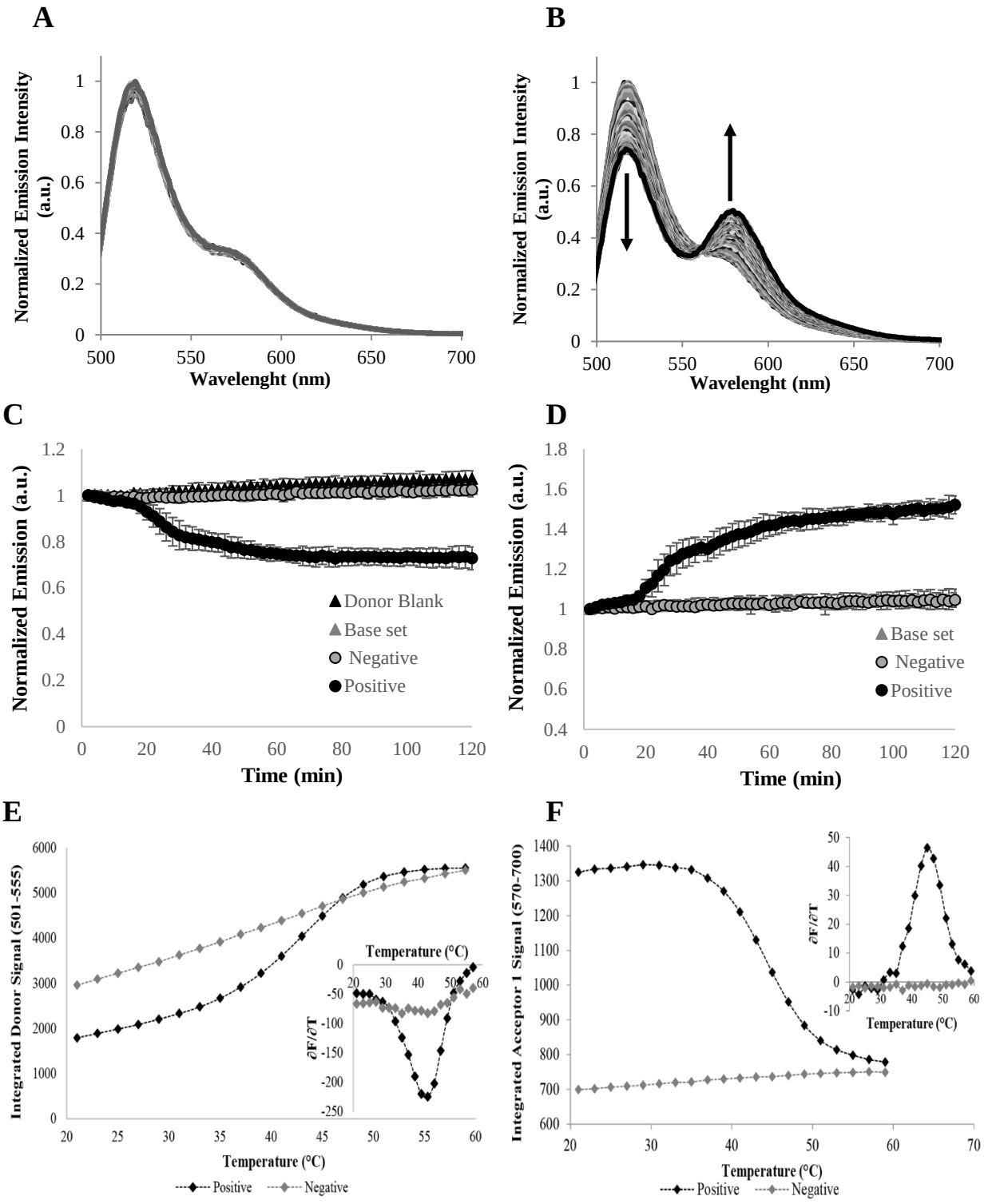

Figure 3.7. Emission variation of the donor and acceptor emission as a function of time and temperature. A) Time-dependent emission spectra of negative reaction; B) Time-dependent emission spectra of positive reaction; C) Donor channel variation over time; D) Acceptor channel variation over time; Black arrows indicate the direction of the observed variation. Black triangles - donor emission in the presence of complementary target in the absence of revelator; Gray triangles - donor and acceptor emission in the absence of target; Gray circles - donor and acceptor emission in the presence of a non-complementary target; Black circles - donor and acceptor emission in the presence of complementary target. Data expressed as mean ± standard deviation of normalized values for $I_{t=0}$ of at least 5 independent assays. Kinetic assays Performed in buffer d); E) Donor melting profile; F) Acceptor Melting Profile. Melting assays performed in buffer e).

The FRET efficiency in each situation was determined by the decrease in the donors' emission in the final structure in comparison with the donor in the same structure but in the presence of a non-labeled revelator – hence no FRET. See Equation 3.1 (3).

$$Et(\%) = \left(1 - \frac{FDA}{FD}\right) * 100 \qquad \text{Equation 3.1.}$$

For the situation depicted in Figure 3.7 C, a decrease of ≈30 % in the donor channel can be observed corresponding to an apparent Φ_{ET} to the acceptor molecule. This value is far from the theoretical 96%, presented in Table 3.1. The theoretical FRET efficiency assumes that 100 % the donor and acceptor populations are involved in the energy transfer processes. However, in the presented system, the approximation of the donor and acceptor is governed by two hybridization process (target to hairpin and opened hairpin to the revelator). Considering that not all hairpins will hybridize to their target sequence, and not all hybridized hairpins will hybridize to the revelator, the apparent experimental FRET efficiency will be influenced by the emission of isolated donors that are not quenched due to energy transfer. The labeling efficiencies of the hairpin and revelator can also have an impact on the experimental determined Et, for the same reasons presented above. To improve the efficiency of hybridization, the concentration of NaCl was increased to 154 mM. The melting profile presented on Figure 3.7 E and F were performed with this NaCl concentration, and at 20 °C a higher apparent energy transfer can be observed in both channels (1.28- vs 1.39-fold change for the donor channel and 1.52- vs 1.9-fold change for the acceptor channel). This apparent increase in the hybridization efficiency is probably due to the higher concentration of Na^+ ion which are known for decreasing the electrostatic repulsion between interacting DNA strands (263), leading to an improvement of the hybridization process. As such, the final concentration of NaCl in the hybridization buffer was set for 154 mM for subsequent reactions.

Together, this data suggests that: 1) at the working concentrations, the mean distance between the donor and acceptor fluorophores in solution is not compatible with FRET as only when the formation of the pair donor/acceptor occurs a FRET signal can be observed – as stated in the literature, were for R_0 up to 60 Å, the critical concentration occurs at the mM range (34); 2) the tcMB ensemble can be triggered by the presence of a complementary target to the loop portion of the hairpin; 3) in the final ensemble, the donor and acceptor are in a FRET compatible distance; 4) the presence of the revelator sequence is not able to disrupt the hairpin conformation by strand displacement and hybridize to the palindromic sequence in the absence of the complementary target, at least not to an extent that is perceivable by the emission spectra.

3.4.2 **Specificity and selectivity of the designed sequences.**

The target model used in this work – CML – presents itself in heterozygosity (264), where any given individual will always harbor one healthy copy of ABL and one of the BCR. This way, the designed tcMB should be able to differentiate between a fully – (the fusion sequence of BCR-ABL), a non-complementary and partial complementary (either BCR or ABL) targets. As such, the output signal of tcMB was accessed in the described conditions – see Figure 3.8 A variation in the donor emission and Figure 3.8 B for the variation in the acceptor emission.

In this situation, the FRET signal was only triggered by the presence of the complementary fusion sequence (denoted as positive in Figure 3.8 to Figure 3.10). The presence of the non-complementary target (negative) or partial complementary (BCR, ABL and e13a2) targets didn't induce a relevant signal alteration in both the donor or acceptor emission. These results suggest that the designed hairpin can form the tcMB in a sequence-specific manner.

A

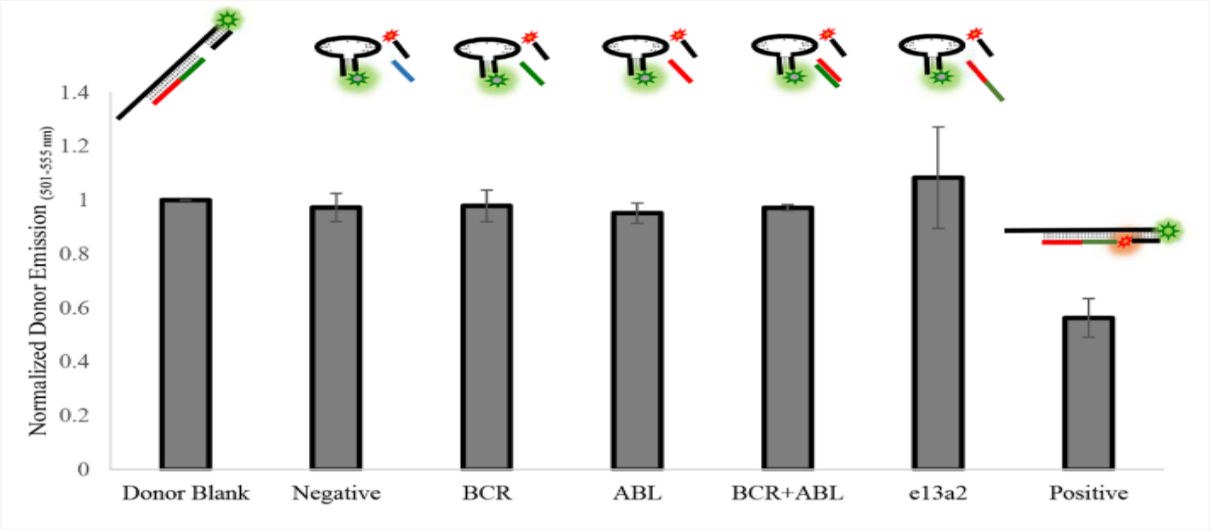

B

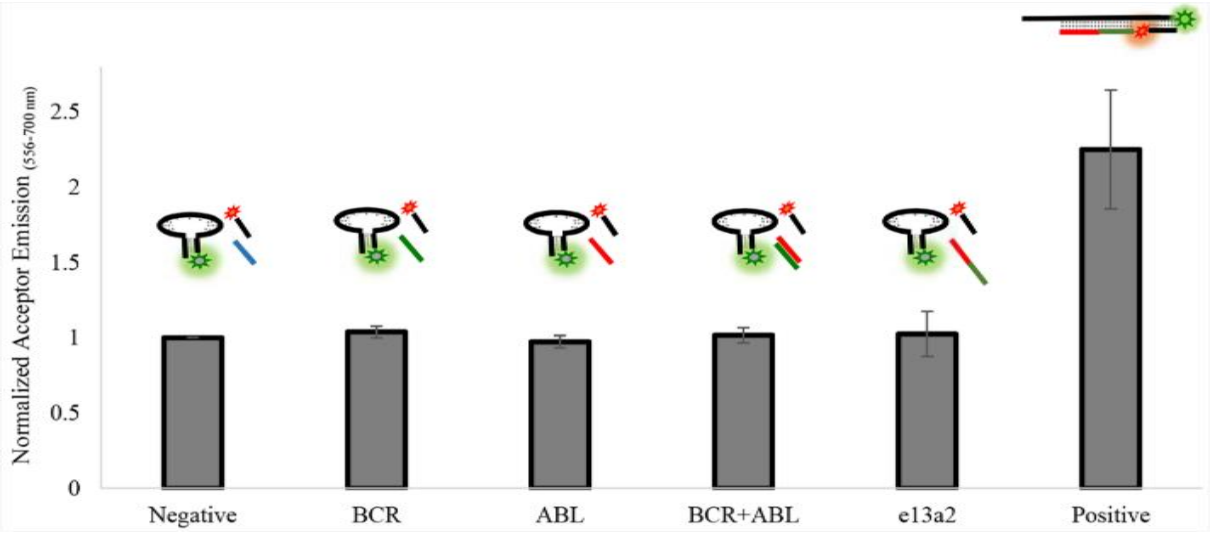

Figure 3.8. Signal variation of donor and acceptor in the presence of different targets for hairpin/revelator pair 2. A) Donor (FAM) channel; B) Acceptor (TAMRA) channel. Donor channels normalized to the donor channel in donor blank. Acceptor channels normalized to the acceptor channel in the negative reaction. Data presented as means ± standard deviation of at least 3 independent assays. Performed in buffer e).

The tcMB design with a loop with at least 21 nt and a palindromic sequence of at least 10 nt with 1 nt as spacer between the portion of the hairpin, was extended to the design of the probe sequence towards the fusion sequence e13a2. This yielded a 43 bp hairpin with its respective 10 bp revelator that was labeled with the ROX fluorophore (pair 3). The specificity of this hairpin was assessed, both in buffer e) and f), in the presence of the same targets stated before – See Figure 3.9 for the end-point signal variation of the tested condition in both the donor and acceptor channels (Figure 3.9 A and B, respectively). As with the previous situation, the hairpin/revelator pair towards the fusion sequence e13a2, only generated the expected FRET signal in the presence of the e13a2 complementary sequence, in both buffers. However, in the buffer f) a

higher Φ_{ET} can be observed (45.65 % vs 22.69 % - Figure 3.9 A) in the presence of the complementary target in comparison with the reaction performed in buffer e). As such, the hybridization buffer used in the subsequent reactions were performed in buffer f (0.5× TBE pH 8.3, 154 mM NaCl).

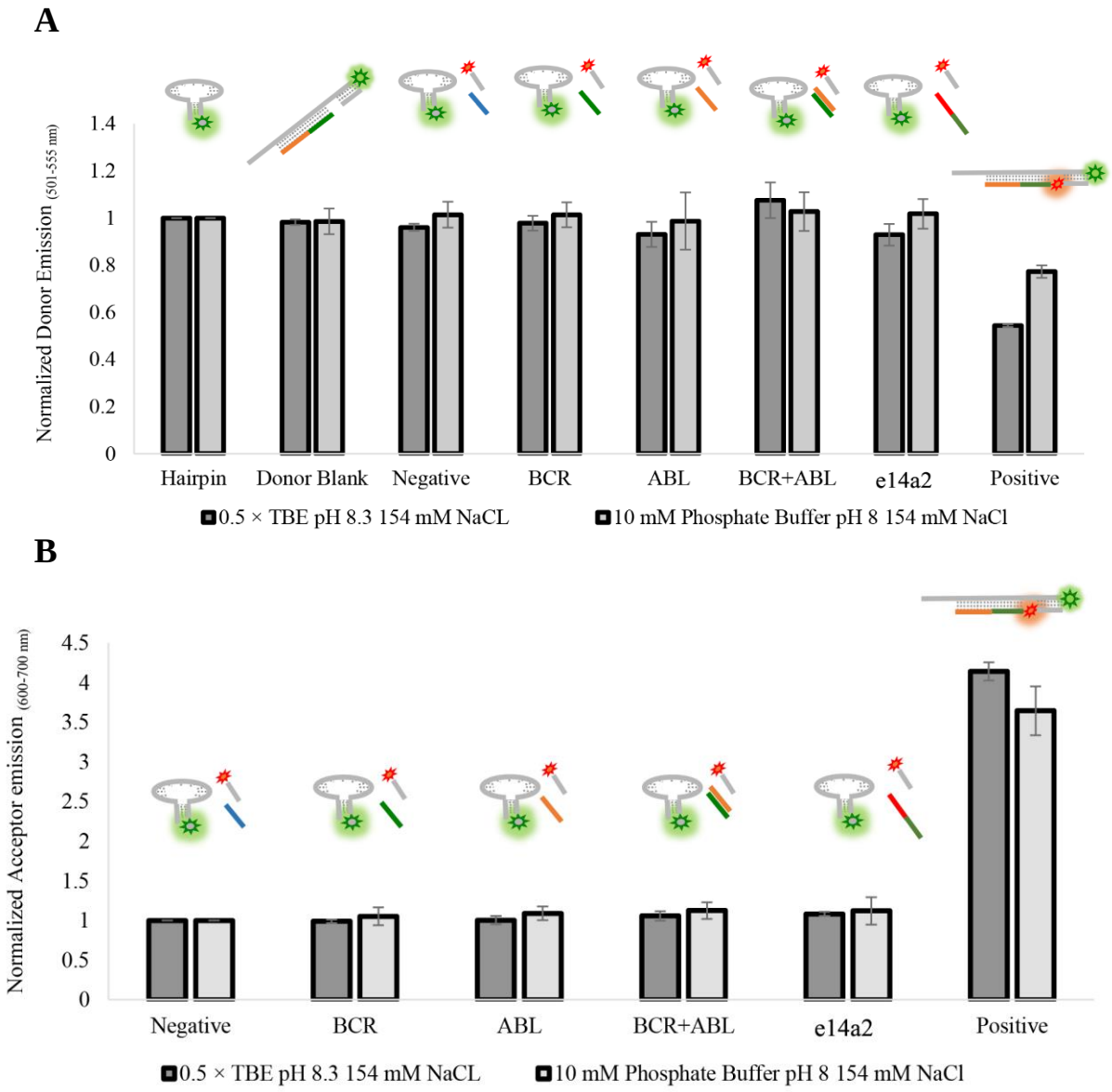

Figure 3.9. Signal variation of donor and acceptor in the presence of different targets for hairpin/revelator pair 3. A) Donor channel (FAM); B) Acceptor channel (ROX). Donor channels normalized to the donor channel in donor blank. Acceptor channels normalized to the acceptor channel in negative reaction. Data presented as means ± standard deviation. Dark gray bars represent signal collected in buffer f); light gray bars represent signal collected in buffer e)

Different donor/acceptor pairs, FAM/Dy-520 Xl Mega Stokes and Cy3/ Dy-520 Xl Mega Stokes were also tested as labels for the 43 bp hairpin towards the fusion sequence e14a2 (hairpin/revelator pair 4 and 5, respectively), while keeping the same sequences the same as in pair 2. These fluorophore pairs were

considered due to the smaller overlap of the Dy-520 Xl Mega Stokes acceptor with the AuNP LSPR – See Figure 3.10 for specificity characterization.

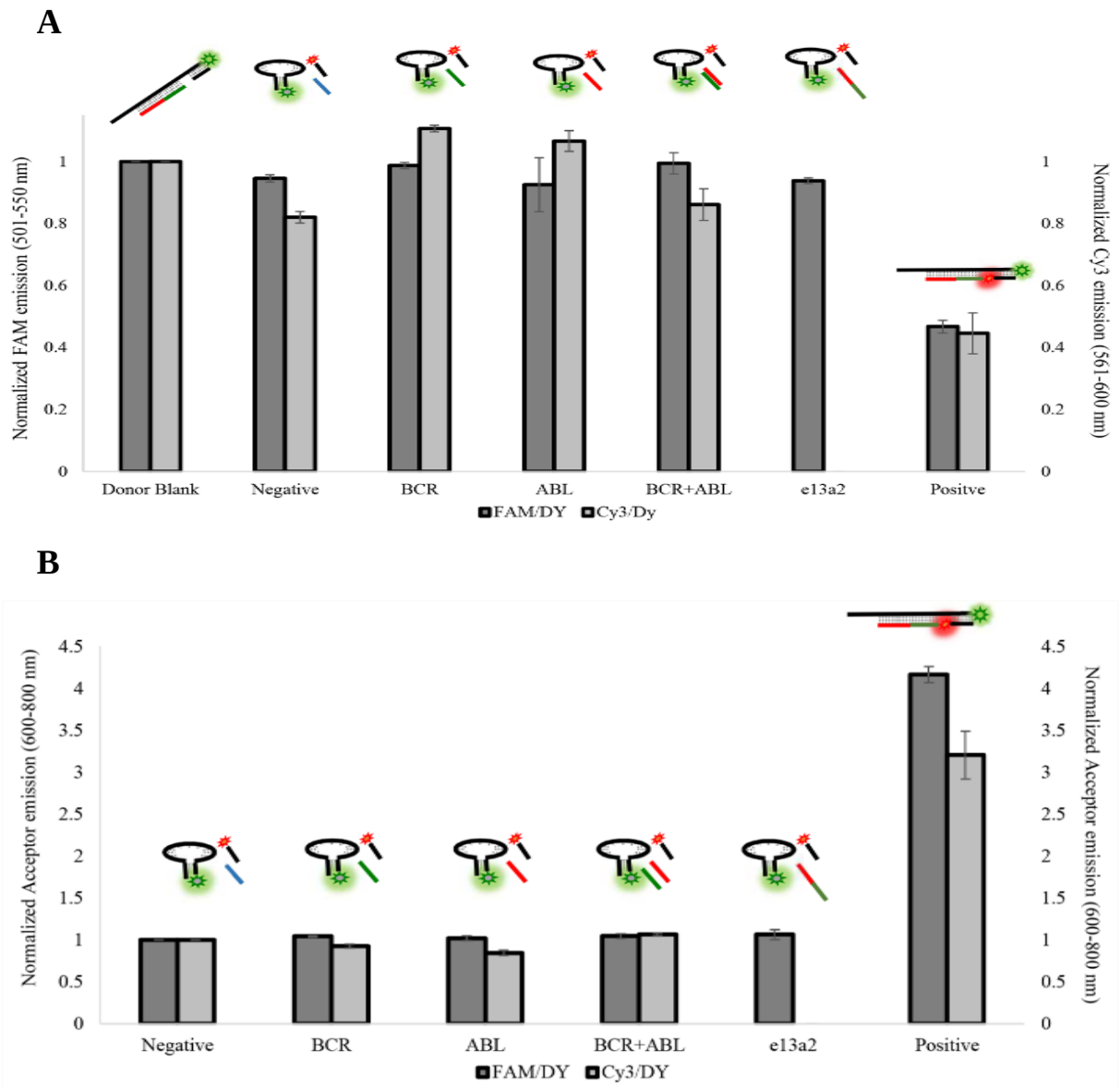

Figure 3.10. Signal variation of fluorophore pairs FAM/Dy and Cy3/Dy in the presence of different targets for hairpin/revelator pair 4 and 5, respectively. A) Donor channel (FAM or Cy3); B) Acceptor channel (Dy-520 Xl MegaStokes). Donor channels normalized to the donor channel in donor blank. Acceptor channels normalized to the acceptor channel in negative reaction. Data presented as means ± standard deviation. Dark gray bars represent signal obtained for FRET pair FAM/DY f); Light gray bar represents signal obtained for FRET pair Cy3/Dy. Performed in buffer e).

As described in the previous situation, the formation of the desired ensemble is only triggered by the presence of a fully complementary target. The only relevant difference in the obtained signal is in the acceptor emission of the positive reaction, where the FRET pair FAM/Dy had a higher level of enhancement

in comparison with the pair Cy3/Dy. For the hairpin/revelator pairs 6 to 8 (pair 6 towards the fusion sequence e13a2 and 7-8 towards the fusion sequence e14a2) labeled with the Donor-Acceptor pairs FAM/ROX, Cy3/Dy-520XL MegaStokes, FAM/DY-520XL MegaStokes respectively, the palindromic sequences of the hairpins were increased to 12 bp and the final nucleotides at the 3' end were substituted by adenine. The specificity of these hairpins towards the fully/non-and partial complementary targets were accessed – See Figure V.I to V.III, Appendix V. These longer hairpin/revelators, as with the previous ones, only generated a measurable FRET signal in the presence of the fully complementary targets, with the partial complementary targets generating a signal similar to the respective negative controls (either donor blank or donor and acceptor in the presence of a non-complementary target). A melting analysis was performed with the hairpin/revelator pairs 3, 4 – Figures IV, Appendix V- and pair – 6 and 8, Figure V.V, Appendix V. The melting analysis shows a sharp decrease in the acceptor channel with the concomitant increase of the donor channel, only in the presence of the fully complementary target. This distinct profile is only observed for the situation where the complex is formed, with the signals (donor and acceptor) of all the scenarios converging at high temperatures due to the melting (disassembly) of the tcMB.

The specificity of the revelator sequences was accessed using the hairpin/revelator pairs 3 and 4 (43bp hairpin_e13/ROX and 43bp hairpin_e14/dy) where each hairpin was incubated in the presence of their respective target and each other revelator. These emission spectra were compared with the donor blank control reaction and negative reaction where the fusion sequence was replaced by the non-complementary target. See Figure 3.11 A) for the 43bp_hairpin_e13 and Dy labeled revelator and 3.11 B) for the 43 bp_hairpin_e14 and the ROX labeled revelator.

The spectra presented in Figure 3.11 shows the specificity of the palindromic sequence considering that both hairpins (either 43bp_hairpin_e13 and 43bp_hairpin_e14) are in the open conformation (due to the presence of their respective complementary target) and in the presence of each other revelator (crossed revelators - 43bp_hairpin_e13 is in the presence in of the revelator towards the 43bp_hairpin_e14 and vice-versa). The solid black line in both Figure 3.11 A) and B) indicates an absence of hybridization of the revelators to the hairpin, considering that the emission of both the donor and acceptor in the presence of the fully complementary target are not distinguishable from the negative reaction and the donor blank.

These hairpins are to be functionalized on the surface of AuNP with an average size of 13-15 nm.

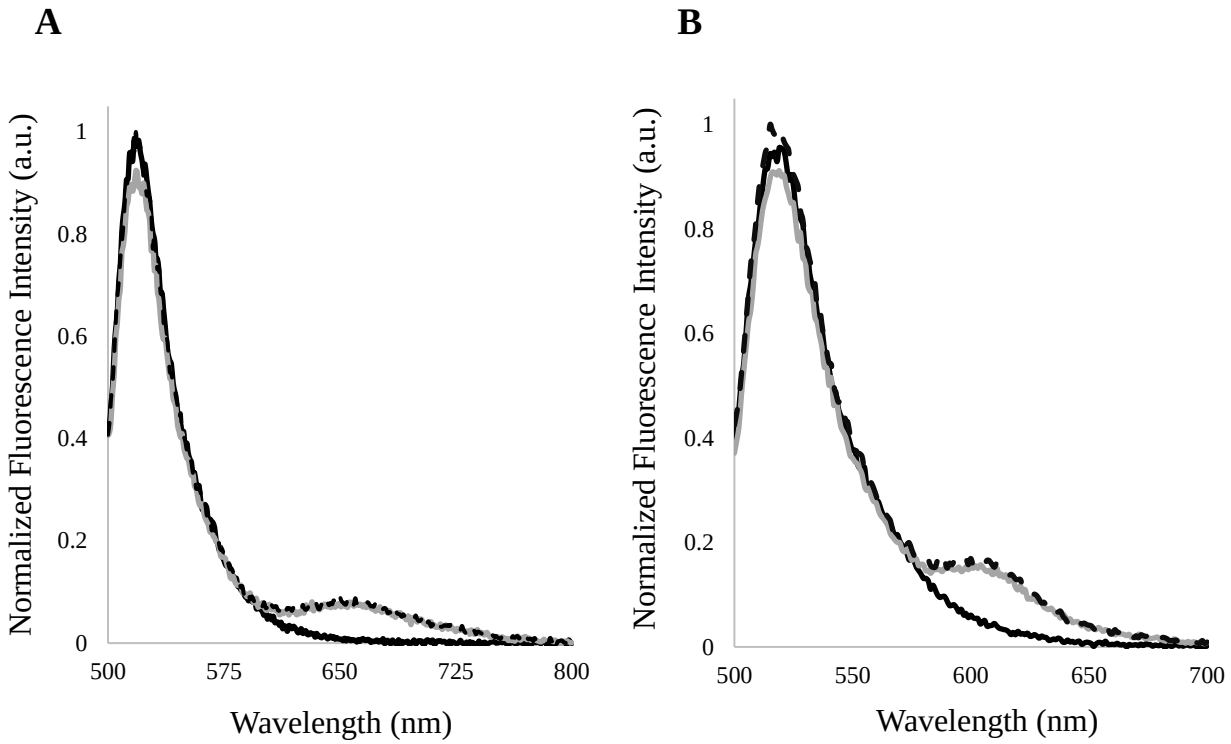

Figure 3.11. Specificity assessment of the 10bp revelator for 43bp_hairpin_e13 and 43bp_hairpin_e14. A) Revelator labeled with Dy-520XL MegaStokes towards the 43bp_hairpin_e14 in the presence of 43bp_hairpin_e13 and e13a2 target sequence; B) Revelator labeled with ROX towards the 43bp_hairpin_e14 in the presence of 43bp_hairpin_e13 and e13a2 target sequence; Solid Black line – Donor Blank; Solid Gray line – Negative control; Dashed black line – Revelator specificity assessment.

3.4.3 **Mixture characterization**

To evaluate the occurrence of FRET in a complex mixture, where more than one pair of donor/acceptors pairs may be present, the experimental spectra can be generated through the sum of all the relative emission of each fluorophore, given that no chemistry occurs between the fluorophores. As such, the experimental spectra can be fitted through the linear combination of the weighted individual components, i.e emission of each fluorophore at the same concentration found in the experimental spectra using the same excitation wavelength – see Equation 3.2 (34) for a general case.

$$F_{Experimental(\lambda)} = a_1 f_{d_{1(\lambda)}} + a_2 f_{d_{2(\lambda)}} + \cdots + a_i f_{D_{i(\lambda)}} + b_1 f_{A_{1(\lambda)}} + b_2 f_{A_{2(\lambda)}} + \cdots b_j\, f_{A_{j(\lambda)}}$$

Equation 3.2.

Where $F_{Experimental(\lambda)}$ corresponds to the experimental spectrum obtained upon excitation at a λ wavelength, the coefficient a_i and b_i used to fit the emission spectrum of each component of the reaction ($f_{d(x)}$ and $f_{A(x)}$ for the emission spectra of the donors and acceptor, respectively). Considering the nature of the FRET signal, if a donor molecule is in the vicinity of and appropriate acceptor, the value of its weighted coefficient will decrease in a manner related with the Φ_{ET} of the said pair (considering that all the donor population is interacting with all the acceptor population). Therefore, the emission spectrum of the donor in the presence of FRET ($F_{D(D-A)}$) is given by Equation 3.3 (34), where f_D correspond to the emission of the donor in the absence of FRET due to direct excitation.

$$F_{D(D_{i-}A_j)} = f_D \cdot \left(1 - \Phi_{\mathrm{ET}_{D_iA_j}}\right) \qquad \text{Equation 3.3.}$$

For the acceptor emission in the presence of FRET, the value of its weighted coefficient will increase in a manner related to the Φ_{ET} and to the absorption coefficient of the donor at the excitation wavelength (λ_{exc}), as shown in Equation 3.4. In this situation is important to consider that part of the absorbed energy by the donor fluorophore will be transferred to the acceptor. $f_{A_{i_\lambda}}$ correspond to the emission of the acceptor in the absence of FRET due to cross-excitation at the donor excitation wavelength; $\varepsilon_{A_{i_\lambda}}$ correspond to the acceptor absorption coefficient at the excitation wavelength; $\varepsilon_{D_{j_\lambda}}$ correspond to the donor absorption coefficient at the excitation wavelength.

$$F_{A(D_iA_j)} = f_{A_{i\lambda}}\left(1 + \frac{\varepsilon_{D_{j_\lambda}}}{\varepsilon_{A_{i_\lambda}}}\,\Phi_{\mathrm{ET}_{D_iA_j}}\right) \qquad \text{Equation 3.4.}$$

This approach was tested by mixing equimolar concentration of hairpin/revelator pair 2 and 3 and measuring the respond of this mixture in the presence of: 1) one complementary target (either e13a2 or e14a2 sequence); 2) presence of both complementary targets; 3) Presence of non-complementary targets and partial complementary targets (BCR and ABL sequences) – see Figure 3.12 for emission spectra of the tested conditions. These spectra were fitted using the isolated emission spectrum of the donor blank and the isolated spectra of the acceptors. A simplified version of Equation 3.2 was used for the fitting, considering the presence of one donor and two acceptors – Equation 3.5, which corresponds to the situation presented in Figure 3.12). An iteration of the coefficient values was performed as to minimize the sum of the square difference between the experimental spectra and the fitting spectra (theoretical spectra). This fit between the experimental and theoretical spectra generated the experimental coefficient that was normalized to the

values obtained in the negative reaction (situation where the generation of FRET does not occur) and presented on Table 3.3

$$F_{Experimental(\lambda)} = a_1 f_{d_{1(\lambda)}} + b_1 f_{A_{1(\lambda)}} + b_2 f_{A_{2(\lambda)}} \qquad \text{Equation 3.5.}$$

Figure 3.12 shows the spectral responses of the mixture of hairpin/revelator pair 3 and 4 upon direct excitation of the donor fluorophore. The emission centered at ≈520 nm corresponds to the donor emission due to direct excitation and the background emission at ≈605 and 650 nm correspond to the cross-excitation of the acceptor ROX and Dy-520XL MegaStokes, respectively. Here, the presence of either the non-complementary or partial complementary target (either BCR sequence, ABL sequence, both BCR and ABL sequence), failed to induce any spectral alteration, as demonstrated in the previous section using the isolated pairs. However, a spectral alteration can be observed in the presence of one fusion sequence or both, and these three situations are clearly distinguishable from the controls situation and each other (presence of just e13a2/e14a2 or both). In the presence of either fusion sequences (e13a2 or e14a2), the donor emission decreases around 30% with the concomitant increase of the respective acceptor (ROX for sequence e13a2 and Dy-520XL MegaStokes for sequence e14a2 – solid and dotted light gray line, respectively). When both fusion sequences are present the donor emission decreases around 55%, considering that in this situation the donor of both hairpins are involved in the energy transfer, whereas in the presence of only one target, only one of the hairpin population is involved in the energy transfer. Likewise, an enhancement of both acceptors can be observed when both targets are present. Table 3.3 shows the same tendency, considering that both the donor and acceptors coefficients in the control reactions are very close to one and in the presence of one complementary target, the donor coefficient decreases to similar values in the presence of either the fusion sequence. This occurs due to the very similar R_0 of both pairs and same hybridization conditions. In the presence of both complementary targets, the donor coefficient is lower than the situation where only one complementary target is present, for the same reason stated above. Likewise, the acceptor contribution for the overall experimental spectra is higher (higher coefficients) in the situation where the respective target is present (target e13a2 for the ROX coefficient, target e14a2 for the Dy-520XL MegaStokes coefficient). As such, this approach allows for the quantification of the signal variation in a situation where more than one pair of donor/acceptors may form in solution.

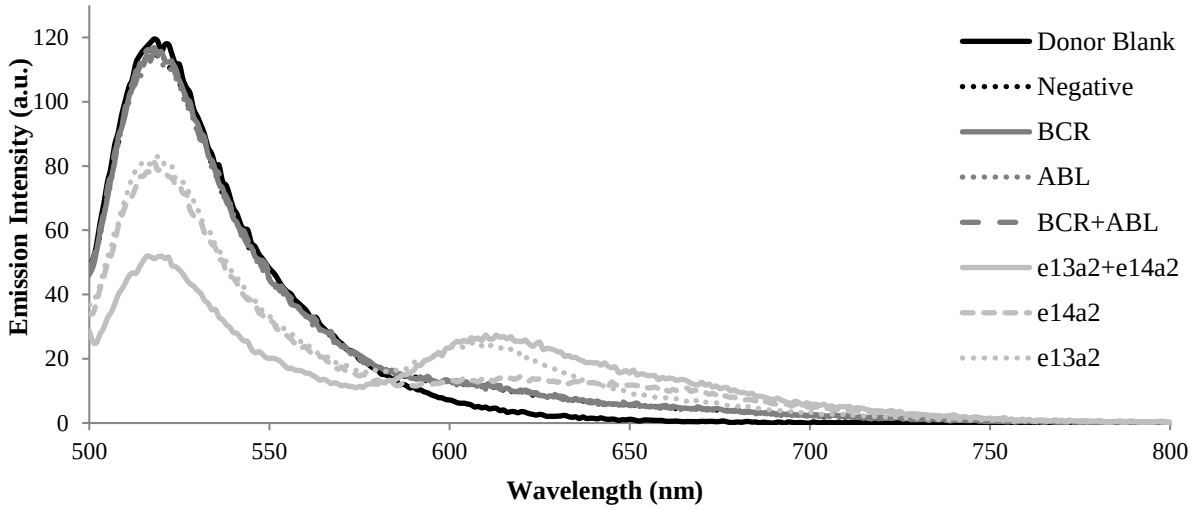

Figure 3.12. Emission spectra of a mixture containing hairpin/revelator 3 and 4 in the presence of various targets. Solid black line – Donor blank; Dotted black line – non-complementary target; Solid dark gray line – BCR target; Dotted dark gray line – ABL target; Dashed dark gray line – BCR and ABL targets; Solid light gray line – e13a2 + e14a2 fusion sequences; Dashed light gray line – e14a2 fusion sequence; Dotted light gray line – e13a2 fusion sequence.

Table 3.3. Fitting coefficients derived from spectra presented on Figure 3.12.

	Negative	**BCR**	**ABL**	**BCR+ABL**	**e14a2**	**e13a2**	**e13a2+e14a2**
FAM	1.00	1.00	0.99	1.01	**0.68**	**0.71**	**0.44**
ROX (e13a2)	1.00	1.02	1.00	1.09	1.38	**3.42**	**3.80**
Dy-520XL MegaStokes (e14a2)	1.00	1.03	0.96	1.04	**2.71**	1.08	**2.93**

3.5 **Binding affinity characterization**

3.5.1 **Isothermal Titration Calorimetry**

Isothermal titration calorimetry (ITC) is a technique that can be used to characterize the interactions at the molecular level. ITC directly measures the heat generated or absorbed upon chemical reaction or physical interaction. This heat variation allows the determination of binding affinities (K_A and K_D), entalphy changes (ΔH) and binding stoichiometry (n) (265). This is performed by the titration of a ligand against the target molecule and measuring the energy required to maintain a minimum difference of temperature between the reaction and reference cell (266). The direct heat variation measurement of the ITC assay means that the interacting partners can be unlabled and that detection of the binding event must be performed in

solution. It is important to guarantee the saturation of the target with the binding partner, where the injection of the ligand after the point of saturation only generates heat of dilution. This heat (average of values of the last 3-4 injections) is subtracted to the signal obtained due to binding of the interacting strands. Considering that the hybridization of the complementary target sequence to the hairpin structure is expected to occur in a 1 to 1 ratio, the K_a and binding stoichiometry of reaction was determined by fitting the data using the Wiseman Isotherm binding model ('independent model') included in the software package (267, 268). The free energy variation (ΔG) and the entropy variation (ΔS) were inferred using Equation 3.6 and 3.7 (respectively), where R refers to the ideal gas constant, T refers to the temperature at which the measurements were performed.

$$\Delta G = RT\ln(\frac{1}{K_a}) \qquad \text{Equation 3.6.}$$

$$\Delta G = \Delta H - T\Delta S \qquad \text{Equation 3.7.}$$

The peaks of the injection profile (top of Figures 3.13 A to F) are then integrated and plotted against the mole ratio of titrant:target molecule, generating the dose-response curves (herein ITC binding isotherms) (bottom of Figure 3.13 A to F). The binding isotherms for the 43bp_hairpin_e13 and complementary target sequence e13a2 complex formation are presented at the bottom of Figure 3.13 A to C. The parameters obtained through the fitting of the model to the experimental data are presented on Table 3.4. These reactions were then titrated with the respective revelator sequence – see the top of Figure 3.13 D to F. The volume of chamber was adjusted and the initial concentration of the hairpin-target complex was corrected using the stoichiometry parameter obtained in the formation of the hairpin-target complex (Table 3.4).

The binding isotherms presented in Figure 3.13 A to C show that the data distribution is clearly sigmoidal, the typical distribution of experimental values that allow the determination of the fitting parameters via the fitting model – see Table 3.4. These parameters did not exhibit a concentration dependent variation, as expected (269), considering that the initial concentration of hairpin varied by a factor of 3.5. The binding affinity for the hybridization of the target sequence e13a2 and 43bp_hairpin_e13 is 5.33 ± 1.8 ($\times 10^7$) M^{-1}, a similar value obtained through ITC characterization of interacting DNA strands with similar length (270). The stoichiometry of the reaction should be closer to 1 considering the hybridization of two DNA strands (the mean of the assays sets the stoichiometry of this reaction at 0.81 ± 0.04). This difference could be due to an erroneous concentration determination by a sub-standard extinction coefficient provided by the supplier (the concentration of the oligonucleotides solutions were confirmed by the absorbance at 260 nm via UV-Vis spectroscopy prior to each ITC measurement). The oligonucleotide purity can also be a factor,

considering that a deviation from a single population per batch of oligonucleotide can result in a different stoichiometry parameter (the presence of noninteracting strands, i.e. shorter strands, produced during synthesis that but contribute to the absorbance at 260 nm – even though the oligonucleotides were purified by HPLC.

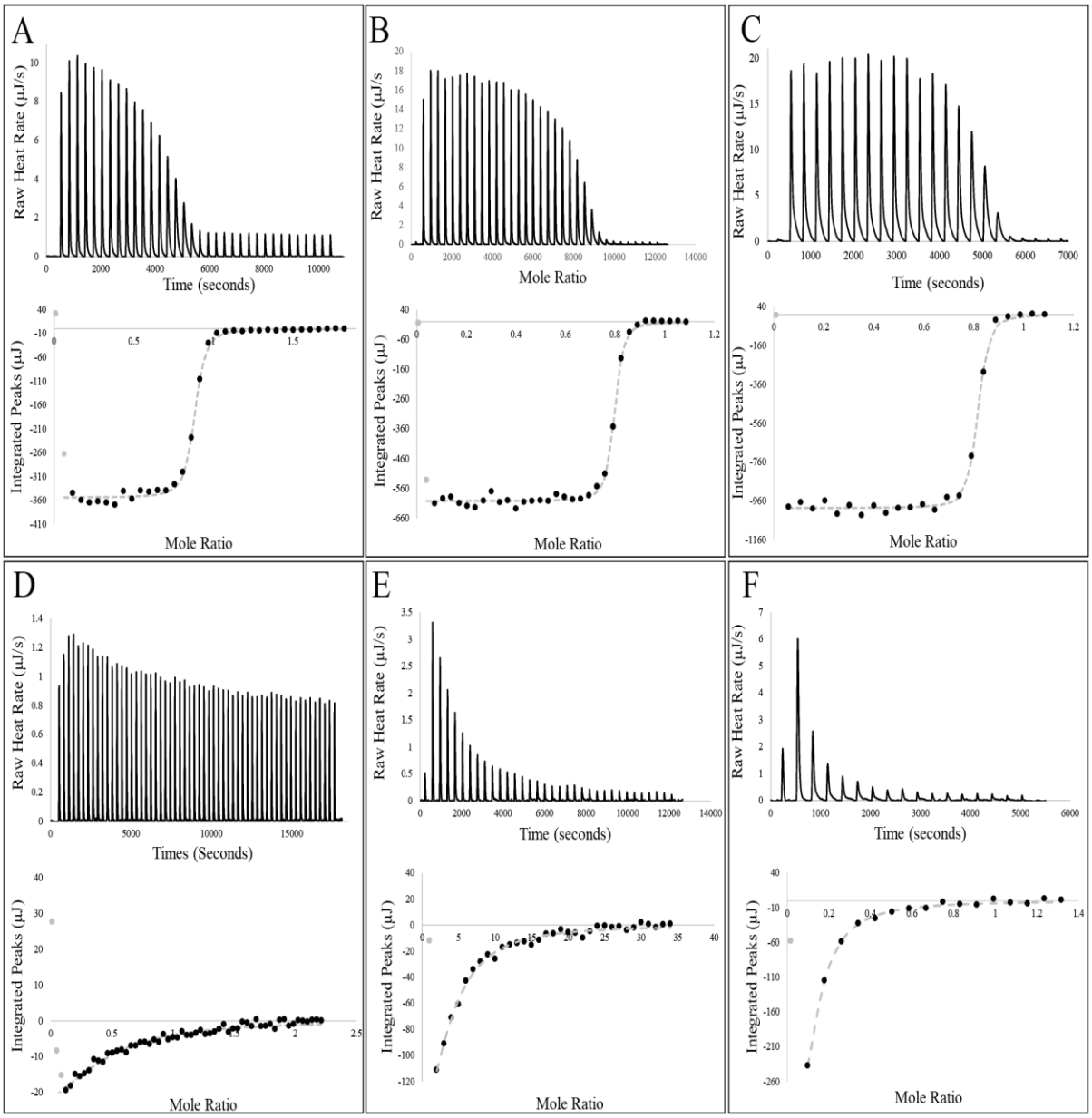

Figure 3.13. Isothermal titration calorimetry injection profile and binding isotherms of the formation of the tcMB towards fusion sequence e13a2. A) 15 µM of 43bp_hairpin_e13 vs 35 injection of 5 µl of e13a2 sequence at 150 µM; B) 42.59 µM of 43bp_hairpin_e13 vs 34 injections of 3µl e13a2 sequence at 452.51 µM; C) 51.11 µM of 43bp_hairpin_e13 vs 23 injection of 5 µl of e13a2 sequence at 468.05 µM; D) 12.87 µM of 43bp_hairpin_e13-target e13a2 complex vs 60 injection of 3 µl of revelator sequence at 150 µM; E) 42.59 µM 43bp_hairpin_e13-target e13a2 complex vs 34 injections of 3µl e13a2 sequence a 415 µM; F) 34.63 µM of 43bp_hairpin_e13-target e13a2 complex vs 17 injection of 5 µl of revelator sequence at 631.77 µM. Gray out points were considered outliers for the fitting model. Data were fitted with NanoAnalyse software using independent model. The raw ITC injection profile is shown in the top graphs.

Table 3.4. Parameters derived from the ITC experiments of 43bp_hairpin_e13 binding to e13a2 sequence at 20 °C.

	Hairpin at 15 µM		Hairpin at 42.59 µM		Hairpin at 51.11 µM	
Parameter	**Value**	**Confidence Interval (±)**	**Value**	**Confidence Interval (±)**	**Value**	**Confidence Interval (±)**
K_D (M)	1.82×10^{-8}	3.69×10^{-9}	1.56×10^{-8}	3.32×10^{-9}	2.45×10^{-8}	7.46×10^{-9}
n	0.86	0.005	0.78	0.002	0.79	0.003
ΔH (kJ/mol)	-459.30	5.779	-448.4	3.691	-414.60	4.207
ΔS (J/mol·K)	-1418.47	-	-1380.24	-	-1268.47	-
ΔG (kJ/mol)	-43.44	-	-43.82	-	-42.72	-
-TΔS (kJ/mol)	415.82	-	404.62	-	371.85	-
K_A (M^{-1})	5.49×10^{7}	-	6.41×10^{7}	-	4.09×10^{7}	-

The negative values of ΔG, ΔH and ΔS shows: 1) that this reaction is spontaneous as predicted by the NUPACK software and observed in the fluorescence assays; 2) the hybridization is enthalpic driven, due to the formation of the hydrogen bonds between strands and hydrophobic interactions within the strands (base sacking), but entropically unfavorable (271); and 3) The thermodynamic parameters (fitting values) for this hybridization is within the values presented in the literature (269).

From the injection profile of the revelator against the ≈13 µM of 43bp_hairpin_e13, top of Figure 3.13 D, the occurrence of hybridization is not clear, considering the minimal difference of signal obtained in the first injections in comparison with the last ones. The lack of a clear hybridization signal could be due to low heat transfer generated from this hybridization event. The binding profile presented on the bottom of Figure 3.13 D is concordant with a low C-Value ($\frac{[M]}{K_d}$) (272), typical for low affinity binding assays, and cannot be used for the correct determination of the fitting parameters. To obtain a sigmoidal distribution of the ITC data, higher concentrations of pre-formed hairpin-target complex was attempted. As such, the initial concentration of the hairpin in the reaction chamber was increased and titrated with a higher concentration of the e13a2 complementary sequence (Figure 3.13 B and C). The revelator sequence was then titrated against the target/hairpin complex (Figure 3.13 D and E). However, the profile of the binding isotherm was similar with the previous one with the difference that a higher heat was generated upon injection of the revelator. The difference in the heat release in the initial injections can be clearly distinguished from the heat of dilution, an indication of interaction, i.e. hybridization. However, the lack of a sigmoidal distribution of the experimental data, hinders retrieval of the thermodynamic parameters via the model fit. This is an indication that the titration of the revelator should be performed using higher concentrations of the preformed hairpin-target complex. An alternative is to perform competitive assays in which (272, 273): 1) a higher affinity ligand is used as titrant against the target molecule, 2) a mixture of the ligand in study and the high affinity ligand. The apparent fitting parameters can be deconvoluted as described in Zhang *et al* (273). However, this implies the use of a different or longer palindromic sequence which would defeat the purpose of the characterization of this system.

The same procedure was performed for the 43bp_hairpin_e14 and the respective complementary target sequence e14a2. The injection profile and binding isotherms for the formation of the 43bp_hairpin_e14-target e14a2 sequence are presented in Figure VI.I of appendix VI. The binding isotherm profile is within the acceptable for the retrieval of the thermodynamic parameters through the model fit (272). Table VI.I shows the fitting parameters for the tested conditions. However, the model fit to the experimental data is not complete (as seen in the lack of overlap between the prediction model and experimental data on the last points of experimental data). The injection profile (top of Figure VI.I of Appendix VI) indicates that a longer temporal separation between injections was desirable, for a more precise determination of the fitting

parameters. As with the previous condition, the stoichiometry parameter is lower than expected (mean of assays sets stoichiometry at 0.456 ± 0.008). The retrieved ΔG, ΔH and ΔS are similar to the 43bp_hairpin_e13-target e13a2, but the pair 43bp_hairpin_e14-target e14a2 shows a lower K_A(3.385 ± 0.08 $\times 10^5$ vs 5.33 ± 1.17 $\times 10^7$). Although the NUPACK software determined that the binding of the target sequence to the hairpin was more favourable for the e14 case, denoted by the lower ΔG – see Figure 3.5 vs Figure II.3 from Appendix II. This difference in K_A was not expected, considering that the number of base pairs (21 bp for the e14a2 target and 22 bp for the e13a2 target) and guanine/citosine content of the loop portion of both hairpins is very similar (47.6% for the e14a2 target vs 50% for the e13a2 target). This is likely due to the incomplete fit of the model to the experimental data, and will be addressed in the next section. Regarding the hibridization of the revelator to the 43bp_hairpin_e14/target sequence e14a2 – Figure VI.2, Appendix VI – is also consistent with a low C-Value (272), and as such it is not possible to derive accurately the fitting parameters of this binding event. Considering the high amount of oligonucleotide needed to improve the ITC assay, further optimization of the technique was not performed. In this context, the principle of MicroScale Thermoforesis (MST) was used to characterize this interacion.

3.5.2 MicroScale Thermophoresis

MicroScale thermophoresis (MST) was used to determine the binding affinity of the target e14a2 to the 43bp_hairpin_e14 and the binding affinity of the revelator sequence to the pre-formed complex. MST is based on the movement of molecules within a temperature gradient (coupling of heat-flow with mass-flow), known as thermodiffusion or Soret effect (274). The thermal gradient (∇T) is induced via a IR laser which leads to the variation of the biomolecule concentration (accumulation or depletion (275, 276)), within the focal volume. The concentration gradient depends on the size, conformation, charge, and hydration shell, parameters that are influenced molecular interaction. In this approach, one of the binding partners must be labeled with a fluorophore. The labeled molecule (reporter) is titrated with a variable amount of ligand and the concentration dependent thermophoresis profile (herein denoted as MST profile) is used to determine the binding affinity. The MST profile is obtained through measuring the initial fluorescence of each condition (i.e. to determine the emission of the cold region, ensure a constant emission of the labeled molecule in all the capillaries and to exclude the occurrence of binding dependent emission variation - see Figure VII.I, Appendix VII, for the initial fluorescence scan for the hybridization of the target and hybridization of the revelator sequence, respectively). The IR laser is then switched on and generates a temperature gradient (2-6 °C) in the focal volume, with a continuous emission monitoring – see Figure 3.14.

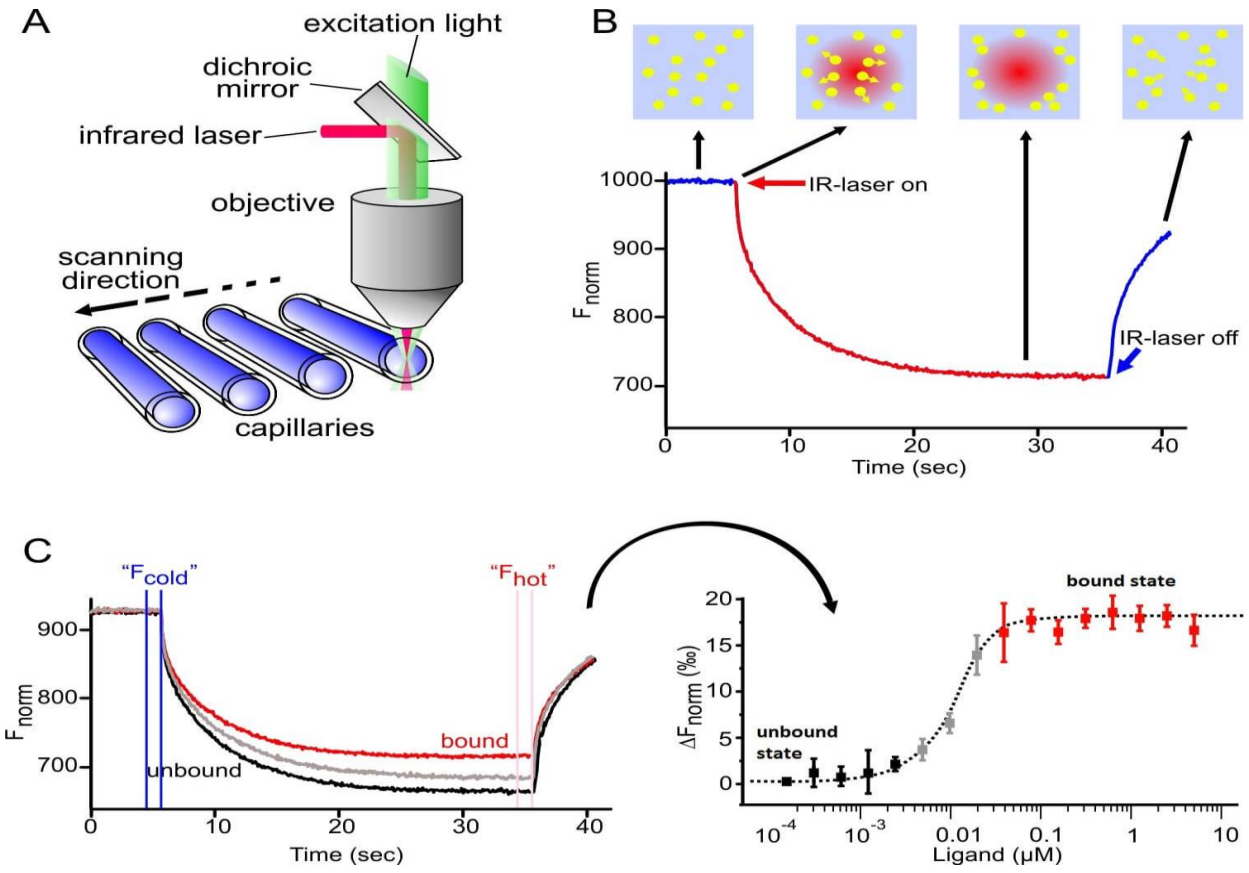

Figure 3.14. Schematic representation of MST setup and experiments. A) Schematic representation of MST optics. A focused IR-Laser is used to locally heat a defined sample volume. Thermophoresis of fluorescent molecules through the temperature gradient is detected (B) Typical signal of a MST experiment. Initially, the molecules are homogeneously distributed and the constant ‘‘initial fluorescence’’ is detected. Within the first second after activation of the IR laser, a rapid change in fluorophore properties due to the fast temperature change. Subsequently, thermophoretic movement of the fluorescence-labeled molecules out of the heated sample volume can be detected. After deactivation of the IR-Laser the diffusion’ of molecules, which is solely driven by mass diffusion. Titration of the non-fluorescent ligand results in a gradual change in thermophoresis, which is plotted to yield a binding curve. From (275).

The thermal variation of the quantum yield of the reporter dye is inevitable, however by using the same dye at the same concentration in all conditions, it is ensured that the observed signal is due to a concentration-dependent thermophoresis. The reporter molecule (43bp_hairpin_e14) was titrated with the complementary target, in a range of concentrations of 10 µM to 0.31 nM (prepared in a 1:1 serial dilution). The K_D was inferred from the dose-response curve (binding curve) that was generated from all the MST profiles, from the unbound to fully hybridized state – orange line and green line of Figure 3.15 A, respectively. For the target hybridization, the binding curve has a sigmoidal shape, with the unbound hairpin displaying a lower MST than the fully hybridize hairpin – black circles in Figure 3.15 B. The K_D for this interaction is 10×10^{-8} M ($\pm$ 1.9×10^{-8} M) (K_a of 1×10^{7} M^{-1}), which is in line with the K_a obtained for the same reaction using the 43bp_hairpin_e13 via ITC (see section 3.5.1). The specificity of the 43bp_hairpin_e14 was tested using

the e13a2 as target sequence, and no concentration dependent thermophoresis was observed, seen by the MST profile of Figure VII.2 A and by the gray circles in the binding curve of Figure 3.15 B.

To determine the affinity of the revelator towards the palindromic sequence, the reporter was pre-hybridized to the respective target (using a target concentration of at least 2 times the K_D - at least 200 nM, but a concentration of 240 nM was used), and the revelator sequence was used to titrate this complex (using a range of concentrations of 30 µM to 0.9 nM, prepared in a 1:1 dilution) – see Figure 3.15 C for the MST profile and Figure 3.15 D for the binding curve. From this binding curve, a K_D of 3.3× 10^{-7} (± 4.4× 10^{-8} M) M (K_a of 3.03 × 10^{6} M^{-1}) was determined.

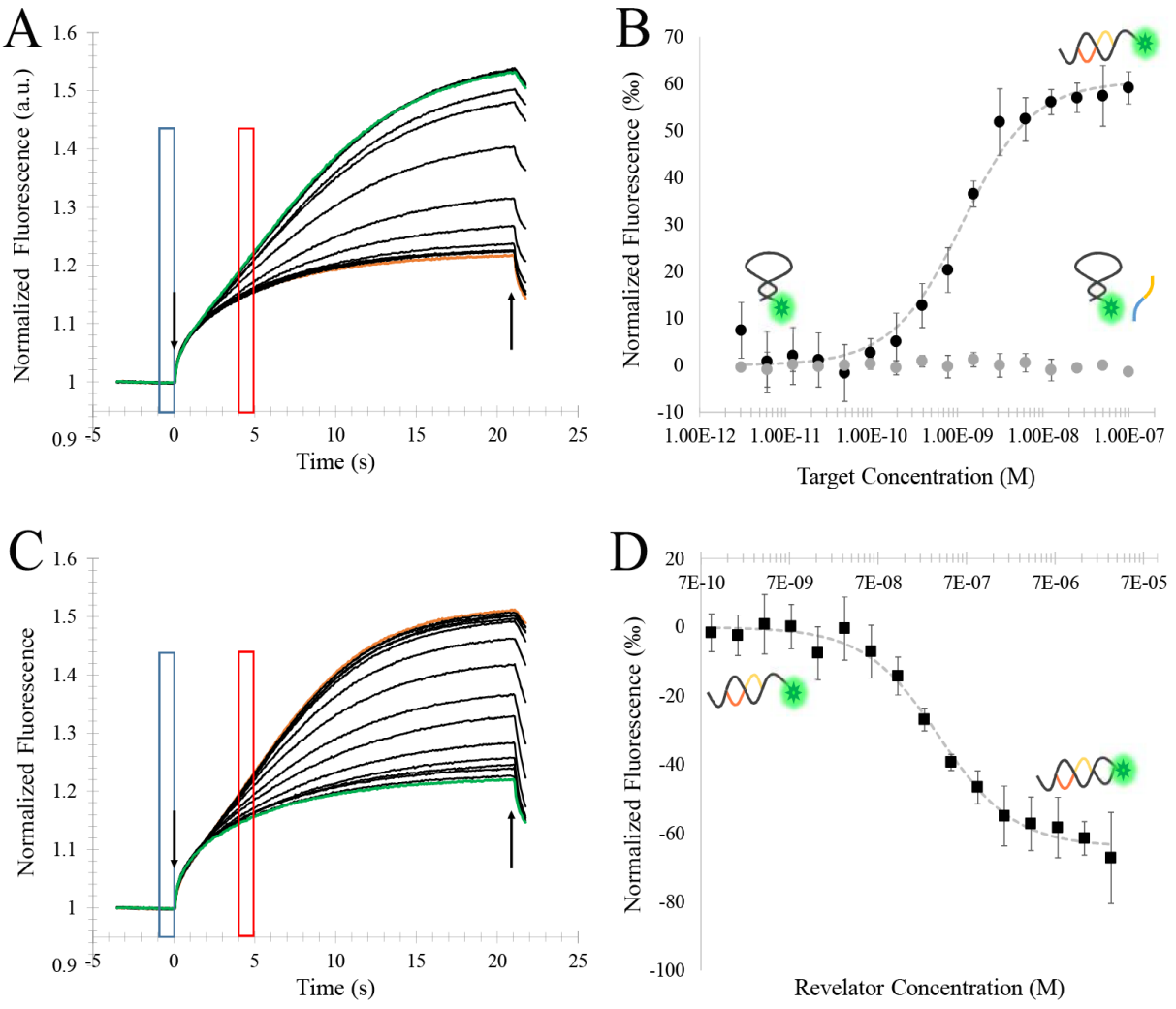

Figure 3.15. Determination of binding affinities for the hybridization of the target e14a2 and revelator sequence to the FAM labeled 43bp_hairpin_e14. A) MST profile for the hybridization of e14a2 target sequence to hairpin; B) Binding curve of the e14a2 target sequence to hairpin (black circles); Binding curve of the e13a2 target sequence to the hairpin; C) MST profile for the hybridization of the revelator sequence to the hairpin bound to the respective target sequence. The orange line represents the unbound state; Green line represents the fully hybridized state. The downward facing arrow represents the IR laser on; Upward facing arrow represents the IR laser off. Blue rectangle represents the time frame used for emission integration of the cold region. Red rectangle represents the time frame used for emission integration of the hot region. Data presented as mean ± standard deviation of three independent assays.

The hybridization of the revelator was expected to be less favorable than the hybridization of the target (as demonstrated by the lower K_a) considering that the revelator is shorter than the target sequence (less hydrogen bonds and lower base stacking). To be noted that in Figure 3.15 A and C, the fluorescence intensity jump is triggered by the focusing of the IR laser (down facing black arrow) on the focal volume of the capillary. This is an indication that this system has a negative thermophoresis profile, caused by the accumulation of FAM labeled hairpin within the hotter region of the thermal gradient. The literature reports that, depending on the reaction parameters and on the length and secondary structure, DNA can exhibit both positive thermophoresis (276–278) (depletion of molecules in the hotter region of the thermal gradient) and negative thermophoresis (276, 279, 280). Interestingly, the MST profile for the hybridization of the target sequence to the revelator is the inverse of that obtained for the hybridization of the revelator, with latter inducing a lower MST response (seen by the inversion of the binding profiles on Figure 3.15 B and C). This is an indication that different forces govern the thermophoresis of these two binding events. One hypothesis is that the hybridization of the target to the hairpin (situation presented on Figure 3.15 B) has a higher impact on the size of the complex and solvation entropy, Debye length and charge of the labeled hairpin (due to the disruption of the hairpin structure by a 21 nt target), whereas the hybridization of the revelator (10 bp) would mostly impacts the solvation entropy (to a lesser extent than the target hybridization (281) and charge.

3.6 **Analysis of the ensemble formation through SAXS and electrophoretic mobility.**

The formation of the desired ensemble (tcMB) was structurally characterized by SAXS and confirmed by native acrylamide gel electrophoresis. SAXS is a structural technique that allows the characterization of biomolecules and assemblies in solution. SAXS can be applied to electron dense molecules of a broad range of molecular weights (from kDa to MDa). These measurements can be performed under virtually any arbitrary biocompatible solution (e.g. different solvents, ionic strengths and temperatures) (282, 283). The elastic scattering of the X-rays by the molecules in solution is detected at low angles (0.1 – 10 °), allowing the retrieval of the overall shape and size of molecules ranging from 5 to 25 nm (283) (lowering the angle of the detector, bigger molecules can be resolved). The SAXS scattering profile is based on the contrast of elastic scattering of X-rays photons between a given analyte (here, DNA) and respective solvent. Due to the electron-rich phosphate backbone, DNA has a high contrast from the dispersion/hybridization buffer. As such, DNA SAXS experiment does not require prior chemical modification/labeling (like fluorophores for fluorescence spectroscopy or isotope labeling for NMR). Moreover, this assay is performed in a homogenous format which allows for a more precise approximation of the real scenario, when compared with others structural techniques such as X-ray crystallography (that requires a crystalline sample) or atomic

force microscopy or electron microscopy, that are performed in anhydrous samples. However, this technique yields lower resolution structural information than the before mentioned techniques due to the averaging of the random reorientation molecules.

The formation of the desired ensemble was tested using the non labeled sequences of hairpin/revelator 3 and 4 pairs and the overall shape determined by SAXS. Data was collected in different scenarios, for each of the components alone (isolated hairpin (e13A – for 43bp_hairpin_e13; e14A – for 43bp_hairpin_e14), target (e13B – for e13a2 sequence; e14B – for e14a2 sequence) and revelator (e13C – revelator of e13A; e14C – revelator for e14A), and each step of the ensemble formation (hairpin hybridized to the target sequence (e13AB and e14AB) and final ensemble (e13ABC and e14ABC)). The presence of a partial complementary target was also tested. The overall structural parameters for each component, intermediate and final ensemble estimated from SAXS profile are shown in Table 3.5.

The scattering profile of the hairpins alone (e13A and e14A) provides R_g and D_{max} values that are compatible with a symmetrical hairpin structure with 43 nt (considering a base separation of 3.4 Å (284)). These parameters are slightly higher for hairpin e14A (R_g 2.93 nm and D_{max} 12.5 nm) than for e13A (R_g of 2.36 nm and D_{max} of 8.0 nm) suggesting that the latter is more compact (Table 3.5 and Figure 3.16). These values serve as a baseline for the close hairpin structure and used to infer the occurrence of hybridization. For the situation where the hairpins are in the presence of their respective complementary target (e13AB and e14AB), the SAXS data shows a significant structural alteration, based on the near duplication of the R_g and D_{max} parameters (e13AB: R_g 5.40 nm and D_{max} 20.0 nm; e14AB: R_g 5.85 nm and D_{max} 22.5 nm). This increase in the SAXS parameters is due to the disruption of the symmetrical hairpin upon hybridization to the target molecule, forming a more extended structure – Table 3.5 and Figure 3.16.

SAXS also allows the determination of *ab initio* bead models that are represented for the hairpin e13A and e14A are represented in Figure 3.17, respectively.

Table 3.5. The overall structural parameters estimated from SAXS data. R_g – radius of gyration, D_{max} – maximum size of the particle, V_P – excluded volume of the particle, χ^2 - fit quality of ab initio models to experimental data.

Sample	R_g nm	D_{max} nm	V_P nm^3	χ^2
e13A	2.36	8.0	24	1.58
e13B	1.86	7.0	13	0.85
e13C	1.32	5.0	8	0.86
e13AB	5.40	20.0	103	1.85
e13ABC	4.56	18.0	59	1.78
e14A	2.93	12.5	34	1.34
e14B	2.05	9.0	15	0.93
e14C	1.29	5.0	7	0.91
e14AB	5.85	22.5	159	1.31
e14ABC	5.21	20.0	105	1.87
e13A-e14B-e13C	3.95	18.0	65	0.76
e14A-e13B-e14C	3.80	14.0	42	1.29

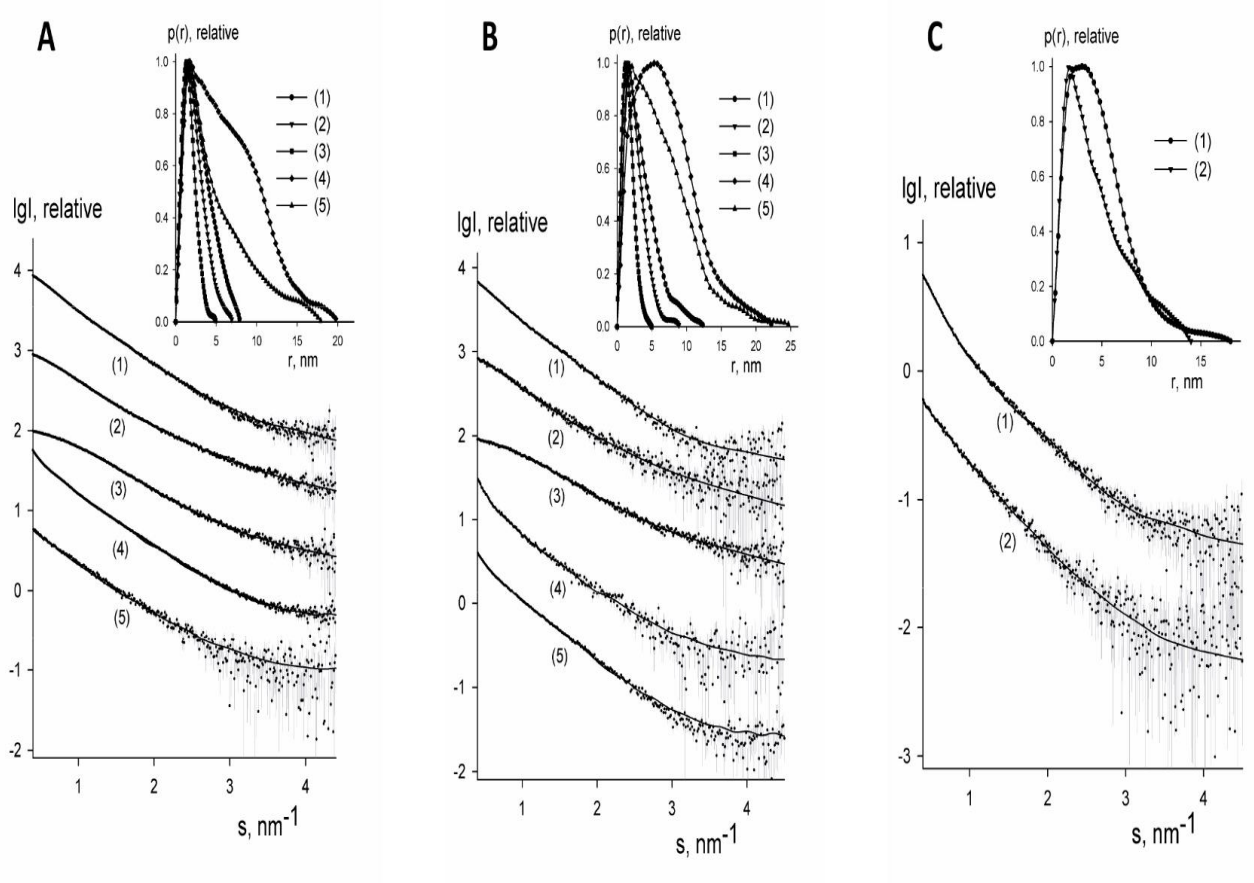

Figure 3.16. Experimental SAXS patterns (dots with error bars) and scattering calculated from the *ab initio* models (continuous line). Panel A - e13A (curve1), e13B (curve2), e13C (curve3), e13AB (curve4), e13ABC (curve5), Panel B - e14A (curve1), e14B (curve2), e14C (curve3), e14AB (curve4), e14ABC (curve5), Panel C – e13A-e14B-e13C (curve1), e14A-e13B-e14C (curve2). The plots display the logarithm of the scattering intensity as a function of momentum transfer. The curves are shifted by one logarithm order for better visualization. The inserts contain distance distribution functions P(r).

The estimation of the excluded volume – Table 3.5 - of the DNA strands points to the formation of e13AB/e14AB complexes. The same effect can be observed in acrylamide gel electrophoresis (Figure 3.18). Here, the bands that correspond to hairpins alone were used as the reference to calculate the retention factor (R_f), which is defined as the ratio of a given band and the reference band (usually the dye front). This allows to infer the impact of the hybridization on the electrophoretic mobility of the reference molecule. The dye used to post-stain the acrylamide gel (Gel Red®) has a lower sensitivity towards ssDNA, and as such, neither the targets or revelators are visible in these conditions. These bands can be seen when the electrophoresis is carried out in 5 % agarose gel, using longer staining times and in the presence of 100 mM of NaCl – see Figure VIII.1, Appendix VIII.

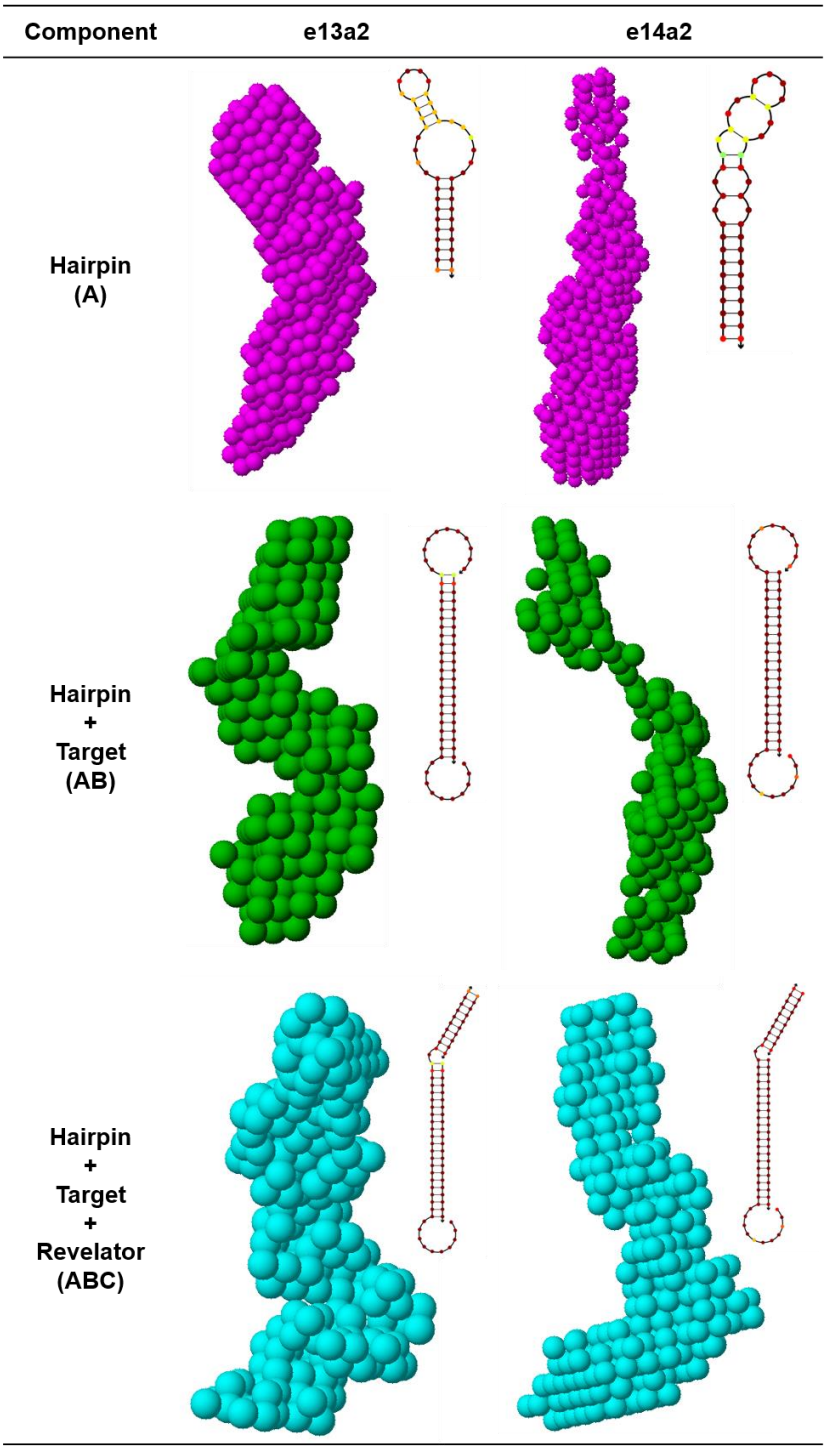

Figure 3.17. *Ab initio* models of the several tested conformations. Hairpin (magenta), disrupted hairpin after target hybridization (green) and final ensemble (blue). Inserts: NUPACK structure prediction of each situation at 283 K.

The hairpins hybridized to their respective target, e13AB (R_f = 0.177) and e14AB (R_f = 0.181) complex (Figure 3.18 lane 2A and 2B, respectively) have shorter migration levels than the components alone (Figure 3.18 – lane 1A for e13A (with a R_f = 1) and lane 1B for e14A (R_f = 1)), indicating of a successful

hybridization. The *ab initio* model for this condition shows a bigger and more distended overall structure in comparison to the hairpin alone, supported by the electrophoretic profile.

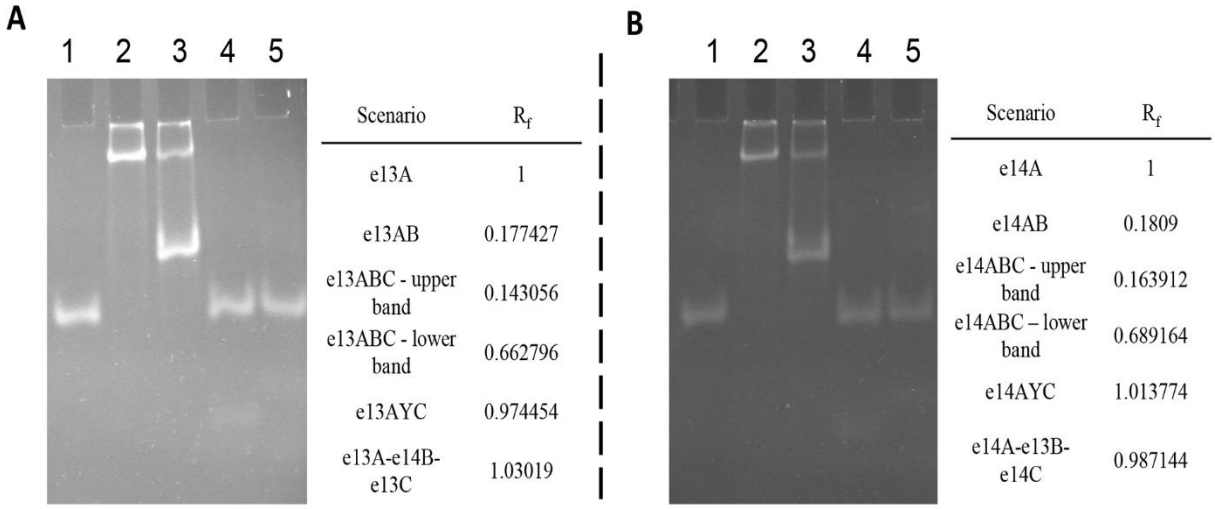

Scenario	R_f
e13A	1
e13AB	0.177427
e13ABC - upper band	0.143056
e13ABC - lower band	0.662796
e13AYC	0.974454
e13A-e14B-e13C	1.03019

Scenario	R_f
e14A	1
e14AB	0.1809
e14ABC - upper band	0.163912
e14ABC – lower band	0.689164
e14AYC	1.013774
e14A-e13B-e14C	0.987144

Figure 3.18. Acrylamide gel electrophoresis of the isolated hairpin, intermediate ensemble and final ensemble. A. Lane 1 – e13A; Lane 2 – e13AB; Lane 3 – e13ABC; Lane 4 – e13AYC; Lane 5 – e13A-e14B-e13C; B. Lane 1 – e14A; Lane 2 – e14AB; Lane 3 – e14ABC; Lane 4 – e14AYC; Lane 5 – e14A-e13B-e14C; Running conditions: 20% acrylamide in 1×TBE; 16 hours at 20V, 277 K. R_f: relative migration distance was calculated using the ImageJ software package.

As demonstrated by the previous analysis (Fluorescence Spectroscopy and MicroScale Thermophoresis Figure 3.9, Figure 3.10 of section 3.4.2, and Figure 3.15 of section), the presence of the target sequence e14a2 is not able to disrupt the 43bp_hairpin_e13 conformation, situation corroborated by the electrophoretic profile, as seen in lane 5A of Figure 3.15 for the 43bp_hairpin_e14 ($R_f = 1$) and lane 5B of Figure 3.18 for the 43bp_hairpin_e14 in the presence of the e13a2 sequence ($R_f = 1$). However, the R_g and D_{max} values derived from the SAXS curves are higher than the ones obtained for the hairpins alone and very close to the ones obtained for the hybridized hairpin – Table 3.4. This difference could be derived from the presence of a mixture of free molecules in solution or, on the contrary, to the formation of a 1:1:1 complex – this last hypothesis is not supported by the overall data. However, it should be noted that the concentrations and temperature conditions used to perform each type of measurements are very different. In the case of SAXS, scattering data is collected at concentrations several folds higher and at lower temperatures in comparison to the fluorescence spectroscopy and gel electrophoresis. Such a high concentration at low temperatures may induce the hybridization of the hairpin with the partial complementary target (285), as simulated by the NUPACK software – Table III.1 Appendix II. However, the concentration range used in SAXS (equimolar concentration of the various component is in the order of 101 µM) is incompatible for

fluorescence spectroscopy, due to inner filter effects, detector saturation and cost associated with the use of such concentration range.

For the two final complexes, the R_g and D_{max} values obtained for complex from the 43bp_hairpin_e13 and 43bp_hairpin_e14 (R_g: 4.56 and 5.21 nm, D_{max}: 18 and 20 nm, respectively) are higher than the ones obtained for the corresponding hairpins alone, as expected for an open hairpin hybridized with its target sequence (Table 3.5). Furthermore, these values are slightly lower than the ones observed for the intermediate state (hairpin hybridized to its respective target), probably due to the formation of a more compact structure upon the duplex formation at the 3' end of the open hairpin. This is supported by the electrophoretic profile (Figure 3.18), where the complexes e13ABC (R_f= 0.663) and e14ABC (R_f= 0.689) migrate beyond the e13AB (R_f= 0.143) or e14AB pairs (R_f= 0.181) (Figure 3.18 – lanes 3A and 3B in comparison to lane 2A and lane 2B, respectively).

From the excluded volume estimate – Table 3.5 – e13ABC can be comparable with a 1:1:1 (stoichiometry ratio) complex, whereas e14ABC can apparently form the complex with higher stoichiometry ratio (Table 3.5, Figure 3.16). The higher stoichiometry ratio for the e14ABC, suggests that at these concentration levels, the final ensembles could interact with each other. The ab initio bead models obtained for the assemble tcMB assembly are represented in the left panel of Figure 3.17 A and B. Here, the calculated models also reinforce the evidence that e13(e14)ABC forms a more compact structure when compared with e13(e14)AB.

The overall data indicates that: 1) the hybridization of the three strands occurs and is sequential, since the hybridization of the acceptor-labeled oligonucleotide is dependent on the pre-hybridization of the target; 2) the presence of a partial complementary target with 55.6% identity with the fully complementary target is not able to disrupt the hairpin structure, resulting in the lack of a FRET signal and a similar electrophoretic profile as the hairpin alone; 3) The SAXS measurements are concordant with the *in silico* simulations, with the emission spectra and gel electrophoresis, indicating that this technique can be a valuable tool for the characterization of DNA structures.

3.7 **Conclusion**

In this chapter, the optimization and characterization of the tcMB was performed using mainly the FRET specific signals generated in the presence of the target sequence, and compared to several controls (absence of target, presence of non-complementary target and presence of partially complementary target). The recognition of the target sequence by the donor labeled ssDNA with a hairpin conformation disrupts this secondary structure, exposing the palindromic sequence. This palindromic sequence can be targeted by an

acceptor-labeled oligonucleotide, generating a FRET signal (decrease of donor emission with concomitant enhancement of the acceptor emission), that is only observed in the presence of the fully complementary target. The formation of the tcMb was further characterized using electrophoretic mobility, SAXS, MST and ITC measurement. The SAXS data indicate that the formation of this final complex is sequential and specific, and the alteration of the thermophoretic mobility upon target and revelator binding also supports the formation of the desired structure. SAXS indicates a near duplication of the size of the hairpin upon target recognition and a slight decrease after the hybridization of the acceptor-labeled oligonucleotide, with the formation of a 1:1:1 complex. This work describes a methodology that can be used for designing and characterizing molecular beacons for fast and accurate detection of the sequence associated with the development of pathologies associated with genetic translocations.

Considering the obtained results, the characterized hairpins (43bp_hairpin_e13 and 43bp_hairpin_e14) were used to functionalize the synthesized gold nanoparticles in section 4.

4 BioCode Gold-Nanobeacon for the detection of fusion transcripts causing Chronic Myeloid Leukemia

The work presented within this Chapter resulted in the following publication:

Cordeiro M.; Giestas L.; Lima J.C.; Baptista P.M.V. BioCode gold-nanobeacon for the detection of fusion transcripts causing chronic myeloid leukemia. *Journal of Nanobiotechnology* **2016**, 14, 38.

Milton Cordeiro was responsible for the experimental work, data analysis and manuscript drafting.

4.1 Introduction

The main objective of this chapter is to develop an AuNP molecular beacon based biosensor coupled to a wavelength shift mediated by FRET – BioCode Au-nanobeacon, using the hairpin structures developed in the previous section. Briefly, the presence of the target sequence is signaled by a conventional Au-nanobeacon, through the partial recovery of the emission of the fluorophore labeling the hairpin functionalized on the surface of the AuNP. The AuNP acts both as a scaffold were multiple hairpins can be grafted and acts as a dark quencher for the donor fluorophore. In the closed state, the donor is quenched by its proximity to the AuNP surface—donor quenching (Figure 4.1 a); upon hybridization to the target sequence (BCR-ABL fusion sequence), the hairpin structure is disrupted, increasing the distance between donor and the AuNP surface, causing a partial recovery of fluorescence emission, while expositing the palindromic sequence of the hairpin (Figure 4.1 b). Once the palindromic sequence is exposed, the acceptor-labeled oligonucleotide hybridizes, allowing FRET between both fluorophores (Figure 4.1 c) and, leading to a dual channel signal output. The occurrence of FRET allows for a wavelength shift of the hybridization fluorescence signal to wavelengths that should not be affected by the high absorption of the AuNP.
This design was tested using the fusion sequences e13a2 and e14a2 (accession numbers: AJ131467.1 and AJ131466.1, respectively), biomarkers for the development of CML.

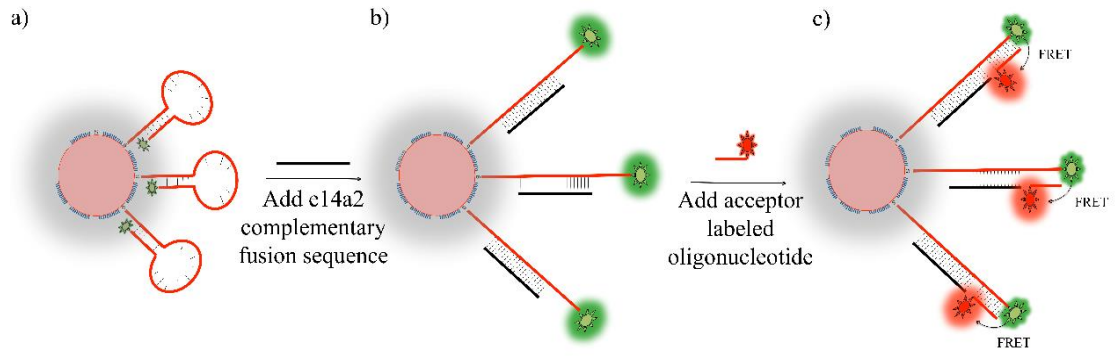

Figure 4.1. Schematic representation of the BioCode Au-nanobeacon. a) The hairpin in its closed conformation strongly suppresses fluorescence. b) A complementary target disrupts the hairpin and the donor breaks away from the AuNP surface leading to partial recovery of the donor's fluorescence. c) Hybridization to the target sequence exposes the palindromic sequence, which can then be targeted by the revelator triggering the enhancement of the acceptor emission due to the specific FRET between the fluorophores that codify each possible target sequence. From (264)

4.2 AuNP characterization

The AuNP were synthesized via the citrate reduction method, optimized to yield spherical citrate-capped AuNP (AuNP@citrate) with an average size between 13 and 15 nm. This choice of particle synthesis, morphology and size was based on reproducibility of the methodology, the possibility of surface modification using the strong gold-thiol bond allowed by the thiol-citrate exchange. This AuNP synthesis has been used in previous work performed within the Nanomedicine@FCT group, where the AuNP were synthesized by this approach yielded functional Au-nanobeacons (115, 175, 286). The synthesized AuNP were characterized via transmission electronic microscopy (TEM), dynamic light scattering (DLS) and UV-Vis spectroscopy – see Figure 4.2 for a representative characterization of AuNP@citrate during the course of this work.

The TEM micrograph presented on Figure 4.2 A1 and A2, shows a spherical population of nanoparticle with a size distribution centered at 14 nm (mean ± standard deviation obtained by through the histogram presented on Figure 4.2 B1: 14.56 ± 1.65 nm and B_2: 13.95 ± 1.79 nm). The absorption spectrum of the synthesized AuNP shows that the LSPR is centered at 519 nm, giving the AuNP the characteristic ruby red color. The LSPR of 14 nm AuNP centered at this wavelength is consistent with the literature (225), and the Abs ratio of 520/450 nm is also consistent with the methodology proposed by Haiss *et al* (287), where this ratio should be around 1.61 for 14 nm AuNP. Here, the ratio obtained is of 1.63 and 1.64 which sets the average size of AuNP between 14 and 16 nm which is concordant with the TEM analysis.

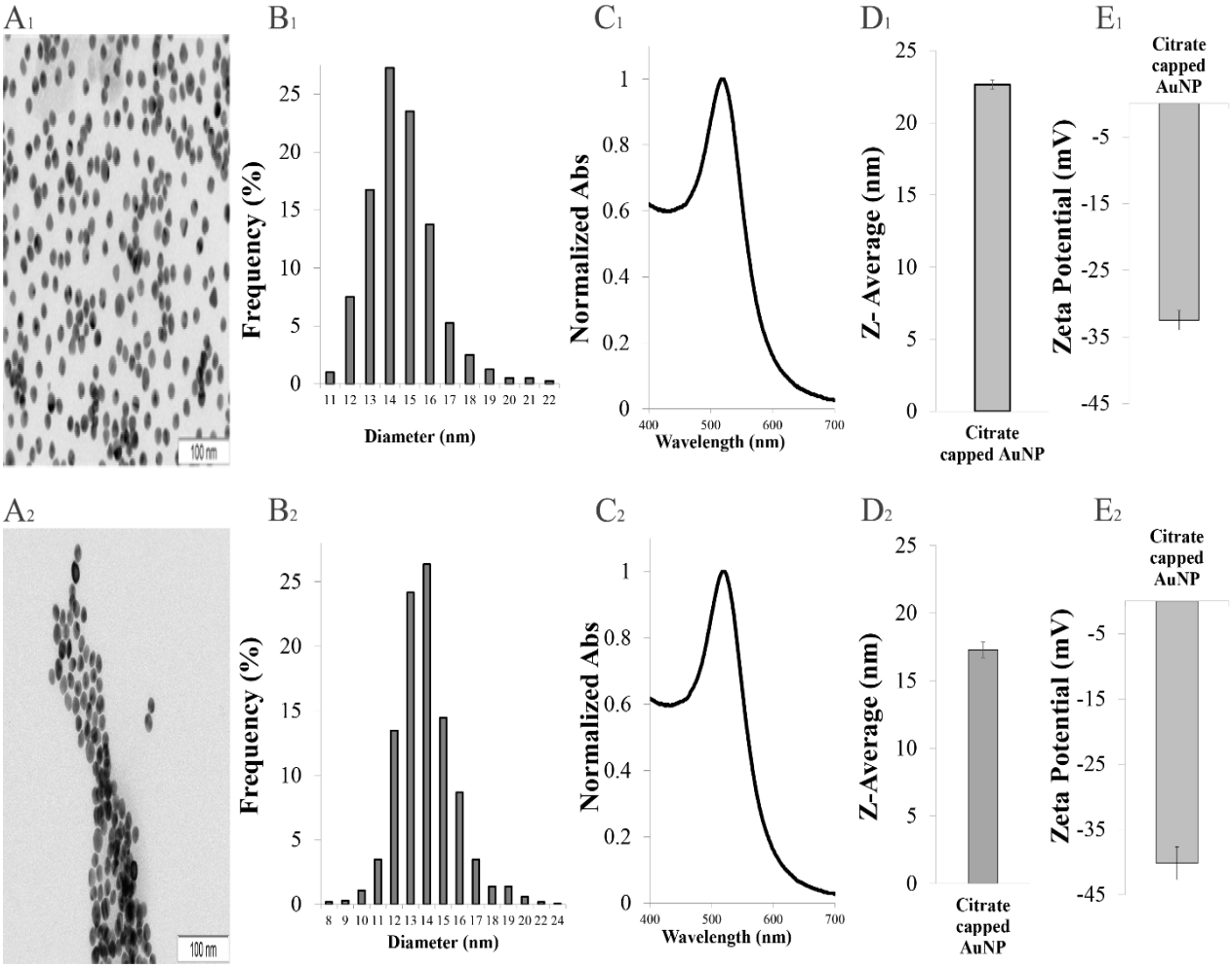

Figure 4.2. Characterization of citrate-capped AuNPs. A_1, A_2) Transmission electron microscope of two independent batches; B_1, B_2) Size distribution of the synthesized AuNPs. The average size of the citrate-capped AuNP were: B_1:14.56 ± 1.65 nm, B_2: 13.95 ± 1.79 nm; C_1, C_2) Normalized absorption spectra of the synthesized AuNP; D_1, D_2) Z-Average calculated by DLS: D_1:22.64 ± 0.32 nm (Pi: 0.064 ± 0.03), D2: 17.28 ± 0.58 nm (Pi: 0.142 ± 0.126); E_1, E_2) Zeta potential of the AuNP: E_1: -32.48 ± 1.43 mV, E_2: -40.2 ± 2.51 mV.

The DLS measurements, Figure 4.2 D_1 and D_2, set the average hydrodynamic diameter (Z-average) of the synthesized AuNP diameter between 17 and 23 nm, higher than the measurements obtained by the TEM micrographs. This is expected considering that the TEM micrograph are only able to detect conducting substrates (the gold core (288)), whereas the DLS measurements are based on the Brownian motion of the particles which is influenced not only by the 'core' of the particle but also by the solvation sphere responsible for the solubility of the metal core (289, 290). This solvation layer includes the citrate corona, the stern layer (a firmly attached layer of counter ions), and diffuse layer (where a gradient of ions exists due to the presence of the stern layer). According to the Derjaguin–Landau–Verwey–Overbeek theory (DLVO (291, 292)), the colloidal stability is governed by the equilibria of Van der Waals interactions (generally attractive forces) and electrostatic interactions (can be either attractive and repulsive). For two identical particles, the electrostatic interactions tend to be of a repulsive nature considering the same

electrical double layer (a stern layer composed of a firmly attached opposing charge ions and a diffuse layer of both positive and negative ions that are in equilibria with the bulk solution) surrounding both particles. For a stable colloid, the electrostatic repulsions must outweigh the attractive forces. One way to infer the stability of a colloidal solution is to measure its zeta potential, the potential measured in the interface between the stern layer and diffuse layer (this potential varies as a function of the surface potential). This potential is related to the electrophoretic mobility of the particles within an electric field. The zeta potential measurements show that the mean of these values for the AuNP@citrate is around -30 mV. This value is considered a threshold for stable colloids due to enough repulsion between the particles to avoid aggregation/flocculation (293). For the synthesized AuNP, the negative charged surface is conferred by the citrate molecules which acts as a stabilizing capping agent. This value is within what is expected for metallic nanoparticles (294).

4.3 Optimization of AuNP surface coverage with thiolated Poly-ethylene Glycol

Before the functionalization with the hairpin structures, the synthetized AuNP were functionalized with a commercial hetero-functional PEG-modified with a thiol group (O-(2-mercaptoethyl)-O'-methylhexa(ethylene glycol)). The reasoning behind this functionalization is the minimization of unspecific interaction between DNA strands and the gold surface, allowing faster hybridization kinetics to ssDNA immobilized on said surfaces (295), as well as increasing the colloidal stability of the functionalized AuNP (296). The PEG length, with a theoretical distended length of 25.96 Å (297–299) is shorter than the minimum 34 Å of the palindromic sequence of the detection hairpin. This allows the protruding of the oligonucleotides to be functionalized to allow a successful hybridization (300). The PEG loading capability of the synthetized AuNP was determined by incubation a fixed amount of AuNP with increasing concentrations of thiolated PEG. After the saturation of the surface of the AuNP (100 % surface coverage), the excess of thiolated PEG stays dispersed in solution and can be detected via the Ellman reaction[1]. The saturation point (100% surface coverage) for the synthetized AuNP was determined to be at 0.01 mg/ml, in line with previous studies (183) – see Figure IX.1 and IX.2 of Appendix IX, for calibration curve and thiolated PEG saturation profile of the 14 nm AuNP.

[1] Reaction of thiol linked to the PEG molecule with 5,5'-dithiobis-(2-nitrobenzoic acid), generates a colored product that can be detected via UV-vis spectroscopy

To determine the appropriate PEG surface coverage for target recognition, the FAM labeled hairpin (43bp_hairpin_e14) was used to functionalize AuNP with different surface coverage (30 %, 45% and 60%), yielding Au-nanobeacons. These were incubated with an excess of target at two different concentration of the Au-nanobeacon (1 and 2.5 nM) – see Figure 4.3.

From the solid black line in Figure 4.3 it is possible to observe that, the basal emission of the Au-nanobeacon decreases as a function of the AuNP surface coverage with the PEG molecules. In the highest surface coverage tested (60%), the fluorophore emission (centered at 520 nm) is barely observable – Figure 4.3 C and D. This is due to the crowding of the AuNP surface with the thiolated PEG that does not allow the further incorporation of thiolated molecules, as previous studies demonstrated (295). The dashed black line represents the emission of the FAM fluorophore after incubation with the complementary target e14a2, and no difference in emission is observed. For the 30% and 45% PEG coverage – Figure 4.3 C,D and E,F, respectively – the fluorophore presents a higher emission than in the 60 % of PEG coverage, as more hairpin can be incorporated into the surface of the AuNP. The incubation of these constructs with the complementary target induces an increase of the donor emission band – dashed black line. This is concordant with the hybridization of the target sequence to the hairpin structure immobilized onto the surface of the AuNP. This hybridization disrupts the secondary structure, responsible for keeping the fluorophore near to the AuNP surface where the quenching effect is the strongest. For the 60% of PEG coverage, no emission difference is observable, probably due to the low density of recognition probes immobilized on the surface of the AuNP.

The highest difference between the hybridized and non-hybridized configuration of the Au-nanobeacon is found in Figure 4.3 C and D, which corresponds to the 45% surface coverage. This higher emission recovery must be related to the higher degree of hybridization between the target sequence and the immobilized hairpin in comparison to the situation where the AuNP has a 30% of surface coverage with PEG. This can be explained by a higher probe separation on the surface of the AuNP, minimizing the electrostatic repulsion between strands. This has been reported to promote hybridization of DNA onto DNA grafted on the surface of AuNP (301). As such the 45% of PEG coverage was chosen to proceed with the studies.

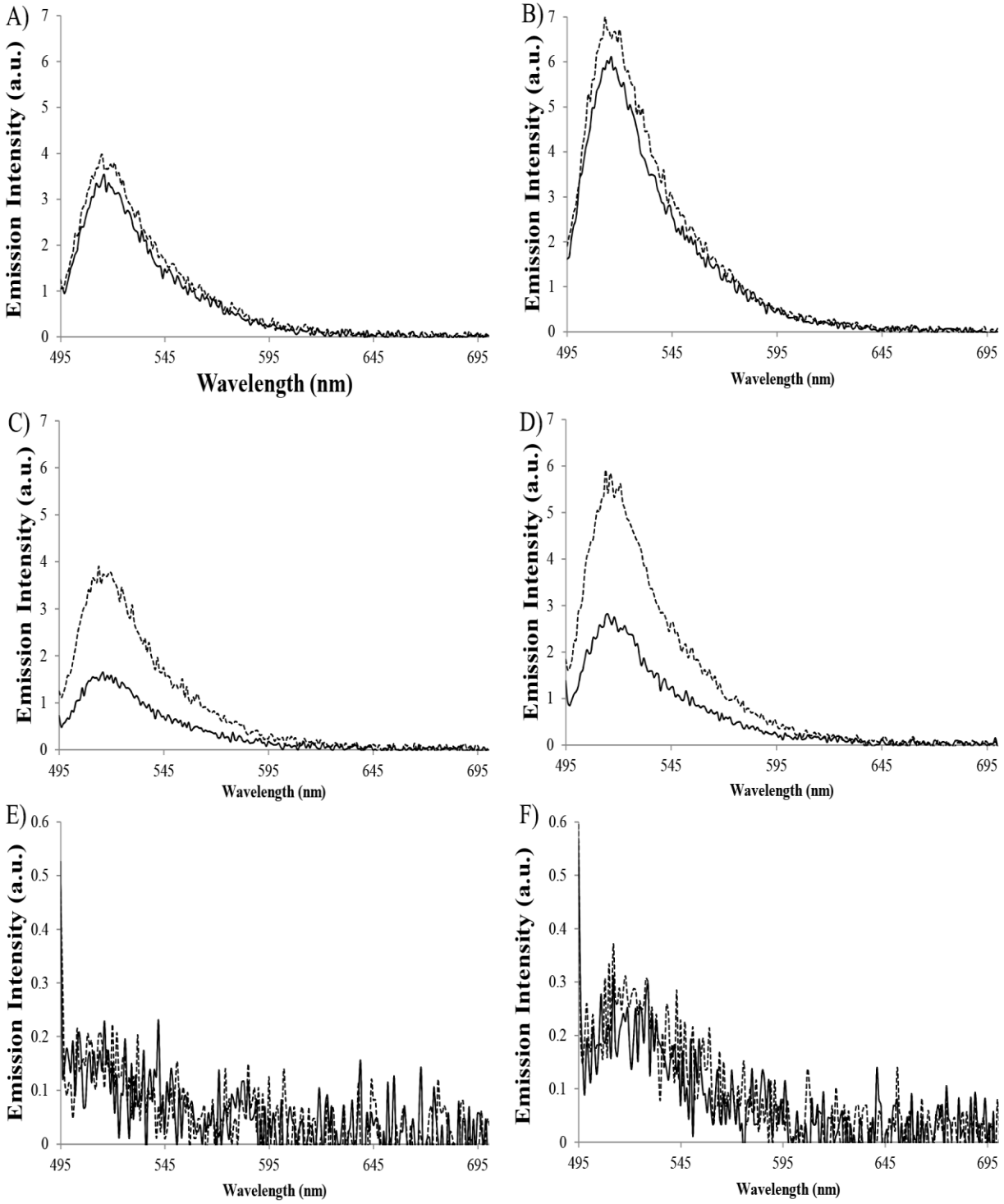

Figure 4.3. Donor signal variation upon incubation with the complementary target. A), B) 30% surface coverage with PEG using 1 nM and 2.5 nM of the Au-nanobeacon, respectively; C), D) 45% surface coverage with PEG using 1 nM and 2.5 nM of the Au-nanobeacon, respectively; E), F) 60% surface coverage with PEG using 1 nM and 2.5 nM of the Au-nanobeacon, respectively; Solid black line refers to the Au-nanobeacon in the absence of the complementary target. The dotted black line refers to the Au-nanobeacon emission in the presence of 1 µM of complementary target

4.4 **BioCode Au-nanobeacon characterization**

The AuNP with a 45% surface coverage were further functionalized with the oligonucleotide with a hairpin structure modified with a six-carbon linker on the 5' and with the donor on the 3' (either FAM or Cy3). After the functionalization using the hairpin sequence of pair 2 (denoted as BioCode-43bp-e14-FAM-1), the number of hairpins per particle was determined by subtractive assessment of the supernatants. The number of hairpins per AuNP for this nanoconstruct was determined to be 59. The calibration curve used for the quantification is presented on Figure X.1 of Appendix X. To determine the hydrodynamic diameter of the Au-nanobeacon when the hairpins are in the closed conformation, DLS measurements were performed at 25 ℃, in absence of target and in the presence of 1 μM of complementary target This measurement was repeated at 60 ℃ in the absence of target – See Figure 4.4 – to further ensure surface functionalization.

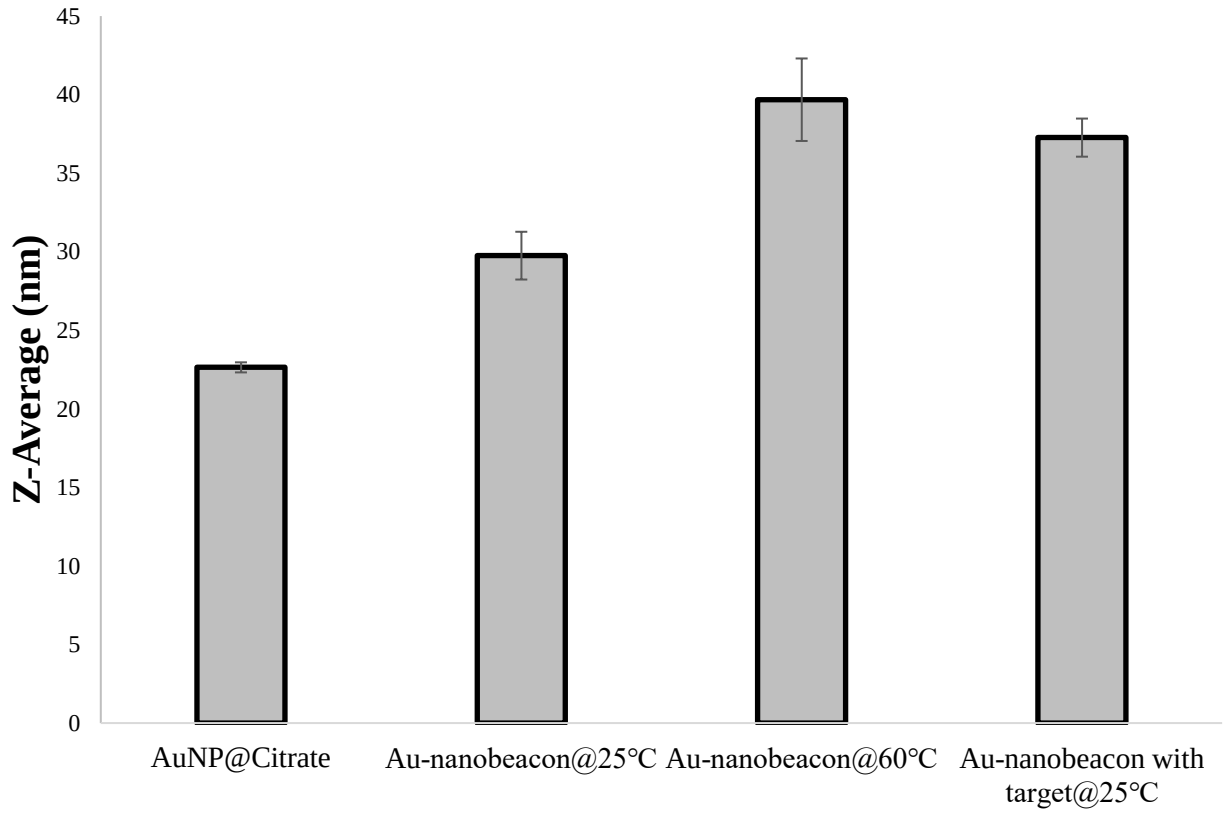

Figure 4.4. Hydrodynamic diameter of AuNP@citrate and Au-nanobeacon (from BioCode-43bp-e14-FAM-1) in different conditions. From left to right: AuNP@citrate measured at 25 °C; Au-nanobeacon measured at 25 °C; Au-nanobeacon measured at 60 °C; Au-nanobeacon incubated with fully complementary target measured at 25 °C. Data expressed as mean ± standard deviation of at least 5 independent assays.

The Z-average determined at 25 °C for the AuNP@citrate and the Au-nanobeacon shows an increase in the latter one, due to the grafting of the hairpins in the surface of the AuNP. This is compatible with a successful functionalization, considering that the attachment of the oligonucleotides increases the solvation shell of the AuNP and, therefore for, decreases the Brownian motion of the whole complex (parameter by which the solvation shell is inferred). The measurements performed at 60°C, a temperature above the melting temperature of the palindromic sequence of the hairpin, shows an increase in the measured hydrodynamic diameter. This suggests the disruption of the hairpin, which leads to the protruding of the oligonucleotide further from the surface (linearization of the hairpin), thereby increasing the solvation shell of the nanoconstruct. This effect is also observable upon hybridization of the complementary target which also disrupts the secondary structure of the hairpin – see Figure 4.4 and Figure 4.5.

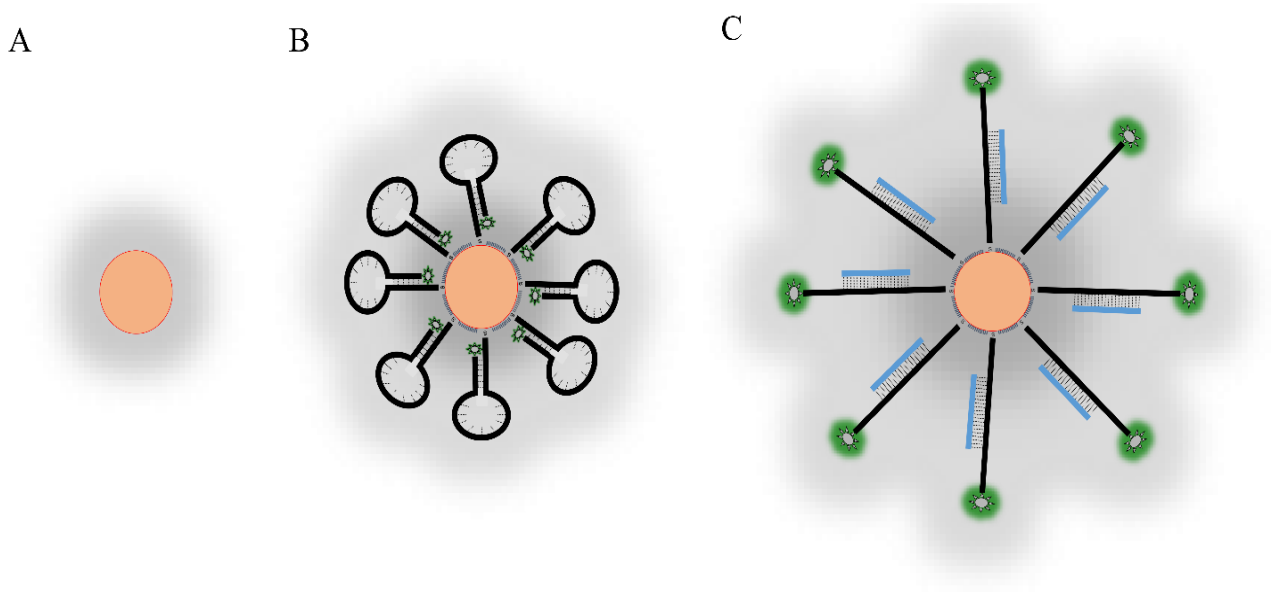

Figure 4.5. Representation of the solvation shell of the AuNP in the different phases of functionalization. A) AuNP@citrate; B) Au-nanobeacon with the hairpins in the closed conformation; C) Au-nanobeacon with the hairpins in the open conformation. The gray glow represents the hydration shell of the constructs. Components relative size is not to scale.

For the functionalization using pair 3 (denoted as BioCode-43bp-e13-FAM, where the donor is FAM) and pair 5 (denoted BioCode-43bp-e14-Cy3, where the donor is cy3), a detailed characterization is presented on Figure 4.6. Here the functionalization process did not an impact on the measured core size (13.43 ± 2.01 nm for BioCode-43bp-e13-FAM and 13.721 ± 1.883 nm for BioCode-43bp-e14-Cy3) - as expected, since the TEM micrograph only detects the conducting substrates – see Figure 4.6 A) for the size distribution histograms. The hydrodynamic diameter of these BioCodes (50.56 ± 1.54 nm for BioCode-43bp-e13-FAM and 33.88 ± 1.93 nm for BioCode-43bp-e14-Cy3) shows an increased in comparison to the AuNP@citrate (22.53 ± 0.32 nm) - Figure 4.6 B. The same effect is observed in the zeta potential (ζ-potential) experiments,

were both BioCodes present a lower ζ-potential (-85.77 ± 1.56 mV for BioCode-43bp-e13-FAM and -55 mV for BioCode-43bp-e14-Cy3) than the AuNP@citrate (-31.95 ± 6.96 mV) – Figure 4.6 C. This indicates that the grafting of the hairpin onto the surface of the AuNPs, with the interchange of the adsorbed citrate anions with the highly negative phosphate backbone via a quasi-covalent (S-Au), increases the surface charge which increases their colloidal stability.

The UV–Vis spectra for these BioCodes show a slight decrease in the SPR frequencies and a broader full-width-at-half-maximum – Figure 4.6 D.

The number of nucleotides per particle was determined, as in the previous situation, via subtractive assessment of the supernatants with approximately 63 hairpins labeled with the donor FAM for BioCode-43bp-e13-FAM (using the calibration curve presented on Figure 4.6 E) and approximately 51 hairpins labeled with the donor Cy3 for BioCode-43bp-e14-Cy3 (using the calibration curve presented on Figure 4.6 F). Worth noting that a considerable lower Zeta potential was determined for the BioCode-43bp-e14-Cy3, despite the similar number of hairpin per particle. This is could be due to the different charges of the donor dyes at pH 8.0, where the FAM molecule is negatively charged, whilst the Cy3 is positively charged.

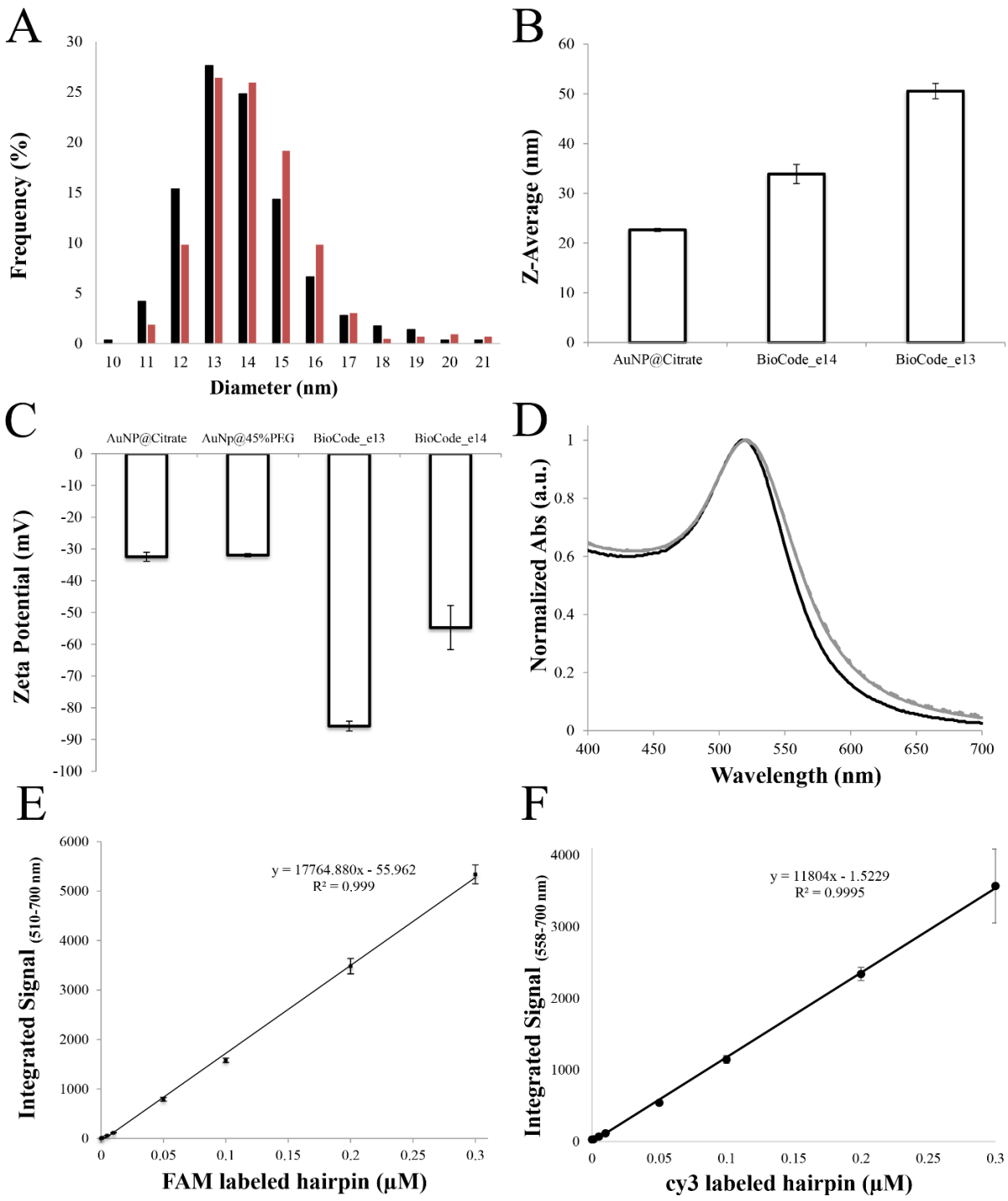

Figure 4.6. Characterization of the BioCode-43bp-e13-FAM and BioCode-43bp-e14-Cy3 and comparison with AuNP@citrate and AuNP@45% PEG. A) Size distribution of the BioCode-43bp-e13-FAM (Black bars; n=289) and BioCode-43bp-e14-Cy3 (Red Bars; n=428); B) Hydrodynamic diameter of the AuNP@citrate, BioCode-43bp-e13-FAM and BioCode-43bp-e14-Cy3; C) zeta potential of AuNP@citrate, AuNP@45%PEG and BioCodes; D) UV-Vis spectra of the AuNP@citrate (solid black line), BioCode-43bp-e13-FAM (solid gray line) and BioCode-43bp-e14-Cy3 (dashed gray line); E) calibration curve for the quantification of hairpins per AuNP for the BioCode-43bp-e13-FAM; F) calibration curve for the quantification of hairpins per AuNP for the BioCode-43bp-e14-Cy3. Error bars correspond to 3 independent assays.

A similar trend is found when the hairpin from pair 4 are functionalized onto the surface of the AuNP@45%PEG (BioCode-43bp-e14-FAM-2 – Figure 4.7). Here a broadening of the UV-Vis spectrum is observed (in comparison with the AuNP@citrate – Figure 4.2 C_1 and C_2. The hydrodynamic increases from 19.29 ± 0.9 nm (AuNP@citrate) to around 41.27 ± 0.4 nm and the ζ-potential decreases from -40.2 ± 2.51 mV to around -92.87 ± 1.94 mV. The number of oligonucleotides per particle for this nanoconstruct was determined to be 88.

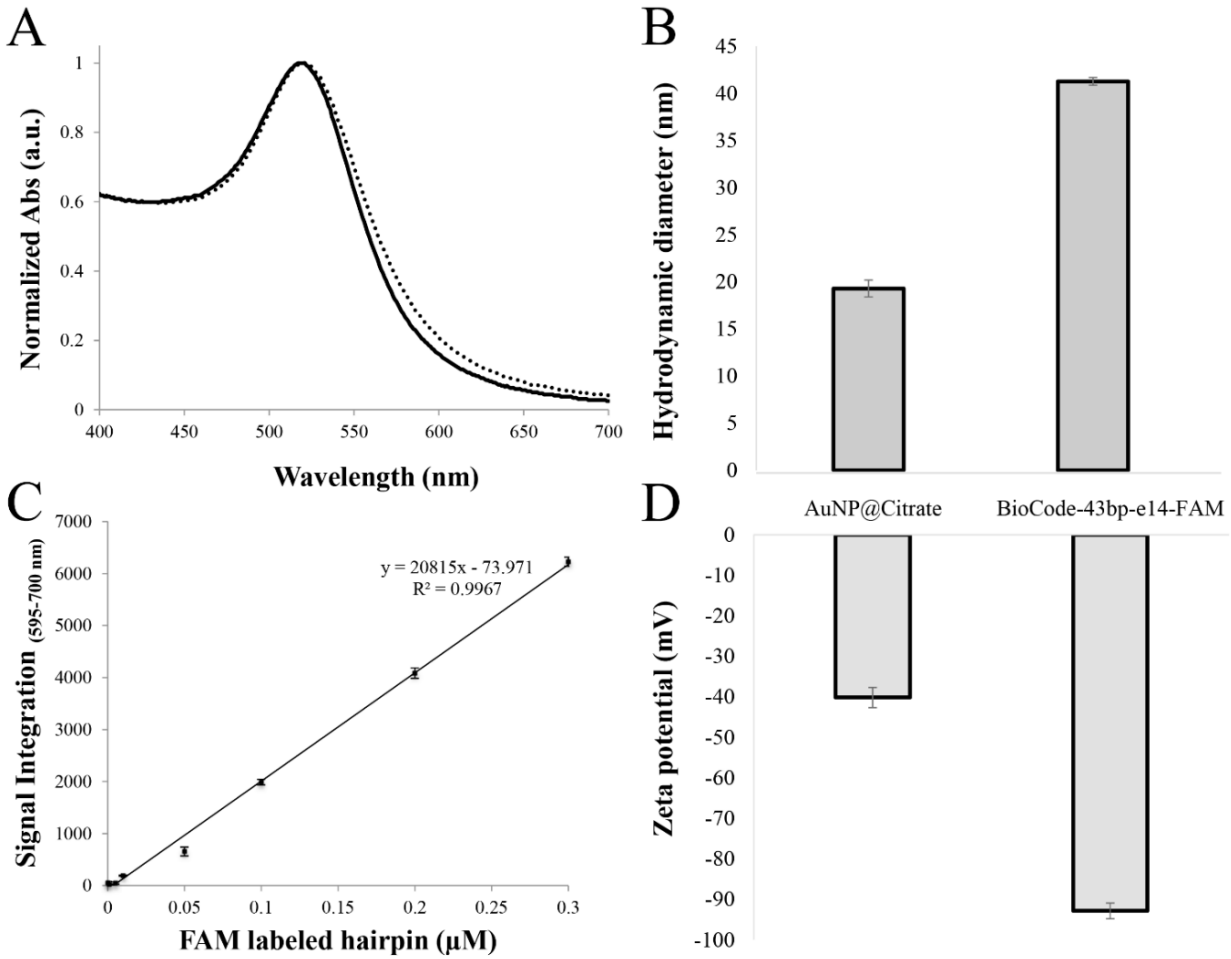

Figure 4.7. Characterization of the BioCode-43bp-e14-FAM. A) UV-Vis spectra of the AuNP (solid black line) and BioCode-43bp-e14-FAM (dotted gray line); B) Hydrodynamic diameter of AuNP@citrate and BioCode-43bp-e14-FAM; C) Zeta potential of AuNP@citrate and BioCode-43bp-e14-FAM; D) calibration curve used for the quantification of hairpins per AuNP for BioCode-43bp-e14-FAM.

For pair 6 and 7 (see Figure 4.8), the gold core size (from TEM micrographs) is 13.72 ± 1 .54 and 13.44 ± 1.64 (Figure 4.8 A) for the BioCode-47bp-e13-FAM and BioCode-47bp-e14-Cy3 (respectively). The UV-Vis spectra are broader after functionalization (Figure 4.8 B).

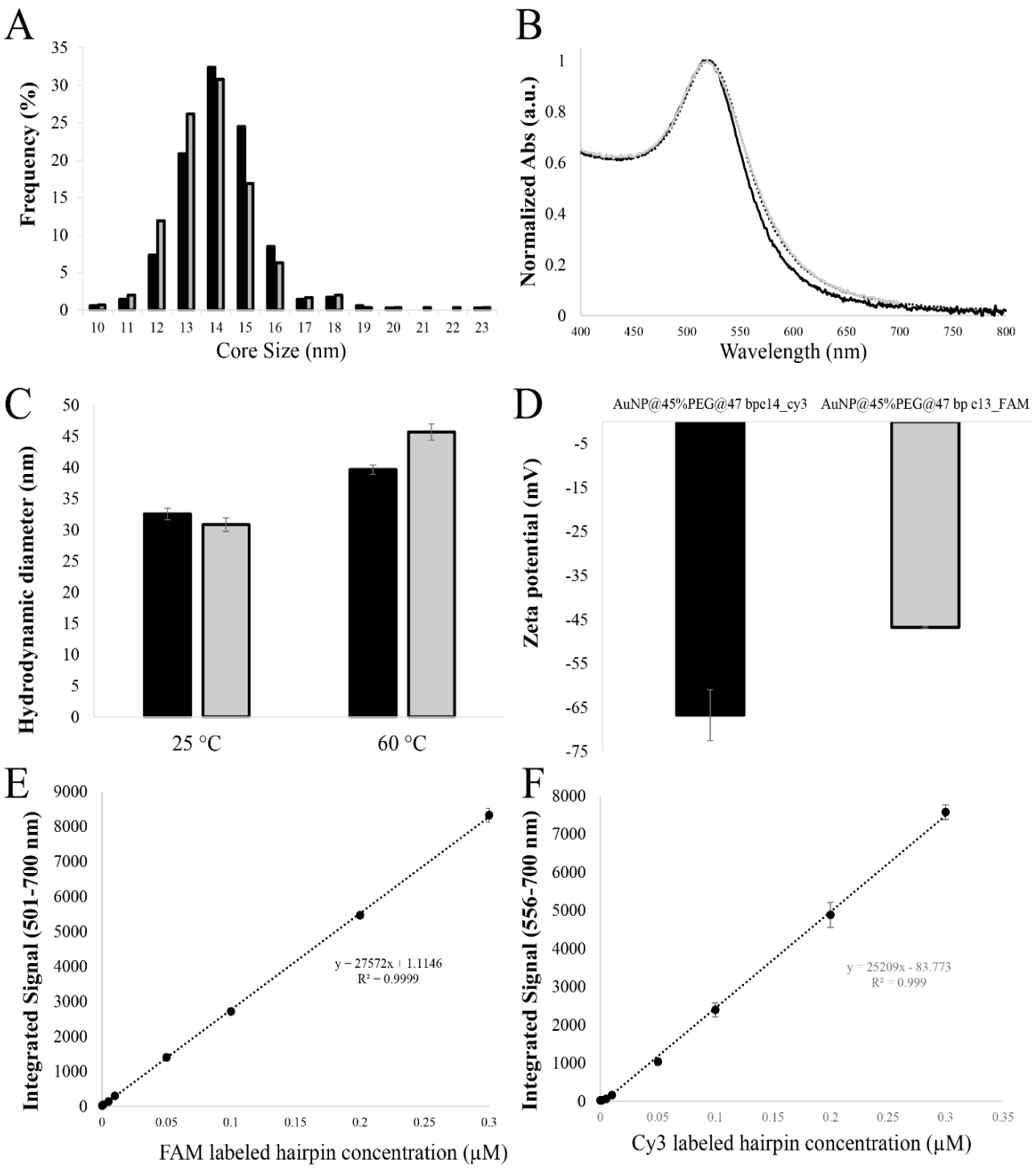

Figure 4.8. Characterization of the BioCode-47bp-e13-FAM and BioCode-47bp-e14-Cy3, formed using pair 6 and 7. A) Size distribution of the BioCode-47bp-e13-FAM (Black bars; n=355) and BioCode-47bp-e14-Cy3 (gray Bars; n=302); B) UV-Vis spectra of the AuNP@citrate (solid black line), BioCode-47bp-e13-FAM (dotted black line) and BioCode-43bp-e14-Cy3 (solid gray line) C) Hydrodynamic diameter of the BioCode-47bp-e13-FAM (black bar) and BioCode-47bp-e14-Cy3 (gray bar) at 25 °C and 60 °C; D) Zeta potential of BioCode-47bp-e13-FAM (gray bar) and BioCode-47bp-e14-Cy3 (black bar); E) Calibration curve for the quantification of hairpins per AuNP for the BioCode-47bp-e13-FAM; F) Calibration curve for the quantification of hairpins per AuNP for the BioCode-47bp-e14-Cy3; values presented as means ± standard deviation of at least three assays.

The hydrodynamic diameter, at 25 °C, of these constructs were determined to be 32.55 ± 0.91 and 30.83 ± 1.09 (respectively), while at 60 °C the hydrodynamic diameter of these constructs increases to 39.63 ± 0.75 and 45.67 ± 1.3, respectively (Figure 4.8 C). This is concordant with disruption of the hairpin structure functionalized at the surface of the AuNP. ζ-potential measured was of -46.77 ± 0.25 mV (BioCode-47bp-e13-FAM) and -66.74 ± 5.8 mV (BioCode-47bp-e14-Cy3), indicating stable constructs (Figure 4.8 D). The hairpins per AuNP was determined to be 30 (using the calibration curve presented on Figure 4.8 E for BioCode-47bp-e13-FAM) and 60 (using the calibration curve presented on Figure 4.8 E for BioCode-47bp-e14-Cy3.

For functionalization using Pair 8 (BioCode-47bp-e14-FAM), the gold core size was measured at 13.7 ± 1.9 nm, the UV-Vis spectra show a broadening upon hairpin functionalization and the number of hairpin per particle was determined to be 22, but not further characterization was performed – see Figure X.2 from Appendix X.

For the co-functionalization using pair 6 and 8 (BioCode-47bp-e13-e14-FAM), the characterization is presented on Figure 4.9. Here, the AuNP core size is of 13.23 ± 1.24 (Figure 4.9 A). The UV-Vis spectra follow the same broadening trend as previously described (Figure 4.9 B). As with previous situation, the hydrodynamic diameter increases upon hairpin functionalization (from 16.77 ± 0.65 nm of the AuNP@citrate to 25.60 ± 0.44 nm of the double-labeled BioCode) and further increases upon target hybridization (to 34.93 ± 1.3 nm) – Figure 4.9 D. The linear regression of the measured Z-average plotted against the temperature of the measurement shows a slope of 0.18 for the nanoconstruct (R^2= 0.96) and a slope 0.04 (4.5 times lower) for the AuNP@citrate (R^2=0.64), indicating a much higher temperature dependent variation due to the hairpin disruption and consequent increase of the solvation shell– Figure 4.9 C. The hydrodynamic diameter measured at 60 °C (33.12 ± 1.31 nm) is very close to one measured after the hybridization to the target sequences (34.93 ±1.3), supporting the hypothesis of hairpin disruption due to hybridization and the thermal instability of the hairpin structure at 60 °C. ζ-potential measurements show an increase of the surface charge upon hairpin grafting, inferred by the decrease in the ζ-potential (-39.20 ± 0.57 mV for the AuNP@citrate and -67.13 ± 15.77 mV after functionalization).

The characterization data presented supports the successful functionalization of the AuNP@45%PEG with the donor labeled hairpin. The detection capability of these nanoconstructs was tested in the next section.

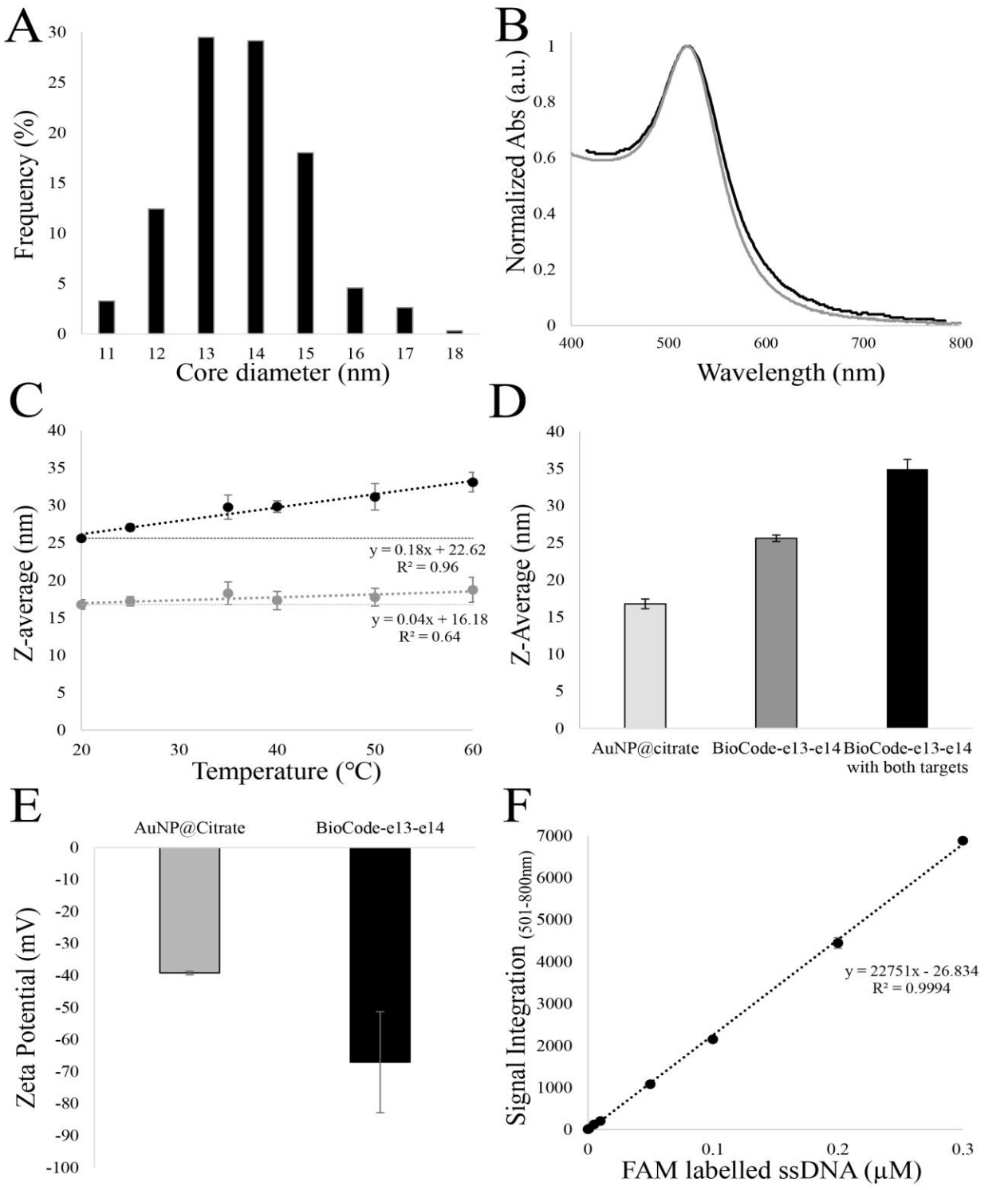

Figure 4.9. Characterization of the double-labeled BioCode, formed using pair 6 and 8. A) Size distribution of double-labeled BioCode. (n=305 counts); B) UV-Vis spectra of the AuNP@citrate (solid gray line) and double-labeled BioCode (solid black line); C) Hydrodynamic diameter as a function of the temperature of measurement of double-labeled BioCode (black dots) and AuNP@citrate (gray dots) with respective linear regressions; D) Hydrodynamic diameter of AuNP@citrate (light gray bar), Double labeled BioCode (dark gray bar) and Double labeled BioCode hybridized with both e13a2 and e14a2 targets; E) Zeta potential of AuNP@citrate (gray bar) and double-labeled BioCode (black bar); F) Calibration curve for the quantification of hairpins per AuNP for the double-labeled BioCode;

4.5 **BioCode SAXS/SANS characterization**

To study the interaction between the nanoparticle and DNA, SAXS data was collected for the AuNPs (with 14 nm diameter) functionalized with ~70 hairpins (for the variant e13a2) per particle, with the corresponding target and revelator sequences already hybridized - BioCode-43bp-e13 (construct without fluorescent labels). The scattering profile derived from a series of dilutions between 10, 5, 2.5 e 1.13 nM in buffer F were obtained at 277 K – Figure 4.10., applying the same steps described for the different biosensor components in solution – see section 3.6.

The R_g and D_{max} parameters obtained (8.0 nm and 28.9 nm, respectively) for this experiment are much larger than those expected for the particles which have a mean diameter of 14 nm determined by TEM – see Figure 4.2. The SAXS values correspond rather to particles an average diameter of 30 nm, which is in agreement with a successful functionalization.

Standard SAXS methods for *ab initio* determination (such as DAMMIF (222)) are not suitable for AuNPs functionalized with DNA data, since the particles and oligonucleotide molecules have significantly different scattering densities. The program MONSA(302) from the ATSAS software was used as an alternative, since it allows fitting simultaneously multiple curves. However, one assumption of this software is the monodispersity of the solution, which is doubtful due to the polydispersity of AuNPs/functionalized AuNPs samples. The predominant scattering derives from the metal core, which compromises the detection of the biological component. In this context, SANS – Small-Angle Neutron scattering arise as an alternative. SAXS and SANS are highly complementary methods, whereby the former technique is faster, requires less material and yields usually more precise data. SANS is sensitive to isotopic H/D exchange, which is experimentally used for contrast variation involving measurements in different H_2O/D_2O mixtures, providing unique information about complex particles. AuNPs functionalized with the 43bp_e13 in 100% and 70% of D_2O (Sigma-Aldrich) were prepared and measured at Heinz Maier-Leibnitz (FRM II) at Garching, Germany. The SANS data for the nanoconstruct in 100% D_2O, both AuNP and DNA are visible, and for the same sample in 70% D_2O, the AuNP is close to its matching point, so only the DNA contribution is detected. This information can be used to deconvolve the collected SAXS data. The results are promising but need further optimization.

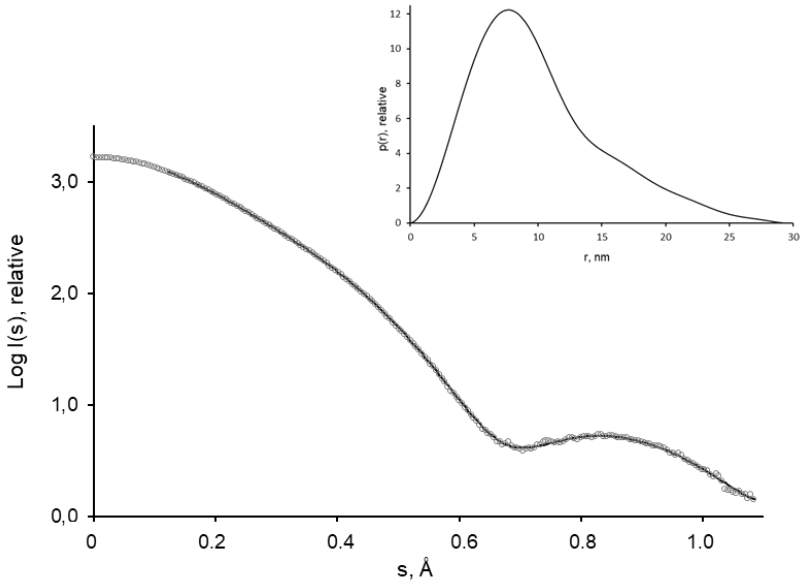

Figure 4.10. SAXS scattering data (points) and GNOM fit (line) for AuNP functionalized with the full biosensor ensemble for e13a2 (hairpin, target and revetator). The data was collected at ESRF (France), beamline BM29. Insert: distance distribution function, *p*(*r*).

4.6 **BioCode- target detection**

The characterized BioCodes Au-nanobeacon target recognition performance was firstly assessed for different experimental conditions: (1) absence of target (reaction blank); (2) non-complementary target (negative reaction); (3) oligonucleotides harboring either the e13a2 or the e14a2 fusion site, depending on the nanoconstruct (positive reaction); and (4) absence of target and acceptor (donor blank). In this approach, the donor emission can be influenced by two quenching processes, nanoparticle surface energy transfer (NSET (303)) or by FRET (in the case of a positive hybridization) to an acceptor fluorophore. As such, it is necessary to determine the effect of either process in the donor emission. The donor blank provides the highest possible fluorescence intensity of the donor due to minimization of NSET (in this situation the donor is the furthest away from the surface of the AuNP due to the disruption of the hairpin structure) and absence of FRET (acceptor labeled oligonucleotide is not present). The reaction blank and negative reaction indicates the basal fluorescence of the assay in absence of FRET. This of paramount relevance considering that the cross-excitation of the acceptors at the excitation wavelength of the donor needs to be accounted for to allow for a clear signal output (34).Upon direct excitation of the donor (495 nm for FAM or at 550 nm for Cy3), the donor/acceptor pair formed in solution is revealed through the increased fluorescence of the respective acceptor, TAMRA, ROX or Dy-520XL MegaStokes, with the emission band centered around 570, 605 and 650 nm, respectively. These spectra were compared to the control reactions to infer the

occurrence of hybridization of target sequence (by the partial recovery of the donor emission) and acceptor labeled revelator (by the enhancement of the acceptor emission).

Figure 4.11 A to D, shows a representative emission spectra collected over time of BioCode-43bp-e14-FAM-1 in the absence of target (Figure 4.11 A), before and after the addition of a fully complementary target – Donor Blank (Figure 4.11 B), TAMRA labeled revelator and non-complementary target – negative reaction (Figure 4.11 C) and TAMRA labeled revelator and fully complementary target – positive reaction (Figure 4.11 D). The overall spectra were divided into the donor and acceptor channels and each channel was integrated, normalized and plotted as a function of time (Figure 4.11 E to H). From Figure 4.11 A is possible to observe that in the absence of a complementary target, the emission of the BioCode-43bp-e14-FAM remains constant. This is obvious when observing the integrated and normalized signal over time presented on Figure 4.11 E. In Figure 4.11 B – donor blank – the collected emission spectra show that the addition of the complementary sequence induces an increase of the donor emission over time (denoted by the upward facing arrow) as previously described for the output signal of a positive detection using the Au-nanobeacon approach. The kinetic data show that the emission of the BioCode-43bp-e14-FAM increases 1.99 ± 0.07 folds upon full hybridization with the complementary target. The emission spectra of the negative reaction are constant over time, with no observable variation on the donor and acceptor channel. Upon addition of the complementary target e14a2 sequence (positive reaction), the donor enhancement is observed, however to a less extent than observed in the donor blank, with a fold increase of 1.48 ± 0.06.

This difference in enhancement could be due to the additional quenching of the donor by a FRET process. However, the lack of an observable enhancement in the acceptor channel does not provide a dual channel confirmation for the occurrence of FRET. As such, TAMRA revelator based BioCode was not considered for further characterization.

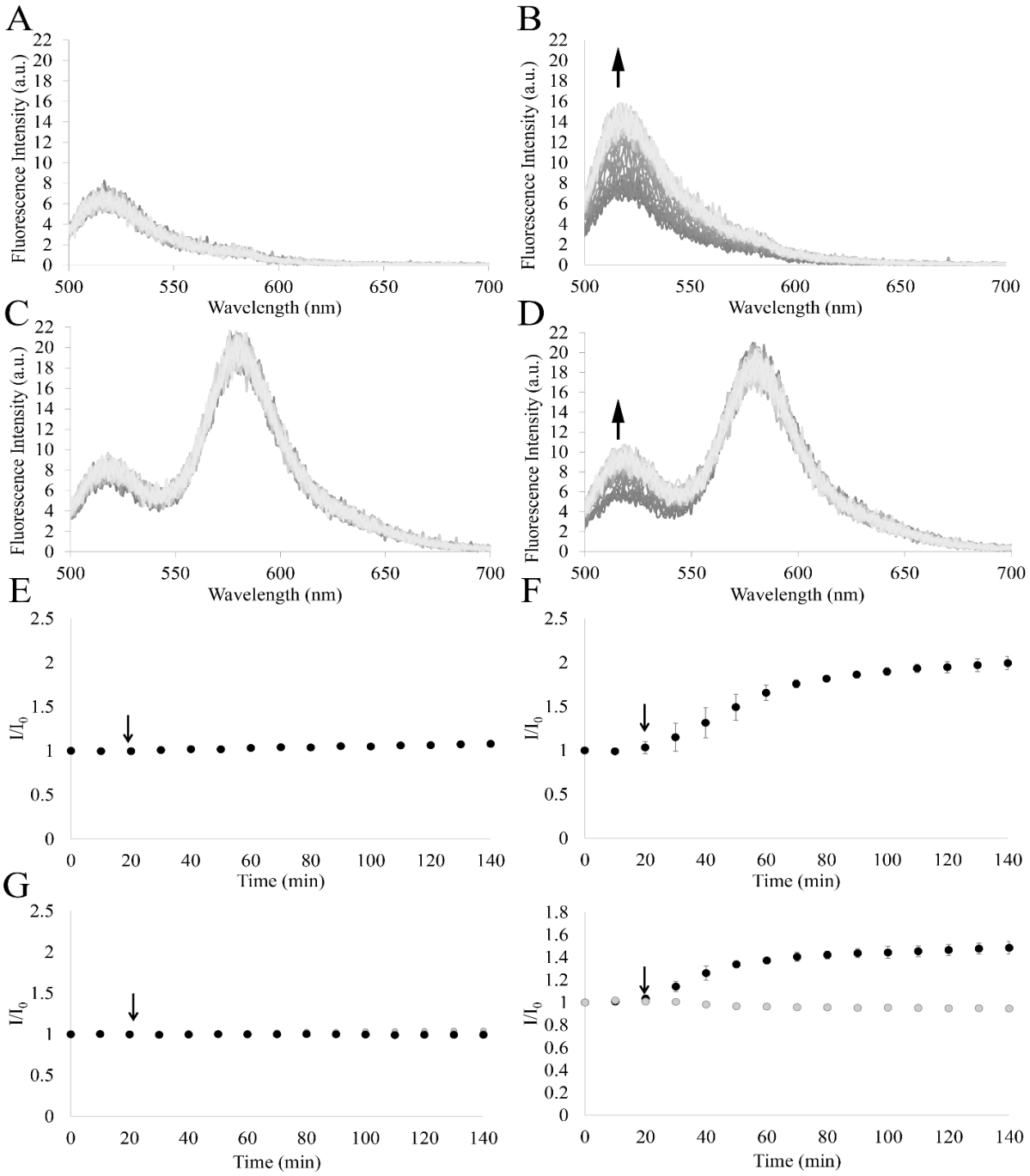

Figure 4.11. Hybridization assays of BioCode-43bp- e14-FAM in presence of different target sequences. A) BioCode-43bp-FAM donor emission in the absence of complementary target sequence; B**)** BioCode-43bp-e14-FAM donor emission in the presence of e14a2 complementary target sequence; C) BioCode-43bp- e14-FAM donor and acceptor emission in the presence of a non-complementary target sequence; D) BioCode-43bp- e14-FAM donor and acceptor emission in the presence of a e14a2 complementary target sequence; E) Integrated and normalized BioCode-43bp-FAM emission (black circles); F) Integrated and normalized BioCode-43bp-FAM emission in the presence of the e14a2 complementary target sequence; G) Integrated and normalized BioCode-43bp-FAM emission (black circles) and TAMRA labeled revelator (gray circles) in the presence of a non-complementary target sequence; H) Integrated and normalized BioCode-43bp-FAM emission (black circles) and TAMRA labeled revelator (gray circles) in the presence of the e14a2 complementary target sequence. Data presented as mean ± standard deviation of three independent assays.

Figure 4.12 A and B shows the emission spectra of the BioCode-43bp-e13-FAM (pairing with the ROX-labeled revelator sequence) and BioCode-43bp-e14-Cy3 (that pairs with the 10 bp oligonucleotide labeled with the Dy – 520 Xl MegaStockes acceptor) after incubation with different targets, respectively. The dashed black line represents the emission spectra of both BioCodes after the hybridization to the complementary targets – donor blank. Here, as in the previous case, the donor emission is at its maximum, considering the displacement the donor from the surface of the AuNP and the absence of the quenching from FRET. The gray spectra correspond to the control reactions (solid light gray line – reaction control; solid dark gray line – negative control) where the donor is quenched due to the proximity of the AuNP surface while the acceptor is unbound and directly excited at the donor excitation wavelength, since the hairpin is in close conformation blocking the hybridization of the acceptor labeled revelator. The background emission centered at 605 and 650 nm in Figure 4.12 A and B, respectively is due to the direct excitation of the acceptors at the donor maximum of absorption.

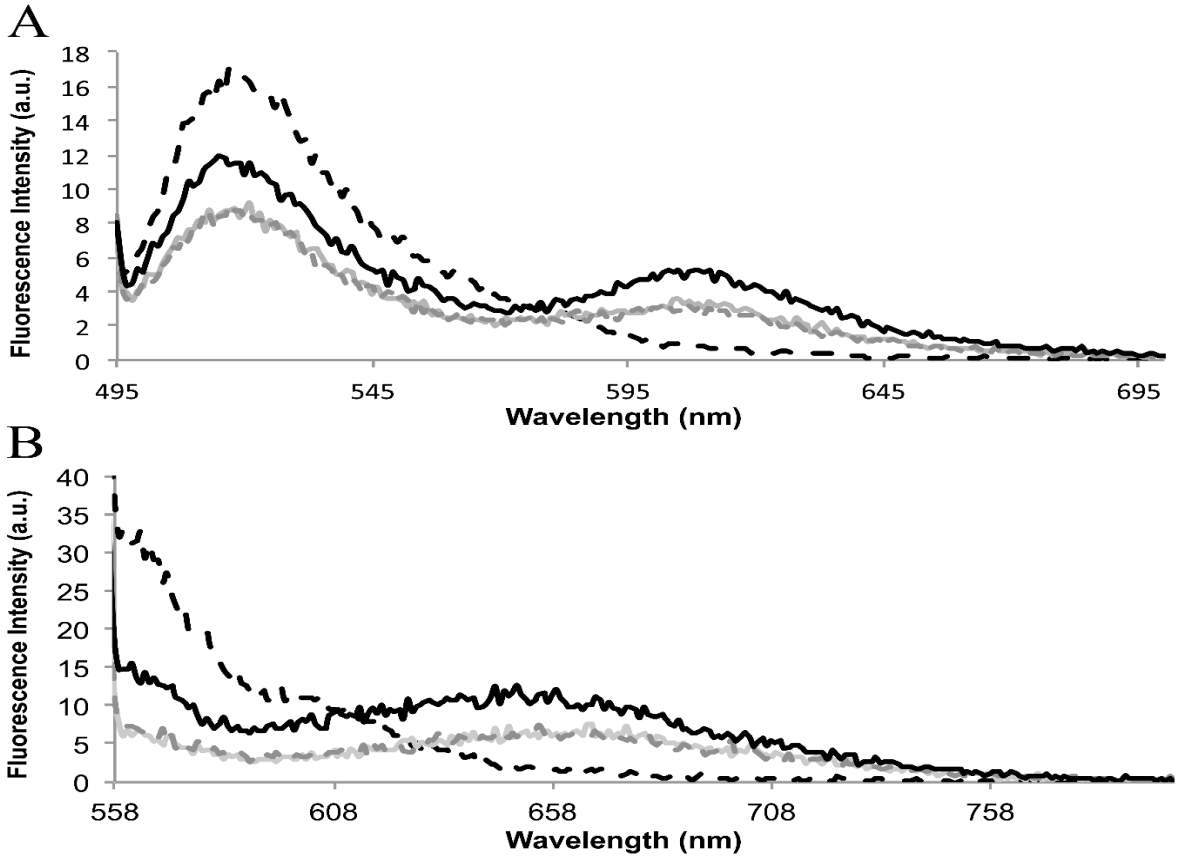

Figure 4.12. A) Emission spectra after hybridization in different reaction condition using BioCode-e13. B) Emission spectra after hybridization in different reaction condition using BioCode-e14; B) Emission spectra of donor blank reaction (dashed black line); positive reaction (solid black line); reaction blank (solid light gray line); negative reaction (dashed dark gray line).

When the complementary target is incubated with the BioCodes (positive reaction – dashed black line), an increase in both donor and acceptor emission bands is observed in comparison to the previously described situations. The donor emission in the positive reaction increases due to the increase in distance with respect to the AuNP surface but suffers a decrease due to the energy transfer to the acceptor and, therefore, does not reach values as high as for the donor blank. Since all fluorophore and AuNP concentrations are kept constant in the different situations, FRET shows a clear signature on the emission decrease at 520 and 560 and increase at 605 or 650 nm (Figure 4.12 A for Biocode-43bp -e13-FAM and Figure 4.12 B for Biocode-43bp-e14-cy3, with ROX and Dy – 520 Xl MegaStockes revelators, respectively), with respect to the direct excitation emission observed in the controls. Therefore, the partial recovery of fluorescence of the donor is coupled to the increase of the fluorescence of the acceptor, i.e., a dual channel specific hybridization spectral signature. This presents a crosscheck confirmation over the same hybridization event.

The dual channel spectral signature – BioCode – was used to follow the hybridization process over time. The channels were defined as follows: (1) donor channel is the integrated emission between 506 and 560 nm (for donor FAM – BioCode-e13) or the integrated emission between 559 and 600 nm (for donor Cy3 – BioCode-e14); (2) acceptor channel is the integrated emission from 600 to 700 nm (Acceptor-ROX) or 650–800 nm (Acceptor-Dy); the acceptors limits were set to minimize contribution from donor emission. All data were normalized to the fluorescence signal prior to the addition of target (I_0) for each situation.

For BioCode-43bp-e13-FAM, the evolution of the emission channels upon addition of BCR-ABL sequence (Figure 4.13 A, B), non-complementary target (Figure 4.13 C, D), BCR (Figure 4.13 E, F) and ABL (Figure 4.13 G, H) show that only the addition of the fully complementary target leads to the simultaneous increase in both channels. The addition of BCR sequence induces a slight a change in the signal of the donor channel but no significant variation in the acceptor channel, showing that the use of two channels increases detection selectivity. This increase in selectivity arises due to the more stringent condition imposed by the second hybridization processes. The same behavior is observed for 43bp_biocode-e14-Cy3 (see Figure XI.1 from Appendix XI), 43bp_biocode-e14-FAM (Figure XI.2 from Appendix XI), 47bp_biocode-e13-FAM (see Figure XI.3 from Appendix XI), 47bp_biocode-e14-FAM (see Figure X.IV from Appendix XI), 47bp_biocode-e14-FAM (see Figure XI.5 from Appendix XI.5), and the double-labeled BioCode for each fusion sequence BCR-ABL (e14a2 target sequence – see Figure XI.6; e13a2 target sequence – see Figure XI.7). Table 4.1 summarizes the fluorescence signal percentage for both channels for both BioCode after the addition of the before mentioned targets.

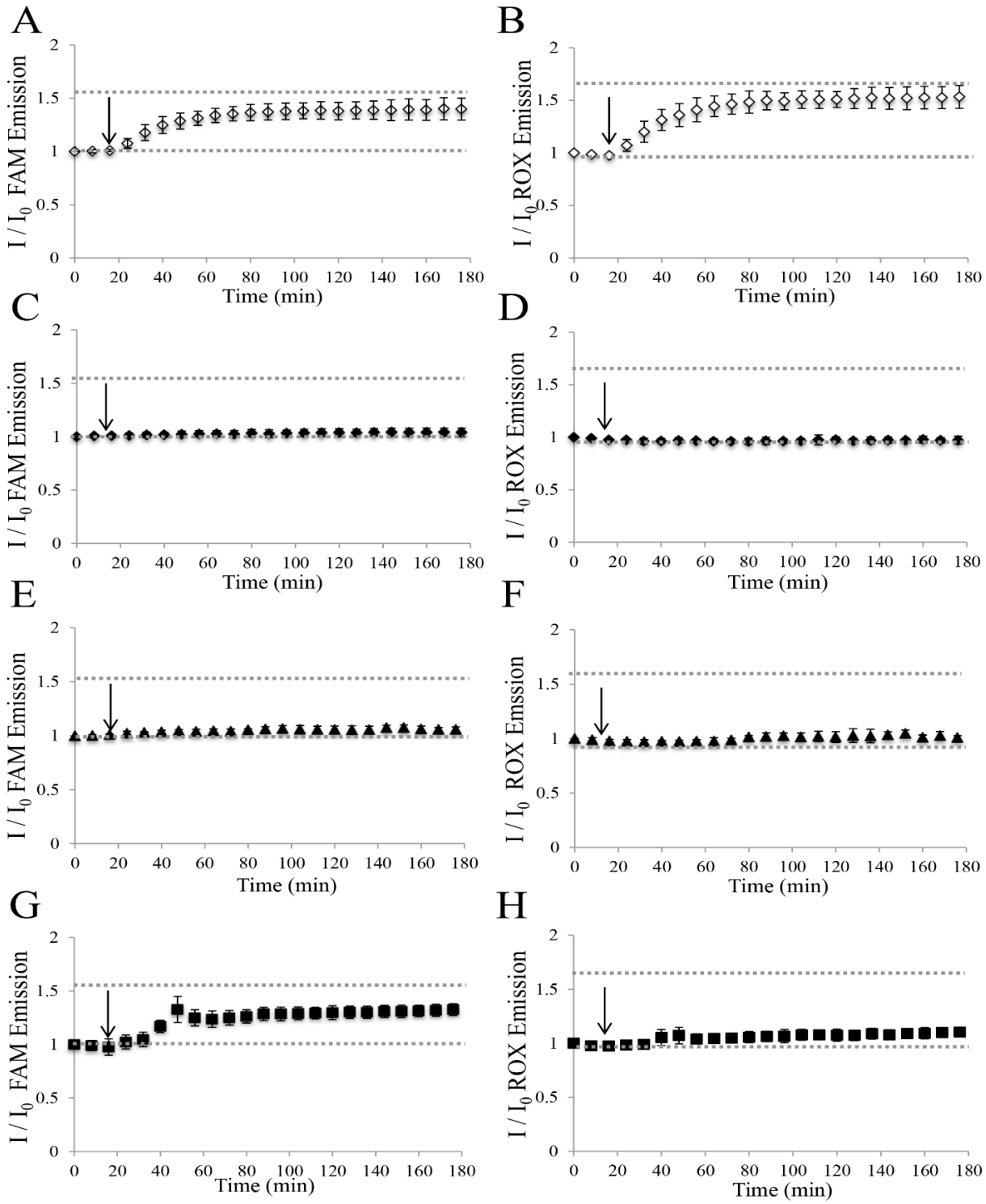

Figure 4.13. Hybridization assays of Biocode-43bp -e13-FAM in presence of different target sequences. A) Biocode-43bp -e13-FAM donor emission in the presence of e13a2 complementary target (white diamonds); B) acceptor-ROX emission in the presence of e13a2 complementary target; C) Biocode-43bp -e13-FAM donor emission in the presence of non-complementary target (black diamonds); D) acceptor-ROX emission in the presence of non-complementary target (black diamonds); E) Biocode-43bp -e13-FAM donor emission in the presence of e ABL derived target (black squares); F) acceptor-ROX emission in the presence of ABL derived target (black squares); G) Biocode-43bp -e13-FAM donor emission in the presence of exon 13 BCR derived target (black diamonds); H) acceptor-ROX emission in the presence of exon 13 BCR derived target (black diamonds). The black arrow represents the addition of the target sequence.

Table 4.1. Fold variation of donor and acceptor channels of the formulated BioCodes after target addition. Data presented as mean ± standard deviation of the I/I_0 of at least 3 experiments.

		Reaction Blank	ABL	BCR	NEG	POS
Donor-Channel Variation	**BioCode -43bp-e13-FAM**	1.01 ± 0.08	1.06±0.02	1.33±0.05	1.04±0.04	1.4±0.1
	BioCode -43bp-e14-Cy3	1.09 ± 0.09	1.18±0.1	1.79±0.03	1.02±0.07	2.35 ± 0.31
	BioCode -43bp-e14-FAM	1.17 ± 0.04	1.20±0.02	1.67±0.04	1.16±0.04	2.05±0.05
	BioCode -47bp-e13-FAM	1.02 ± 0.09	1.37±0.03	1.64±0.19	1.29±0.03	3.38±0.17
	BioCode -47bp-e14-Cy3	0.88 ± 0.3	1.09±0.29	1.09±0.45	0.69±0.33	2.71±0.1
	BioCode -47bp-e14-FAM	1.25 ± 0.03	-	-	-	2.55±0.17
Acceptor Channel Fold Variation	**BioCode -43bp-e13-FAM**	0.92±0.04	1.01±0.02	1.1±0.04	0.97±0.04	1.53±0.1
	BioCode -43bp-e14-Cy3	0.97±0.04	0.99±0.02	1.00±0.11	0.95±0.02	1.51 ±0.13
	BioCode -43bp-e14-FAM	1.11±0.02	1.06±0.03	1.24±0.03	1.03±0.06	1.47±0.09
	BioCode -47bp-e13-FAM	0.97±0.05	1.07±0.02	1.04±0.14	1.05±0.01	1.95±0.05
	BioCode -47bp-e14-Cy3	1.00±0.12	0.99±0.04	1.03±0.01	0.95±0.09	1.33±0.02
	BioCode -47bp-e14-FAM	1.05±0.01	-	-	-	1.31 ± 0.04

The endpoint signal variation of the donor signal shows a clear difference between the positive reaction (presence of a fully complementary target), negative reaction (presence of a non-complementary target) and the ABL reaction (partially complementary target). The presence of the BCR sequence (derived from either the e13a2 or e14a2 fusion sequence) generates a consistent increase in the donor signal in all BioCodes, probably generated from the hybridization of these target to the BioCodes (to a lesser degree than the fully complementary target). However, a much clearer difference can be observed in the acceptor channel in all the presented BioCodes. This illustrates the importance of this second channel (acceptors emission) for the confirmation over the same hybridization event. This second channel profits from added stringency of the

second hybridization event as well as the wavelength shift mediated by FRET, where the donor's excitation energy is transferred to an acceptor whose emission has a lower degree of overlap with the AuNPs' LSPR.

For the BioCode-43bp-e13-FAM the donor channel emission recovery is comparable with the positive reaction (BCR-e13 - 1.33 ± 0.05 vs. positive -1.4 ± 0.1, respectively). However, the acceptor channel allows for the differentiation between the presence of the partial complementary target form the presence of the BCR-e13 partial complementary target (positive—1.53 ± 0.1-fold vs BCR-e13 - 1.11 ± 0.04, respectively).

For BioCode-43bp-e14-Cy3, the presence of the BCR sequence induces an increase of 1.79 ± 0.03 fold on the donor channel (also in the presence of the ABL sequence —1.18 ± 0.1), whereas the positive reaction induces a 2.35 ± 0.31 fold increase, allowing clear differentiation of both situations. Again, the signal fold change on acceptor channel is residual for the ABL and BCR situations (0.99 ± 0.02 and 1.003 ± 0.11, respectively), while the positive reaction shows a clearly higher signal fold variation (1.51 ± 0.13). The same interpretation can be made for the remaining BioCodes.

Considering that a positive identification involves the increase of both emission channels, the possibility of the donor emission enhancement cross-contaminate the acceptor emission was confirmed. To do so, the donor band of the positive reactions and control reaction blank was mathematically removed from the emission spectra, confirming that the enhancement observed in the acceptor channel is not due to the donor partial recovery of emission, but due to the occurrence of energy transfer - Figure XI.8 of Appendix XI.

4.7 **Acceptor titration against double labeled Biocode**

Considering the results obtained in the previous section, AuNP were co-functionalized with the hairpins with a longer stem portion - sequences from the pair 6 and 8 (see Table 2.2 for sequences, Figure V.I and V.III for specificity assessment, respectively). The longer palindromic sequences were chosen due to the higher hairpin/revelator hybridization stability and that these pairs can generate an unequivocal FRET signal, as demonstrated in section 4.4. Hairpins with the Cy3 donor (such as pairs 5 and 7 – Table 2.2 for sequences, Figures 3.10 and V.II for specificity assessment, respectively) were not considered due to the non-negligible overlap with the ROX acceptor (used to label the revelators of the e13 hairpins). This overlap results in an intense cross-excitation of acceptor ROX at the Cy3 donor wavelength.

The working principle of the double labeled BioCode is similar to the single labeled one, and is illustrated in Figure 4.14

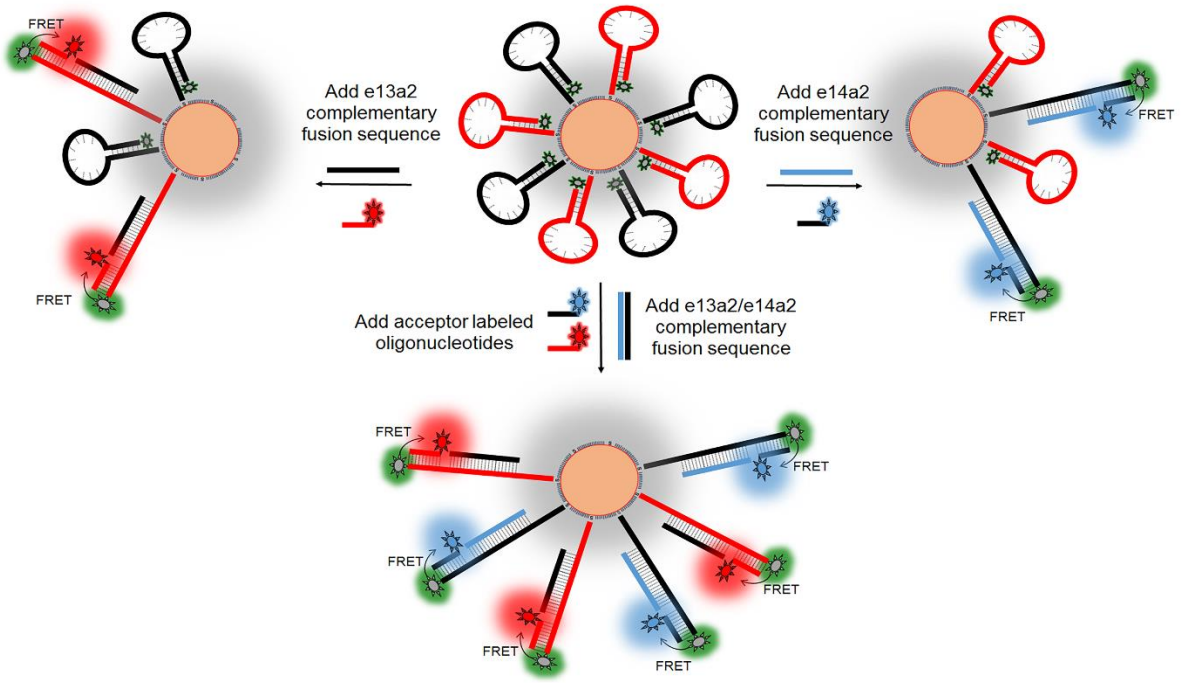

Figure 4.14. Schematic representation of the working principle of the double labeled BioCode. Central panel: In the absence of target, the double labeled BioCode is in its close conformation, leading to the quenching of the donor flurophores. Left panel: In the presence of the e13a2 fusion sequence, hairpin anti-e13a2 opens and are available to hybridize to the ROX labeled revelator. Right panel: In the presence of the e14a2 fusion sequence, hairpin anti-e14a2 opens and are available to hybridize to the Dy labeled revelator. Bottom panel: In the presence of both target sequences, both hairpin are in the open conformation and able to hybridize to both revelators.

To determine what concentration of the revelator should be used with the double-labeled BioCode, the nanoconstruct was incubated with either an excess of the fully complementary target or with an excess of non-complementary target. The double labeled BioCode was then titrated with the two revelators. To evaluate the enhancement of the acceptor channel the donor band was subtracted from the emission spectra – Figure 4.15 for the e14a2 sequence. See Figures XI.9 for the double-labeled BioCode hybridized with the e13a2 fusion sequence titrated with the ROX-labeled revelator. Upon reaching the hybridization end-point, the emission spectra were collected, the donor emission band was removed - Figures 4.15 A through 4.15 D for a final Dy-revelator of 0.001 µM, 0.01 µM, 0.05µM and 0.1 µM, respectively. Except for Figure 4.15 A, where no acceptor emission band is observed, the presence of the complementary target induces an enhancement of the acceptor channel. The negative reaction allows to determine the basal fluorescence of the reaction and serves as the baseline to determine the occurrence of FRET. From the data presented on Figure 4.15, the situations for the final concentration of 0.001 µM and 0.01 µM of the dy-labeled revelator were not considered due to their low fluorescence. The final concentration of 0.05 µM was chosen considering a lower signal variation than the 0.1 µM. The same final concentration was chosen for the ROX-labeled acceptor.

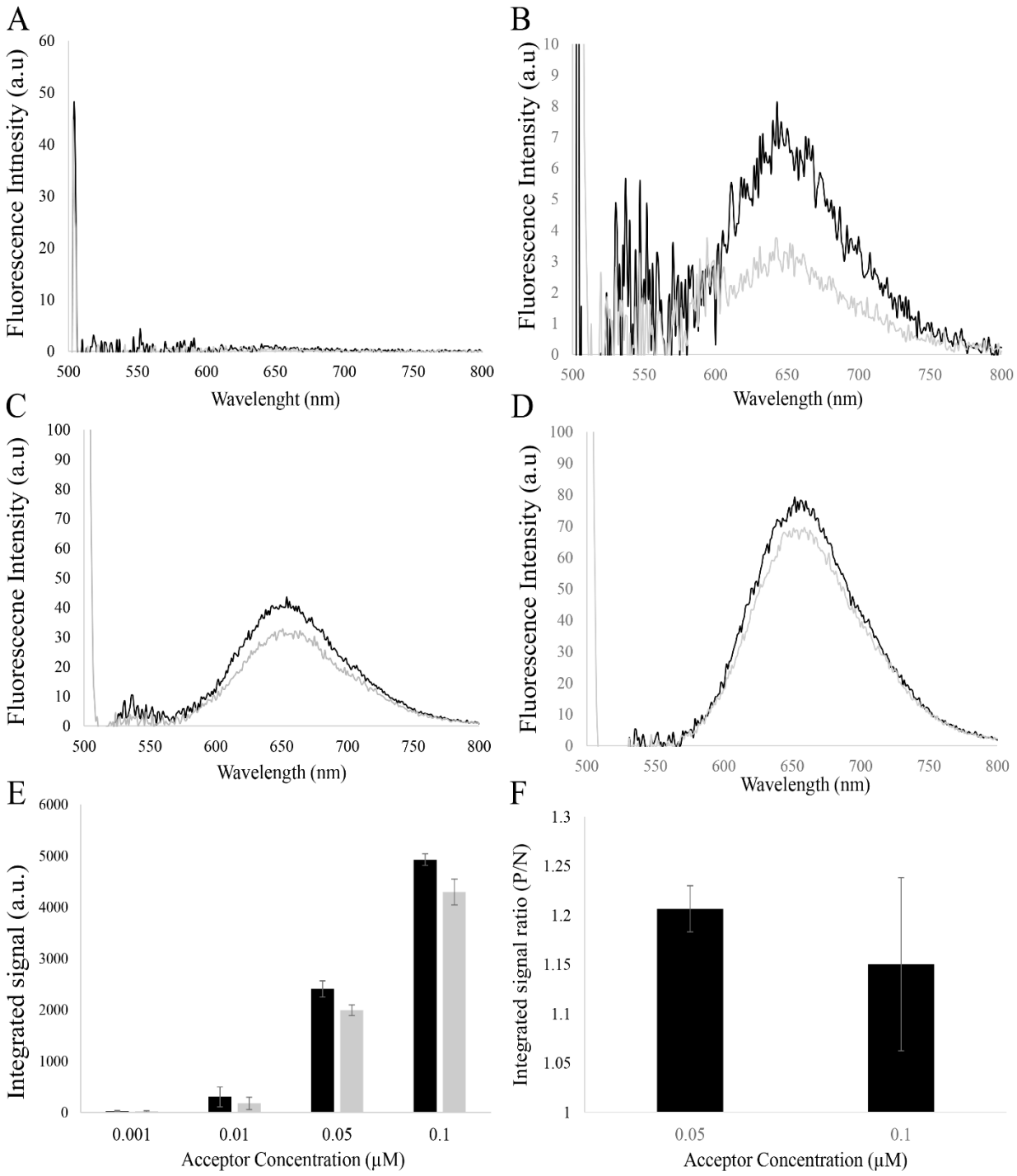

Figure 4.15. Emission spectra of double-labeled BioCode incubated with an excess of fully complementary target or non-complementary target titrated with Dy labeled revelator. A) revelator emission band at 0.001 µM in the presence of fully complementary target (black line) and non-complementary target (gray line); B) revelator emission band at 0.01 µM in the presence of fully complementary target (black line) and non-complementary target (gray line); C) revelator emission band at 0.05 µM in the presence of fully complementary target (black line) and non-complementary target (gray line); D) revelator emission band at 0.1 µM in the presence of fully complementary target (black line) and non-complementary target (gray line); The donor emission band was removed mathematically. E) Signal integration of emission band using the tested revelator concentration; F) Ratio of the integrated signal (Positive/negative reaction)

4.8 **Target detection using double labeled BioCode**

To ensure that this construct can detect both e14a2 and e13a2 sequence, the double-labeled BioCode was incubated with either the sequence and the respective controls. The spectra collected after hybridization spectra is presented on Figure 4.16 A and B for the presence of the presence of the sequence e13a2 and e14a2, respectively.

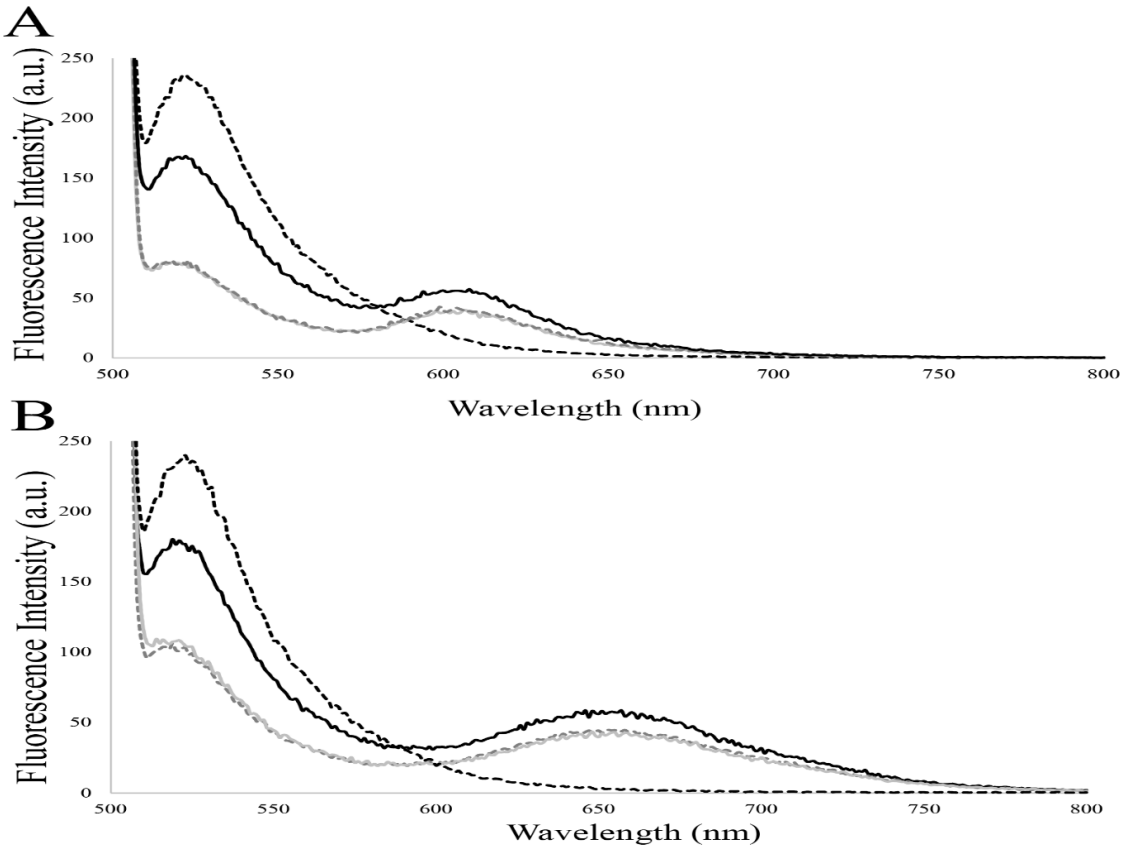

Figure 4.16. Emission spectra after hybridization in different reaction condition using double labeled BioCode in the presence of the e13a2 (A) and e14a2 (B) fusion sequence. Emission spectra of donor blank reaction (dashed black line); positive reaction (solid black line); reaction blank (solid light gray line); negative reaction (dashed dark gray line).

The profile of the different emission spectra observed in Figure 4.16 has the same profile as the one obtained for the BioCode functionalized with one hairpin sequence (Figure 4.12 of section 4.4). This is an indication that the double-labeled BioCode has the ability to detect both target sequences and act as a single labeled BioCode when in the presence of only one complementary target. Emission spectra were also collected before the addition of the different targets and, upon target addition, the emission spectra of these reactions were collected over time. See Figure 4.17. for the kinetic profile of the hybridization of the double-labeled

BioCode in the presence of the e13a2 sequence and respective controls. The e13a2 fusion sequence (A, B), non-complementary target (C, D), BCR (E, F) and ABL (E, H) show that only the presence of a fully complementary target can trigger a simultaneous increase in both the donor and acceptor channels. In this configuration, the ABL portion leads to a slight increase in donor channel, while the acceptor remains practically constant. The same profile is observed for the double-labeled BioCode in the presence of the e14a2 fusion sequence. Table 4.2, for the presence of the e13a2 target sequence, it is possible to see that at the positive reaction the donor and the acceptor channel suffered a 2.15 ± 0.08 and 1.62 ± 0.12-fold variation, respectively, and distinct from the negative (donor channel: 1.04±0.002; acceptor channel: 0.98±0.03), ABL (donor channel: 1.20±0.02; acceptor channel: 1.005 ± 0.01), BCR (donor channel: 1.006±0.011; acceptor channel: 0.92 ± 0.03). The same interpretation can be made for the double-labeled BioCode in respect to the presence of the e14a2, where a fold increase of 1.62 ± 0.12 and 1.20 ± 0.01 can be observed in the donor and acceptor channel, respectively. Here, the controls presented a residual fold variation such as negative (donor channel: 1.01±0.01; acceptor channel: 0.97±0.03), ABL (donor channel: 1.24±0.01; acceptor channel: 1.005 ± 0.01), BCR (donor channel: 1.01±0.006; acceptor channel: 0.948 ± 0.001). Figure 4.18 represents the dose-response curve of the double-labeled BioCode in the presence of each respective acceptor towards the target sequence that was present in solution.

This data suggests that the Bio Code can detect both sequences and discriminate the fully complementary target from the partial complementary targets, BCR and ABL.

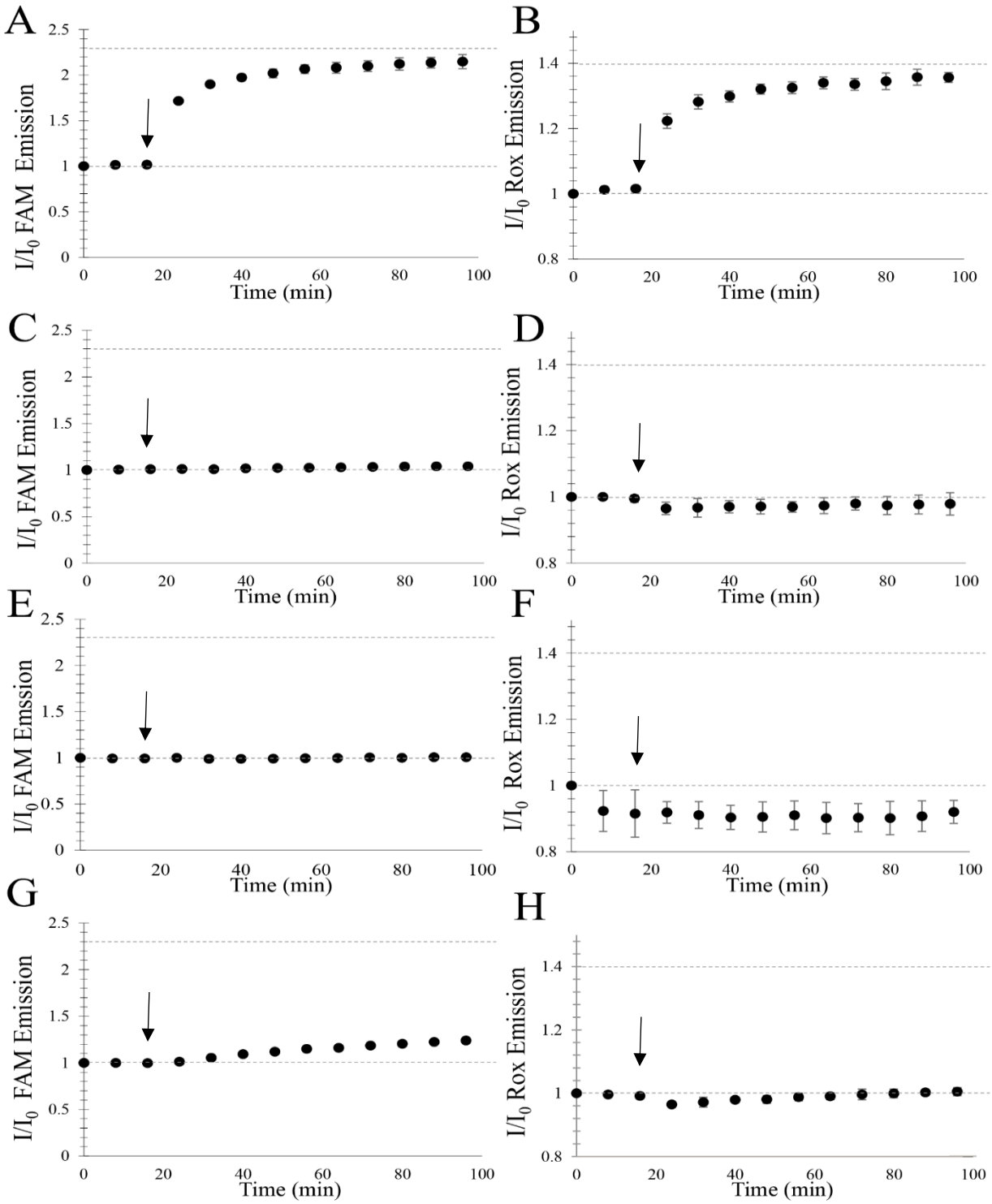

Figure 4.17. Hybridization assays of double-labeled BioCode in presence of different target sequences. A) double-labeled BioCode donor emission in the presence of e13a2 complementary target; B) acceptor-ROX emission in the presence of e13a2 complementary target; C) double-labeled BioCode donor emission in the presence of non-complementary target; D) acceptor-ROX emission in the presence of non-complementary target; E) double-labeled BioCode donor emission in the presence of exon 13 BCR derived target; F) acceptor-ROX emission in the presence of exon 13 BCR derived target; G) double-labeled BioCode donor emission in the presence of ABL target; H) acceptor-ROX emission in the presence of ABL target. The black arrow represents the addition of the target sequence.

Table 4.2. Fold variation of donor and acceptor channels of double-labeled Biocode after target addition. Data presented as mean ± standard deviation of the I/I_0 of at least 3 experiments.

	Donor				
	Reaction Blank	ABL	BCR	NEG	POS
Double labeled BioCode (e13a2)	1.03±0.01	1.20±0.02	1.006±0.011	1.04±0.002	2.15±0.08
Double labeled BioCode (e14a2)	1.01±0.02	1.24±0.01	1.01±0.006	1.01±0.01	1.62±0.12
	Acceptor				
Double labeled BioCode (e13a2)	0.92±0.02	1.005±0.01	0.92±0.03	0.98±0.03	1.36±0.02
Double labeled BioCode (e14a2)	0.95±0.05	0.97±0.01	0.948 ± 0.001 -	0.97±0.03	1.20±0.01

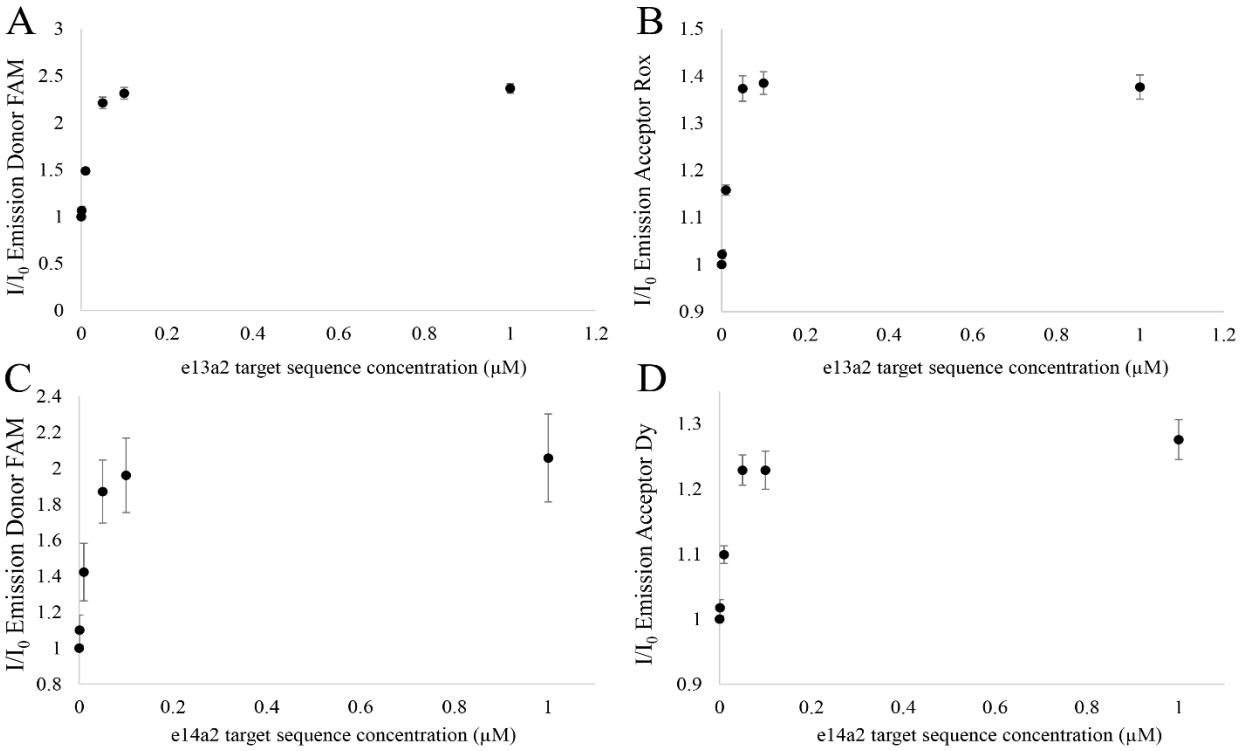

Figure 4.18. Dose response curve of double-labeled BioCode in the presence of either the e13a2 or e14a2 fusion sequence in the presence of each respective revelator. A) double-labeled BioCode donor emission in the presence of e13a2 complementary target; B) double-labeled BioCode acceptor ROX emission in the presence of e13a2 complementary target; C) double-labeled BioCode donor emission in the presence of e14a2 complementary target; D) double-labeled BioCode acceptor Dy emission in the presence of e13a2 complementary target. Data presented as mean I/I_0 ± standard deviation.

4.9 Target detection using double labeled BioCode and two acceptors

The performance of the double-labeled BioCode for the simultaneous detection of the target sequences e13a2 and e14a2 was evaluated in several conditions: 1) in the absence of revelators: 1.1) in the absence of a complementary target – to determine the basal emission of the double-labeled BioCode in the closed conformation (Figure 4.19 – solid black line); 1.2) in the presence of either the e13a2 sequence (Figure 4.19 – dashed gray line) or e14a2 target sequence (Figure 4.19 – solid gray line); 1.3) with both the e13a2 and e14a2 target sequence (Figure 4.19 – dashed black line); 2) in the presence of both acceptors: 2.1) in the presence of a non-complementary target, to be used the emission baseline; 2.2) in the presence of one of the targets (Figure 4.19 – dashed gray line for e13a2 target sequence and solid gray line for the e14a2 target sequence); 2.3) in the presence of both targets (Figure 4.19 –dashed black line for e13a2 target sequence and e14a2 target sequence).

From Figure 4.19 A, it is possible to see that the lower donor emission is found in the absence of target, due to the closed conformation of both hairpin population in the Au-BioCode (solid black line). In the presence of one complementary fusion sequence (either e13a2 – solid gray line, or e14a2- dashed gray line), an emission increase for the donor is observed (disruption of one population of hairpin) and is similar to both sequences. The highest emission is observed when both target sequences are present in solution (disruption of both hairpin populations), indicating that the double-labeled BioCodes generates different signals in the case of the detection one or both complementary targets are in solution (in terms of donor emission recovery). The coupling of the wavelength shift approach via the addition of the revelators allows the identification of which target hybridized to the double-labeled BioCode – as seen in Figure 4.19 B. Here, when the BioCode is incubated with one target (either e13a2 or e14a2) or both targets, an increase of the respective revelator can be observed. For example, in the presence of the e13a2 fusion sequence (dashed gray line), an enhancement can be seen in the donor channel and the acceptor emission centered at 605 nm. The same is observed in the presence of the e14a2 target sequence (solid gray line), where acceptor emission is centered at 650 nm. For the presence of both targets, an enhancement of all fluorophores can be observed. All situations generate a different spectral signature, indicating that this construct can perform the simultaneous detection of both target sequences.

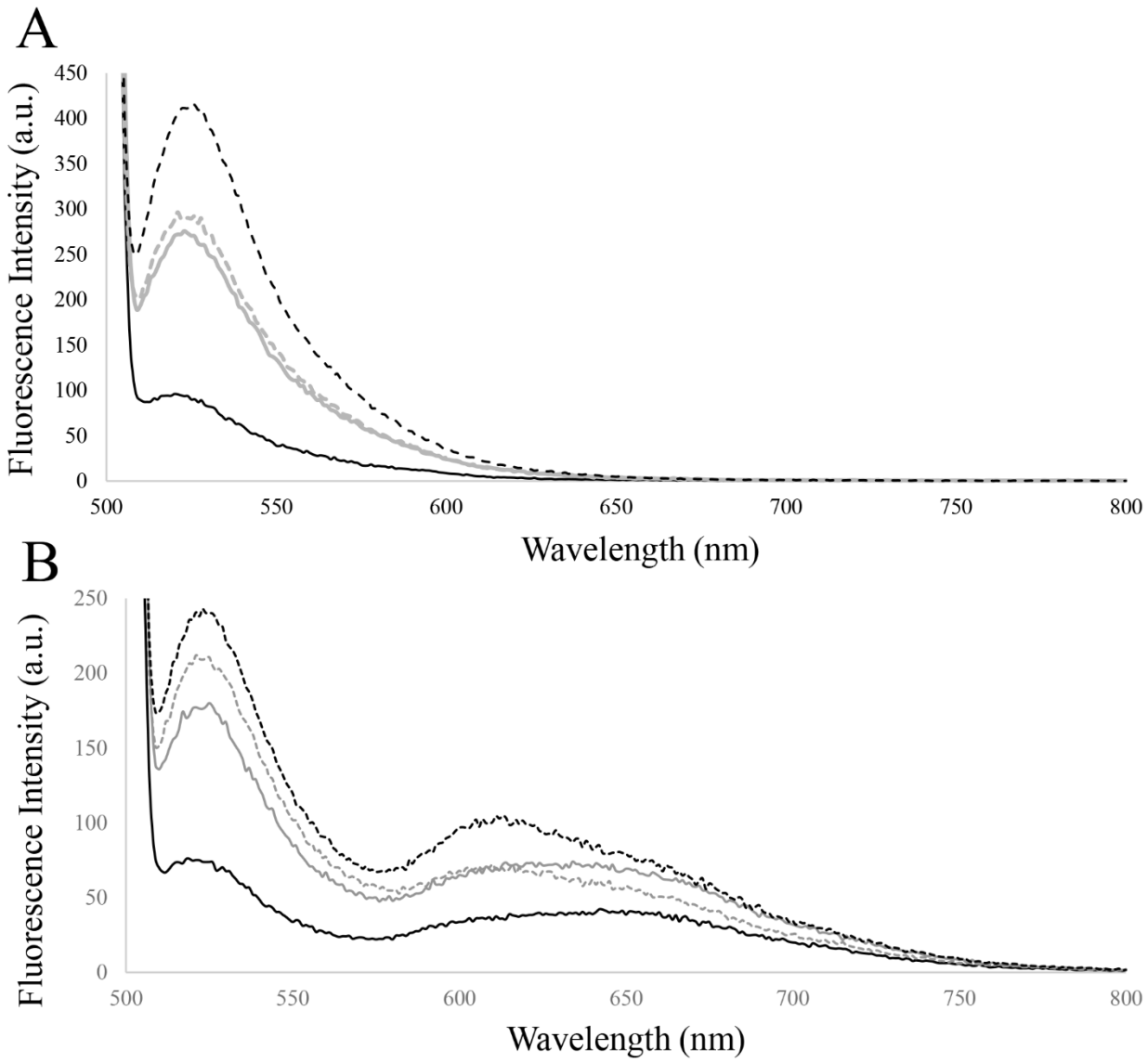

Figure 4.19. Emission spectra after hybridization in different reaction condition using the double-labeled oligonucleotide. A) Emission spectra of double-labeled Au-nanobeacon incubated with different target sequences. B) Emission spectra of BioCode incubated with different target sequences. Presence of non-complementary target (solid black line); Presence of e13a2 fusion sequence (dashed gray line); Presence of e14a2 fusion sequence (solid gray line); presence of both e13a2 and e14a2 target sequence (dashed black line)

To perform the acceptor enhancement quantification, the same approach as presented on section 3.4.3 was performed, however, in this situation, the donor band was firstly mathematically removed – Figure 4.20 A. Briefly, the isolated emission spectra of the Dy and ROX acceptors were used to fit the emission spectra of the experimental spectra, with the donor emission band removed – Figure 4.20 B.

A

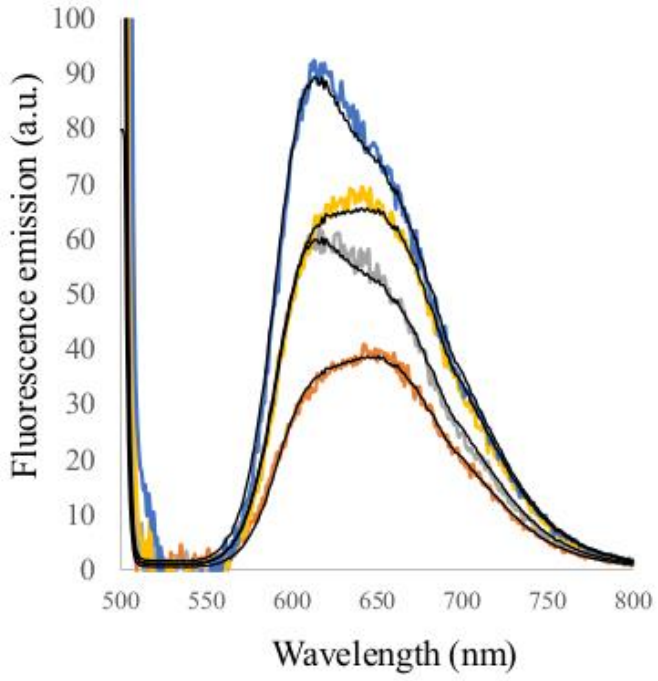

B

Target / Coefficient	Non complementary	e13a2	e14a2	e13a2+e14a2
Dy	1	1.20	1.65	1.65
ROX	1	2.13	1.9	3.29

Figure 4.20. A) Acceptor emission after the incubation of the different targets with the double-labeled BioCode fitted with the isolated emission bands of the acceptors. B) Coefficient table of the fitted spectra. The values were normalized to the negative reaction. The blue line represents the emission band of both acceptors after incubation with the e13a2 and e14a2 fusion sequences; The yellow line represents the emission band of both acceptor after incubation of the e14a2 fusion sequence. The gray line represents the emission band of both acceptor after incubation of the e13a2 fusion sequence; The orange line represents the emission band of both acceptor after incubation of a non-complementary target. The donor band was mathematically removed before the acceptors band fitting. Black line represents the fitted spectra that generated the coefficients presented on B.

From Figure 4.20, it is possible to observe that the presence of either the fusion sequence e13a2 or e14a2 leads to an increase of the respective acceptors (ROX for e13a2 and Dy for e14a2), but also for the other revelator (i.e the e13a2 fusion sequence increases the Dy acceptor emission and the e14a2 fusion sequence increases the ROX emission). From Figure 4.20 B, this effect is more pronounced with the target e14a2, where the coefficient of both ROX and Dy (1.65 and 1.9, respectively) in comparison with the ones obtained for the presence of the e13a2 (1.2 and 2.13) are well above the base set values of the negative reaction. However, this signal is unstable as seen by the error bars in Figure 4.21 A. In Figure 4.21 A, the spectra were fitted using the three fluorophores (FAM, ROX and Dy), and in Figure 4.21 B, the donor band was removed prior to fitting. The presence of the e13a2 induces a more pronounced increase in the ROX coefficient, while inducing a small variation on the Dy coefficient. However, the presence of the e14a2

fusion sequence induces an increase in both coefficients that is not distinguishable considering the experimental signal variation, suggesting an unspecific interaction between the e14a2 target and the e13-hairpin. The increase in these coefficients was also observed for the presence of both target sequences, to a higher degree the previous case, as the presence of both complementary targets induces a higher degree of hybridization between the interacting strands.

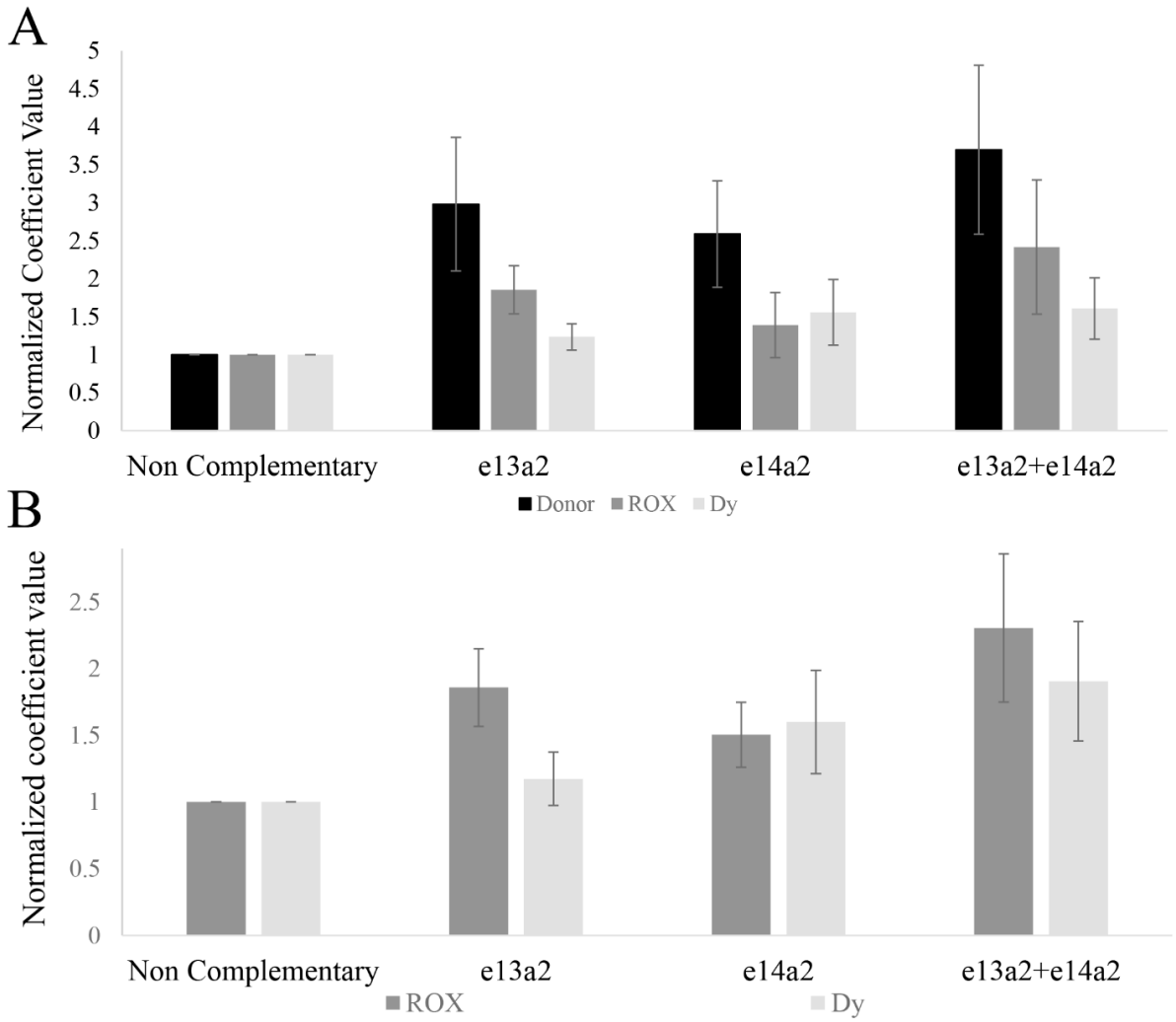

Figure 4.21. Coefficient values obtained through the fitting of the isolated spectrum of each fluorophore to the experimental spectra obtained after the incubation with different targets. A) Donor and acceptors coefficients; B) Acceptor coefficients after the removal of the donor emission band.

4.10 **BioCode RNA detection**

The detection of the fusion sequences in total RNA was attempted using the BioCode -47bp-e13-FAM, BioCode-47bp-e14-Cy3 and double-labeled BioCode. The human cell lines K562 (BCR-ABL e14a2

positive), BV173 (BCR-ABL e13a2 positive (304)) and THP1 (BCR-ABL negative for the BCR-ABL fusion sequence (305)) were used as sources of total RNA. To confirm the presence of the said sequences, the extracted RNA from the three cell lines was converted to cDNA and this cDNA was used as template for a nested PCR. The gel electrophoresis reveals a band with almost 400 bp from the line K562 and one with around 300 bp from the cell line BV173, which are compatible with the transcript lengths of e14a2 (360 bp) and e13a2 (280 bp) No band was observed from the amplification using the cDNA derived from the THP1 cell line – Figure XII.1, Appendix XII. As such, the RNA derived from the k562 and BV173 were used as positive samples for the e14a2 and e13a2 fusion sequences while the RNA from THP1 was used as negative control for the BCR-ABL fusion sequences (306). The BioCode-47bp-e13-FAM, BioCode-47bp-e14-Cy3 and the double-labeled BioCode were incubated with different amounts of total RNA from the different cell lines and the signal variation was measured at end-point, or with a fixed amount of RNA in an over-time measurement. However, the signal variation for each situation was not stable and was highly dependent on the quality of the RNA extraction. As such the results are presented individually to better observe the concentration dependent signal variation – Figure 4.22 for the signals obtained for the BioCode-47bp-e13-FAM and Figure XII.2 for the BioCode-47bp-e14-Cy3. In Figure 4.22 A, the endpoint spectra of the BioCode-47bp-e13-FAM in the absence of target (dotted black line) and incubated with 66.7 ng/µl of total RNA derived from either the BV173 (solid black line) or THP1 (dotted black line) cell line is presented. The presence of the THP1 total RNA induces the enhancement of the donor emission band in comparison to the absence of target, while the acceptor emission overlaps with this control. This indicates the disruption of the hairpin structures in the surface of the AuNP with a barely noticeable hybridization of the revelator, even though this cell lines do not express the BCR-ABL fusion sequence. The presence of the RNA derived from the BV173 cell line induces an increase in both emission bands, indicating a successful assembly of the tcMB on the surface of the AuNP. However, this positive identification is not stable as seen in Figures 4.22 B-C, D-E and F-G (for the donor-acceptor signal variation). The same profile is observed for the BioCode-47bp-e14-Cy3 when incubated with RNA derived from the K562 cell line.

The signal fold variation observed for the double-labeled BioCode incubated with RNA derived from either RNA derived from either BV173 (Figure 4.23 and XII.3, panel A and B – Appendix XII), or K562 (Figure 4.23 and XII.3 panel C and D – Appendix XII), shows that the double-labeled BioCode is not able to discriminate between the RNA derived from K562 or from THP1, considering that the presence of the THP1 RNA has a higher impact on the double-labeled BioCode signals than the RNA from K562. The double labeled BioCode signal variation is more dependent on the RNA concentration of the BV173 RNA, indicating that this construct has a higher discrimination ability towards the fusion sequence e13a2.

Detection attempts were performed using the products of an asymmetric PCR, without purification – Figure XII.4, Appendix XII. This PCR was designed to yield ssDNA of the complementary sequence to the loop portion of the hairpin. Incubation with 5µl of water was compared to the incubation with 1 µl, 2 µl and 5

µl, over time. However, these reactions only induced an increase of the donor channel, while the acceptor channel had the same signal variation as the control. The same was observed for the reaction performed using ethanol precipitated PCR products – Figure XII.5 from appendix XII.

The signal fold change obtained in the presence of the synthetic oligonucleotides are clearer than the ones obtained in the presence of cell lines derived RNA, indicating that the tested BioCodes are not optimized for RNA detection and further optimization are required.

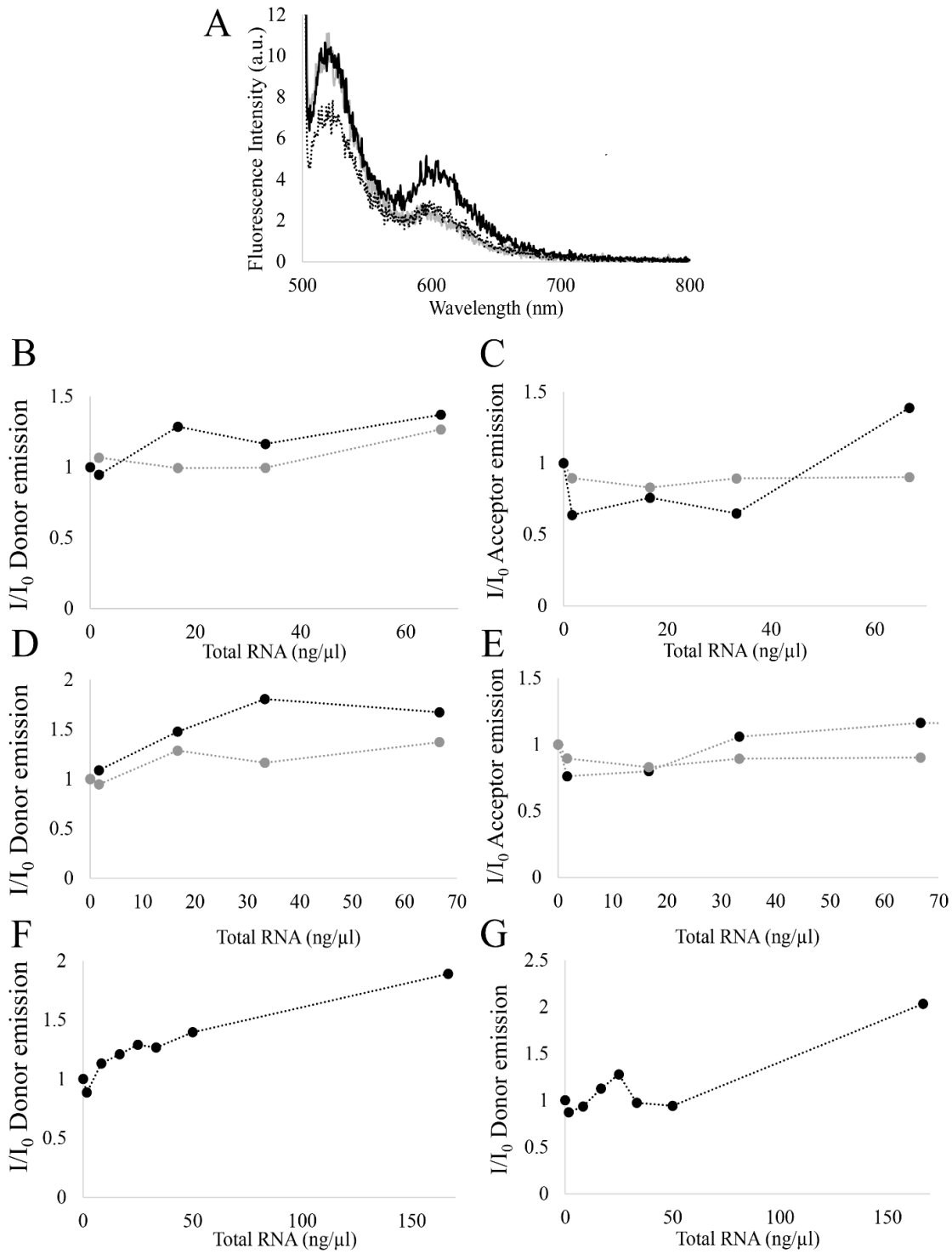

Figure 4.22. Signal variation of BioCode-47bp-e13-FAM incubated with RNA derived from BV173 cell lines. A) emission spectra of BioCode in the presence of 66.7 ng/µl of total RNA from BV173 (black line) and THP1 (gray line). B, D, F) Donor channel emission variation using different concentration of total RNA of k562 cell line (black circles) and THP1 (gray circles); C, E, G) Acceptor channel emission variation using different concentration of total RNA of k562 cell line (black circles) and THP1 (gray circles).

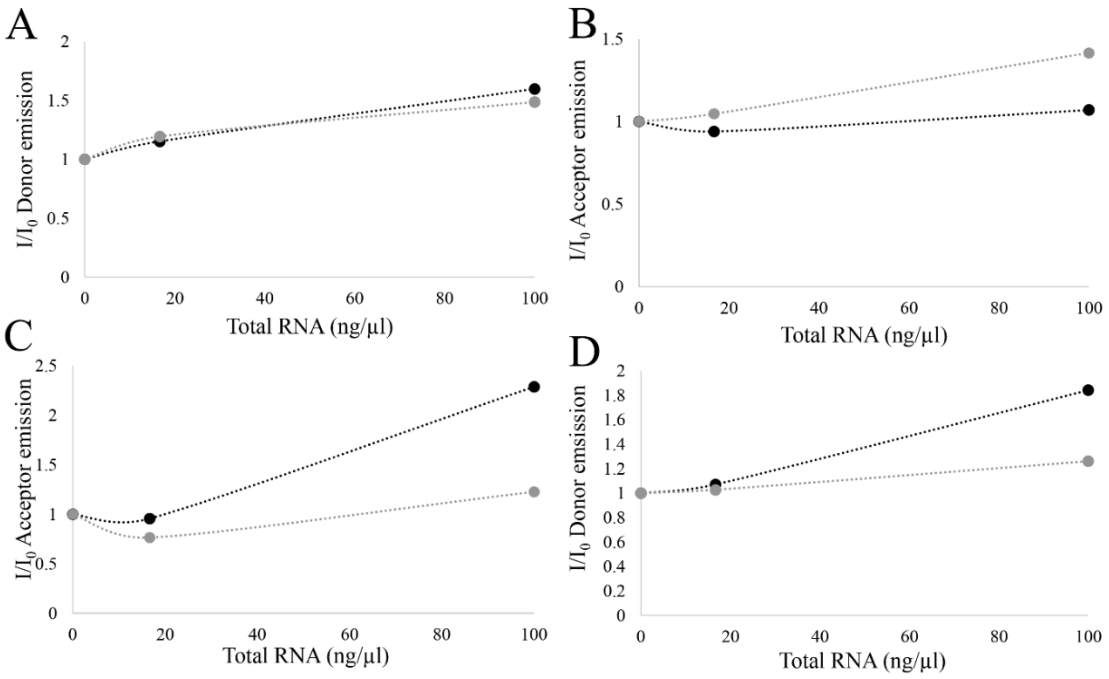

Figure 4.23. Signal variation of double labeled BioCode incubated with total RNA. A) Donor channel emission variation using different concentration of total RNA of k562 cell line (black circles) and THP1 (gray circles); B) channel emission variation using different concentration of total RNA of k562 cell line (black circles) and THP1 (gray circles); C) Acceptor channel emission variation using different concentration of total RNA of BV173 cell line (black circles) and THP1 (gray circles); D) Acceptor channel emission variation using different concentration of total RNA of BV173 cell line (black circles) and THP1 (gray circles).

4.11 **Conclusion**

In this chapter, the development of BioCode Au-nanobeacons was presented. This platforms showed to be suitable for the selective detection of similar synthetic targets in solution. This FRET based Au-nanobeacon system was applied to the selective detection of specific molecular targets that are of clinical interest for real life situations. As a proof-of-concept, the BioCode Au-nanobeacons were designed to detect either one of the most common fusion sequences causing chronic myeloid leukemia, e13a2 and e14a2. The BioCode is a detection strategy based on two successive hybridization events: hybridization of the target molecule opens the nanobeacon and allows for partial recovery of the donor's emission and exposes the palindrome sequence that is the target for the acceptor labeled oligonucleotide. The FRET signal is generated solely under selective recognition of the complimentary target, overlooking any signal originated by the presence of partially complementary targets. This is of utmost relevance since unequivocal detection of similar sequences, such as CML, must exclude the unwanted hybridization events resulting from healthy ABL or BCR expressed mRNAs that are always present in any given sample. The cross-reactivity of the healthy counterparts is the most common reason for false positive results in current molecular

characterization methods for CML. However, when this platform is used in the detection of total RNA derived from human cell lines, it is evident that further optimization is required. This because, this platform cannot discriminate the target sequences from a pool of total RNA.

5 Gold Nanobeacons for *in Vitro* Imaging and Tracking Gene Silencing in Zebrafish

The work presented within this Chapter resulted in the following publication:

Cordeiro M.; Carvalho L.; Silva J.; Saúde L.; Fernandes A.R.; Baptista P.V. Gold Nanobeacons for Tracking Gene Silencing in Zebrafish. *Nanomaterials* **2017**,*7*, 10.

Milton Cordeiro was responsible for the gold nanobeacons design and characterization, microinjection of the gold nanobeacon into the zebrafish embryos, some data analysis and manuscript drafting.

5.1 Introduction

The use of antisense oligonucleotides (ASO) as therapeutic agents was proposed for the first time by Zamecnik and Stephenson in 1978 (307). These molecules are used to specifically knockdown gene expression, through the hybridization and formation of a complex with the target mRNA. The hybrid duplex (DNA-mRNA) is responsible for the recruitment of the RNAse H enzyme, which hydrolyzes the RNA portion of the duplex. The antisense DNA may then hybridize to another mRNA molecule (240), leading to gene expression knockdown. However, these molecules require the use of transfection agents to promote cell internalization, and upon entry, the activity of endogenous nucleases leads to short persistence of the antisense molecules (due to the antisense sequence hydrolysis). The use of AuNPs has shown the capacity to bypass these limitations (176). Particularly, we have shown the increased knockdown efficiency of gene expression (oligonucleotides have an added protection from enzymatic degradation), while simultaneously reducing the toxicity and immune response problems associated with the most common transfection systems. In addition, AuNPs have the capability to quench the fluorescence of nearby fluorophores in a distance-dependent manner. As such, the functionalization with fluorescence-labeled single-strand DNA (ssDNA) with a hairpin structure leads to fluorescence quenching due to the fluorophore's proximity to the AuNP surface. Upon hybridization to the target sequence, the fluorophore breaks away from the surface of the AuNP, leading to a partial recovery of the fluorescence emission – Au-nanobeacons (175, 183). This dynamic formulation allows the fluorescent detection of the silencing event, considering the partial fluorescence recovery upon hybridization to the target sequence. Additionally, Au-nanobeacons were demonstrated to be viable silencer agents both *in vitro* and in vivo without toxicity (98). However, further studies using more complex in vivo models are paramount to demonstrate the efficacy but also infer the induction of malformations/toxicity. *Danio rerio* (zebrafish) is one of the most reliable and well-established *in vivo* models fora multitude of studies and screenings, including carcinogenesis and developmental studies, as well as toxicity assays (286, 308, 309), including environmental toxicity and nanoparticle toxicity (310, 311).The advantages of using this in vivo model are mainly their fast reproduction, the high number of fingerlings, the optical transparency of embryos which allows real-time monitoring of the development process and of fluorescence markers, the ease of manipulation and maintenance (286, 312–314), and high homology to the human genome (315). Here, Au-nanobeacons showed to suitable and efficient platforms for *in vivo* imaging of intracellular mRNA in K562 cell lines and in embryos of a fli-enhanced green fluorescence protein (fli-EGFP) transgenic zebrafish line (300), and constitute a valuable tool to track and localize *in vivo* as the silencing occurs without hampering the embryo's development or killing the organism. This way, these Au-nanobeacons may become a valuable tool in zebrafish studies involving gene modulation.

5.2 Methodology

5.2.1 Synthesis and functionalization of AuNPs

AuNPs were synthesized using the procedure described by Turkevich and later optimized by Lee and Meisel (70, 72), yielding citrate-capped AuNP (AuNP@citrate). The AuNP@citrate were functionalized as described in (175, 183). Briefly, AuNPs were functionalized with a 30% surface coverage using O-(2-Mercaptoethyl)-O0-methyl-hexa(ethylene glycol) and further functionalized with a 3' Cy3 fluorophore-labeled hairpin-ssDNA (50-tttgccgctcctggacgtagccttcgggggcaaa-30) bearing a thiol on the 5' end, as to act as an Au-nanobeacon. Direct excitation of Cy3 at 550 nm was used to quantify the unbound ssDNA in the supernatants collected during the washing steps. The emission spectra of the supernatants collected from the washing steps was converted into molar concentration through the interpolation in a calibration curve, prepared with known concentrations of oligonucleotide in the same reactional conditions as the supernatants. The difference between the added oligonucleotides and the washed oligonucleotide was used to calculate the average number of functionalized oligonucleotides. The Au-nanobeacon were characterized by UV-Vis absorption spectroscopy, zeta potential and by DLS as previously described (183). The zeta potential and DLS assays were performed in DI water.

5.2.2 Ethics statement

Experiments involving animals were approved by the Animal User and Ethical Committees at Instituto de Medicina Molecular (Lisboa, Portugal), according to the directives from Direcção Geral Veterinária.

5.2.3 *In Vitro* imaging of Au-nanobeacon within human cell line

The K562, BV173 cell lines were maintained as stated in section 2.9.1. The HL60 were maintained in RPMI 1640 + 2mM Glutamine + 10-20% Fetal Bovine Serum. 10^4 cell from each cell line were incubated with 0.5 nM of Au-nanobeacon formed using sequence 5 of table 2.2. When appropriate, the Au-nanobeacon was also incubated with 25 nM of acceptor labeled oligonucleotide. The Images were acquired in a Leica

DMRA2 fluorescence microscope using the following filter – Excitation 540 – 552 nm / Emission 590-4095 nm / Splitter 580 nm. The images were analyzed with the software ImageJ 1.49v and the integrated density of each condition was determined and compared with the respective controls.

5.2.4 Zebrafish line

The fli-EGFP transgenic zebrafish (316, 318) line was used as animal model and maintained in a recirculating system with a 14 h/day and 10 h/night cycle at 28 °C. After fertilization, the embryos were collected as described in the Zebrafish Book (318) and maintained in E3 zebrafish embryo medium (5.03 mM NaCl, 0.17 mM KCl, 0.33 mM $CaCl_2.H_2O$, 0.33 mM $MgSO_4.7H_2O$, 0.1% (w/v) methylene blue) at 28 °C, until reaching the developmental stage required.

5.2.5 Microinjection of zebrafish embryos

The fli-EGFP transgenic zebrafish line was chosen due to its EGFP stained vasculature, providing an easy model to evaluate the silencing efficacy of the Au-nanobeacon. Post-fertilized fli-EGFP embryos were collect and embryos at the sphere stage were divided into different groups and injected with: 50 nM of AuNPs@citrate and 50 nM of AuNPs@PEG as controls and 150 nM of Au-nanobeacon, using a PV-820 pico-injector (World Precision Instruments) and a Narashige micromanipulator. The free oligonucleotides molecules were also injected at the same concentration administered in the Au-nanobeacon. The embryos were incubated in 90 cm Petri dishes (Sarstedt) at 28 °C using embryo medium, until 24 h post-fertilization, a time-point where blood vessels are already formed and therefore the levels of EGFP expression could be evaluated.

5.2.6 Silencing and imaging

Live embryos were anesthetized by addition of 500 µl of 1% (v/v) Tricaine (Western Chemical) per 25 mL of embryo medium in 90 cm Petri dishes. Pictures were taken using an Olympus MVX10 magnifying glass with an incorporated AxioCam ICc3 (Olympus) and acquired by ZEN software, Blue Edition 2011

(Oberkochen). EGFP and Cy3 emission were determined by the quantification of pixels' intensity using the software ImageJ 1.49v. Each experiment was normalized to the respective control.

5.2.7 Toxicity assessment in zebrafish embryos

To evaluate the toxicity effects of the tested constructs, the mortality/survival rates and the number of morphological malformations in zebrafish embryos were assessed after microinjection. AuNPs@citrate, AuNPs@PEG, Au-nanobeacon and free oligonucleotide were injected in the same conditions as described previously, and effects evaluated 24 h post-fertilization. The number of malformations, mortality and survival percentages were determined in comparison to injection of 10 mM phosphate buffer pH 8.0.

5.3 Results and Discussion

5.3.1 Gold nanobeacons for *in Vitro* Imaging

The BioCode-43bp-e14-FAM was used for the transfection of k562, BV173 and Hl60 cell lines. This was performed to test if the designed nanoconstruct has the ability to hybridize specifically to the presence of the e14a2 fusion (using the e14a2 fusion transcript expressing cell line, K562), thus allowing the visualization of the expression of the fusion sequence e14a2. This was performed at several time points, 6, 24 and 48 hours. Parallelly, the same transfection procedure was performed in the BV173 and HL60 cell lines. The first expresses the e13a2 fusion transcript and serves to determine the specificity of the construct and the last do not express any fusion sequence and serves as a negative control for the signal variation due to the cellular environment. As additional controls, these cell lines were exposed just to water, only the acceptor-labeled oligonucleotide and only the Au-nanobeacon. Figure 5.2 A shows fluorescent microscope photos of the mentioned condition and Figure 5.2 B, shows the mean fluorescence per cell in the several tested conditions.

In all the tested condition, 6 hours after the addition of the appropriate stimulus, the emission of the cells in the observed fluorescence channel (excitation 540-552 nm; emission; 590 – 4095 nm; with a splitter at 580 nm) is residual. The emission in this channel greatly increases in the k562 cell lines after 24 hours and 48 hours, but is kept at a constant value in the BV173 and HL60 cell lines. This is concordant with the specific

hybridization of the BioCode-43bp-e14-FAM to the e14a2 fusion transcript. This increase could also be due to the reduction of the thiol-label of the hairpin, thus removing the Cy3 fluorophore from the surface of the AuNP, minimizing the quenching effect from the gold surface. The hydrolysis of the hairpin by the activity of endo/exonucleases could also be responsible for this increase. However, these two hypotheses are not likely considering that this increase in the emission in the channel 590-4095 nm is not observable in the other cell lines, that should have a similar cellular environment and nuclease expression. The loss of emission in this channel in the presence of the revelator, could be due to the occurrence of energy transfer. Although the AuNP has been shown to act as a transfection agent, and therefore promote the internalization of the donor labeled hairpin, no transfection agent was used for the internalization of the revelator. The lack of use of the transfection agent impairs the internalization of the revelator, and therefore the assembly of the BioCode in the presence of the fusion transcript. However, this should be confirmed using an appropriate microscopy approach, such as Fluorescence Lifetime Imaging or Fluorescence Recovery After Photobleaching (319).

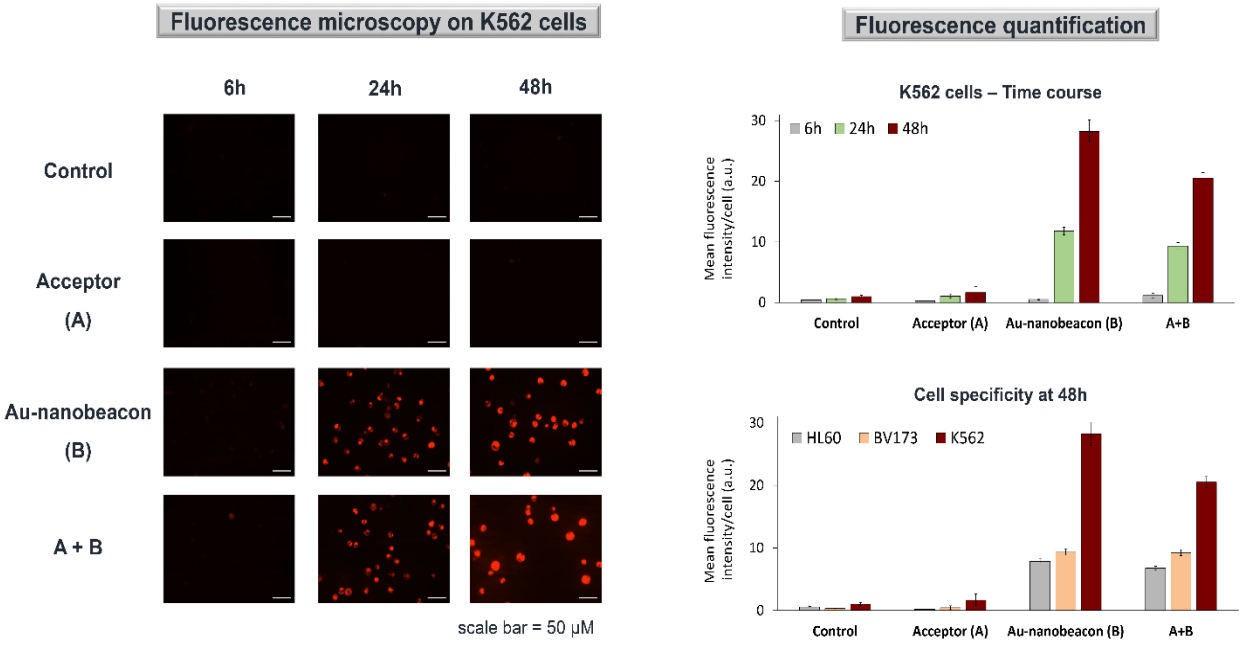

Figure 5.1. A) Fluorescent photos of K562 cell lines in the tested condition. B) Mean fluorescence intensity per cell of the tested condition.

5.3.2 Synthesis and characterization of the Au-Nanoconjugates for EGFP silencing in zebraFish

The Turkevich synthesis yielded citrate-capped AuNPs (AuNP@citrate) (70) with an average core size of 13.95 ± 1.79 nm (Figure 5.2 a), which were functionalized with O-(2-Mercaptoethyl)-O0-methylhexa(ethylene glycol), $C_{15}H_{32}O_7S$, 356.48 Da), generating PEGylated AuNPs (AuNP@PEG) (175, 183). A 30% surface coverage of the AuNP@citrate was used following the procedure described in (175), which allows for incorporation of the thiolated ssDNA molecules while conferring stability and increased biocompatibility. The AuNP@PEG was further functionalized with 6 ± 2 Cy3 labeled ssDNA oligonucleotides bearing the EGFP antisense sequence (see Figure 5.2 d for calibration curve used), yielding Au-nanobeacons. The UV-visible (UV-Vis) absorption spectra showed an increase of the full width at half maximum of the localized surface plasmon resonance (LSPR) of the Au-nanobeacon compared to the AuNP@citrate (Figure 5.2 b), indicating a broader size dispersion of AuNPs in solution. Dynamic light scattering (DLS) measurements (Figure 5.2 c) showed an increase in the hydrodynamic diameter (expressed as the z-average) from 17.3 ± 0.6 nm for the AuNP@citrate to 42.3 ± 1.4 nm for the Au-nanobeacon due to the ssDNA stem-loop isotropic functionalization (on every side of the AuNPs) (Figure 5.2c), corroborated by the decrease in the zeta potential with a value of -78.8 ± 1.3 mV (Figure 5.2 e). Together, these data show that the AuNPs were successfully functionalized and the Au-nanobeacon product is stable.

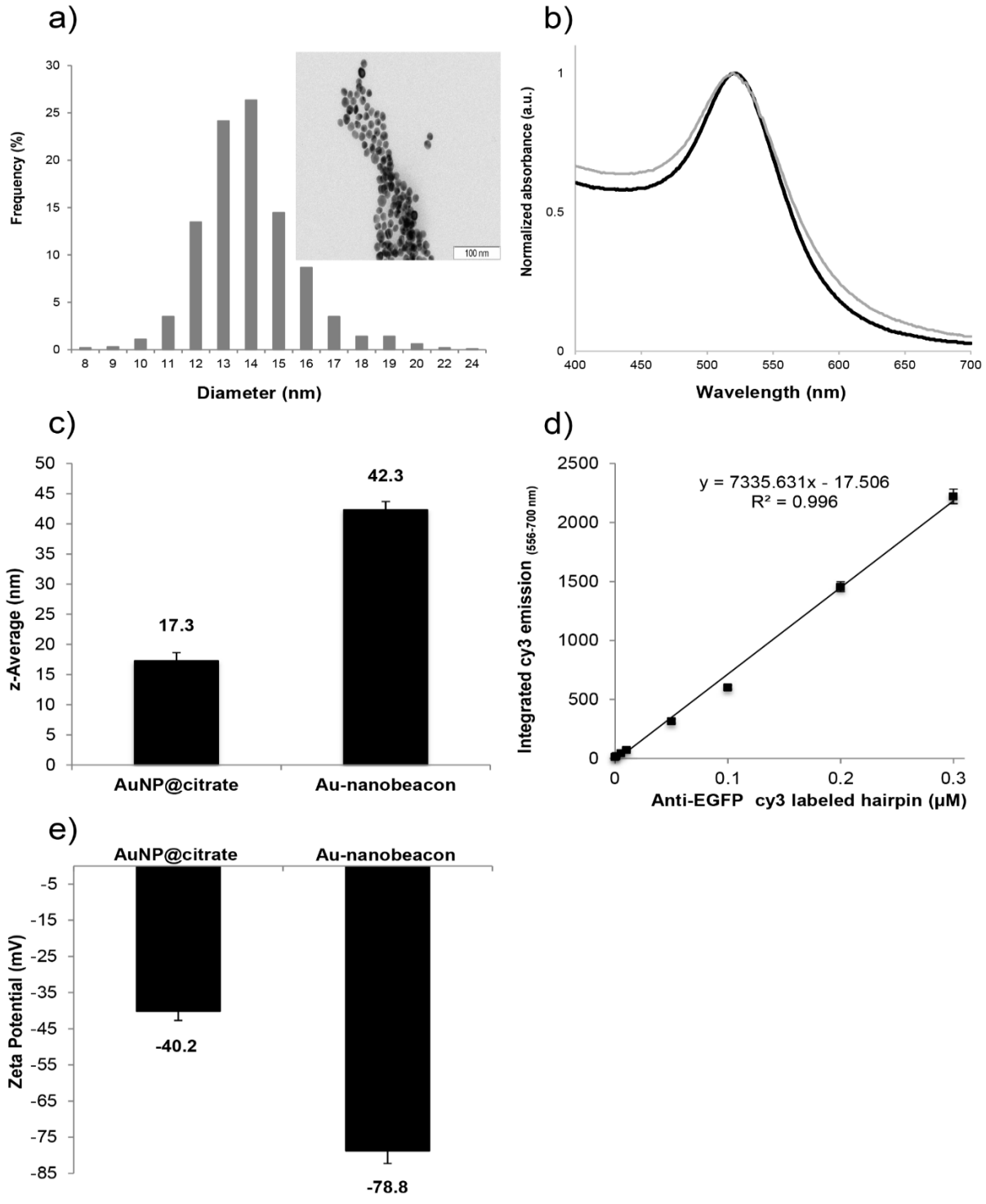

Figure 5.2. Characterization of the synthesized AuNP@citrate and Au-nanobeacon. (a) Size distribution of the synthesized AuNP@citrate.; Inset: TEM image of the AuNP@citrate (scale bar: 100 nm); (b) UV-Vis spectra of the AuNP@citrate (solid black line) and Au-nanobeacon (solid gray line); (c) Hydrodynamic diameter of AuNP@citrate and Au-nanobeacon; (d) Calibration curve for the quantification of the number of hairpins per PEGylated AuNPs; (e) Zeta potential of AuNP@citrate and Au-nanobeacon.

5.3.3 **Silencing efficiency**

The silencing efficiency of the synthesized Au-nanobeacon was evaluated in an in vivo model, the fli-EGFP transgenic zebrafish. The level of silencing was correlated with the EGFP emission (green channel) and the Au-nanobeacon output was correlated with the Cy3 emissions (red channel). The injection of 150 nM of Au-nanobeacon led to a 22.7% ± 16.6% reduction of the emissions in the green channel (Figure 5.3 a vs. Figure 5.3 d), with a concomitant increase of 62.2% ± 28.0% in the red channel in comparison to the control (Figure 5.3 b vs. Figure 5.3 e) – the white arrows highlight the measured embryos). The overlay of the green and red channels of the injected group allows the co-localization of both the green and red channels – Figure 2c, whereas the overlay of both channels in the control group only allows for the observation of the green channel – Figure 5.3 f. See Figure 5.3 h for an amplification of affected zebrafish. The intensity quantification is represented in Figure 5.3 g. These results suggest that injection of the designed Au-nanobeacon causes a decrease in the green channel intensity, which correlates with the hybridization of the Au-nanobeacon to the target mRNA, leading to a reduction of the gene expression. The red channel shows a higher intensity in the injected group, suggesting that target recognition induces the opening of the hairpin, resulting in the separation.

The silencing efficiency of the Au-nanobeacon was compared with the microinjection of the free antisense oligonucleotide anti-EGFP at the same concentration administered through the AuNPs. For the free EGFP antisense oligonucleotide, the reduction of the EGFP emission was negligible at 2.8% ± 2.3%, in comparison to the 22.7% ± 16.6% obtained with the Au-nanobeacon (Figure 5.3 g), demonstrating the advantage of the Au-nanobeacon for anti-sense oligonucleotide delivery when compared to the administration of the free oligonucleotide.

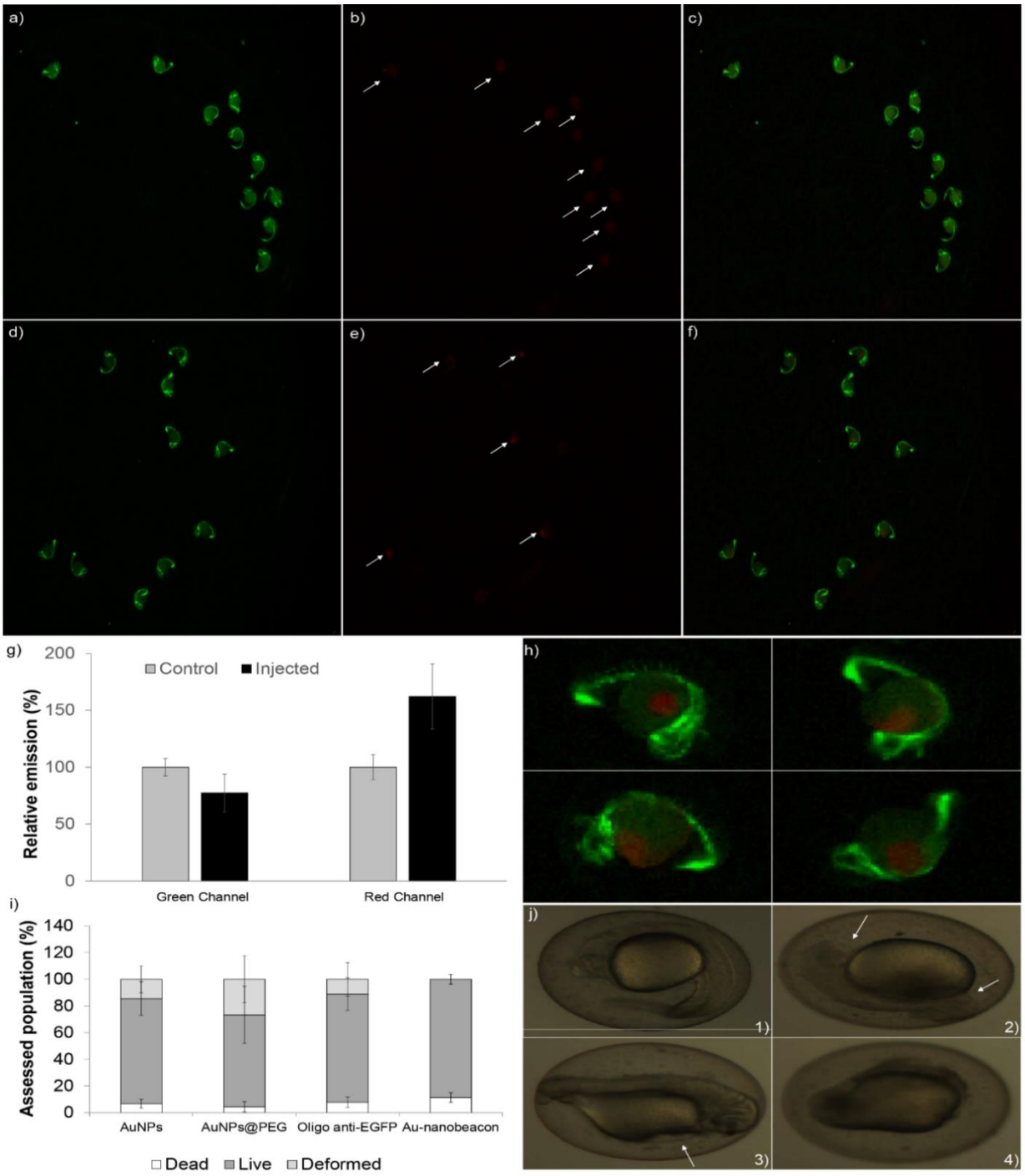

Figure 5.3. Au-nanobeacon silencing efficiency of the enhanced green fluorescence protein (EGFP) and acute toxicity assessment. Fluorescence imaging of whole embryos after injection (amplification 8.1×); (a) Green channel of control embryos; (b) Red channel of control embryos; (c) Merged channels for control embryos; (d) Green channel of injected embryos; (e) Red channel of injected embryos; (f) Merged channels for injected embryos (8.1× amplification); (g) Quantification of fluorescence in whole embryos using Image J. The results were normalized to the respective channel of the control. The data are expressed as mean ± standard deviation of five embryos); (h) Zoom of 32.4 of the injected embryos' merged channels (400% of 8.1); (i) Quantification of death, survival and morphological malformations upon microinjection of AuNP@citrate, AuNP@PEG, Oligo anti-EGFP and Au-nanobeacon; Error bars correspond to standard deviation of at least 50 embryos; (j) Example of embryos observed after microinjection of AuNP@citrate, AuNP@PEG, Oligo anti-EGFP and Au-nanobeacon: (j1) Normal embryo; (j2) Head and tail malformation; (j3) Pericardial edema; (j4) Underdeveloped embryo.

5.3.4 Toxicity in zebrafish embryos

Acute toxicity is of paramount importance for the successful application of the developed Au-nanobeacon for gene therapy. Toxicity was assessed based on the determination of the percentage of survival, death and malformation 24 h post-fertilization in the presence of the different nanoconjugates (at least 50 embryos per assay). Results presented in Figure 5.3 i shows that the injection of the Au-nanobeacon led to a mortality of 11.3% ± 3.6%, which is the highest among the different conditions tested, in agreement with previously published work (320). Administration of the same concentration of free oligonucleotide led to 84.1% ± 12.2% survival (Figure 5.3 i). Furthermore, malformations were detected in 10% ± 12.5% after the administration of free oligonucleotide. Injection of free oligonucleotide resulted in: Normal development (Figure 5.3 j1), head and tail malformations (Figure 5.3 j2), pericardial edema (Figure 5.3 j3) as well as totally undeveloped embryos (Figure 5.3 j4). These findings demonstrate an interference in the embryonic development process of zebrafish and greater toxicity associated with the administration of such free molecules. It has been demonstrated that AuNPs with different coatings appear to have no toxic effects in zebrafish embryos and concluded that this absence of toxicity was due to the lack of internalization of the AuNPs (320, 321). However, in this study, upon the injection of the Au-nanoconjugates directly into the zebrafish embryos, it is showned the in vivo silencing potential (loss of green fluorescence simultaneously with the increase of red fluorescence due to the opening of the hairpin) with relatively low toxicity/malformations.

5.4 Conclusions

In this chapter, AuNPs functionalized with a ssDNA with a hairpin conformation bearing the Cy3 fluorophore (Au-nanobeacon), which act as antisense oligonucleotides were used towards endogenous EGFP mRNAin Zebrafish and towards the e14a2 fusion transcript. A reduction of the EGFP emission was observed, indicating a downregulation of EGFP expression, with a concomitant increase of the fluorophore emission. No changes in the expression of EGFP were seen when the free oligonucleotide molecules were injected, indicating that the AuNPs are a suitable vehicle for antisense oligonucleotides. The Au-nanobeacon showed eight times higher silencing capability in comparison to the free oligonucleotide and is more biocompatible than AuNP@citrate and AuNP@PEG. This is the first proof-of-concept of using Au-nanobeacons for gene silencing in an in vivo zebrafish model. For the in vitro visualization of the e14a2 fusion transcript, the recovery of the cy3 emission (Au-nanobeacon) is concordant with the hybridization

to the target fusion transcript. This increase in the Cy3 emission was not observed for the BV173 cell line nor the HL60 cell line.

6 General conclusions and future perspectives

Nanomaterials, such as AuNPs, present a vast and unique set of properties useful for the development of bio-detection platforms (Biosensors). In this thesis, the development of Au-nanobeacon coupled with a wavelength shift mediated by FRET was presented. To so, the design of a conventional molecular beacon was optimized and a two-component molecular beacon was devised. Instead of the common output signal, where the hybridization of the target sequence induces the enhancement of the fluorophore emission, in the design system, this first step is optically inactive. This step serves to expose the palindromic sequence where an acceptor-labeled oligonucleotide can be targeted. This hybridization triggers the energy transfer between the donor that labels the hairpin structure and the acceptor. The design of the tcMB was guided through the NUPACK software, and several possible designs were experimentally assessed using fluorescence spectroscopy. Upon the design optimization, the specificity of the tcMB was tested using fluorescence spectroscopy after the incubation of the tcMB with the following targets: non-complementary targets, partial complementary targets, BCR and ABL, and fusion sequences with a high level of identity. The melting profile of some of the designs were collected as to infer the thermal stability of the complexes. The formation of the tcMb was further characterized using electrophoretic mobility, SAXS and MST measurement. The SAXS data indicate that the formation of this final complex is sequential and specific, and the alteration of the thermophoretic mobility upon target and revelator binding also supports the formation of the desired structure. The molecular envelope indicates a near duplication of the size of the hairpin upon target recognition and a slight decrease after the hybridization of the acceptor-labeled oligonucleotide, with the formation of a 1:1:1 complex. Although indicating interaction, the performed ITC assays still require optimization, considering that this is the only approach that shows that these interactions are not occurring in a 1:1 stoichiometry. The complete alignment of the SAXS data with all of the additional techniques demonstrate that SAXS is a viable technique to study nucleic acids ensembles in solution, such as DNA Origamis and nucleic acids nanotechnology ensembles, without the need for prior labeling.

After the optimization of the tcMB for the specific detection of the most common BCR-ABL fusion sequences, they were used to functionalize the surface AuNP – generating a BioCode Au-nanobeacon. In this configuration, the hybridization of a target molecule to the hairpin structure is no longer optically inactive, since the AuNP acts as a scaffold and an emission modulation entity. Around 45% of the AuNP surface was previously functionalized with thiolated PEG molecules, as this surface coverage maximizes the hybridize to the non-hybridized signal. The BioCode is a single-step detection strategy based on two successive hybridization events: 1) the hybridization of the target molecule opens the nanobeacon, and allowing the partial recovery of the donor's emission; 2) exposes the palindrome sequence that is the target for the acceptor-labeled oligonucleotide. The FRET signal is generated solely under selective recognition of the complementary target, overlooking any signal originated by the presence of partially complementary targets. This is of utmost relevance since unequivocal detection of similar sequences, such as CML, must exclude the unwanted hybridization events resulting from healthy ABL or BCR expressed mRNAs (that are always present in any given sample). The cross-reactivity of the healthy counterparts is the most common

reason for false positive results in current molecular characterization methods for CML. Noteworthy is that the presence of partially complementary targets induces an increase in the donor channel, indicating a partial opening of the hairpin in the surface of the AuNP. This partial hybridization is not observed in the specificity assessment of the free oligonucleotides, which indicates that the functionalization of the ssDNA hairpin structures on the surface of the AuNP, decreases its specificity. The SAXS and SANS characterization of these nanoconstructs was attempted, but further optimization of the measuring conditions and data analysis is required. The direct detection of the fusion transcripts from total extracted RNA must also be optimized. This detection must be tested using an isothermal nucleic acid amplification technique, such as rolling circle amplification, as to simplify the integration of the developed system into a microfluidic device. The nature of the bioreceptor can also be optimized, and a peptide nucleic acids (PNA) could be employed. These PNA are uncharged and, as such, the electrostatic repulsion of the target and bioreceptor could be minimized. Considering that only AuNP of 14 nm were tested, the size of the nanoparticle should be optimized to tune the quenching/enhancement of FRET. This size was chosen to maximize the interaction between the donor fluorophore and the LSPR of the AuNP. However, this complete overlay of the donor emission band and the LSPR can be detrimental to the energy process due to the excitation light competition. As such, different degrees of overlap between the donor and the LSPR should be tested.

Other types of nanoparticles can be tested such as silver and silica nanoparticles. Testing the use of silica particles, that are optical inactive, is the crucial importance. This because, in the absence of the AuNP, the observable acceptor enhancement reached a 4-fold increment, while in the presence of the AuNP, the same donor/acceptor pair only reached ±1.5-fold enhancement.

The BioCode towards the e14a2 fusion sequence was used for the *in vitro* imaging of the expression of the e14a2 fusion transcripts after the transfection of the k562 human cell lines, BV173 and HL60 cell lines. An increase in the donor emission was observed for the k562 cell line (that expresses the complementary e14a2 fusion transcript), while no variation was observed for the BV173 (expresses the e13a2 fusion sequence) and for the HL60 (do not expresses any fusion sequence). In this experimental configuration, it is not possible to assess if the BioCode was assembled within the mentioned cell lines considering that donor and acceptor channels could not be assessed individually due to the used experimental setup. However, since no transfection agent was used for the uptake of the acceptor-labeled oligonucleotide, it is highly unlikely that this oligo was uptaken be the cells. To improve this assay, different microscopy approaches should be performed, such as FLIM of FRAP, and a transfection agent can be used to maximize the uptake of the acceptor labeled oligonucleotide.

The Au-nanobeacon technology was also used for the silencing of endogenous EGFP mRNA of transgenic zebrafish. Here, a reduction of the EGFP emission was observed, indicating a downregulation of EGFP expression, with a concomitant increase of the fluorophore emission. No changes in the expression of EGFP were seen when the free oligonucleotide molecules were injected, indicating that the AuNPs are a suitable

vehicle for antisense oligonucleotides. The Au-nanobeacon showed eight times higher silencing capability in comparison to the free oligonucleotide and is more biocompatible than the unmodified AuNP and AuNP@PEG.

In summary, the main objective of this thesis – the development of an Au-nanobeacon coupled to a FRET mediated wavelength shift mechanism that work in a homogenous format – was achieved. It was possible to devise a tcMB, that can generate a FRET signal only in the presence of a fully complementary target. This specific FRET signature was confirmed using several distinct techniques. This bioreceptor was then used to functionalize the surface of PEGylated AuNP and to detect the presence of synthetic oligonucleotides with the fusion sequence of the most common fusion sequences of BCR-ABL. However, for this system to be a reliable alternative for the diagnosis of CML, a heavy optimization must be performed. This because, only a proof of concept was achieved, as the detection of the fusion transcript from total RNA derived from the human cell was not possible. Considering that in a clinical scenario, the number of cells is significantly lower than the 10^4 used for the RNA extraction, the proposed detection system still requires a heavy optimization. As such, the devised biosensor still lack the needed robustness to be considered a viable alternative for the current existing technologies, such as q-PCR or FISH. However, due to the optical signal output and sensor small features, the devised platform can be easily coupled to a microfluid device. This coupling would allow the tackle of some of the performance issue, by tethering a chamber for isothermal amplification to the detection chamber.

7 References

1. Atkins,P. and Paula,J.D.E. Physical Chemistry Eighth Edi. Oxford University Press, Oxford.
2. Harvey,D. (2000) Modern Analytical Chemistry Peterson,K.A., Oberbroeckling,S.R. (eds) James M. Smith.
3. Lakowicz,J.R. (2006) Principles of Fluorescence Spectroscopy 3 nd. Academic,K. (ed) Plenum Publishers, New York.
4. Suppan,P. (1994) Chemistry and light The Royal Society of Chemistry, Cambridge.
5. Rohatgi-Murkherjee (1986) Fundamentals of photochemistry Revised ed. Wiley Eastern Limited, New Delhi.
6. Valeur,B. (2001) Molecular Fluorescence - Principles and Applications Second. Wiley-VCH (ed).
7. Albani,J.R. (2007) Principles and applications of fluorescence spectroscopy Blackwell, Oxford.
8. Fery-Forgues,S. and Lavabre,D. (1999) Are Fluorescence Quantum Yields So Tricky to Measure? A Demonstration Using Familiar Stationery Products. *J. Chem. Educ.*, **76**, 1260.
9. Tredwell,C.J. and Keary,C.M. (1979) Picosecond time resolved fluorescence lifetimes of the polymethine and related dyes. *Chem. Phys.*, **43**, 307–316.
10. Loken,M.R., Gohlke,J.R. and Brand,L. (1973) Fluorescence Techniques in Cell Biology. In Thaer,A.A., Sernetz,M. (eds), *Fluorescence Techniques in Cell Biology*. Springer-Verlag, Berlin.
11. Chen,H., Ahsan,S.S., Santiago-Berrios,M.B., Abruna,H.D. and Webb,W.W. (2010) Mechanisms of Quenching of Alexa Fluorophores by Natural Amino Acids. *J. Am. Chem. Soc.*, **132**, 7244–7245.
12. Webber,S.E. (1997) The Role of Time-Dependent Measurements in Elucidating Static Versus Dynamic Quenching Processes. *Photochem. Photobiol.*, **65**, 33–38.
13. Eftink,M.R. and Ghiron,C.A. (1981) Fluorescence quenching studies with proteins. *Anal. Biochem.*, **114**, 199–227.
14. Didenki V. (2006) Fluorescent Energy Transfer Nucleic Acid Probes 1st ed. Didenko,V. V. (ed) Humana Press, New Jersey.
15. Jennes,J.R. (1928) Effect temperature the upon the fluorescence of some organic solutions. *Phys. Rev.*, **31**, 1275.
16. Kubin,R.F. and Fletcher,A.N. (1982) Fluorescence quantum yields of some rhodamine dyes. *J. Lumin.*, **27**, 455–462.
17. Kemnitz,K. and Yoshihara,K. (1991) Entropy-driven dimerization of xanthene dyes in nonpolar solution and temperature-dependent fluorescence decay of dimers. *J. Phys. Chem.*, **95**, 6095–6104.
18. Patil,N.R., Melavanki,R.M., Patil,H.D., Nagaraja,D. and Sanningannavar,F.M. (2013) Effect of Temperature on the Fluorescence Quenching of Biologically Active Carboxamide. *Int. J. life Sci. pharma Res.*, **3**, 64–76.
19. Tansi,F.L., Rüger,R., Rabenhold,M., Steiniger,F., Fahr,A. and Hilger,I. (2015) Fluorescence-quenching of a Liposomal-encapsulated Near-infrared Fluorophore as a Tool for In Vivo Optical Imaging. *JoVE (Journal Vis. Exp.*, 10.3791/52136.

20. Margulies,D., Melman,G. and Shanzer,A. (2005) Fluorescein as a model molecular calculator with reset capability. *Nat. Mater.*, **4**, 768–771.
21. Enoki,S., Saeki,K., Maki,K. and Kuwajima,K. (2004) Acid denaturation and refolding of green fluorescent protein. *Biochemistry*, **43**, 14238–14248.
22. Resch-Genger,U., Grabolle,M., Cavaliere-Jaricot,S., Nitschke,R. and Nann,T. (2008) Quantum dots versus organic dyes as fluorescent labels. *Nat. Methods*, **5**, 763–775.
23. Randolph,J.B. and Waggoner,A.S. (1997) Stability, specificity and fluorescence brightness of multiply-labeled fluorescent DNA probes. *Nucleic Acids Res.*, **25**, 2923–2929.
24. Antonov,L., Gergov,G., Petrov,V., Kubista,M. and Nygren,J. (1999) UV-Vis spectroscopic and chemometric study on the aggregation of ionic dyes in water. *Talanta*, **49**, 99–106.
25. Arbeloa,F.L., Ojeda,P.R. and Arbeloa,I.L. (1988) On the aggregation of rhodamine B in ethanol. *Chem. Phys. Lett.*, **148**, 253–258.
26. Forster,T. (1948) Zwischenmolekulare Energiewanderung und Fluoreszenz. *Ann. Phys.*, **248**.
27. Clegg,R.M. (2006) The history of FRET : From conception through the labors of birth. *Rev. Fluoresc.*, **3**, 1–45.
28. Berney,C. and Danuser,G. (2003) FRET or no FRET: A quantitative comparison. *Biophys. J.*, **84**, 3992–4010.
29. Obeng,E.M., Dullah,E.C., Danquah,M.K., Budiman,C. and Ongkudon,C.M. (2016) FRET spectroscopy—towards effective biomolecular probing. *Anal. Methods*, **8**, 5323–5337.
30. Schmid,J. a and Sitte,H.H. (2003) Fluorescence resonance energy transfer in the study of cancer pathways. *Curr. Opin. Oncol.*, **15**, 55–64.
31. Shi,J., Tian,F., Lyu,J. and Yang,M. (2015) Nanoparticle based fluorescence resonance energy transfer (FRET) for biosensing applications. *J. Mater. Chem. B*, **3**, 6989–7005.
32. Dexter,D.L. (1953) A Theory of Sensitized Luminescence in Solids. *J. Chem. Phys.*, **21**, 836.
33. Giestas,L., Ferreira,G., Baptista,P. and Lima,J. (2008) Multiplexed spectral coding for simultaneous detection of DNA hybridization reactions based on FRET. *Sensors Actuators B*, **134**, 146–157.
34. Giestas,L., Petrov,V., Baptista,P. V and Lima,J.C. (2009) General FRET-based coding for application in multiplexing methods. *Photochem. Photobiol. Sci.*, **8**, 1130–1138.
35. Cordeiro,M., Giestas,L., Lima,J.C. and Baptista,P. (2013) Coupling an universal primer to SBE combined spectral codification strategy for single nucleotide polymorphism analysis. *J. Biotechnol.*, **168**, 90–94.
36. T,K.K.J. (2005) Nanotechnology in clinical laboratory diagnostics. *Clin. Chim. Acta*, **358**, 37–54.
37. Kumar,C.S.S.R. ed. (2007) Nanomaterials for biosensors John Wiley & Sons.
38. Jianrong,C., Yuqing,M., Nongyue,H., Xiaohua,W. and Sijiao,L. (2004) Nanotechnology and biosensors. *Biotechnol. Adv.*, **22**, 505–18.
39. Yeh,Y.-C., Creran,B. and Rotello,V.M. (2012) Gold nanoparticles: preparation, properties, and

applications in bionanotechnology. *Nanoscale*, **4**, 1871.

40. Tran,Q.H., Nguyen,V.Q. and Le,A.-T. (2013) Silver nanoparticles: synthesis, properties, toxicology, applications and perspectives. *Adv. Nat. Sci. Nanosci. Nanotechnol.*, **4**, 33001.
41. Huang,S., Pfeiffer,C., Hollmann,J., Friede,S., Chen,J.J.-C., Beyer,A., Haas,B., Volz,K., Heimbrodt,W., Montenegro Martos,J.M., *et al.* (2012) Synthesis and characterization of colloidal fluorescent silver nanoclusters. *Langmuir*, **28**, 8915–8919.
42. Khodashenas, Bahareh,G. (2005) Synthesis of silver nanoparticles with different shapes. *Mater. Lett.*, **59**, 1760–1763.
43. Mott,D., Galkowski,J., Wang,L., Luo,J. and Zhong,C.J. (2007) Synthesis of size-controlled and shaped copper nanoparticles. *Langmuir*, **23**, 5740–5745.
44. Stepanov AL, Golubev AN,N.S. (2013) Synthesis and Applications of Platinum Nanoparticles : A Review. *Nanotechnology*, **2**, 173–199.
45. Long,N.V., Chien,N.D., Hayakawa,T., Hirata,H., Lakshminarayana,G. and Nogami,M. (2010) The synthesis and characterization of platinum nanoparticles: a method of controlling the size and morphology. *Nanotechnology*, **21**, 35605.
46. Ali,A., Zafar,H., Zia,M., ul Haq,I., Phull,A.R., Ali,J.S. and Hussain,A. (2016) Synthesis, characterization, applications, and challenges of iron oxide nanoparticles. *Nanotechnol. Sci. Appl.*, **9**, 49–67.
47. Chandra,S., Kumar,A. and Tomar,P.K. (2014) Synthesis of Ni nanoparticles and their characterizations. *J. Saudi Chem. Soc.*, **18**, 437–442.
48. Mussa Farkhani,S. and Valizadeh,A. (2014) Review: three synthesis methods of CdX (X = Se, S or Te) quantum dots. *IET Nanobiotechnol.*, **8**, 59–76.
49. Wang,Y. and Xia,Y. (2004) Bottom-up and top-down approaches to the synthesis of monodispersed spherical colloids of low melting-point metals. *Nano Lett.*, **4**, 2047–2050.
50. Dong,H., Du,S.R., Zheng,X.Y., Lyu,G.M., Sun,L.D., Li,L.D., Zhang,P.Z., Zhang,C. and Yan,C.H. (2015) Lanthanide Nanoparticles: From Design toward Bioimaging and Therapy. *Chem. Rev.*, **115**, 10725–10815.
51. Prasek,J., Drbohlavova,J., Chomoucka,J., Hubalek,J., Jasek,O., Adam,V. and Kizek,R. (2011) Methods for carbon nanotubes synthesis—review. *J. Mater. Chem.*, **21**, 15872.
52. Wang,E. and Wang,A. (2014) Nanoparticles and Their Applications in Cell and molecular biology. *Integr Biol*, **6**, 9–26.
53. Jain,P.K., Huang,X., El-Sayed,I.H. and El-Sayed,M. a (2008) Noble metals on the nanoscale: optical and photothermal properties and some applications in imaging, sensing, biology, and medicine. *Acc. Chem. Res.*, **41**, 1578–86.
54. Eustis,S. and el-Sayed,M. a (2006) Why gold nanoparticles are more precious than pretty gold: noble metal surface plasmon resonance and its enhancement of the radiative and nonradiative properties of

nanocrystals of different shapes. *Chem. Soc. Rev.*, **35**, 209–17.

55. Bera,D., Qian,L., Tseng,T.-K. and Holloway,P.H. (2010) Quantum Dots and Their Multimodal Applications: A Review. *Materials (Basel).*, **3**, 2260–2345.
56. Rivas,G.A., Rubianes,M.D., Rodríguez,M.C., Ferreyra,N.F., Luque,G.L., Pedano,M.L., Miscoria,S.A. and Parrado,C. (2007) Carbon nanotubes for electrochemical biosensing. *Talanta*, **74**, 291–307.
57. Huang,X. and El-Sayed,M. a. (2010) Gold nanoparticles: Optical properties and implementations in cancer diagnosis and photothermal therapy. *J. Adv. Res.*, **1**, 13–28.
58. Eustis,S. and el-Sayed,M. a (2006) Why gold nanoparticles are more precious than pretty gold: noble metal surface plasmon resonance and its enhancement of the radiative and nonradiative properties of nanocrystals of different shapes. *Chem. Soc. Rev.*, **35**, 209–17.
59. Murray,R.W. (2008) Nanoelectrochemistry: Metal nanoparticles, nanoelectrodes, and nanopores. *Chem. Rev.*, **108**, 2688–2720.
60. Chen,M. and Goodman,D.W. (2006) Catalytically active gold: From nanoparticles to ultrathin films. *Acc. Chem. Res.*, **39**, 739–746.
61. Yu Pan, Matthias Bartneck, and W.J.-D. (2012) Cytotoxicity of Gold Nanoparticles. In *Methods in Enzymology*. Elsevier Inc., Vol. 509, pp. 195–224.
62. Tan,B.J.Y., Sow,C.H., Koh,T.S., Chin,K.C., Wee,A.T.S. and Ong,C.K. (2005) Fabrication of size-tunable gold nanoparticles array with nanosphere lithography, reactive ion etching, and thermal annealing. *J. Phys. Chem. B*, **109**, 11100–11109.
63. Xu,X., Duan,G., Li,Y., Liu,G., Wang,J., Zhang,H., Dai,Z. and Cai,W. (2014) Fabrication of gold nanoparticles by laser ablation in liquid and their application for simultaneous electrochemical detection of Cd2+, Pb2+, Cu2+, Hg2+. *ACS Appl. Mater. Interfaces*, **6**, 65–71.
64. Scaramuzza,S., Zerbetto,M. and Amendola,V. (2016) Synthesis of gold nanoparticles in liquid environment by laser ablation with geometrically confined configurations: Insights to improve size control and productivity. *J. Phys. Chem. C*, **120**, 9453–9463.
65. Shahmoon,A., Limon,O., Girshevitz,O., Fleger,Y., Demir,H.V. and Zalevsky,Z. (2010) Tunable nano devices fabricated by controlled deposition of gold nanoparticles via focused ion beam. *Microelectron. Eng.*, **87**, 1363–1366.
66. Chen,Y., Bi,K., Wang,Q., Zheng,M., Liu,Q., Han,Y., Yang,J., Chang,S., Zhang,G. and Duan,H. (2016) Rapid Focused Ion Beam Milling Based Fabrication of Plasmonic Nanoparticles and Assemblies via 'sketch and Peel' Strategy. *ACS Nano*, **10**, 11228–11236.
67. Grzelczak,M., Vermant,J., Furst,E.M. and Liz-Marzán,L.M. (2010) Directed self-assembly of nanoparticles. *ACS Nano*, **4**, 3591–3605.
68. Kinge,S., Crego-calama,M. and Reinhoudt,D.N. (2008) Self-Assembling Nanoparticles at Surfaces and Interfaces. 10.1002/cphc.200700475.
69. Daniell,H. (2009) Biomineralization nanolithography: combination of bottom-up and top-down

fabrication to grow arrays of monodisperse gold nanoparticles along peptide lines. *Angew. Chemie Int. Ed.*, **48**, 2546–2548.

70. Turkevich,J., Stevenson,P.C. and Hillier,J. (1951) A study of the nucleation and growth processes in the synthesis of colloidal gold. *Discuss. Faraday Soc.*, **11**, 55.
71. Frens,G. (1973) Controlled nucleation for the regulation of the particle size in monodisperse gold suspensions. *Nat. Phys. Sci.*, **241**, 20–22.
72. Lee,P.C. and Meisel,D. (1982) Adsorption and surface-enhanced Raman of dyes on silver and gold sols. *J. Phys. Chem.*, **86**, 3391–3395.
73. Kumar,D., Meenan,B.J., Mutreja,I., D'Sa,R. and Dixon,D. (2012) Controlling the Size and Size Distribution of Gold Nanoparticles: a Design of Experiment Study. *Int. J. Nanosci.*, **11**, 1250023.
74. Ji,X., Song,X., Li,J., Bai,Y., Yang,W. and Peng,X. (2007) Size Control of Gold Nanocrystals in Citrate Reduction : The Third Role of Citrate. *J. Am. Chem. Soc.*, **129**, 13939–13948.
75. Brust,M., Walker,M., Bethell,D., Schiffrin,D.J. and Whyman,R. (1994) Synthesis of Thiol-derivatised Gold Nanoparticles in. *J. Chem. Soc.*
76. Ackerson,C.J., Jadzinsky,P.D., Kornberg,R.D., Biology,S., V,S.U., Dri,C. and West,V. (2005) Thiolate Ligands for Synthesis of Water-Soluble Gold Clusters. *J. Am. Chem. Soc.*, **127**, 6550–6551.
77. Liz-Marza,L.M. (2006) Tailoring Surface Plasmons through the Morphology and Assembly of Metal Nanoparticles. *Langmuir*.
78. Martin,M.N., Basham,J.I., Chando,P. and Eah,S.K. (2010) Charged gold nanoparticles in non-polar solvents: 10-min synthesis and 2D self-assembly. *Langmuir*, **26**, 7410–7417.
79. Rama,S., Perala,K. and Kumar,S. (2013) On the Mechanism of Metal Nanoparticle Synthesis in the Brust− Schiffrin Method. *Langmuir*, **29**, 9863–9873.
80. Deraedt,C., Salmon,L., Gatard,S., Ciganda,R., Hernandez,R., Ruiz,J. and Astruc,D. (2014) Sodium borohydride stabilizes very active gold nanoparticle catalysts. *chemcomm*, **50**, 14194–14196.
81. Haiss,W., Thanh,N.T.K., Aveyard,J. and Fernig,D.G. (2007) Determination of size and concentration of gold nanoparticles from UV-vis spectra. *Anal. Chem.*, **79**, 4215–21.
82. Jana,N.R., Gearheart,L. and Murphy,C.J. (2001) Seeding growth for size control of 5-40 nm diameter gold nanoparticles. *Langmuir*, **17**, 6782–6786.
83. Mallick,K., Wang,Z.L. and Pal,T. (2001) Seed-mediated successive growth of gold particles accomplished by UV irradiation: a photochemical approach for size-controlled synthesis. *J. Photochem. Photobiol. A Chem.*, **140**, 75–80.
84. Sato,K., Onoguchi,M., Sato,Y., Hosokawa,K. and Maeda,M. (2006) Non-cross-linking gold nanoparticle aggregation for sensitive detection of single-nucleotide polymorphisms: Optimization of the particle diameter. *Anal. Biochem.*, **350**, 162–164.
85. Wiesner,J. and Wokaun,A. (1989) Anisotropic gold colloids. Preparation, Characterization, and optical properties. *Chem. Phys. Lett.*, **157**, 569–575.

86. Sperling,R.A. and Parak,W.J. (2010) Surface modification , functionalization and bioconjugation of colloidal inorganic nanoparticles. *Philos. Trans. R. Soc. A*, **368**, 1333–1383.

87. Love,J.C., Estroff,L. a, Kriebel,J.K., Nuzzo,R.G. and Whitesides,G.M. (2005) Self-assembled monolayers of thiolates on metals as a form of nanotechnology. *Chem. Rev.*, **105**, 1103–69.

88. Alivisatos,A.P., Johnsson,K.P., Peng,X., Wilson,T.E., Loweth,C.J., Bruchez,M.P. and Schultz,P.G. (1996) Organization of 'nanocrystal molecules' using DNA. *Nature*, **382**, 609–11.

89. Mirkin,C., Letsinger,R., Mucic,R. and Storhoff,J. (1996) A DNA-based method for rationally assembling nanoparticles into macroscopic materials. *Nature*, **382**, 607–609.

90. Wang,L.H., Li,J., Song,S.P., Li,D. and Fan,C.H. (2009) Biomolecular sensing via coupling DNA-based recognition with gold nanoparticles. *J. Phys. D-Applied Phys.*, **42**.

91. Vo-Dinh,T., Wang,H.N. and Scaffidi,J. (2010) Plasmonic nanoprobes for SERS biosensing and bioimaging. *J. Biophotonics*, **3**, 89–102.

92. Podstawka,E., Ozaki,Y. and Proniewicz,L.M. (2005) Part III: Surface-Enhanced Raman Scattering of Amino Acids and Their Homodipeptide Monolayers Deposited onto Colloidal Gold Surface. *Appl. Spectrosc.*, **59**, 1516–1526.

93. Lyandres,O., Yuen,J.M., Shah,N.C., VanDuyne,R.P., Walsh,J.T. and Glucksberg,M.R. (2008) Progress toward an in vivo surface-enhanced Raman spectroscopy glucose sensor. *Diabetes Technol. Ther.*, **10**, 257–65.

94. Ng,B., Xiao,W., West,N.P., Wee,E.J.H., Wang,Y. and Trau,M. (2015) Rapid, Single-Cell Electrochemical Detection of Mycobacterium tuberculosis Using Colloidal Gold Nanoparticles. *Anal. Chem.*, **87**, 10613–10618.

95. He,J.L., Tian,Y.F., Cao,Z., Zou,W. and Sun,X. (2013) An electrochemical immunosensor based on gold nanoparticle tags for picomolar detection of c-Myc oncoprotein. *Sensors Actuators, B Chem.*, **181**, 835–841.

96. Conde,J., Dias,J.T., Grazú,V., Moros,M., Baptista,P. V and de la Fuente,J.M. (2014) Revisiting 30 years of biofunctionalization and surface chemistry of inorganic nanoparticles for nanomedicine. *Front. Chem.*, **2**, 48.

97. Thobhani,S., Attree,S., Boyd,R., Kumarswami,N., Noble,J., Szymanski,M. and Porter,R.A. (2010) Bioconjugation and characterisation of gold colloid-labelled proteins. *J. Immunol. Methods*, **356**, 60–69.

98. Conde,J., Ambrosone,A. and Sanz,V. (2012) Design of multifunctional gold nanoparticles for in vitro and in vivo gene silencing. *ACS Nano*.

99. DeLong,R.K., Reynolds,C.M., Malcolm,Y., Schaeffer,A., Severs,T. and Wanekaya,A. (2010) Functionalized gold nanoparticles for the binding, stabilization, and delivery of therapeutic DNA, RNA, and other biological macromolecules. *Nanotechnol. Sci. Appl.*, **3**, 53–63.

100. Kim,C.K., Ghosh,P., Pagliuca,C., Zhu,Z., Menichetti,S. and Rotello,V.M. (2010) Entrapment of

Hydrophobic Drugs in Nanoparticle Monolayers with Efficient Release into Cancer Cells. *J Am Chem Soc*, **131**, 1360–1361.

101. Maldiney,T., Cyrille,R., Seguin,J., Wattier,N., Bessodes,M. and Scherman,D. (2011) Effect of Core Diameter, Surface Coating, and PEG Chain Length on the Biodistribution of Persistent Luminescence Nanoparticles in Mice. *ACS Nano*, **5**, 854–862.
102. Manson,J., Kumar,D., Meenan,B.J. and Dixon,D. (2011) Polyethylene glycol functionalized gold nanoparticles: the influence of capping density on stability in various media. *Gold Bull.*, **44**, 99–105.
103. Pelaz,B., Del Pino,P., Maffre,P., Hartmann,R., Gallego,M., Rivera-Fernández,S., De La Fuente,J.M., Nienhaus,G.U. and Parak,W.J. (2015) Surface Functionalization of Nanoparticles with Polyethylene Glycol: Effects on Protein Adsorption and Cellular Uptake. *ACS Nano*, **9**, 6996–7008.
104. Stiufiuc,R., Iacovita,C., Nicoara,R., Stiufiuc,G., Florea,A., Achim,M. and Lucaciu,C.M. (2013) One-Step Synthesis of PEGylated Gold Nanoparticles with Tunable Surface Charge. **2013**.
105. Jokerst,J. V, Lobovkina,T., Zare,R.N. and Gambhir,S.S. (2011) Nanoparticle PEGylation for imaging and therapy. *Nanomedicine*, **6**, 715–728.
106. Yang,Q., Jones,S.W., Parker,C.L., Zamboni,W.C., Bear,J.E. and Lai,S.K. (2014) Evading immune cell uptake and clearance requires PEG grafting at densities substantially exceeding the minimum for brush conformation. *Mol. Pharm.*, **11**, 1250–1258.
107. Pelton,M., Aizpurua,J. and Bryant,G. (2008) Metal-nanoparticle plasmonics. *Laser Photonics Rev.*, **2**, 136–159.
108. Cordeiro,M., Ferreira Carlos,F., Pedrosa,P., Lopez,A. and Baptista,P. (2016) Gold Nanoparticles for Diagnostics: Advances towards Points of Care. *Diagnostics*, **6**, 43.
109. Herizchi,R., Abbasi,E., Milani,M. and Akbarzadeh,A. (2015) Current methods for synthesis of gold nanoparticles. *Artif. Cells, Nanomedicine, Biotechnol.*, 10.3109/21691401.2014.971807.
110. Link,S. and El-Sayed,M.A. (2003) Optical properties and ultrafast dynamics of metallic nanocrystals. *Annu. Rev. Phys. Chem.*, **54**, 331–366.
111. Ghosh,S.K., Nath,S., Kundu,S., Esumi,K. and Pal,T. (2004) Solvent and ligand effects on the localized surface plasmon resonance (LSPR) of gold colloids. *J. Phys. Chem. B*, **108**, 13963–13971.
112. Tournebize,J., Boudier,A., Sapin-Minet,A., Maincent,P., Leroy,P. and Schneider,R. (2012) Role of gold nanoparticles capping density on stability and surface reactivity to design drug delivery platforms. *ACS Appl. Mater. Interfaces*, **4**, 5790–5799.
113. Liu,C., Jia,Q., Yang,C., Qiao,R., Jing,L., Wang,L., Xu,C. and Gao,M. (2011) Lateral flow immunochromatographic assay for sensitive pesticide detection by using Fe 3O 4 nanoparticle aggregates as color reagents. *Anal. Chem.*, **83**, 6778–6784.
114. Drexhage,K.H. (1970) Influence of a dielectric interface on fluorescence decay time. *J. Lumin.*, **1**–**2**, 693–701.
115. Baptista,P., Conde,J. and Rosa,J. (2013) Gold-Nanobeacons as a theranostic system for the detection

and inhibition of specific genes. *Protoc. Exch.*, 10.1038/protex.2013.088.

116. Song,S., Liang,Z., Zhang,J., Wang,L., Li,G. and Fan,C. (2009) Gold-nanoparticle-based multicolor nanobeacons for sequence-specific DNA analysis. *Angew. Chemie*, **48**, 8670–8674.
117. Conde,J., Oliva,N. and Artzi,N. (2015) Implantable hydrogel embedded dark-gold nanoswitch as a theranostic probe to sense and overcome cancer multidrug resistance. *Proc. Natl. Acad. Sci. U. S. A.*, **112**, E1278-87.
118. Wang,W., Kong,T., Zhang,D., Zhang,J. and Cheng,G. (2015) Label-Free MicroRNA Detection Based on Fluorescence Quenching of Gold Nanoparticles with a Competitive Hybridization. *Anal. Chem.*, **87**, 10822–10829.
119. Yao,Y., Guo,W., Zhang,J., Wu,Y., Fu,W., Liu,T., Wu,X., Wang,H., Gong,X., Liang,X., *et al.* (2016) Reverse Fluorescence Enhancement and Colorimetric Bimodal Signal Readout Immunochromatography Test Strip for Ultrasensitive Large-Scale Screening and Postoperative Monitoring. *ACS Appl. Mater. Interfaces*, **8**, 22963–22970.
120. Dulkeith,E., Ringler,M., Klar,T.A., Feldmann,J., Javier,A.M. and Parak,W.J. (2005) Gold nanoparticles quench fluorescence by phase induced radiative rate suppression. *Nano Lett.*, **5**, 585–589.
121. Anger,P., Bharadwaj,P. and Novotny,L. (2006) Enhancement and Quenching of Single-Molecule Fluorescence. *Phys. Rev. Lett.*, **96**, 113002.
122. Kühn,S., H\aakanson,U., Rogobete,L. and Sandoghdar,V. (2006) Enhancement of Single-Molecule Fluorescence Using a Gold Nanoparticle as an Optical Nanoantenna. *Phys. Rev. Lett.*, **97**, 17402.
123. Kang,K. a, Wang,J., Jasinski,J.B. and Achilefu,S. (2011) Fluorescence manipulation by gold nanoparticles: from complete quenching to extensive enhancement. *J. Nanobiotechnology*, **9**, 16.
124. Dubertret,B., Calame,M. and Libchaber, a J. (2001) Single-mismatch detection using gold-quenched fluorescent oligonucleotides. *Nat. Biotechnol.*, **19**, 365–370.
125. Duan,C., Cui,H., Zhang,Z., Liu,B., Guo,J. and Wang,W. (2007) Size-dependent inhibition and enhancement by gold nanoparticles of luminol - Ferricyanide chemiluminescence. *J. Phys. Chem. C*, **111**, 4561–4566.
126. Vo-Dinh,T. (1998) Surface-enhanced Raman spectroscopy using metallic nanostructures. *TrAC - Trends Anal. Chem.*, **17**, 557–582.
127. Wang,J., Moore,J., Laulhe,S., Nantz,M., Achilefu,S. and Kang,K. a (2012) Fluorophore-gold nanoparticle complex for sensitive optical biosensing and imaging. *Nanotechnology*, **23**, 95501.
128. Yun,C.S., Javier,A., Jennings,T., Fisher,M., Hira,S., Peterson,S., Hopkins,B., Reich,N.O. and Strouse,G.F. (2005) Nanometal surface energy transfer in optical rulers, breaking the FRET barrier. *J. Am. Chem. Soc.*, **127**, 3115–3119.
129. Lakowicz,J.R. (2001) Radiative decay engineering: biophysical and biomedical applications. *Anal. Biochem.*, **298**, 1–24.

130. Huang,X., Jain,P.K., El-Sayed,I.H. and El-Sayed,M. a (2008) Plasmonic photothermal therapy (PPTT) using gold nanoparticles. *Lasers Med. Sci.*, **23**, 217–28.

131. Cabral,R.M. and Baptista,P. V (2013) THE CHEMISTRY AND BIOLOGY OF GOLD NANOPARTICLE-MEDIATED PHOTOTHERMAL THERAPY : PROMISES AND CHALLENGES. **3**, 1–18.

132. Liu,X. and Wong,D.K.Y. (2009) Picogram-detection of estradiol at an electrochemical immunosensor with a gold nanoparticle|Protein G-(LC-SPDP)-scaffold. *Talanta*, **77**, 1437–1443.

133. Zamborini,F.P., Leopold,M.C., Hicks,J.F., Kulesza,P.J., Malik,M.A., Murray,R.W., Hill,C. and Carolina,N. (2002) Electron Hopping Conductivity and Vapor Sensing Properties of Flexible Network Polymer Films of Metal Nanoparticles. *J. Am. Chem. Soc.*, **124**, 8958–8964.

134. Saha,K., Agasti,S.S., Kim,C., Li,X. and Rotello,V.M. (2012) Gold Nanoparticles in Chemical and Biological Sensing. *Chem. Rev.*, **112**, 2739–2779.

135. Li,Y., Schluesener,H.J. and Xu,S. (2010) Gold nanoparticle-based biosensors. *Gold Bull.*, **43**, 29–41.

136. Pingarrón,J., Yáñez-Sedeño,P. and González-Cortés (2008) Gold nanoparticle-based electrochemical biosensors. *Electrochim. Acta*, **53**, 5848–5866.

137. Rasheed,P.A. and Sandhyarani,N. (2017) Electrochemical DNA sensors based on the use of gold nanoparticles: a review on recent developments. *Microchim. Acta*, **184**, 981–1000.

138. Uludag,Y. and Köktürk,G. (2015) Determination of prostate-specific antigen in serum samples using gold nanoparticle based amplification and lab-on-a-chip based amperometric detection. *Microchim. Acta*, **182**, 1685–1691.

139. Maltez-Da Costa,M., De La Escosura-Muñiz,A., Nogués,C., Barrios,L., Ibáñez,E. and Merkoçi,A. (2012) Simple monitoring of cancer cells using nanoparticles. *Nano Lett.*, **12**, 4164–4171.

140. Syedmoradi,L., Daneshpour,M., Alvandipour,M., Gomez,F.A., Hajghassem,H. and Omidfar,K. (2017) Biosensors and Bioelectronics Point of care testing : The impact of nanotechnology. *Biosens. Bioelectron.*, **87**, 373–387.

141. Muehlethaler,C., Leona,M. and Lombardi,J.R. (2016) Review of Surface Enhanced Raman Scattering Applications in Forensic Science. *Anal. Chem.*, **88**, 152–169.

142. Alonso-González,P., Albella,P., Schnell,M., Chen,J., Huth,F., García-Etxarri,A., Casanova,F., Golmar,F., Arzubiaga,L., Hueso,L.E., *et al.* (2012) Resolving the electromagnetic mechanism of surface-enhanced light scattering at single hot spots. *Nat. Commun.*, **3**, 684.

143. Wetmur,J.G. (1991) DNA Probes : Applications of the Principles of Nucleic Acid Hybridization. *Crit. Rev. Biochem. Mol. Biol.*, **26**, 227–259.

144. Hu,L., Ru,K., Zhang,L., Huang,Y., Zhu,X., Liu,H., Zetterberg,A., Cheng,T. and Miao,W. (2014) Fluorescence in situ hybridization (FISH): an increasingly demanded tool for biomarker research and personalized medicine. *Biomark. Res.*, **2**, 3.

145. Garibyan,L. and Avashia,N. (2013) Research Techniques Made Simple: Polymerase Chain Reaction

(PCR). *J. Invest. Dermatol.*, **133**, 20382.

146. Notomi,T., Okayama,H., Masubuchi,H., Yonekawa,T., Watanabe,K., Amino,N. and Hase,T. (2000) Loop-mediated isothermal amplification of DNA. *Nucleic Acids Res.*, **28**, E63.
147. Dirks,R.M. and Pierce,N.A. (2004) Triggered amplification by hybridization chain reaction. *PNAS*, **101**, 15275–15278.
148. Trevino,V., Falciani,F. and Barrera-Saldaña,H.A. (2007) DNA Microarrays: a Powerful Genomic Tool for Biomedical and Clinical Research. *Mol. Med.*, **13**, 527–541.
149. Kaur,H., Arora,A., Wengel,J. and Maiti,S. (2006) Thermodynamic , Counterion , and Hydration Effects for the Incorporation of Locked Nucleic Acid Nucleotides into DNA Duplexes †.
150. Pande,V. and Nilsson,L. (2008) Insights into structure, dynamics and hydration of locked nucleic acid (LNA) strand-based duplexes from molecular dynamics simulations. *Nucleic Acids Res.*, **36**, 1508–1516.
151. Braasch,D.A. and Corey,D.R. (2001) Locked nucleic acid (LNA): fine-tuning the recognition of DNA and RNA. *Chem. Biol.*, **8**, 1–7.
152. Shakeel,S., Karim,S. and Ali,A. (2006) Peptide nucleic acid (PNA) – a review. *J. Chem. Technol. Biotechnol.*, **81**, 892–899.
153. Vester,B. and Wengel,J. (2004) LNA (Locked Nucleic Acid): High-Affinity Targeting of Complementary RNA and DNA&#x2020. *Biochemistry*, **43**, 13233–13241.
154. Thaxton,C.S., Georganopoulou,D.G. and Mirkin,C.A. (2006) Gold nanoparticle probes for the detection of nucleic acid targets. *Clin. Chim. Acta*, **363**, 120–126.
155. Vinhas,R., Correia,C., Ribeiro,P., Lourenço,A., Botelho de Sousa,A., Fernandes,A.R. and Baptista,P. V. (2016) Colorimetric assessment of BCR-ABL1 transcripts in clinical samples via gold nanoprobes. *Anal. Bioanal. Chem.*, **408**, 5277–5284.
156. Conde,J., de la Fuente,J.M. and Baptista,P. V (2010) RNA quantification using gold nanoprobes - application to cancer diagnostics. *J. Nanobiotechnology*, **8**.
157. Veigas,B., Pinto,J., Vinhas,R., Calmeiro,T., Martins,R., Fortunato,E. and Baptista,P.V. (2017) Quantitative real-time monitoring of RCA amplification of cancer biomarkers mediated by a flexible ion sensitive platform. *Biosens. Bioelectron.*, **91**, 788–795.
158. Keefe,A.D., Pai,S. and Ellington,A. (2010) Aptamers as therapeutics. *Nat. Rev. Drug Discov.*, **9**, 537–550.
159. Rozenblum,G.T., Lopez,V.G., Vitullo,A.D. and Radrizzani,M. (2016) Aptamers: current challenges and future prospects. *Expert Opin. Drug Discov.*, **11**, 127–135.
160. Hermann,T. and Patel,D.J. (2000) Adaptive recognition by nucleic acid aptamers. *Science*, **287**, 820–825.
161. Rajendran,M. and Ellington,A.D. (2008) Selection of fluorescent aptamer beacons that light up in the presence of zinc. *Anal. Bioanal. Chem.*, **390**, 1067–1075.

162. Lee,K., Ahn,J., Lee,S., Sekhon,S.S., Kim,D., Min,J. and Kim,Y. (2015) Aptamer-based Sandwich Assay and its Clinical Outlooks for Detecting Lipocalin-2 in Hepatocellular Carcinoma (HCC). *Nat. Publ. Gr.*, 10.1038/srep10897.

163. Xu,H., Mao,X., Zeng,Q., Wang,S., Kawde,A. and Liu,G. (2009) Aptamer-Functionalized Gold Nanoparticles as Probes in a Dry-Reagent Strip Biosensor for Protein Analysis. *Anal. Chem.*, **81**, 669–675.

164. Lavu,P.S.R., Mondal,B., Ramlal,S., Murali,H.S. and Batra,H.V. (2016) Selection and Characterization of Aptamers Using a Modified Whole Cell Bacterium SELEX for the Detection of Salmonella enterica Serovar Typhimurium. *ACS Comb. Sci.*, **18**, 292–301.

165. Biosensors,A., September,B. and Chen,A. (2016) Replacing antibodies with aptamers in lateral flow immunoassay. *Biosens. Bioelectron.*, **71**, 230–242.

166. Larguinho,M., Canto,R., Cordeiro,M., Pedrosa,P., Fortuna,A., Vinhas,R. and Baptista,P. V (2015) Gold nanoprobe-based non-crosslinking hybridization for molecular diagnostics. *Expert Rev. Mol. Diagn.*, **15**, 1355–1368.

167. Tighe,P.J., Ryder,R.R., Todd,I. and Fairclough,L.C. (2015) ELISA in the multiplex era: Potentials and pitfalls. *Proteomics - Clin. Appl.*, **9**, 406–422.

168. Chard,T. (1992) Pregnancy tests : a review. *Hum. Reprod.*, **7**, 701–710.

169. Zhu,D., Li,X., Liu,X., Wang,J. and Wang,Z. (2012) Designing bifunctionalized gold nanoparticle for colorimetric detection of Pb2+ under physiological condition. *Biosens. Bioelectron.*, **31**, 505–509.

170. Nanoparticles,G., Virginia,W. and States,U. (2011) Size-Dependent Energy Transfer between CdSe/ZnS Quantum Dots and Gold Nanoparticles. *J. Phys. Chem. Lett.*

171. Jennings,T.L., Schlatterer,J.C., Singh,M.P., Greenbaum,N.L. and Strouse,G.F. (2006) NSET molecular beacon analysis of hammerhead RNA substrate binding and catalysis. *Nano Lett.*, **6**, 1318–24.

172. Thompson,R.B. (2006) FLUORESCENCE SENSORS and BIOSENSORS.

173. Tyagi,S. and Kramer,R. (1996) Molecular Beacons: Probles that Fluoresce upon Hybridization. *Nature*, **14**, 303–306.

174. Crisalli,P. and Kool,E. (2011) Multiple Pathway Quenchers: Efficient Quenching of Common Fluorophores. *Bioconjug. Chem.*, **22**, 211–220.

175. Rosa,J., Conde,J., de la Fuente,J.M., Lima,J.C. and Baptista,P. V (2012) Gold-nanobeacons for real-time monitoring of RNA synthesis. *Biosens bioelectron*, **36**, 161–167.

176. Beni,V., Hayes,K., Lerga,T.M. and O'Sullivan,C.K. (2010) Development of a gold nano-particle-based fluorescent molecular beacon for detection of cystic fibrosis associated mutation. *Biosens. Bioelectron.*, **26**, 307–13.

177. Pan,W., Zhang,T., Yang,H., Diao,W., Li,N. and Tang,B. (2013) Multiplexed Detection and Imaging of Intracellular mRNAs Using a Four-Color Nanoprobe. *Anal. Chem.*, **85**, 10581–8.

178. Meyer,N. and Penn,L.Z. (2008) Reflecting on 25 years with MYC. *Nat. Rev. Cancer*, **8**, 976–90.
179. Aufderklamm,S., Todenhöfer,T., Gakis,G., Kruck,S., Hennenlotter,J., Stenzl,A. and Schwentner,C. (2012) Thymidine kinase and cancer monitoring. *Cancer Lett.*, **316**, 6–10.
180. Taniuchi,K., Cerny,R.L., Tanouchi, a, Kohno,K., Kotani,N., Honke,K., Saibara,T. and Hollingsworth,M. a (2011) Overexpression of GalNAc-transferase GalNAc-T3 promotes pancreatic cancer cell growth. *Oncogene*, **30**, 4843–54.
181. Nicholls,C., Pinto,A.R., Li,H., Li,L., Wang,L., Simpson,R. and Liu,J.-P. (2012) Glyceraldehyde-3-phosphate dehydrogenase (GAPDH) induces cancer cell senescence by interacting with telomerase RNA component. *Proc. Natl. Acad. Sci. U. S. A.*, **109**, 13308–13313.
182. Seferos,D.S., Giljohann,D. a, Hill,H.D., Prigodich,A.E. and Mirkin,C. a (2007) Nano-flares: probes for transfection and mRNA detection in living cells. *J. Am. Chem. Soc.*, **129**, 15477–9.
183. Conde,J., Rosa,J., de la Fuente,J.M. and Baptista,P. V. (2013) Gold-nanobeacons for simultaneous gene specific silencing and intracellular tracking of the silencing events. *Biomaterials*, **34**, 2516–2523.
184. Child,H.W., Hernandez,Y., Conde,J., Mullin,M., Baptista,P., de la Fuente,J.M. and Berry,C.C. (2015) Gold nanoparticle-siRNA mediated oncogene knockdown at RNA and protein level, with associated gene effects. *Nanomedicine*, **10**, 2513–2525.
185. Bao,C., Conde,J., Curtin,J., Artzi,N., Tian,F. and Cui,D. (2015) Bioresponsive antisense DNA gold nanobeacons as a hybrid in vivo theranostics platform for the inhibition of cancer cells and metastasis. *Sci. Rep.*, **5**, 12297.
186. Bunka,D.H.J. and Stockley,P.G. (2006) Aptamers come of age - at last. *Nat. Rev. Microbiol.*, **4**, 588–96.
187. Mairal,T., Ozalp,V.C., Lozano Sánchez,P., Mir,M., Katakis,I. and O'Sullivan,C.K. (2008) Aptamers: molecular tools for analytical applications. *Anal. Bioanal. Chem.*, **390**, 989–1007.
188. Zhang,J., Liu,B. and Liu,H. (2013) Aptamer-conjugated gold nanoparticles for bioanalysis. *Nanomedicine*, **8**, 983–993.
189. Chen,Y., O'Donoghue,M.B., Huang,Y.-F., Kang,H., Phillips,J. a, Chen,X., Estevez,M.-C., Yang,C.J. and Tan,W. (2010) A surface energy transfer nanoruler for measuring binding site distances on live cell surfaces. *J. Am. Chem. Soc.*, **132**, 16559–70.
190. Wang,W., Chen,C., Qian,M. and Zhao,X.S. (2008) Aptamer biosensor for protein detection using gold nanoparticles. *Anal. Biochem.*, **373**, 213–9.
191. Zhang,J., Wang,L., Zhang,H., Boey,F., Song,S. and Fan,C. (2010) Aptamer-based multicolor fluorescent gold nanoprobes for multiplex detection in homogeneous solution. *Small*, **6**, 201–4.
192. Kim,J.H., Han,S.H. and Chung,B.H. (2011) Improving Pb2+ detection using DNAzyme-based fluorescence sensors by pairing fluorescence donors with gold nanoparticles. *Biosens. Bioelectron.*, **26**, 2125–9.
193. Ray,P.C., Fortner,A. and Darbha,G.K. (2006) Gold nanoparticle based FRET assay for the detection

of DNA cleavage. *J. Phys. Chem. B*, **110**, 20745–8.

194. Park,S.Y., Lee,S.M., Kim,G.B. and Kim,Y.-P. (2012) Gold nanoparticle-based fluorescence quenching via metal coordination for assaying protease activity. *Gold Bull.*, **45**, 213–219.
195. Yang,P. (2011) An Indirect Immunoassay for Detecting Antigen Based on Fluorescence Resonance Energy Transfer. *Am. J. Anal. Chem.*, **2**, 484–490.
196. Mayilo,S., Kloster,M. a, Wunderlich,M., Lutich,A., Klar,T. a, Nichtl,A., Kürzinger,K., Stefani,F.D. and Feldmann,J. (2009) Long-range fluorescence quenching by gold nanoparticles in a sandwich immunoassay for cardiac troponin T. *Nano Lett.*, **9**, 4558–63.
197. Guirgis,B.S.S., Sá e Cunha,C., Gomes,I., Cavadas,M., Silva,I., Doria,G., Blatch,G.L., Baptista,P. V, Pereira,E., Azzazy,H.M.E., *et al.* (2012) Gold nanoparticle-based fluorescence immunoassay for malaria antigen detection. *Anal. Bioanal. Chem.*, **402**, 1019–27.
198. Siegel,R.L., Miller,K.D. and Jemal,A. (2016) Cancer statistics. *CA Cancer J Clin*, **66**, 7–30.
199. Jabbour,E. and Kantarjian,H. (2012) Chronic myeloid leukemia: 2012 update on diagnosis, monitoring, and management. *Am. J. Hematol.*, **87**, 1037–1045.
200. Rowley,J.D. (1973) Letter: A new consistent chromosomal abnormality in chronic myelogenous leukaemia identified by quinacrine fluorescence and Giemsa staining. *Nature*, **243**, 290–3.
201. Quintás-Cardama,A. and Cortes,J. (2009) Molecular biology of bcr-abl1-positive chronic myeloid leukemia. *Blood*, **113**, 1619–1630.
202. Chen,M., Gallipoli,P., Degeer,D., Sloma,I., Forrest,D.L., Chan,M., Lai,D., Jorgensen,H., Ringrose,A., Wang,H.M., *et al.* (2013) Targeting primitive chronic myeloid leukemia cells by effective inhibition of a new AHI-1-BCR-ABL-JAK2 complex. *J. Natl. Cancer Inst.*, **105**, 405–423.
203. Chen,Y., Peng,C., Li,D. and Li,S. (2010) Molecular and cellular bases of chronic myeloid leukemia. *Protein Cell*, **1**, 124–132.
204. Melo,J. V and Barnes,D.J. (2007) Chronic myeloid leukaemia as a model of disease evolution in human cancer. *Nat. Rev.*, **7**, 441–453.
205. Melo,J. V. (1996) The Diversity of BCR-ABL Fusion Proteins and Their Relationship to Leukemia Phenotype. *Blood*, **88**, 2375–2384.
206. Heisterkamp, Nora; Groffen,J. (2002) Philadelphia-positive leukemia: a personal perspective. *Nat. Publ. Gr.*, **21**, 8536.
207. Faderl,S., Talpaz,M., Estrov,Z., O'Brien,S., Kurzrock,R. and Kantarjian,H. (1999) The Biology of chronic Myeloid Leukemia. *New Engl. J. Med.*, 10.1056/NEJM199907153410306.
208. Weerkamp,F., Dekking,E., Ng,Y.Y., van der Velden,V.H.J., Wai,H., Böttcher,S., Brüggemann,M., van der Sluijs, a J., Koning,A., Boeckx,N., *et al.* (2009) Flow cytometric immunobead assay for the detection of BCR-ABL fusion proteins in leukemia patients. *Leukemia*, **23**, 1106–1117.
209. Torres,F., Ivanova-Dragoeva,A., Pereira,M., Veiga,J., Rodrigues,A.S., Sousa,A.B., Tavares,P. and Fernandes,A.R. (2007) An e6a2 BCR-ABL fusion transcript in a CML patient having an iliac

chloroma at initial presentation. *Leuk. Lymphoma*, **48**, 1034–7.

210. Balatzenko,G., Vundinti,B.R. and Margarita,G. (2011) Correlation between the type of bcr-abl transcripts and blood cell counts in chronic myeloid leukemia – a possible influence of mdr1 gene expression. *Hematol. Reports (formerly Hematol. Rev.)*, **3**, 4–8.

211. van Dongen,J.J., Macintyre,E. a, Gabert,J. a, Delabesse,E., Rossi,V., Saglio,G., Gottardi,E., Rambaldi, a, Dotti,G., Griesinger,F., *et al.* (1999) Standardized RT-PCR analysis of fusion gene transcripts from chromosome aberrations in acute leukemia for detection of minimal residual disease. Report of the BIOMED-1 Concerted Action: investigation of minimal residual disease in acute leukemia. *Leukemia*, **13**, 1901–28.

212. Baccarani,M. and Castagnetti,F. (2015) A review of the European LeukemiaNet recommendations for the management of CML. - PubMed - NCBI. *Ann. Hematol.*, **94**, 141–147.

213. Press,R.D., Kamel-Reid,S. and Ang,D. (2013) BCR-ABL1 RT-qPCR for monitoring the molecular response to tyrosine kinase inhibitors in chronic myeloid leukemia. *J. Mol. Diagnostics*, **15**, 565–576.

214. Altschul,S.F., Gish,W., Miller,W., Myers,E.W. and Lipman,D.J. (1990) Basic local alignment search tool. *J. Mol. Biol.*, **215**, 403–10.

215. Zadeh,J.N., Steenberg,C.D., Bois,J.S., Wolfe,B.R., Pierce,M.B., Khan,A.R., Dirks,R.M. and Pierce,N.A. (2010) NUPACK: Analysis and Design of Nucleic Acid Systems. *J. Comput. Chem.*, **31**, 2967–2970.

216. Schindelin,J., Arganda-Carreras,I., Frise,E., Kaynig,V., Longair,M., Pietzsch,T., Preibisch,S., Rueden,C., Saalfeld,S., Schmid,B., *et al.* (2012) Fiji: An open source platform for biological image analysis. *Nat. Methods*, **9**, 676–682.

217. Incardona,M.F., Bourenkov,G.P., Levik,K., Pieritz,R.A., Popov,A.N. and Svensson,O. (2009) EDNA: A framework for plugin-based applications applied to X-ray experiment online data analysis. *J. Synchrotron Radiat.*, **16**, 872–879.

218. Franke,D., Kikhney,A.G. and Svergun,D.I. (2012) Automated acquisition and analysis of small angle X-ray scattering data. *Nucl. Instruments Methods Phys. Res. Sect. A Accel. Spectrometers, Detect. Assoc. Equip.*, **689**, 52–59.

219. Franke,D., Petoukhov,M. V., Konarev,P. V., Panjkovich,A., Tuukkanen,A., Mertens,H.D.T., Kikhney,A.G., Hajizadeh,N.R., Franklin,J.M., Jeffries,C.M., *et al.* (2017) *ATSAS 2.8*: a comprehensive data analysis suite for small-angle scattering from macromolecular solutions. *J. Appl. Crystallogr.*, **50**, 1151–1158.

220. Konarev,P. V., Volkov,V. V., Sokolova,A. V., Koch,M.H.J. and Svergun,D.I. (2003) *PRIMUS*: a Windows PC-based system for small-angle scattering data analysis. *J. Appl. Crystallogr.*, **36**, 1277–1282.

221. Svergun,D.I. and IUCr (1992) Determination of the regularization parameter in indirect-transform methods using perceptual criteria. *J. Appl. Crystallogr.*, **25**, 495–503.

222. Franke,D. and Svergun,D.I. (2009) DAMMIF, a program for rapid ab-initio shape determination in small-angle scattering. *J. Appl. Crystallogr.*, **42**, 342–346.

223. Volkov,V. V. and Svergun,D.I. (2003) Uniqueness of ab initio shape determination in small-angle scattering. In *Journal of Applied Crystallography*.Vol. 36, pp. 860–864.

224. Kozin,M.B. and Svergun,D.I. (2001) Automated matching of high- and low-resolution structural models research papers Automated matching of high- and low-resolution structural models. *J. Appl. Crystallogr.*, **34**, 33–41.

225. Conde,J., Doria,G., Fuente,J.M. De and Baptista,P.V. (2012) RNA Quantification Using Noble Metal Nanoprobes: Simultaneous Identification of Several Different mRNA Targets Using Color Multiplexing and Application to Cancer Diagnostics Soloviev,M. (ed) Humana Press, Totowa, NJ.

226. Roma-Rodrigues,C., Pereira,F., Alves de Matos,A.P., Fernandes,M., Baptista,P. V. and Fernandes,A.R. (2017) Smuggling gold nanoparticles across cell types – A new role for exosomes in gene silencing. *Nanomedicine Nanotechnology, Biol. Med.*, **13**, 1389–1398.

227. Doane,T.L., Chuang,C.H., Hill,R.J. and Burda,C. (2012) Nanoparticle ζ-Potentials. *Acc. Chem. Res.*, **45**, 317–326.

228. Koeffler,P. and Golde,D.W. (1980) Human Myeloid Leukemia Cell Lines: A Review. *Blood*, **56**, 344–350.

229. Pegoraro,L., Matera,L., Levis,J., Palumbo,A. and Biagini,G. (1983) Establishment of a Ph1-positive human cell line (BV173). *J Natl Cancer Inst.*, **70**, 443–453.

230. Chanput,W., Mes,J.J. and Wichers,H.J. (2014) THP-1 cell line: An in vitro cell model for immune modulation approach. *Int. Immunopharmacol.*, **23**, 37–45.

231. Wang,K., Tang,Z., Yang,C.J., Kim,Y., Fang,X., Li,W., Wu,Y., Medley,C.D., Cao,Z., Li,J., *et al.* (2009) Molecular engineering of DNA: Molecular beacons. *Angew. Chemie - Int. Ed.*, **48**, 856–870.

232. Pickup,J.C., Hussain,F., Evans,N.D., Rolinski,O.J. and Birch,D.J.S. (2005) Fluorescence-based glucose sensors. *Biosens. Bioelectron.*, **20**, 2555–65.

233. Zheng,J., Yang,R., Shi,M., Wu,C., Fang,X., Li,Y., Li,J. and Tan,W. (2015) Rationally designed molecular beacons for bioanalytical and biomedical applications. *Chem. Soc. Rev.*, **44**, 3036–55.

234. Kawczyk-,A. (2013) The role of fluorescence diagnosis in clinical practice.

235. Yang,L.-H., Ahn,D.J. and Koo,E. (2016) Ultrasensitive FRET-based DNA sensor using PNA/DNA hybridization. *Mater. Sci. Eng. C*, **69**, 625–630.

236. Zhang,C. and Hu,J. (2010) Single quantum dot-based nanosensor for multiple DNA detection. *Anal. Chem.*, **82**, 1921–7.

237. Cordeiro,M., Giestas,L., Lima,J. and Baptista,P. (2016) BioCode gold-nanobeacon for the detection of fusion transcripts causing chronic myeloid leukemia. *J. Nanobiotechnology*, **14**, 38.

238. Koch,W.H. (2004) Technology platforms for pharmacogenomic diagnostic assays. *Nat. Rev. Drug Discov.*, **3**, 749–761.

239. Tyagi,S. and Kramer,F.R. (1996) Molecular Beacons: Probes that Fluoresce upon Hybridization. *Nat. Biotechnol.*, **14**, 303–308.

240. Singh,J., Kaur,H., Kaushik,A. and Peer,S. (2011) A review of antisense therapeutic interventions for molecular biological targets in various diseases. *Int. J. Pharmacol.*, **7**, 294–315.

241. Navarro,E., Serrano-Heras,G., Castaño,M.J. and Solera,J. (2015) Real-time PCR detection chemistry. *Clin. Chim. Acta*, **439**, 231–250.

242. Thelwell,N., Millington,S., Solinas,A., Booth,J. and Brown,T. (2000) Mode of action and application of Scorpion primers to mutation detection. *Nucleic Acids Res.*, **28**, 3752–3761.

243. Nazarenko,I.A., Bhatnagar,S.K. and Hohman,R.J. (1997) A closed tube format for amplification and detection of DNA based on energy transfer. *Nucleic Acids Res.*, **25**, 2516–2521.

244. Du,H., Fuh,R.-C.A., Li,J., Corkan,L.A. and Lindsey,J.S. (1998) PhotochemCAD: A computer-aided design and research tool in photochemistry. *Photochem. Photobiol.*, **68**, 141–142.

245. Loura,L.M.S. (2012) Simple estimation of förster resonance energy transfer (FRET) orientation factor distribution in membranes. *Int. J. Mol. Sci.*, **13**, 15252–15270.

246. Rosa,J., Lima,J.C. and Baptista,P. V (2011) Experimental photophysical characterization of fluorophores in the vicinity of gold nanoparticles. *Nanotechnology*, **22**, 415202.

247. Mujumdar,R.B., Ernst,L. a, Mujumdar,S.R., Lewis,C.J. and Waggoner,A.S. (1993) Cyanine dye labeling reagents: sulfoindocyanine succinimidyl esters. *Bioconjug. Chem.*, **4**, 105–11.

248. Blanco-Canosa,J.B., Medintz,I.L., Farrel,D., Mattoussi,H. and Dawson,P.E. (2010) Rapid covalent ligation of fluorescent peptides to water solubilized quantum dots. *J. Am. Chem. Soc.*, **132**, 10027–10033.

249. Tinland,B., Pluen,A., Sturm,J. and Weill,G. (1997) Persistence Length of Single-Stranded DNA. *Macromolecules*, **30**, 5763–5765.

250. Tsourkas,A., Behlke,M.A., Rose,S.D. and Bao,G. (2003) Hybridization kinetics and thermodynamics of molecular beacons. *Nucleic Acids Res.*, **31**, 1319–1330.

251. Chen,C., Wang,W., Ge,J. and Zhao,X.S. (2009) Kinetics and thermodynamics of DNA hybridization on gold nanoparticles. *Nucleic Acids Res.*, **37**, 3756–3765.

252. Li,H. and Rothberg,L. (2004) Colorimetric detection of DNA sequences based on electrostatic interactions with unmodified gold nanoparticles. *PNAs*, **101**, 14036–14039.

253. SantaLucia,J. (1998) A unified view of polymer, dumbbell, and oligonucleotide DNA nearest-neighbor thermodynamics. *P Natl Acad Sci USA*, **95**, 1460–1465.

254. Dirks,R.M., Bois,J.S., Schaeffer,J.M., Winfree,E. and Pierce,N. a. (2007) Thermodynamic Analysis of Interacting Nucleic Acid Strands. *SIAM Rev.*, **49**, 65–88.

255. Yin,Y. and Zhao,X.S. (2011) Kinetics and dynamics of DNA hybridization. *Acc. Chem. Res.*, **44**, 1172–1181.

256. Bonnet,G., Tyagi,S., Libchaber, a and Kramer,F.R. (1999) Thermodynamic basis of the enhanced

specificity of structured DNA probes. *Proc. Natl. Acad. Sci. U. S. A.*, **96**, 6171–6.

257. Goel,G., Kumar,A., Puniya,A.K., Chen,W. and Singh,K. (2005) Molecular beacon: A multitask probe. *J. Appl. Microbiol.*, **99**, 435–442.
258. Muro,M.A. de (2005) Probe Design, Production, and Applications. In Walker,J.M., Rapley,R. (eds), *Medical Biomethods Handbook*. Humana Press, Totowa, NJ, pp. 13–23.
259. Khan,M., Khan,A.R., Shin,J.-H. and Park,S.-Y. (2016) A liquid-crystal-based DNA biosensor for pathogen detection. *Sci. Rep.*, **6**, 22676.
260. Berg,J., Tymoczko,J. and Stryer,L. (2002) Biochemistry 5th ed. W H Freeman, New York.
261. Yakovchuk,P., Protozanova,E. and Frank-Kamenetskii,M.D. (2006) Base-stacking and base-pairing contributions into thermal stability of the DNA double helix. *Nucleic Acids Res.*, **34**, 564–574.
262. Mergny,J.-L. and Lacroix,L. (2003) Analysis of Thermal Melting Curves. *Oligonucleotides*, **13**, 515–537.
263. Manning,G.S. (1978) The molecular theory of polyelectrolyte solutions with applications to the electrostatic properties of polynucleotides. *Q. Rev. Biophys.*, **11**, 179.
264. Cordeiro,M., Giestas,L., Lima,J.C. and Baptista,P.M. V. (2016) BioCode Gold-Nanobeacon for the detection of fusion transcripts causing chronic myeloid leukemia. *J. Nanobiotechnology*, **14**, 38.
265. Freyer,M.W. and Lewis,E.A. (2008) Isothermal Titration Calorimetry: Experimental Design, Data Analysis, and Probing Macromolecule/Ligand Binding and Kinetic Interactions. *Methods Cell Biol.*, **84**, 79–113.
266. Jelesarov,I. and Bosshard,H.R. (1999) Isothermal titration calorimetry and differential scanning calorimetry as complementary tools to invesitigate the energetics of biomolecular recognition. *J. Mol. Recognit.*, **12**, 3–18.
267. Garbett,N.C. (2011) The Use of Calorimetry to Study Ligand–DNA Interactions. In Janice Aldrich-Wright (ed), *Metallointercalators*. Springer, Vienna, pp. 299–324.
268. Herrera,I. and Winnik,M.A. (2013) Differential binding models for isothermal titration calorimetry: Moving beyond the Wiseman isotherm. *J. Phys. Chem. B*, **117**, 8659–8672.
269. Schwarz,F.P., Robinson,S. and Butler,J.M. (1999) Thermodynamic comparison of PNA/DNA and DNA/DNA hybridization reactions at ambient temperature. *Nucleic Acids Res.*, **27**, 4792–4800.
270. Lang,B. (2010) Hybridization thermodynamics of DNA bound to gold nanoparticles. *J. Chem. Thermodyn.*, **42**, 1435–1440.
271. Kool,E.T. (2001) Hydrogen bonding, base stacking, and steric effects in DNA replication. *Annu. Rev. Biophys. Biomol. Struct*, **30**, 1–22.
272. Turnbull,W.B. and Daranas,A.H. (2003) On the Value of c: Can Low Affinity Systems Be Studied by Isothermal Titration Calorimetry? *J. Am. Chem. Soc.*, **125**, 14859–14866.
273. Zhang,Y.L. and Zhang,Z.Y. (1998) Low-affinity binding determined by titration calorimetry using a high-affinity coupling ligand: a thermodynamic study of ligand binding to protein tyrosine

phosphatase 1B. *Anal. Biochem.*, **261**, 139–148.

274. Jerabek-Willemsen,M., Wienken,C.J., Braun,D., Baaske,P. and Duhr,S. (2011) Molecular Interaction Studies Using Microscale Thermophoresis. *Assay Drug Dev Technol*, **9**, 342–353.
275. Jerabek-Willemsen,M., Andr??,T., Wanner,R., Roth,H.M., Duhr,S., Baaske,P. and Breitsprecher,D. (2014) MicroScale Thermophoresis: Interaction analysis and beyond. *J. Mol. Struct.*, **1077**, 101–113.
276. Duhr,S. and Braun,D. (2006) Why molecules move along a temperature gradient. *Proc. Natl. Acad. Sci. U. S. A.*, **103**, 19678–82.
277. Entzian,C. and Schubert,T. (2017) Mapping the binding site of an aptamer on ATP using microscale thermophoresis. *J. Vis. Exp.*, 10.3791/55070.
278. Braun,D. and Libchaber,A. (2002) Trapping of DNA by thermophoretic depletion and convection. *Phys. Rev. Lett.*, **89**, 188103.
279. Maeda,Y.T., Tlusty,T. and Libchaber, a. (2012) Effects of long DNA folding and small RNA stem-loop in thermophoresis. *Proc. Natl. Acad. Sci.*, **109**, 17972–17977.
280. Yu,L.H. and Chen,Y.F. (2015) Concentration-dependent thermophoretic accumulation for the detection of DNA using DNA-functionalized nanoparticles. *Anal. Chem.*, **87**, 2845–2851.
281. Nakano,M., Tateishi-Karimata,H., Tanaka,S., Tama,F., Miyashita,O., Nakano,S. ichi and Sugimoto,N. (2016) Local thermodynamics of the water molecules around single- and double-stranded DNA studied by grid inhomogeneous solvation theory. *Chem. Phys. Lett.*, **660**, 250–255.
282. Bruetzel,L.K., Gerling,T., Sedlak,S.M., Walker,P., Zheng,W., Dietz,H. and Lipfert,J. (2016) Conformational Changes and Flexibility of DNA Devices Observed by Small-Angle X-Ray Scattering Conformational Changes and Flexibility of DNA Devices Observed by Small-Angle X-Ray Scattering. 10.1021/acs.nanolett.6b01338.
283. Salmon,L., Yang,S. and Al-Hashimi,H.M. (2014) Advances in the Determination of Nucleic Acid Conformational Ensembles. *Annu. Rev. Phys. Chem. Vol 65*, **65**, 293–316.
284. Chi,Q., Wang,G. and Jiang,J. (2013) The persistence length and length per base of single-stranded DNA obtained from fluorescence correlation spectroscopy measurements using mean field theory. *Phys. A Stat. Mech. its Appl.*, **392**, 1072–1079.
285. Markegard,C.B., Gallivan,C.P., Cheng,D.D. and Nguyen,H.D. (2016) Effects of Concentration and Temperature on DNA Hybridization by Two Closely Related Sequences via Large-Scale Coarse-Grained Simulations. *J. Phys. Chem. B*, **120**, 7795–7806.
286. Conde,J., Larguinho,M., Cordeiro,A., Raposo,L.R., Costa,P.M., Santos,S., Diniz,M.S., Fernandes,A.R. and Baptista,P. V (2014) Gold-nanobeacons for gene therapy: evaluation of genotoxicity, cell toxicity and proteome profiling analysis. *Nanotoxicology*, **8**, 521–532.
287. Haiss,W., Thanh,N.T.K., Aveyard,J. and Fernig,D.G. (2007) Determination of size and concentration of gold nanoparticles from UV-Vis spectra. *Anal. Chem.*, **79**, 4215–4221.
288. Lotsch,H.K. V (2007) Surface Plasmon Nanophotonics Brongersma,M.L., Kik,P.G. (eds) Springer,

Dordrecht.

289. Jans,H., Liu,X., Austin,L., Maes,G. and Huo,Q. (2009) Dynamic light scattering as a powerful tool for gold nanoparticle bioconjugation and biomolecular binding studies. *Anal. Chem.*, **81**, 9425–9432.
290. Xu,R. (2014) Light scattering: A review of particle characterization applications. *Particuology*, **18**, 11–21.
291. Bhattacharjee,S., Elimelech,M. and Borkovec,M. (1998) DLVO Interaction between Colloidal Particles: Beyond Derjaguin's Approximation. *Croat. Chem. Acta*, **71**, 883–903.
292. Derjaguin,B. V. (1992) Some results from 50 years' research on surface forces. *Prog. Surf. Sci.*, **40**, 240–251.
293. Hunter,R.J. (1988) Colloid Science 3rd ed. Ottewill,R.H., Rowell,R.L. (eds) Academic Press, London.
294. Tantra,R., Schulze,P. and Quincey,P. (2010) Effect of nanoparticle concentration on zeta-potential measurement results and reproducibility. *Particuology*, **8**, 279–285.
295. Zhang,X., Huang,P.J.J., Servos,M.R. and Liu,J. (2012) Effects of polyethylene glycol on DNA adsorption and hybridization on gold nanoparticles and graphene oxide. *Langmuir*, **28**, 14330–14337.
296. Liu,Y., Shipton,M.K., Ryan,J., Kaufman,E.D., Franzen,S. and Feldheim,D.L. (2007) Synthesis, stability, and cellular internalization of gold nanoparticles containing mixed peptide-poly(ethylene glycol) monolayers. *Anal. Chem.*, **79**, 2221–2229.
297. Pilar,F.L. (1960) Bond-Order/ Bond-Length and Bond-Energy/Bond-Length Relations for Carbon-Oxygen Bonds. *J. Mol. Spectrosc.*, **5**, 72–77.
298. Downard,K.M., Sheldon,J.C., Bowie,J.H., Lewis,D.E. and Hayes,R.N. (1989) Are the elusive ions mercaptomethyl(-CH2SH), hydroxymethyl(-CH2OH), and aminomethyl(-CH2NH2) detectable in the gas phase? A joint ab initio/experimental approach. *J. Am. Chem. Soc.*, **111**, 8112–8115.
299. Energies,C.B., Distances,B., George,B.Y. and Carolina,N. (1958) Carbon-oxygen bond energies and bond distances' . **313**.
300. Takashima,A. and Oishi,M. (2015) Kinetic study of DNA hybridization on DNA-modified gold nanoparticles with engineered nano-interfaces. *RSC Adv.*, **5**, 76014–76018.
301. Ravan,H., Kashanian,S., Sanadgol,N., Badoei-Dalfard,A. and Karami,Z. (2014) Strategies for optimizing DNA hybridization on surfaces. *Anal. Biochem.*, **444**, 41–46.
302. Svergun,D.I. (1999) Restoring low resolution structure of biological macromolecules from solution scattering using simulated annealing. *Biophys. J.*, **76**, 2879–2886.
303. Griffin,J., Singh,A.K., Senapati,D., Rhodes,P., Mitchell,K., Robinson,B., Yu,E. and Ray,P.C. (2009) Size- and distance-dependent nanoparticle surface-energy transfer (NSET) method for selective sensing of hepatitis C virus RNA. *Chemistry*, **15**, 342–51.
304. Patel,H., Marley,S.B., Greener,L. and Gordon,M.Y. (2008) Subcellular distribution of p210BCR-ABL in CML cell lines and primary CD34+ CML cells. *Leukemia*, **22**, 559–571.
305. Vinhas,R., Fernandes,A.R. and Baptista,P. V. (2017) Gold Nanoparticles for BCR-ABL1 Gene

Silencing: Improving Tyrosine Kinase Inhibitor Efficacy in Chronic Myeloid Leukemia. *Mol. Ther. - Nucleic Acids*, **7**, 408–416.

306. De Carvalho,D.D., Binato,R., Pereira,W.O., Leroy,J.M.G., Colassanti,M.D., Proto-Siqueira,R., Bueno-Da-Silva,A.E.B., Zago,M.A., Zanichelli,M.A., Abdelhay,E., *et al.* (2011) BCR–ABL-mediated upregulation of PRAME is responsible for knocking down TRAIL in CML patients. *Oncogene*, **30**, 223–233.
307. Stephenson,M.L. and Zamecnik,P.C. (1978) Inhibition of Rous sarcoma viral RNA translation by a specific oligodeoxyribonucleotide. *Proc. Natl. Acad. Sci. U. S. A.*, **75**, 285–288.
308. Hill,A.J., Teraoka,H., Heideman,W. and Peterson,R.E. (2005) Zebrafish as a model vertebrate for investigating chemical toxicity. *Toxicol. Sci.*, **86**, 6–19.
309. McGrath,P. and Li,C.Q. (2008) Zebrafish: a predictive model for assessing drug-induced toxicity. *Drug Discov. Today*, **13**, 394–401.
310. Lieschke,G.J. and Currie,P.D. (2007) Animal models of human disease: zebrafish swim into view. *Nat. Rev. Genet.*, **8**, 353–367.
311. Lin,S., Zhao,Y., Nel,A.E. and Lin,S. (2013) Zebrafish: an in vivo model for nano EHS studies. *Small*, **9**, 1608–18.
312. Lin,S., Zhao,Y., Xia,T., Meng,H., Ji,Z., Liu,R., George,S., Xiong,S., Wang,X., Zhang,H., *et al.* (2011) High Content Screening in Zebrafish Speeds up Hazard Ranking of Transition Metal Oxide Nanoparticles. *ACS Nano*, **5**, 7284–7295.
313. Teraoka,H., Dong,W. and Hiraga,T. (2003) Zebrafish as a novel experimental model for developmental toxicology. *Congenit. Anom. (Kyoto).*, **43**, 123–32.
314. Spitsbergen,J. and Kent,M. (2003) The State of the Art of the Zebrafish Model for Toxicology and Toxicologic Pathology Research - Advantages and Current Limitations. *Toxicol. Pathol.*, **31**, 62–87.
315. Howe,K., Clark,M.D., Torroja,C.F., Torrance,J., Berthelot,C., Muffato,M., Collins,J.E., Humphray,S., McLaren,K., Matthews,L., *et al.* (2013) The zebrafish reference genome sequence and its relationship to the human genome. *Nature*, **496**, 498–503.
316. Lawson,N.D. and Weinstein,B.M. (2002) In Vivo Imaging of Embryonic Vascular Development Using Transgenic Zebrafish. *Dev. Biol.*, **248**, 307–318.
317. Turkevich,J., Garton,P.C. and Stevenson,G. (1954) The color of colloidal gold. *J. Colloid Sci.*, **9**, 26–35.
318. Westerfield,M. (1995) The Zebrafish Book: A Guide for the Laboratory Use of Zebrafish (Danio rerio) 3rd Editio. University of Oregon Press, Eugene.
319. Swift,S.R. (1989) Basic principles of FRAP , FLIM and FRET.
320. Browning,L.M., Lee,K.J., Huang,T., Nallathamby,P.D., Lowman,J.E. and Xu,X.N. (2010) Random Walk of Single Gold Nanoparticles in Zebrafish Embryos Leading to Stochastic Toxic Effects on Embryonic Developments. *October*, **1**, 138–152.

321. Bar-Ilan,O., Albrecht,R.M., Fako,V.E. and Furgeson,D.Y. (2009) Toxicity assessments of multisized gold and silver nanoparticles in zebrafish embryos. *Small*, **5**, 1897–1910.

8 Appendix

8.1 Appendix I

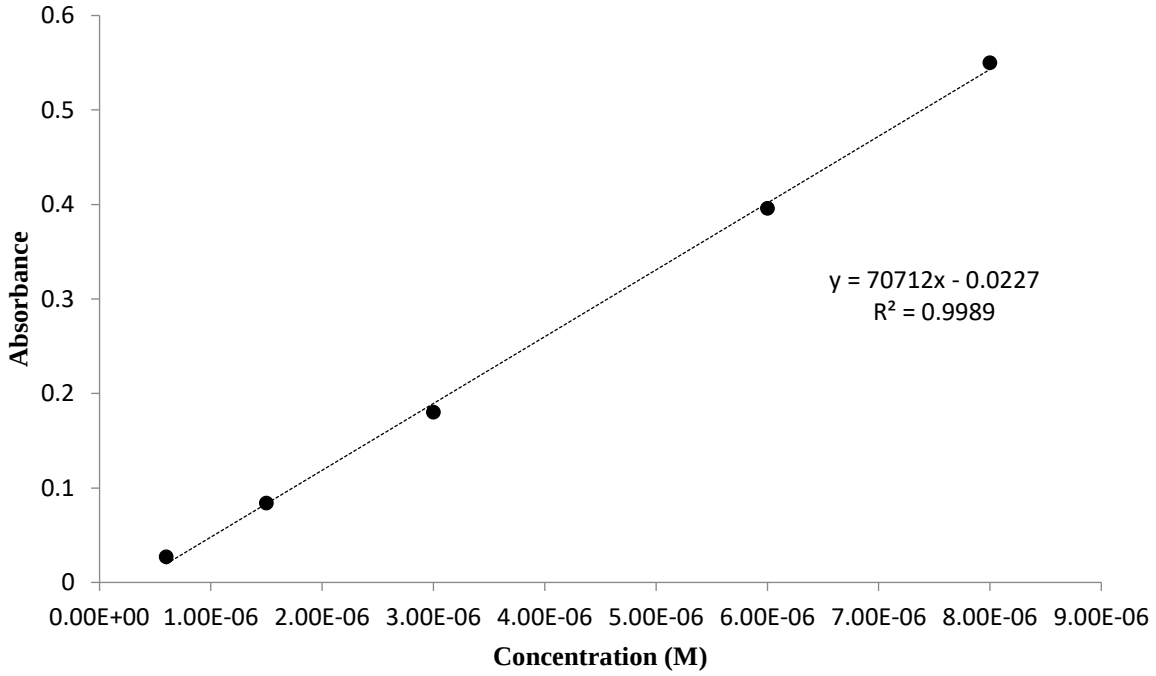

Figure I.1. Extinction coefficient determination of ROX fluorophore bound to revelator sequence.

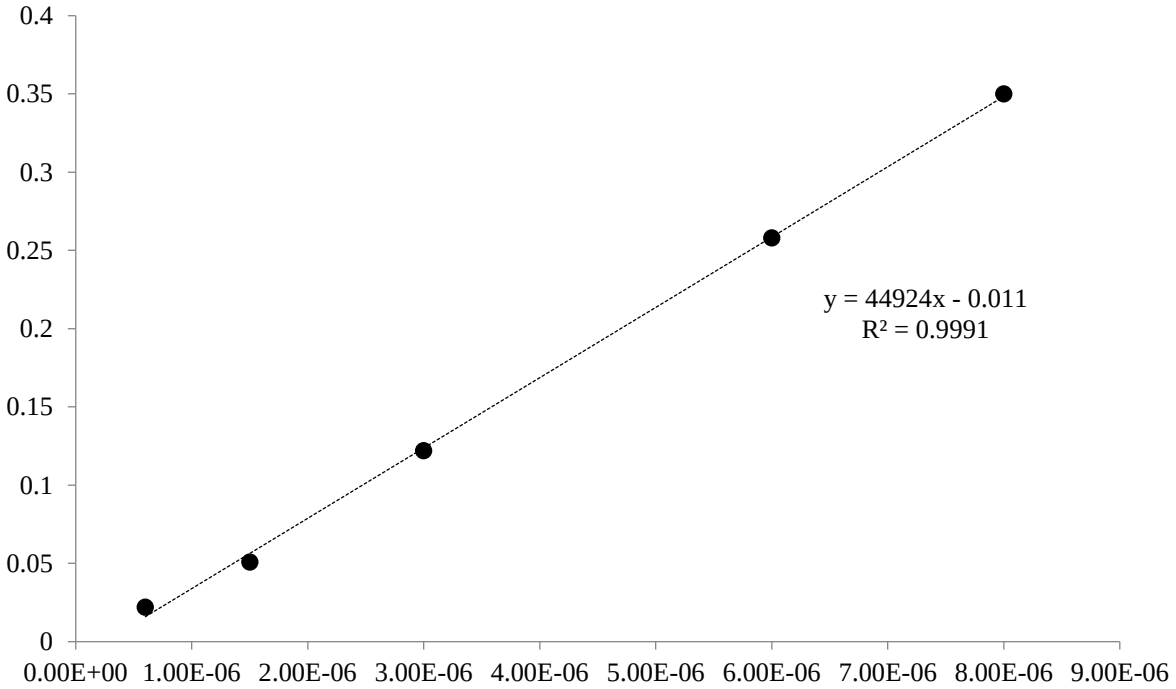

Figure I.2. Extinction coefficient determination of Dy – 520 Xl MegaStockes fluorophore bound to revelator sequence.

8.2 Appendix II

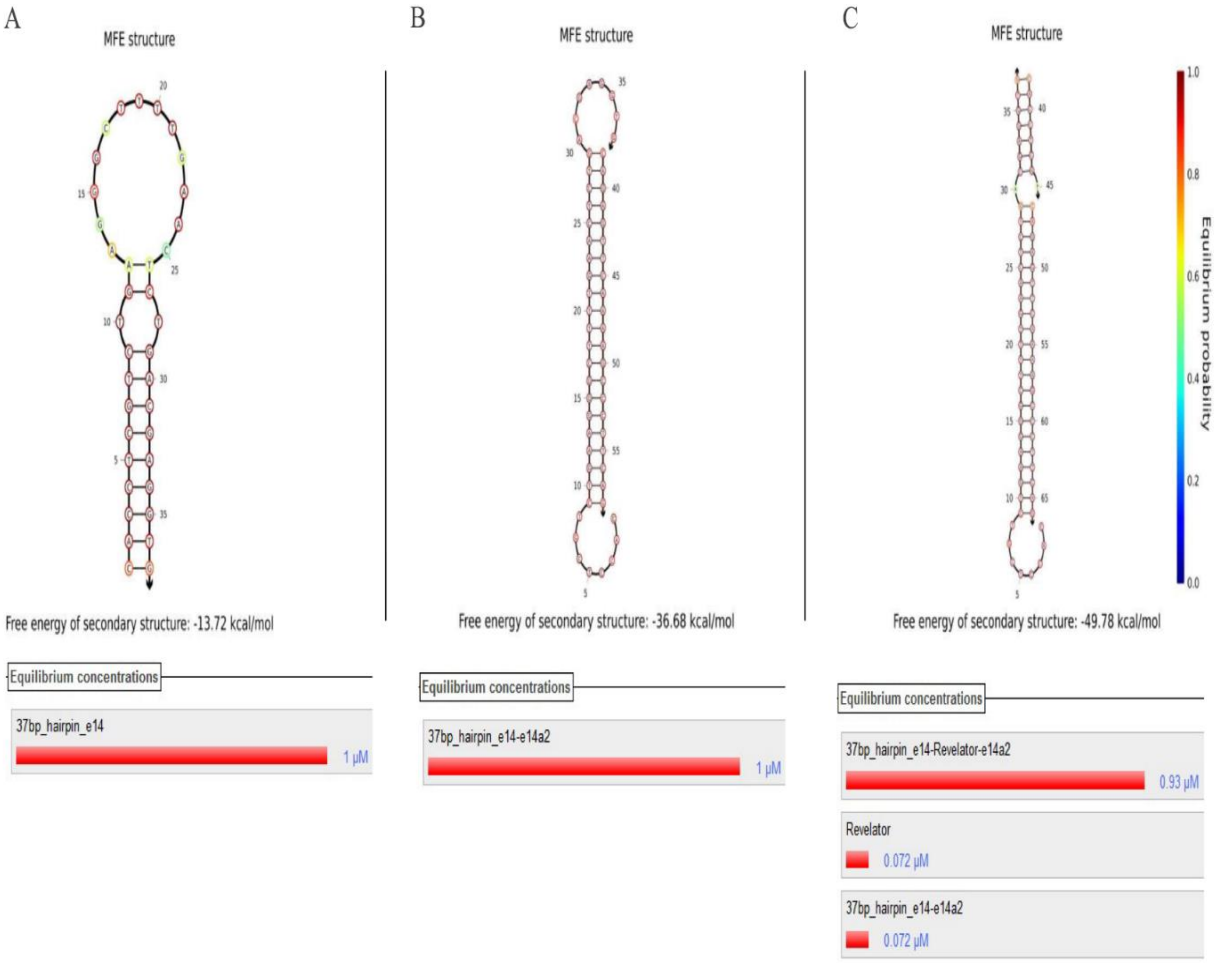

Figure II.1. *In silico* assessment of hybridization of the designed sequences of pair 1 using the software NUPACK. A) 37bp_Hairpin_e14 in absence of target and equilibrium concentration; B) 37bp_Hairpin_e14 in the presence of complementary target and equilibrium concentration; C) 37bp_Hairpin_e14 in presence of complementary target and respective revelator.

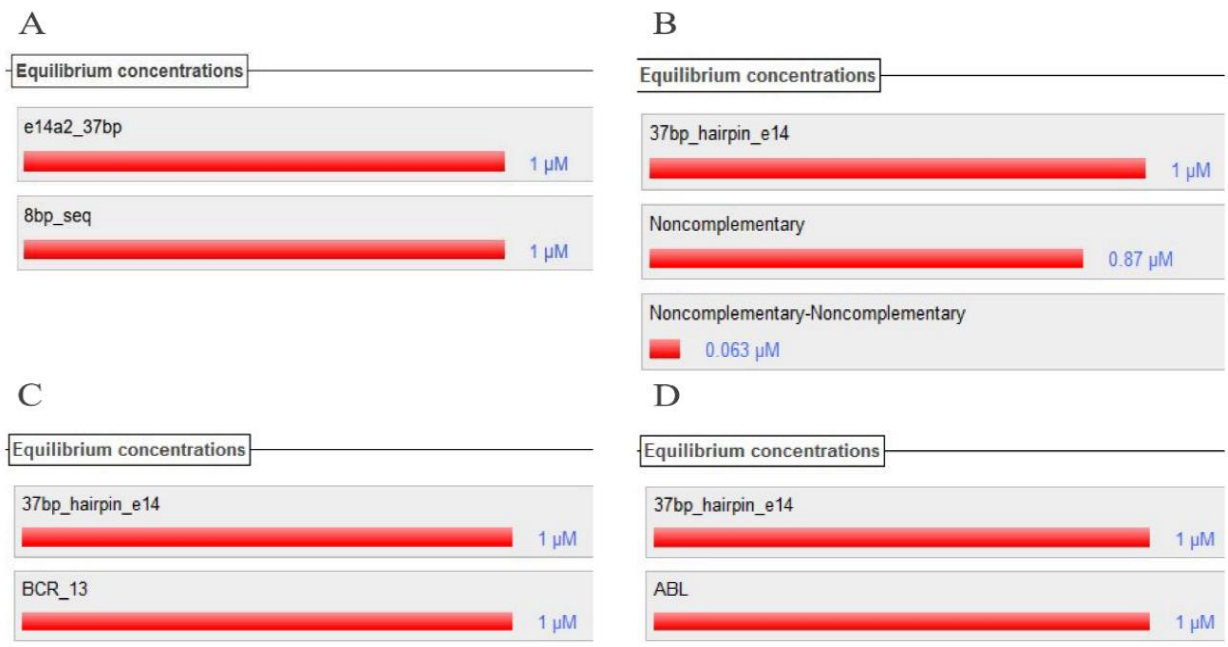

Figure II.2. *In silico* simulation of equilibrium concentrations for the hairpin/revelator pair 1 and different targets using 1 µM of each component. A) 37 bp_hairpin_e14 and respective revelator; 37bp_hairpin_e14 and non-complementary target, C) 37bp_hairpin_e14 and BCR-e14 sequence; D) 37bp_hairpin_e14 and ABL sequence.

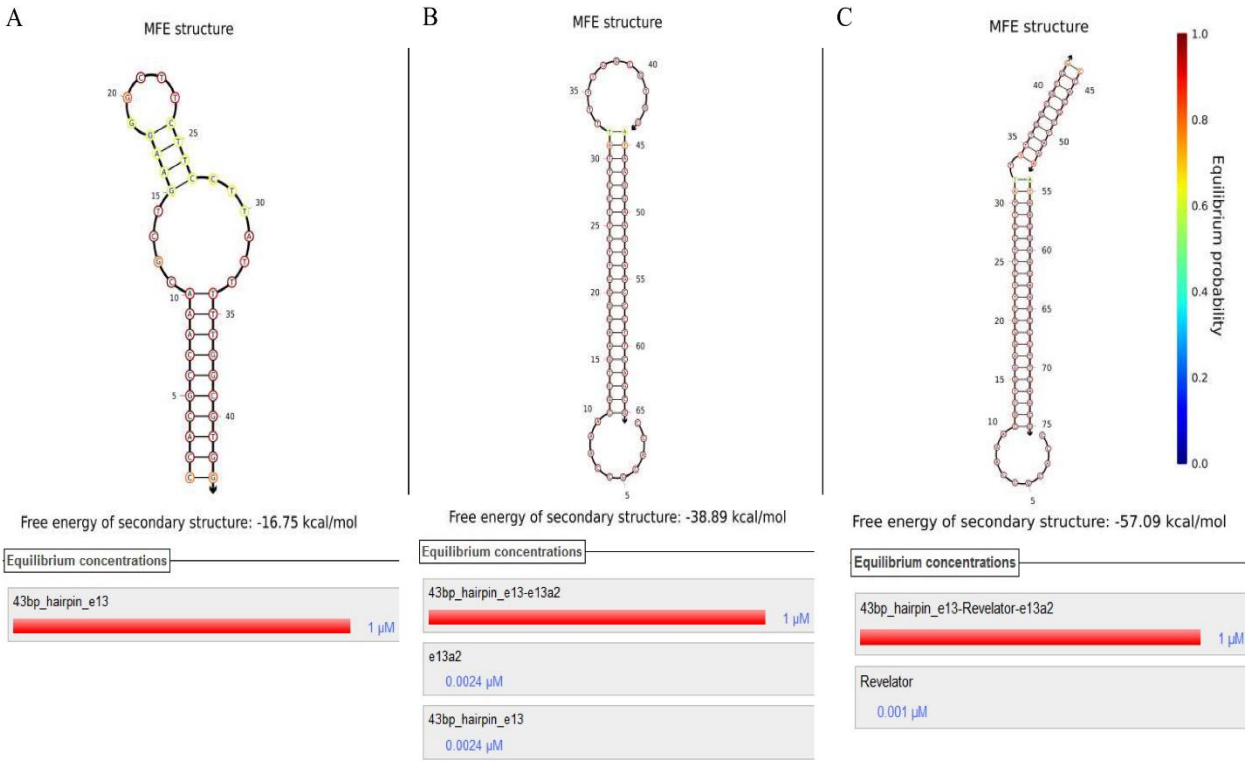

Figure II.3. *In silico* assessment of hybridization of the designed sequences of pair 3 using the software NUPACK. A) 43bp_Hairpin_e14 in absence of target and equilibrium concentration; B) 43bp_Hairpin_e13 in the presence of complementary target and equilibrium concentration; C) 43bp_Hairpin_e13 in presence of complementary target and respective revelator.

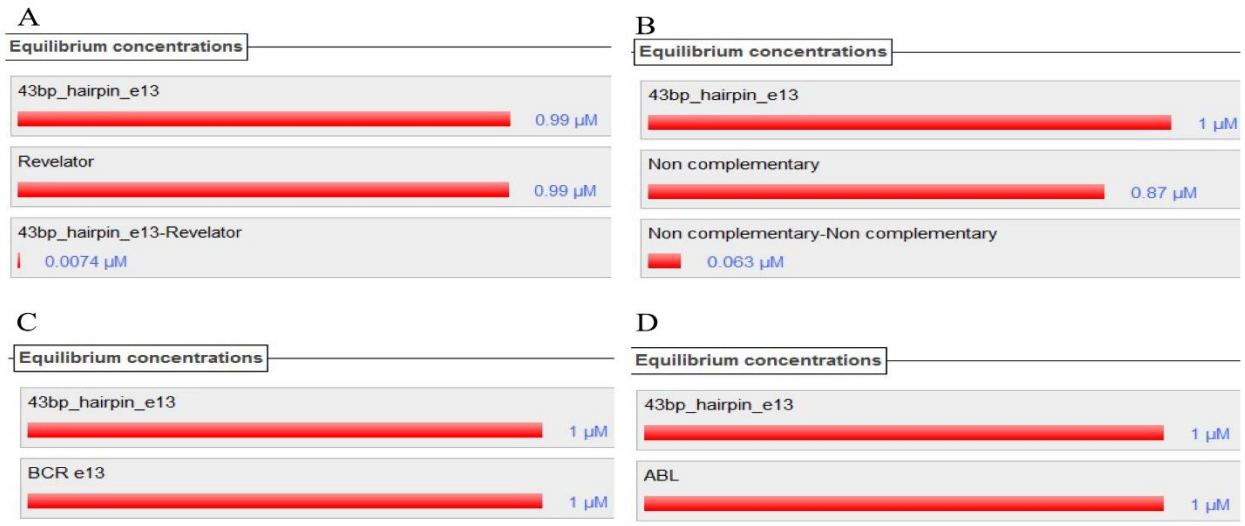

Figure II.4. *In silico* simulation of equilibrium concentrations for the hairpin/revelator pair 3 and different targets using 1 µM of each component. A) 43bp_hairpin_e14 and respective revelator; 43bp_hairpin_e14 and non-complementary target, C) 43bp_hairpin_e14 and BCR-e14 sequence; D) 43bp_hairpin_e14 and ABL sequence.

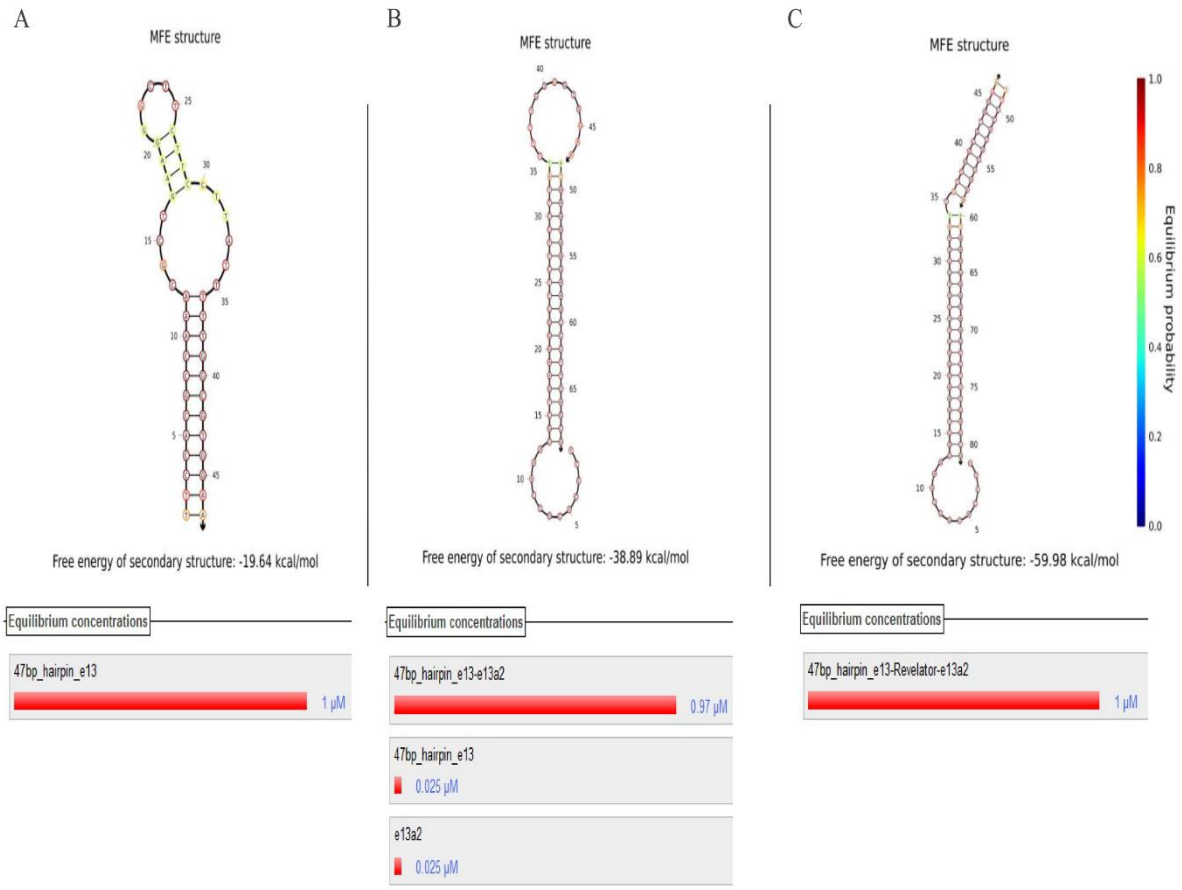

Figure II.5. *In silico* assessment of hybridization of the designed sequences of pair 6 using the software NUPACK. A) 47bp_Hairpin_e13 in absence of target and equilibrium concentration; B) 47bp_Hairpin_e13 in the presence of complementary target and equilibrium concentration; C) 47bp_Hairpin_e13 in presence of complementary target and respective revelator.

Figure II.6. *In silico* simulation of equilibrium concentrations for the hairpin/revelator pair 6 and different targets using 1 µM of each component. A) 47bp_hairpin_e14 and respective revelator; 47bp_hairpin_e14 and non-complementary target, C) 47bp_hairpin_e14 and BCR-e14 sequence; D) 47bp_hairpin_e14 and ABL sequence.

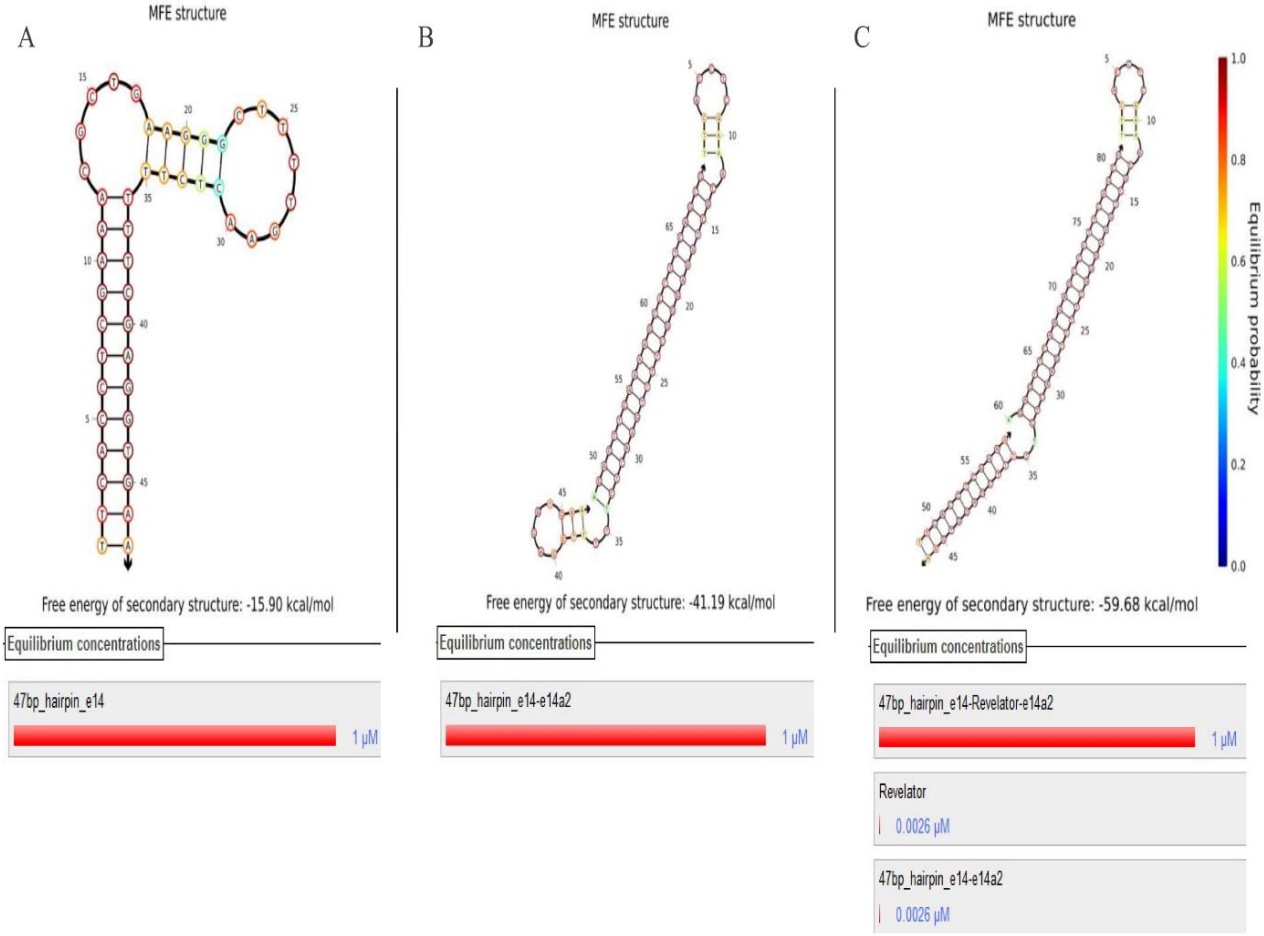

Figure II.7. *In silico* assessment of hybridization of the designed sequences of pair 7-8 using the software NUPACK. A) 47bp_Hairpin_e14 in absence of target and equilibrium concentration; B) 47bp_Hairpin_e14 in the presence of complementary target and equilibrium concentration; C) 47bp_Hairpin_e14 in presence of complementary target and respective revelator.

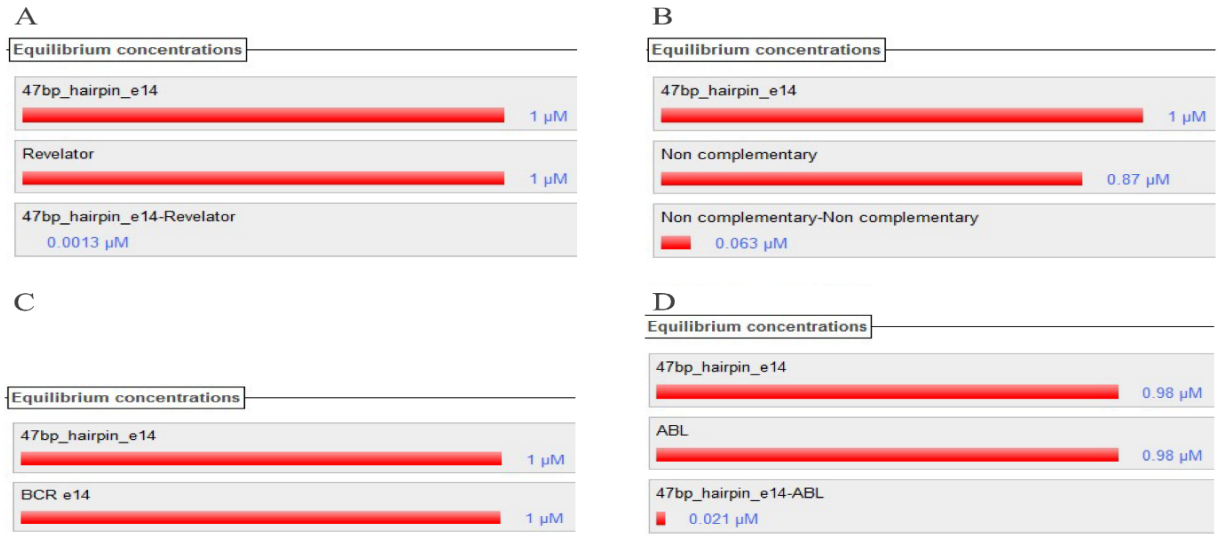

Figure II.8. *In silico* simulation of equilibrium concentrations for the hairpin/revelator pair 3 and different targets using 1 µM of each component. A) 47bp_hairpin_e14 and respective revelator; 47bp_hairpin_e14 and non-complementary target, C) 47bp_hairpin_e14 and BCR-e14 sequence; D) 47bp_hairpin_e14 and ABL sequence.

8.3 Appendix III

Table III.1. *In silico* simulations of the designed sequences. The structures were predicted using NUPACK software.

e13a2		e14a2	
Structures at 4 ºC	**Structures at 10 ºC**	**Structures at 4 ºC**	**Structures at 10 ºC**
e13A 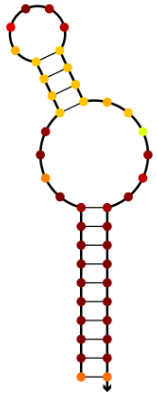 Free energy of secondary structure: -21.77 kcal/mol	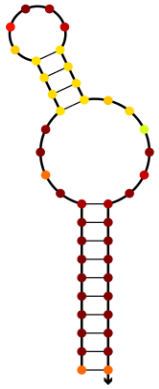 Free energy of secondary structure: -19.89 kcal/mol	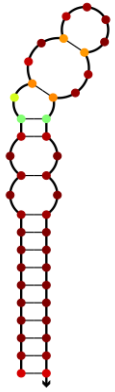 Free energy of secondary structure: -19.27 kcal/mol	e14A 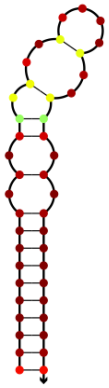 Free energy of secondary structure: -17.08 kcal/mol
e13B 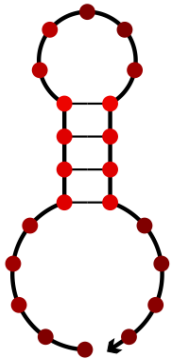 Free energy of secondary structure: -6.12 kcal/mol	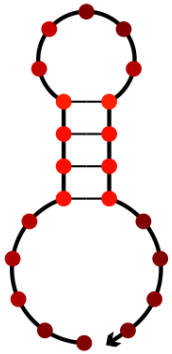 Free energy of secondary structure: -5.44 kcal/mol	e14B 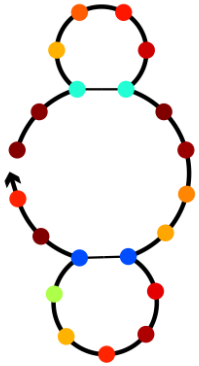 Free energy of secondary structure: -0.98 kcal/mol	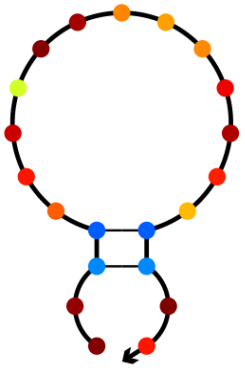 Free energy of secondary structure: -0.52 kcal/mol

Table III.1. *In silico* simulations of the designed sequences (cont). The structures were predicted using NUPACK software.

e13		e14	
Structures at 4 ºC	**Structures at 10 ºC**	**Structures at 4 ºC**	**Structures at 10 ºC**
e13AB 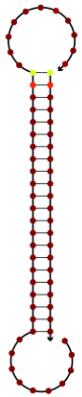 Free energy of secondary structure: -46.23 kcal/mol	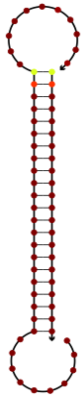 Free energy of secondary structure: -43.47 kcal/mol	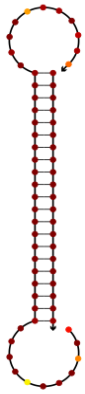 Free energy of secondary structure: -43.62 kcal/mol	e14AB 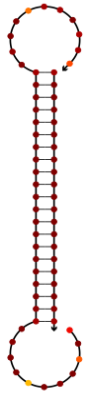 Free energy of secondary structure: -40.86 kcal/mol
e13ABC 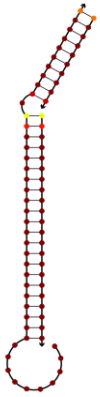 Free energy of secondary structure: -67.70 kcal/mol	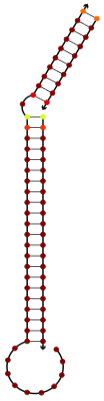 Free energy of secondary structure: -63.72 kcal/mol	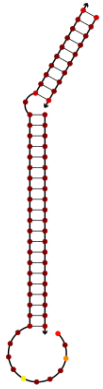 Free energy of secondary structure: -63.24 kcal/mol	e14ABC 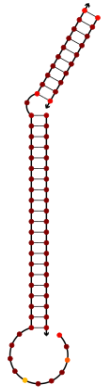 Free energy of secondary structure: -59.32 kcal/mol

Table III.1. *In silico* simulations of the designed sequences (cont2). The structures were predicted using NUPACK software (215)

Structures at 4 ºC	Structures at 10 ºC	Structures at 4 ºC	Structures at 10 ºC
e13A-e14B-e13C		e14A-e13B-e14C	
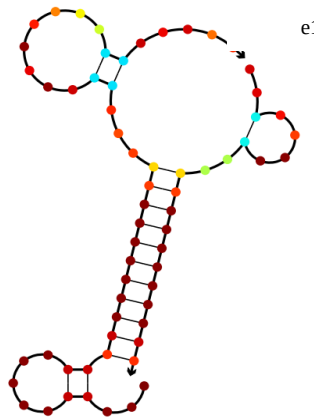	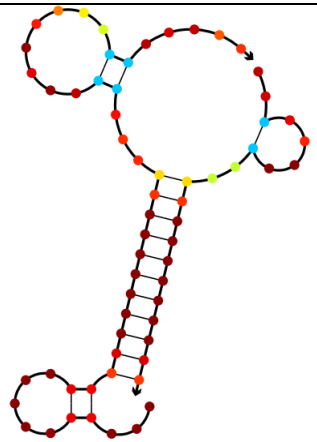	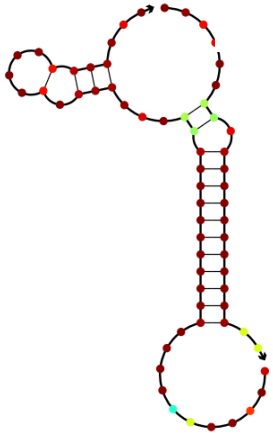	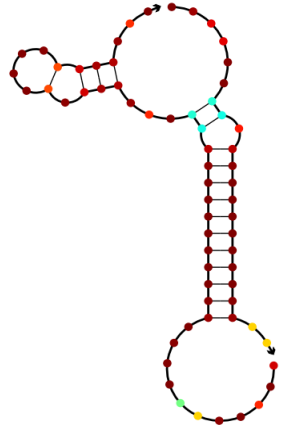
Free energy of secondary structure: -26.66 kcal/mol	Free energy of secondary structure: -24.48 kcal/mol	Free energy of secondary structure: -28.83 kcal/mol	Free energy of secondary structure: -26.31 kcal/mol

1

8.4 Appendix IV

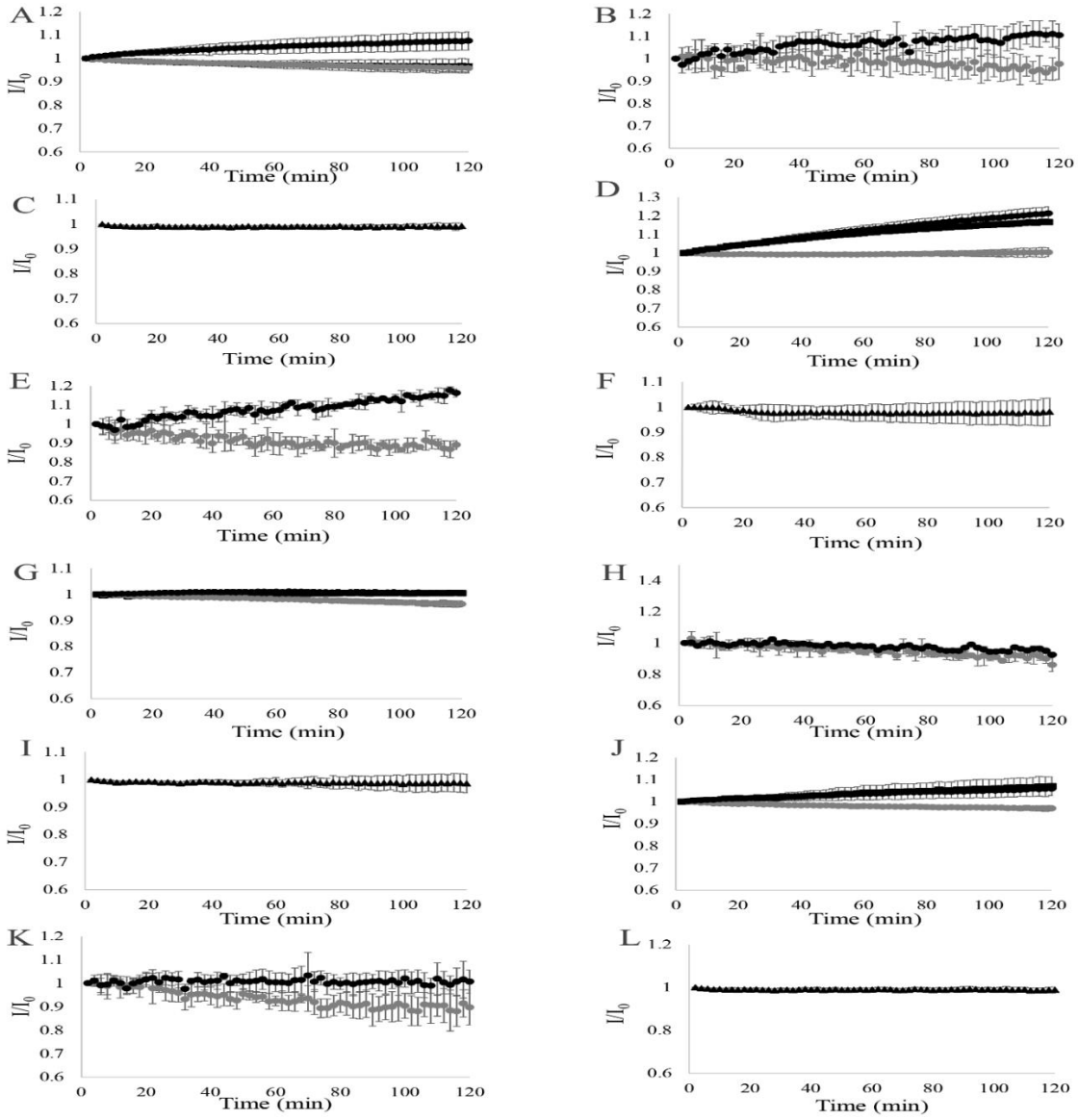

Figure IV.1. Hybridization assays of pair 1 in different buffers. A) Donor emission in Tris-HCl pH 7.5 100mM NaCl; B) Acceptor emission in Tris-HCl pH 7.5 100mM NaCl; C) Acceptor control emission in Tris-HCl pH 7.5 100mM NaCl D) Donor emission in Tris-HCl pH 8.0 100mM NaCl; E) Acceptor emission in Tris-HCl pH 8.0 100mM NaCl; F) Acceptor control emission in Tris-HCl pH 8.0 100mM; G) Donor emission in 10 mM Tris-HCl pH 8.0 50 mM KCl 3.5mM $MgCl_{2;}$ H) Acceptor emission in 10 mM Tris-HCl pH 8.0 50 mM KCl 3.5mM $MgCl_{2;}$ I) Acceptor control emission in 10 mM Tris-HCl pH 8.0 50 mM KCl 3.5mM $MgCl_{2;}$ J) Donor emission in 10 mM Phosphate buffer pH 8.0 100 mM NaCl; K) Acceptor emission in 10 mM Phosphate buffer pH 8.0 100 mM NaCl; L) J) Acceptor control emission in 10 mM Phosphate buffer pH 8.0 100 mM NaCl. Black squares correspond to donor blank; Black circles correspond to positive reaction; Gray circles corresponds to negative reaction; Black triangles corresponds to acceptor emission in positive reaction in the absence of donor

8.5 Appendix V

A

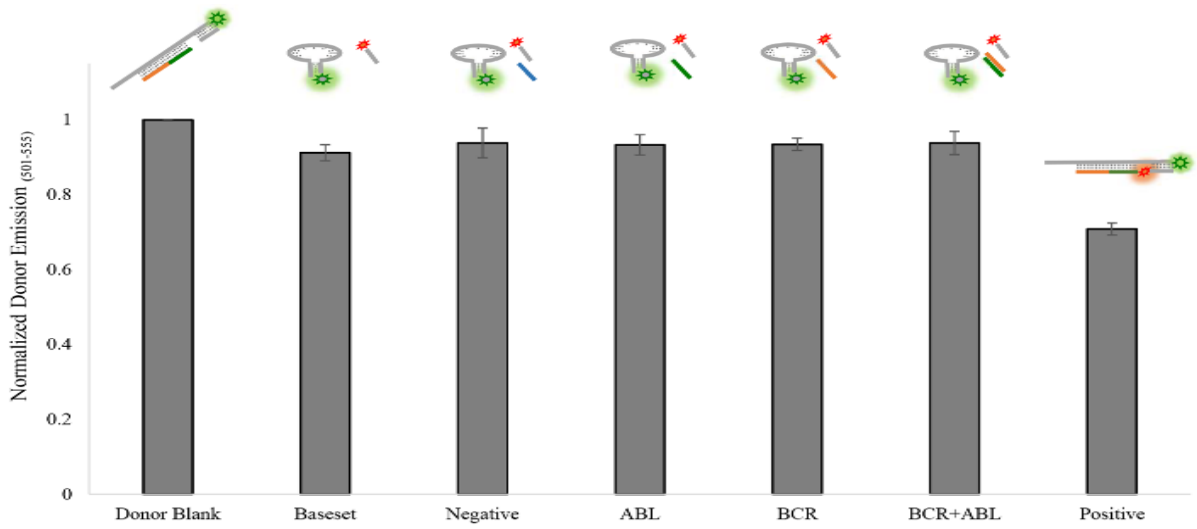

B

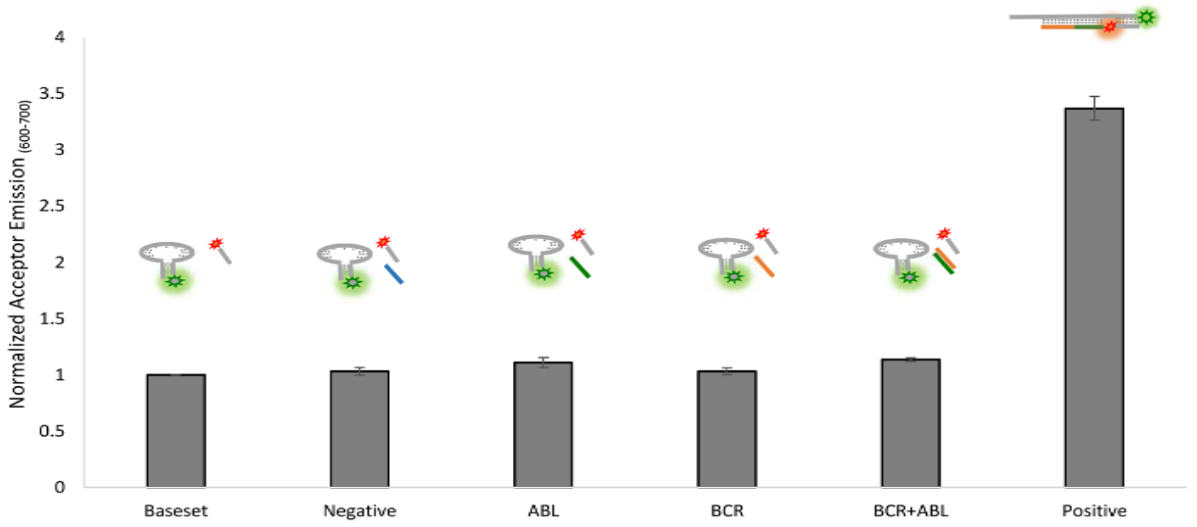

Figure V.I. Signal variation of donor and acceptor in the presence of different targets for hairpin/revelator pair 6. A) Donor channel; B) Acceptor channel. Donor channels normalized to the donor channel in donor blank. Acceptor channels normalized to the acceptor channel in base set reaction. Data presented as mean ± standard deviation of at least 3 independent assays. Performed in buffer e).

A

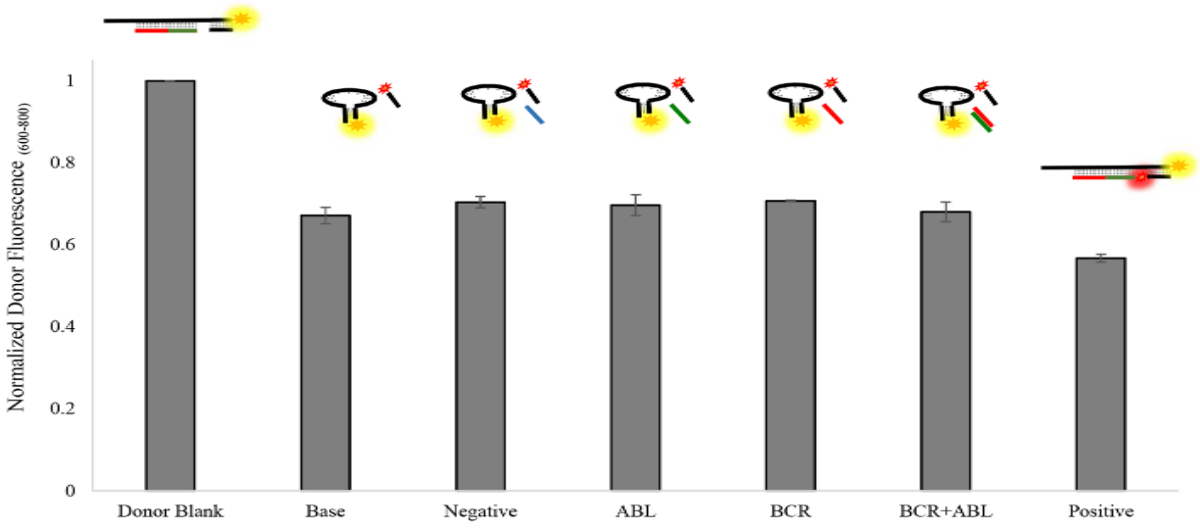

B

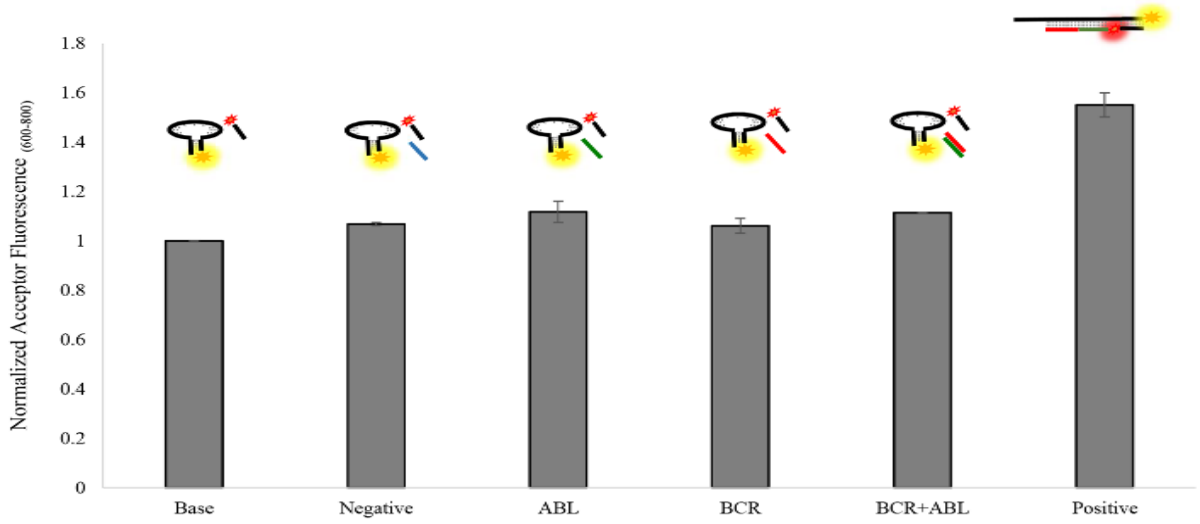

Figure V.II. Signal variation of donor and acceptor in the presence of different targets for hairpin/revelator pair 7. A) Donor channel; B) Acceptor channel. Donor channels normalized to the donor channel in donor blank. Acceptor channels normalized to the acceptor channel in the base set reaction. Data presented as mean ± standard deviation of at least 3 independent assays. Performed in buffer e).

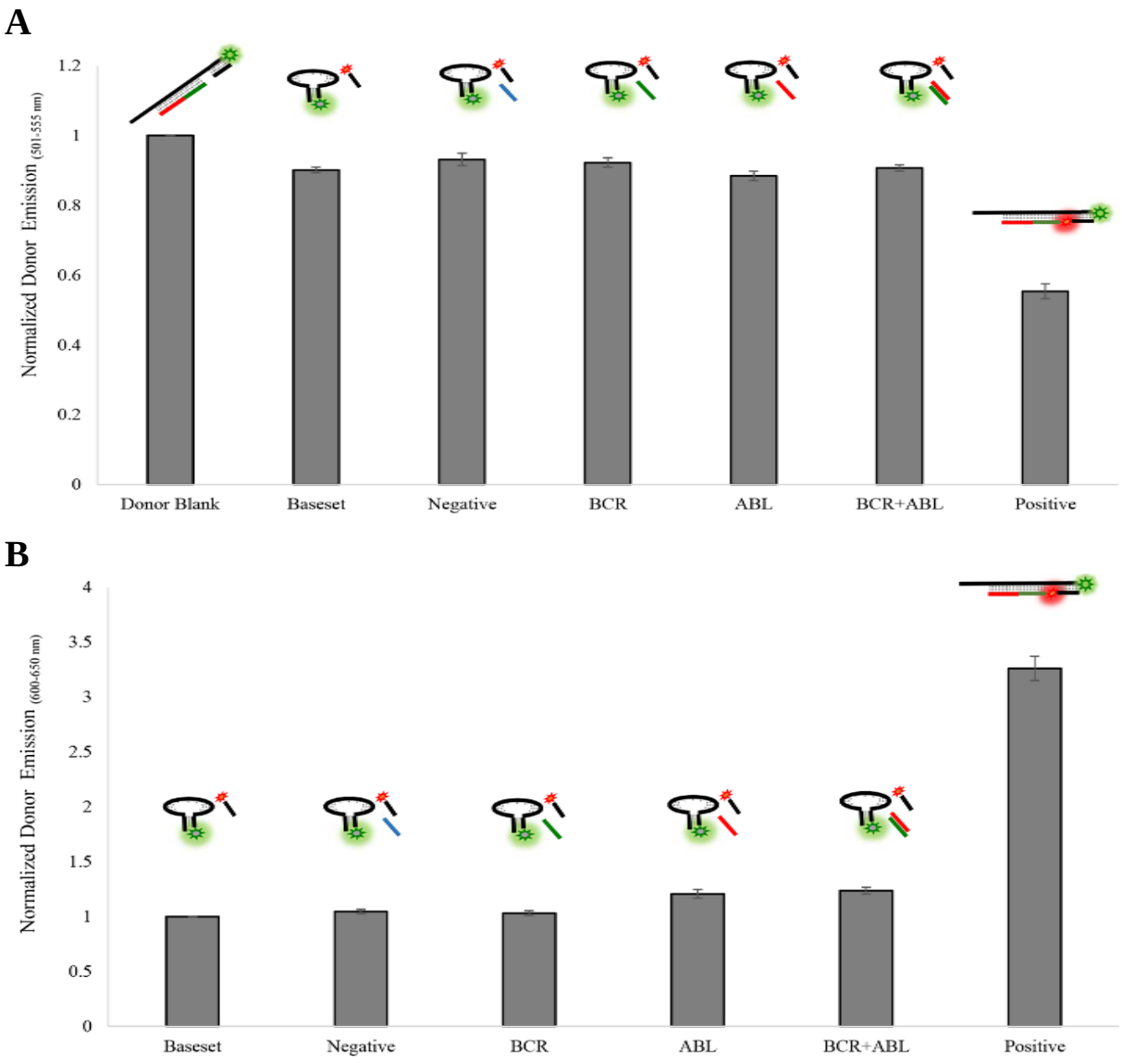

Figure V.III. Signal variation of donor and acceptor in the presence of different targets for hairpin/revelator pair 8. A) Donor channel; B) Acceptor channel. Donor channels normalized to the donor channel in donor blank. Acceptor channels normalized to the acceptor channel in negative reaction. Data presented as means ± standard deviation of at least 3 independent assays. Performed in buffer e).

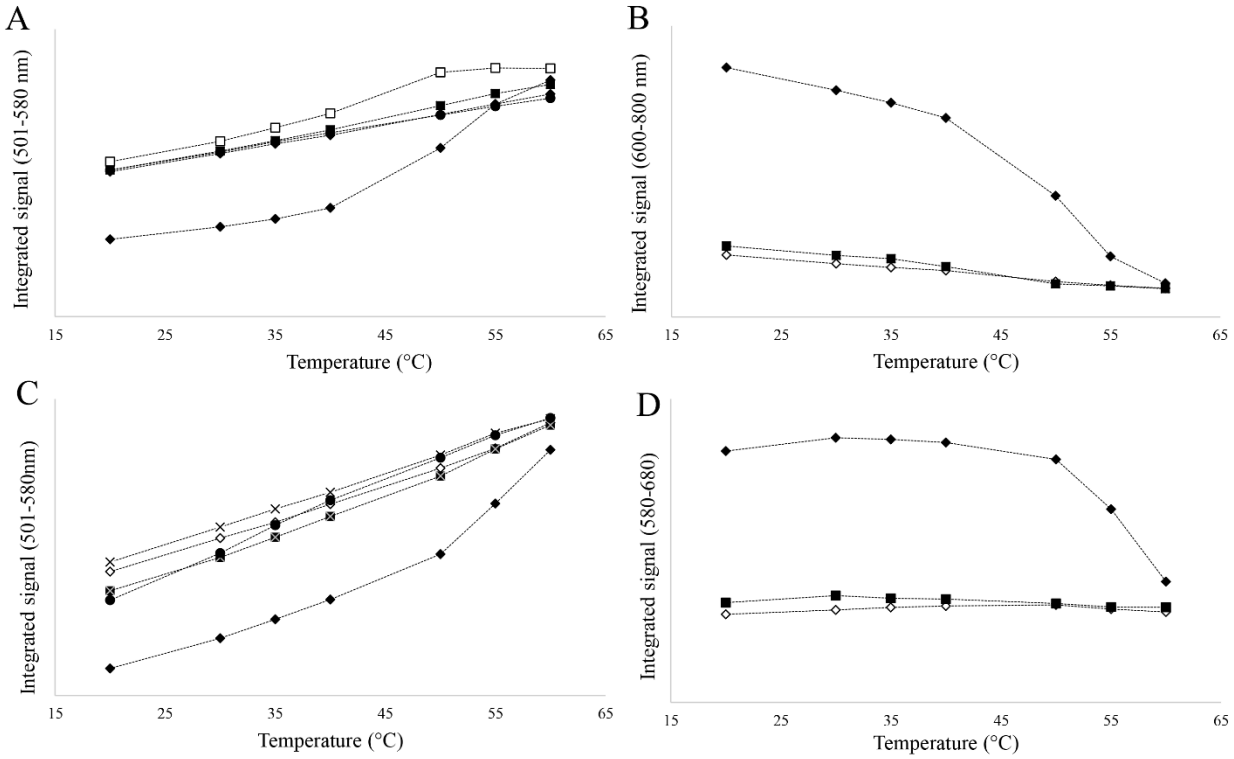

Figure V.1V. Melting profile of the hairpin/revelator pairs 4 and 3. A) Donor channel for pair 4 dataset; B) Acceptor channel for pair 4 dataset; C) Donor channel for pair 3 dataset; D) Acceptor channel for pair 3 dataset. Black circles- melting profile for hairpin alone; White squares – Donor blank melting profile; black squares – Crossed template reaction melting profile; White diamonds – melting profile of negative reaction; Black diamonds – melting profile of positive reaction.

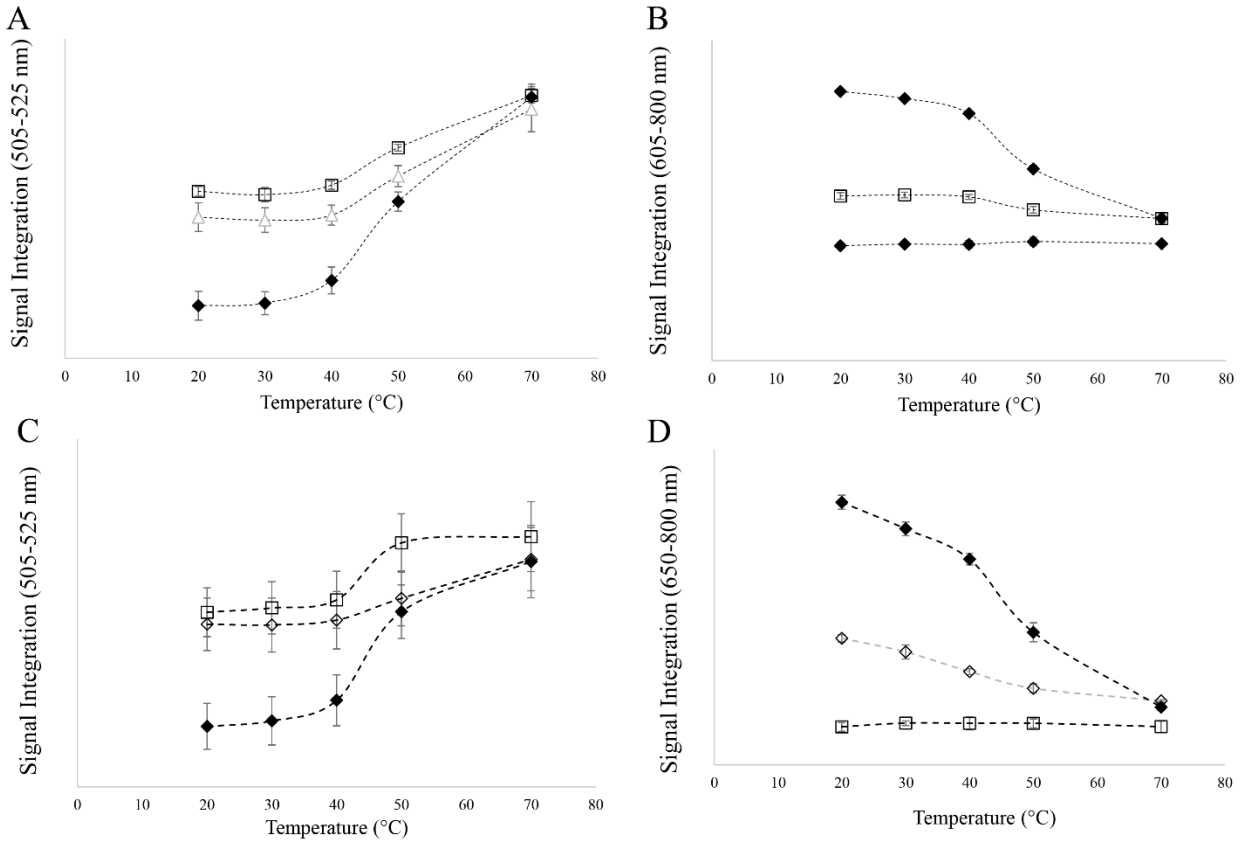

Figure V.V. Melting profile of the hairpin/revelator pairs 6 and 8. A) Donor channel for pair 4 dataset; B) Acceptor channel for pair 4 dataset; C) Donor channel for pair 3 dataset; D) Acceptor channel for pair 3 dataset. Black circles- melting profile for hairpin alone; White square – Donor blank melting profile; black squares – Crossed template reaction melting profile; White diamonds – melting profile of negative reaction; Black diamonds – melting profile of positive reaction.

8.6 Appendix VI

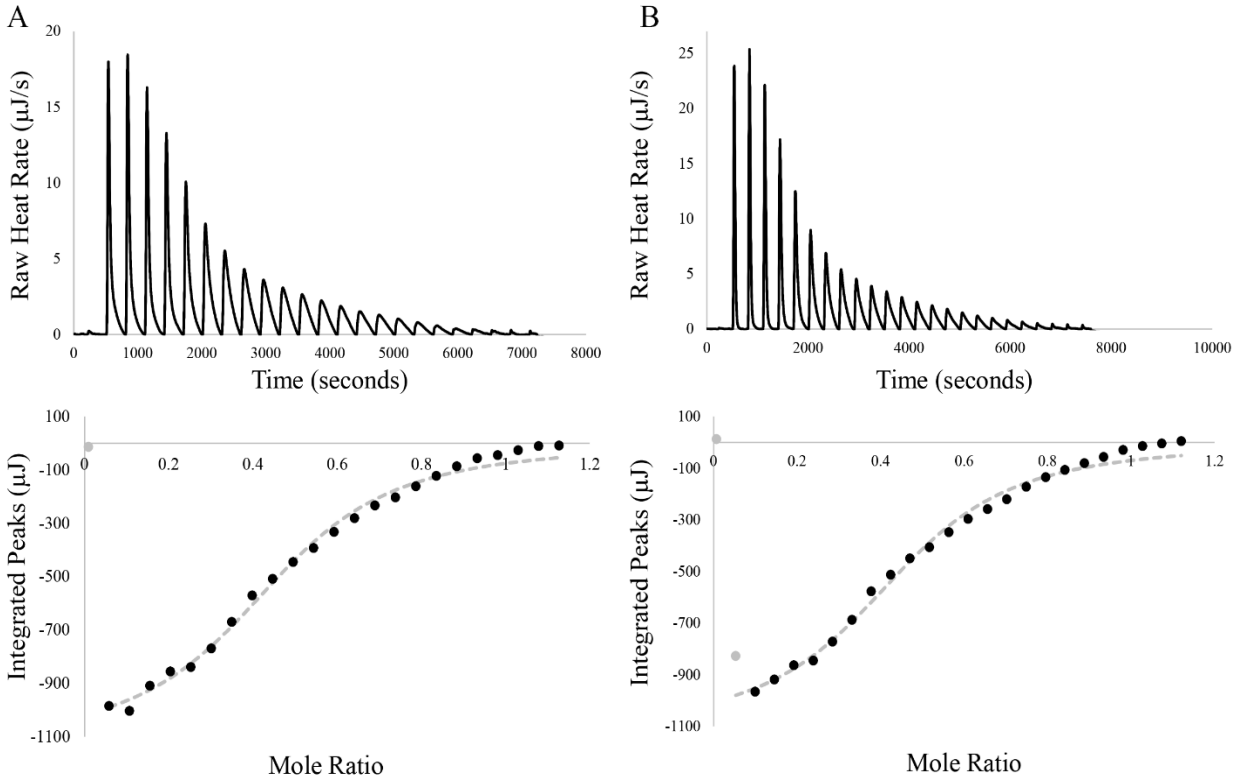

Figure VI.1. Isothermal titration calorimetry of e14a2 sequence to 43bp_hairpin_e14. A) 51.55 µM of 43bp_hairpin_e14 vs 24 injections of 5.14 µl of e14a2 sequence at 469.53 µM; B) 50.69 µM of 25 injections of 5.14 µl e13a2 sequence a 566.84 µM; Gray out points were not considered for the fitting model. Data were fitted with NanoAnalyse software using independent model. The raw ITC data are shown in the top graphs.

Table VI.1. Parameters for the ITC analysis of 43bp_hairpin_e14 binding to e14a2 sequence at 20 °C. Fitting parameters from: A) 51.55 µM of 43bp_hairpin_e14 vs 24 injection of 5.14 µl of e14a2 sequence at 469.53 µM; B) 50.69 µM of 25 injections of 5.14 µl e13a2 sequence a 566.84 µM.

	A		B	
Variable	**Value**	**Confidence Interval (±)**	**Value**	**Confidence Interval (±)**
K_D (M)	3.00×10^{-6}	5.86×10^{-7}	2.91×10^{-6}	7.86×10^{-7}
n	0.461	0.018	0.45	0.021
ΔH (kJ/mol)	-469.7	23.74	-494.5	34.78
ΔS (J/mol·K)	-1496.55	-	-1580.85	-
ΔG (kJ/mol)	-30.995	-	-31.074	-
-TΔS (kJ/mol)	438.71	-	463.43	-
K_A (M^{-1})	3.33×10^{-5}	-	3.44×10^{-5}	-

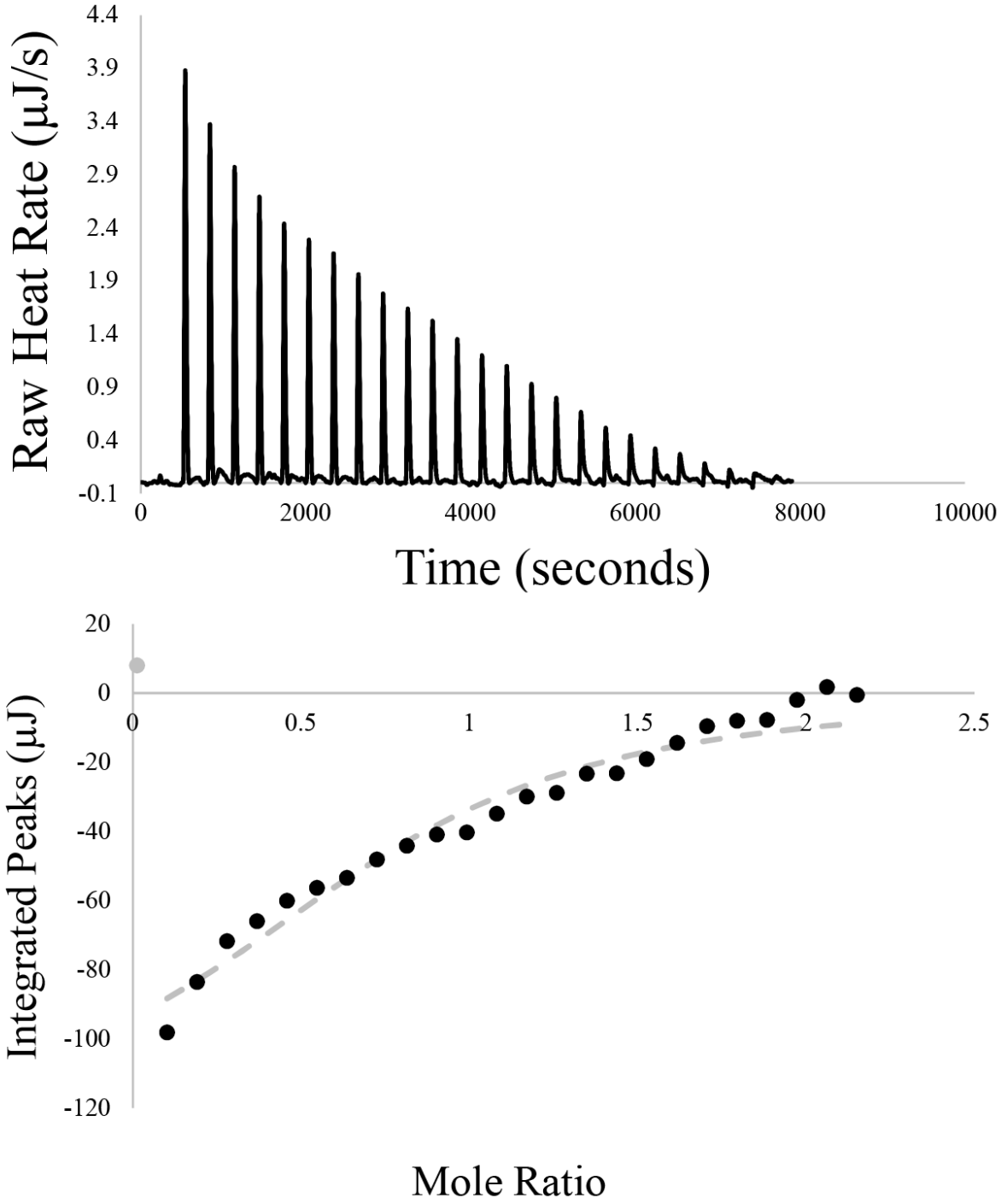

Figure VI.2. Isothermal titration calorimetry of revelator sequence to complex 43bp_hairpin_e14-target e14a2. 22.77 µM of 43bp_hairpin_e14-target e14a2 complex (concentration corrected using stoichiometry parameter presented on tableAX condition B) vs 25 injection of 4 µl of revelator sequence at 488.89 µM. Gray point was not considered for the fitting model. Data were fitted with NanoAnalyse software using independent model. The raw ITC data are shown in the top graphs.

8.7 Appendix VII

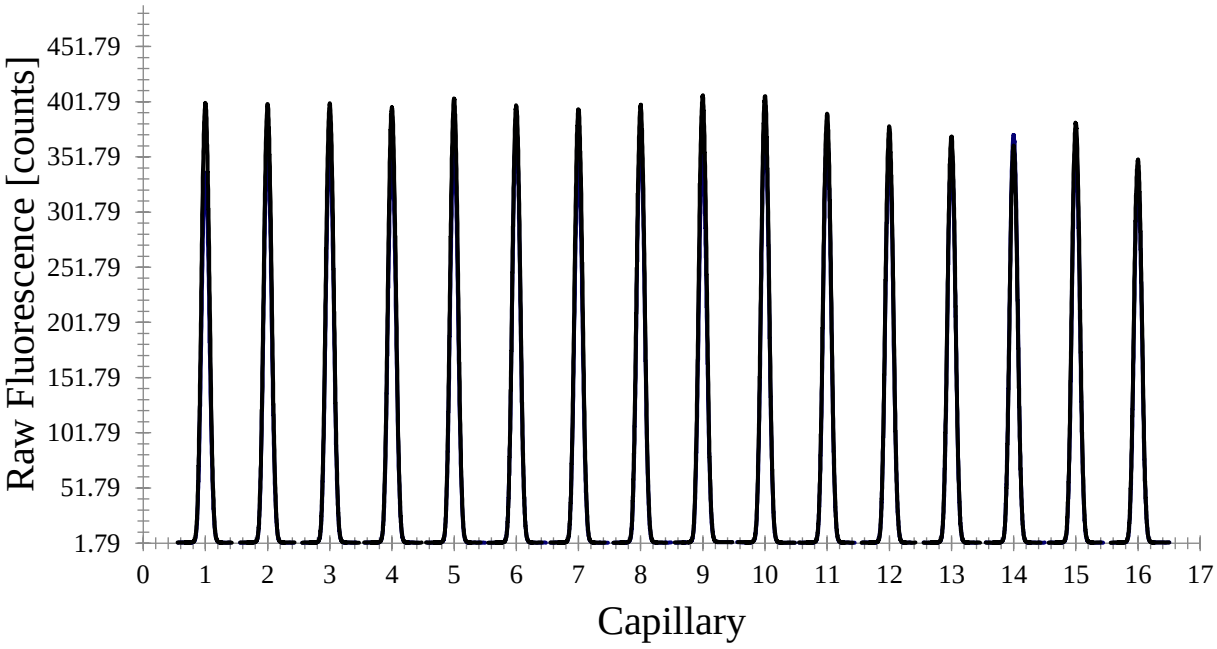

Figure VII.1. Initial fluorescence assessment of the 16 capillaries used to determine the binding affinity of the target e14a2 and 43bp_hairpin_e14. The emission profile is compatible with the absence ligand induced fluorescence change.

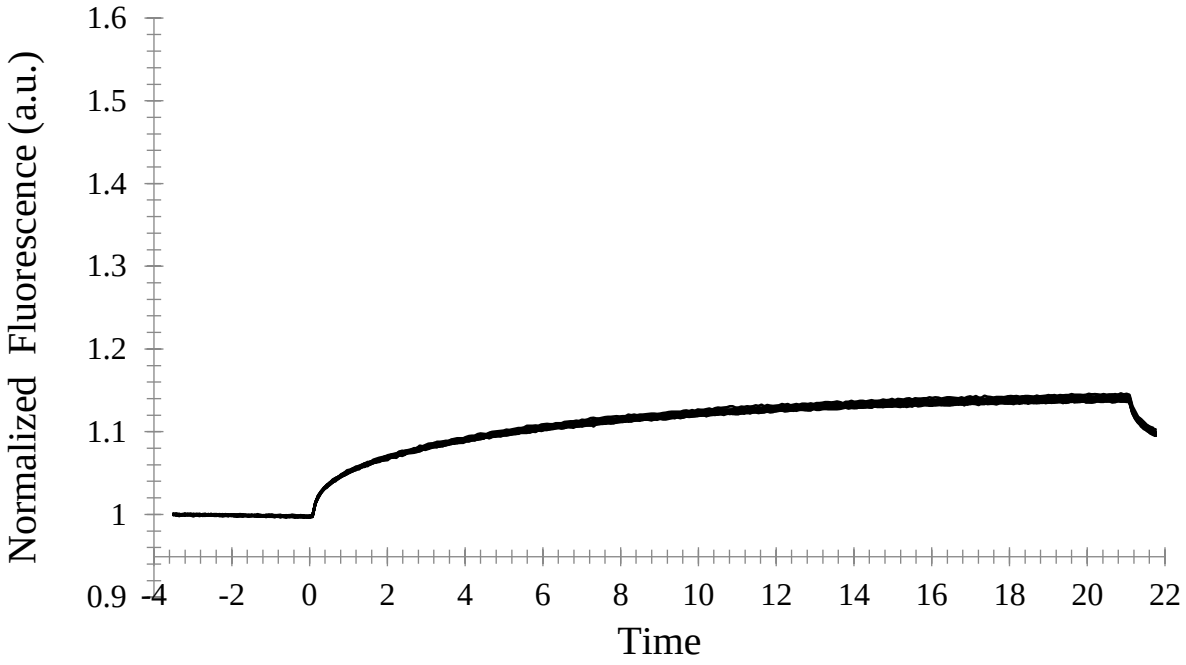

Figure VII.2. MST profile of the cross-reactivity test between the target e13a2 and the 43bp_hairpin_e14.

8.8 Appendix VIII

A

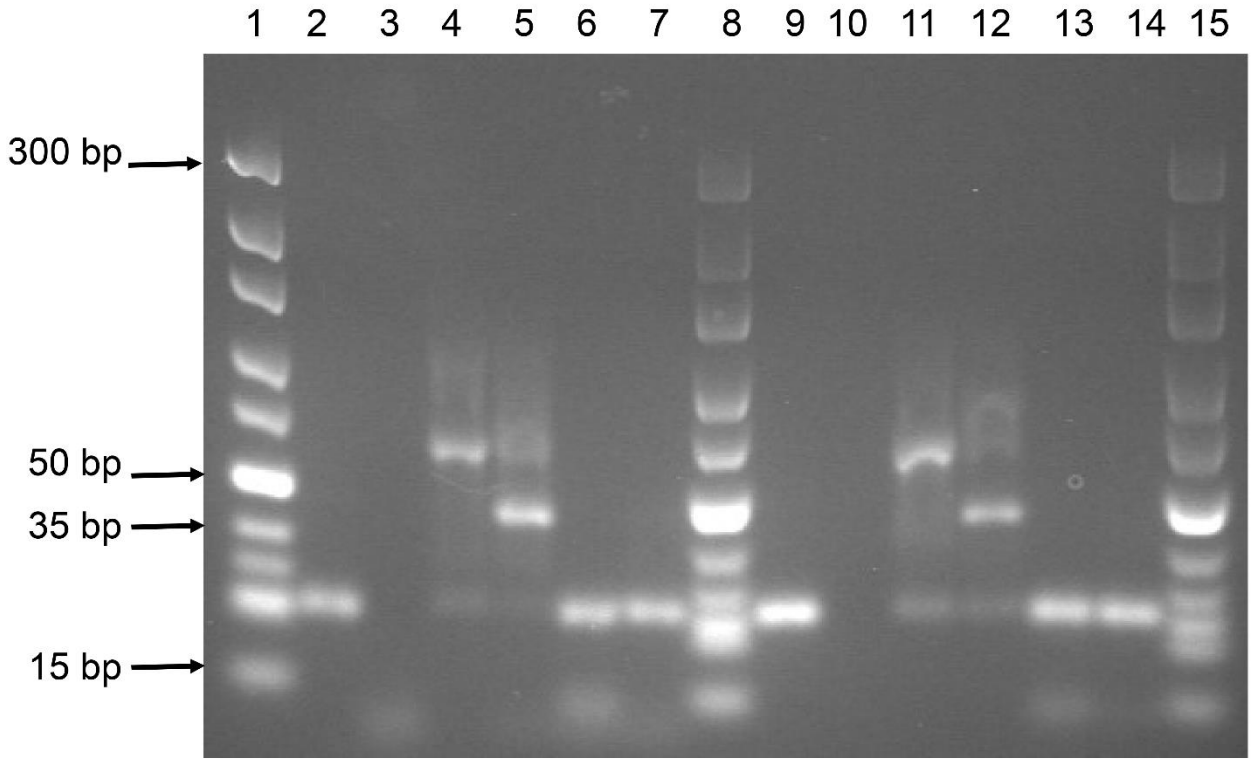

B

Lane	Scenario	Rf	Lane	Scenario	Rf
2	e13A	1.00	**9**	e14A	1.00
4	e13AB (top band)	0.78	**11**	e14AB (top band)	0.75
4	e13AB (lower band)	1.01	**11**	e14AB (lower band)	0.99
5	e13ABC (top band)	0.76	**12**	e14ABC (top band)	0.74
5	e13ABC (middle band)	0.88	**12**	e14ABC (middle band)	0.84
5	e13ABC (lower band)	1.01	**12**	e14ABC (lower band)	1.00
6	e13AYC	1.01	**13**	e14AYC	0.99
7	e13A_e14B_e13C	1.01	**14**	e14A_e13B_e14C	0.99

Figure VIII.1. Agarose gel electrophoresis of the tested scenarios. Lane 1- GeneRuler™ DNA Ladder, Ultra A) Low Range; Lane 2 – e13A; Lane 3 – e13C; Lane 4 – e13AB; Lane 5 - e13ABC; Lane 6 – e13AYC; Lane 7- e13A-e14B-e13C; Lane 8- GeneRuler™ DNA Ladder, Ultra Low Range; Lane 9 – e14A; Lane 10 – e14C; Lane 11 – e14AB; Lane 12 - e14ABC; Lane 13 – e14AYC; Lane 14- e14A-e13B-e14C; Lane 15 - GeneRuler™ DNA Ladder, Ultra Low Range. 5% agarose in 1×TAE; 4 hours at 60V, 4 °C. B) Retention factor of the several scenarios. Hairpin alone used as reference for calculation.

8.9 Appendix IX

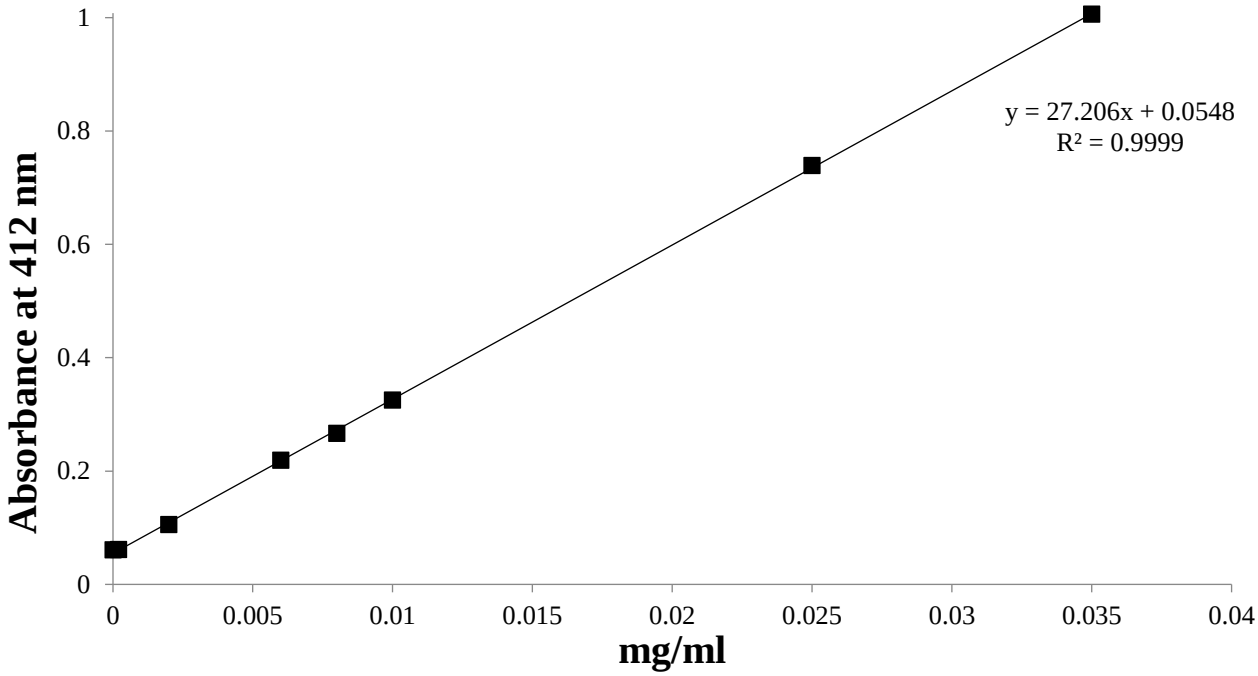

Figure IX.1. Calibration curve used for the quantification of thiolated PEG in the supernatant. The error bars represent 3 independent assays.

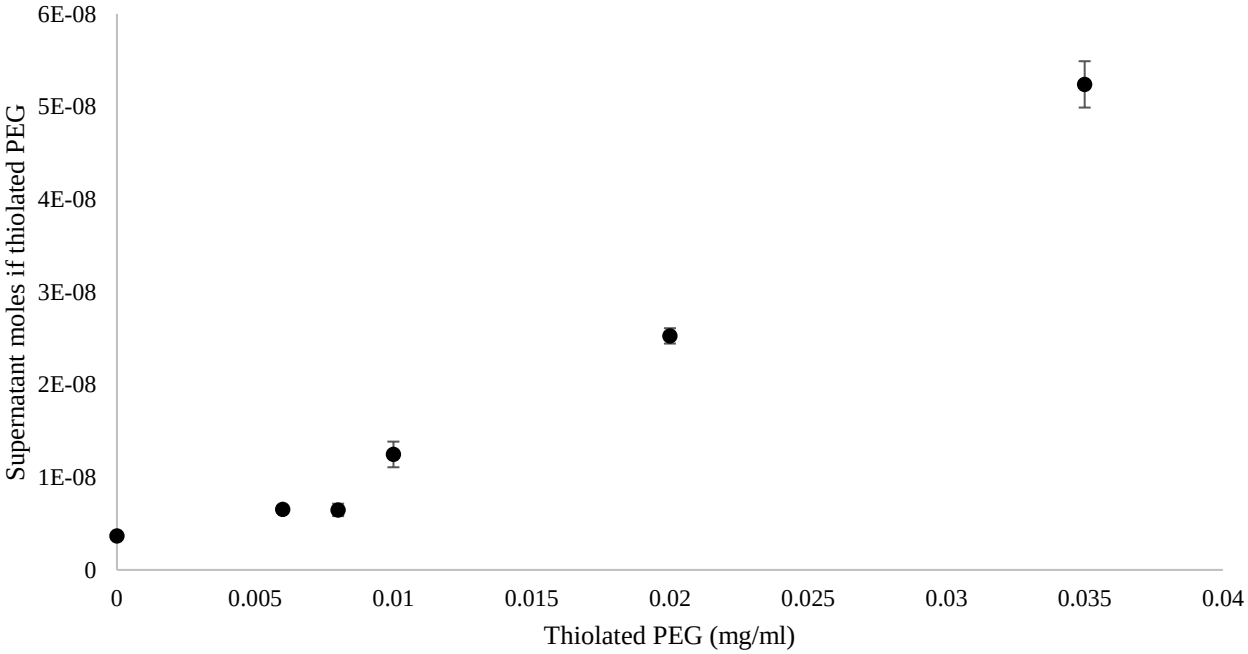

Figure IX.2. Saturation curve of PEG functionalization.

8.10 Appendix X

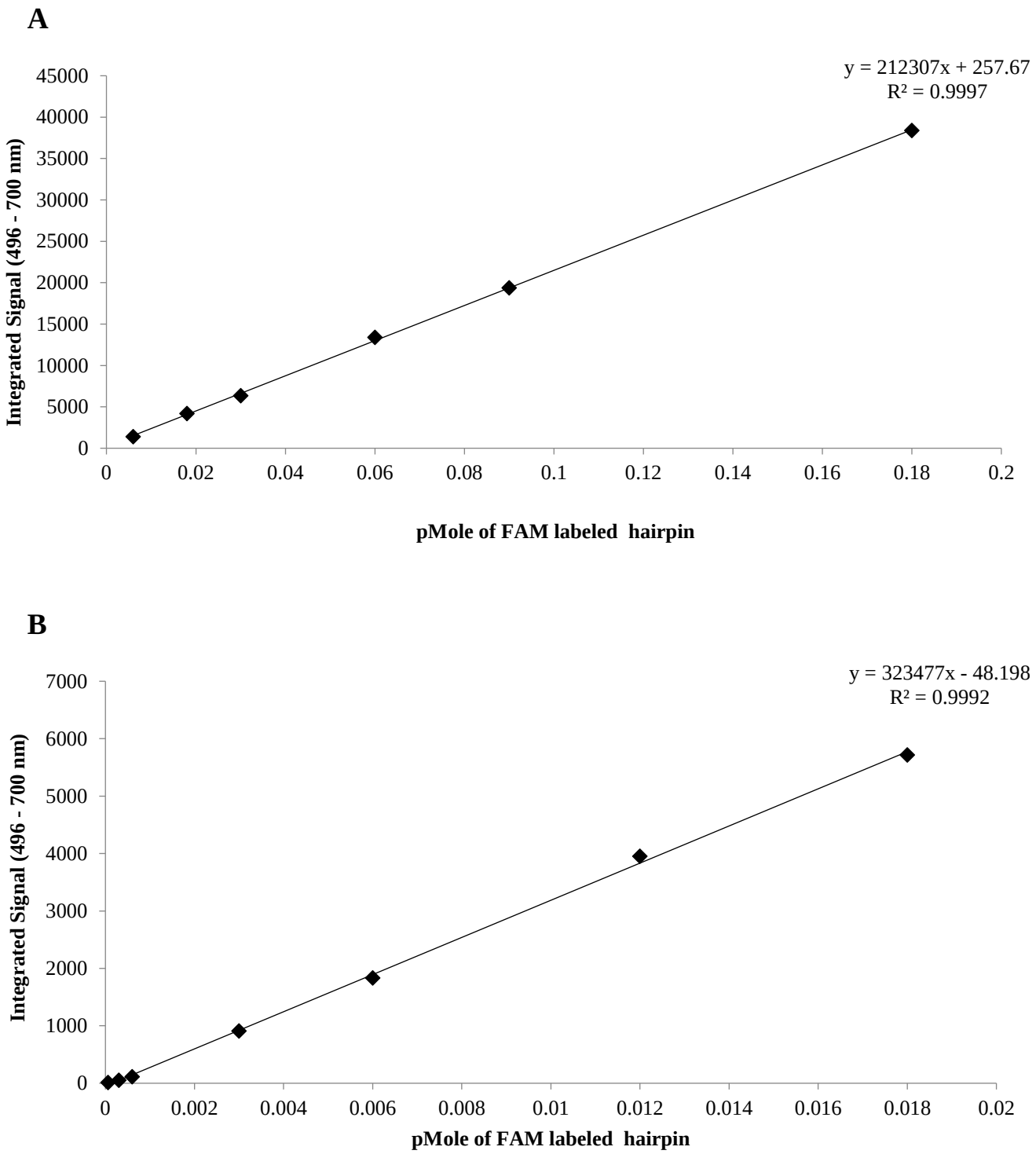

Figure X.1. Calibration curve for the quantification of the number of hairpins per AuNP of BioCode-43bp-e14-FAM-1.

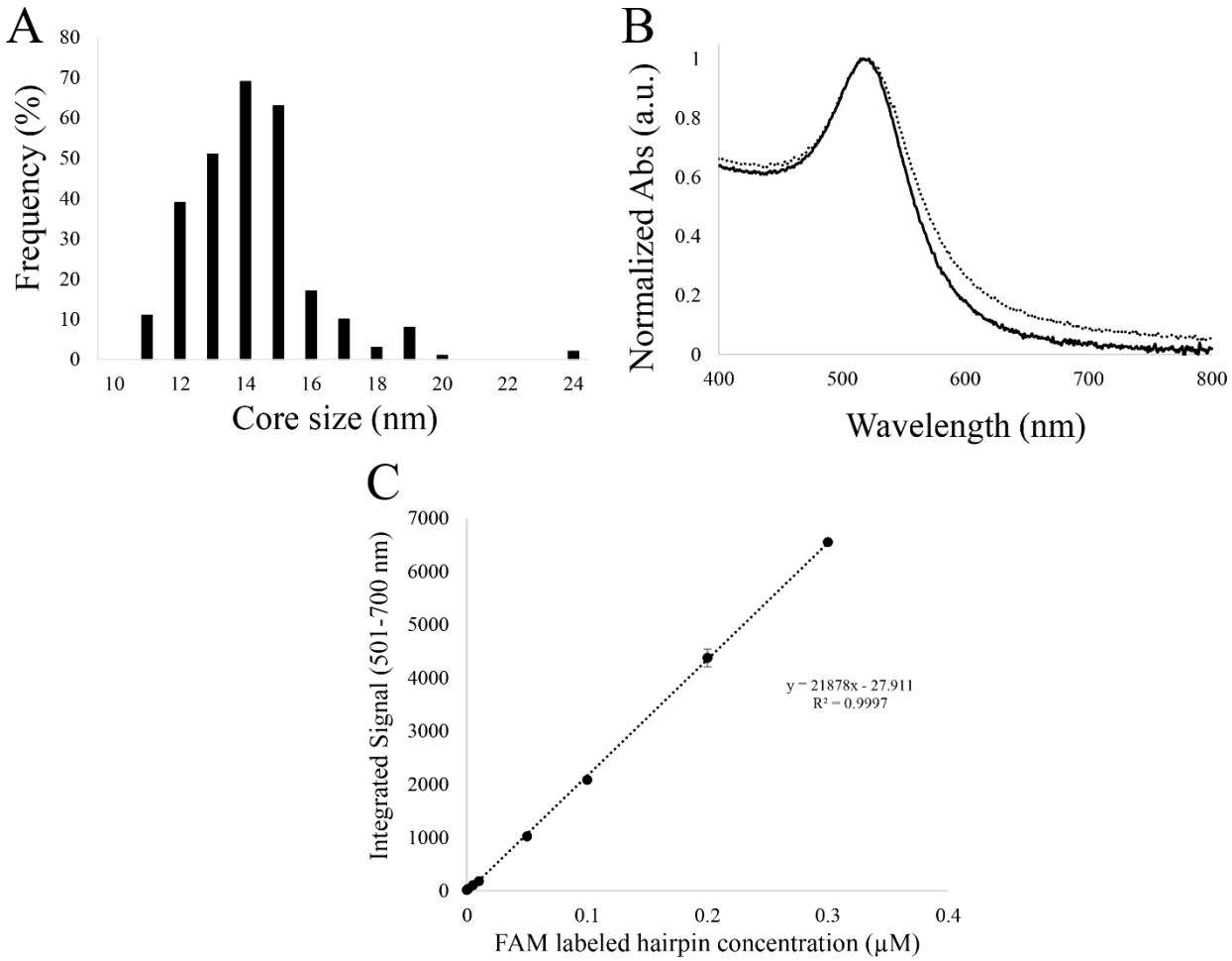

Figure X.2. Characterization performed for BioCode-47bp-e14-FAM. A) Size distribution of the BioCode-47bp-e13-FAM – histogram was constructed using 274 measurements; B) UV-Vis spectra of AunP@citrate (solid black line) and BioCode47bp-e14-FAM (dotted black line) C) Calibration curve used for the quantification o the number of hairpins per AuNP.

8.11 **Appendix XI**

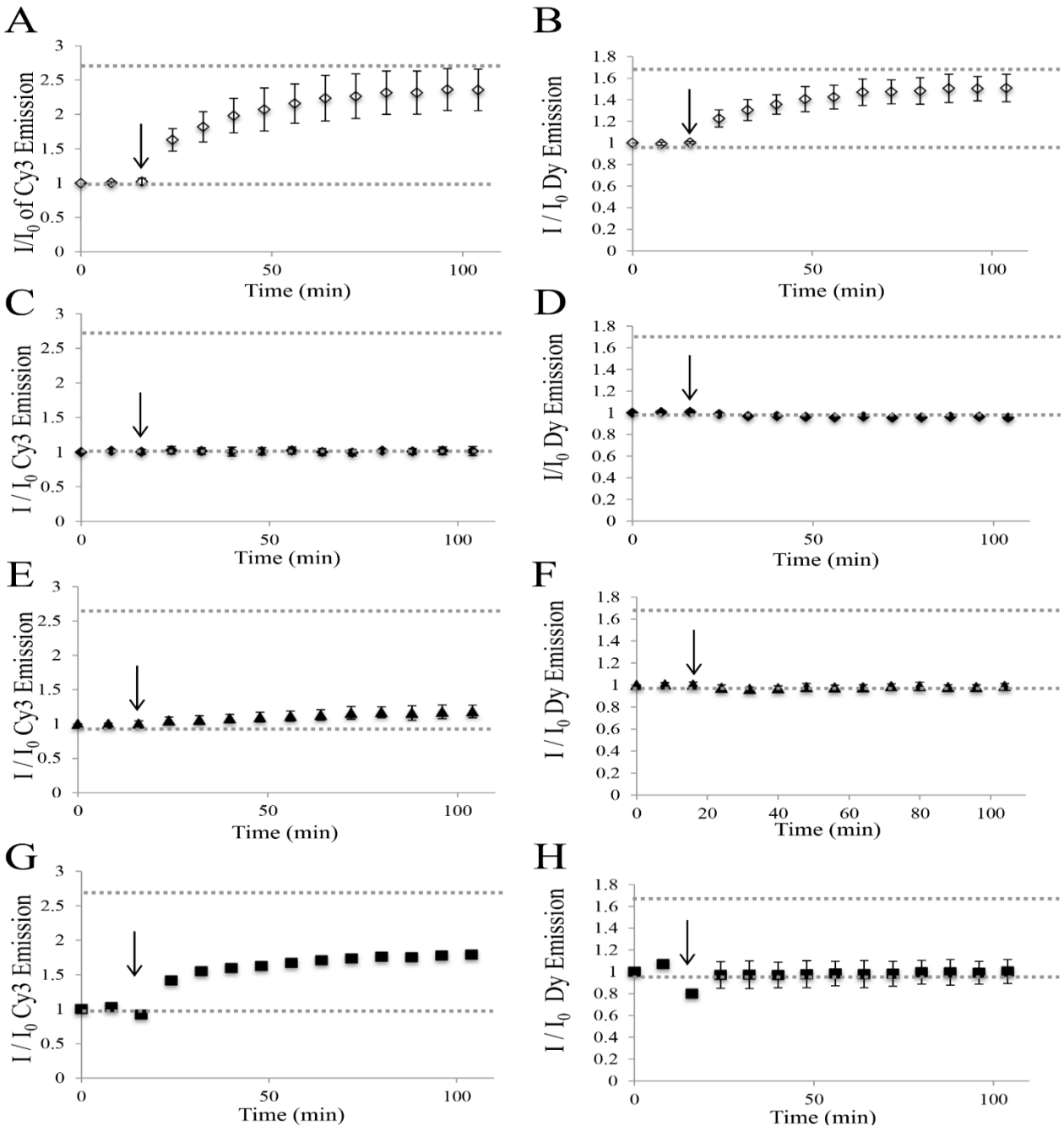

Figure XI.1. Hybridization assays of Biocode-43bp -e14-Cy3 in presence of different target sequences. A) Biocode-43bp -e14-Cy3 donor emission in the presence of e14a2 complementary target (white diamonds); B) acceptor-Dy emission in the presence of e14a2 complementary target; C) Biocode-43bp -e14-Cy3 donor emission in the presence of non-complementary target (black diamonds); D) acceptor-Dy emission in the presence of non-complementary target (black diamonds); E) Biocode-43bp -e14-Cy3 donor emission in the presence of exon 14 BCR derived target (black squares); F) acceptor-Dy emission in the presence of exon 14 BCR derived target (black squares); G) Biocode-43bp -e14-Cy3 donor emission in the presence of ABL target (black diamonds); H) acceptor-Dy emission in the presence of ABL target (black diamonds). The black arrow represents the addition of the target sequence.

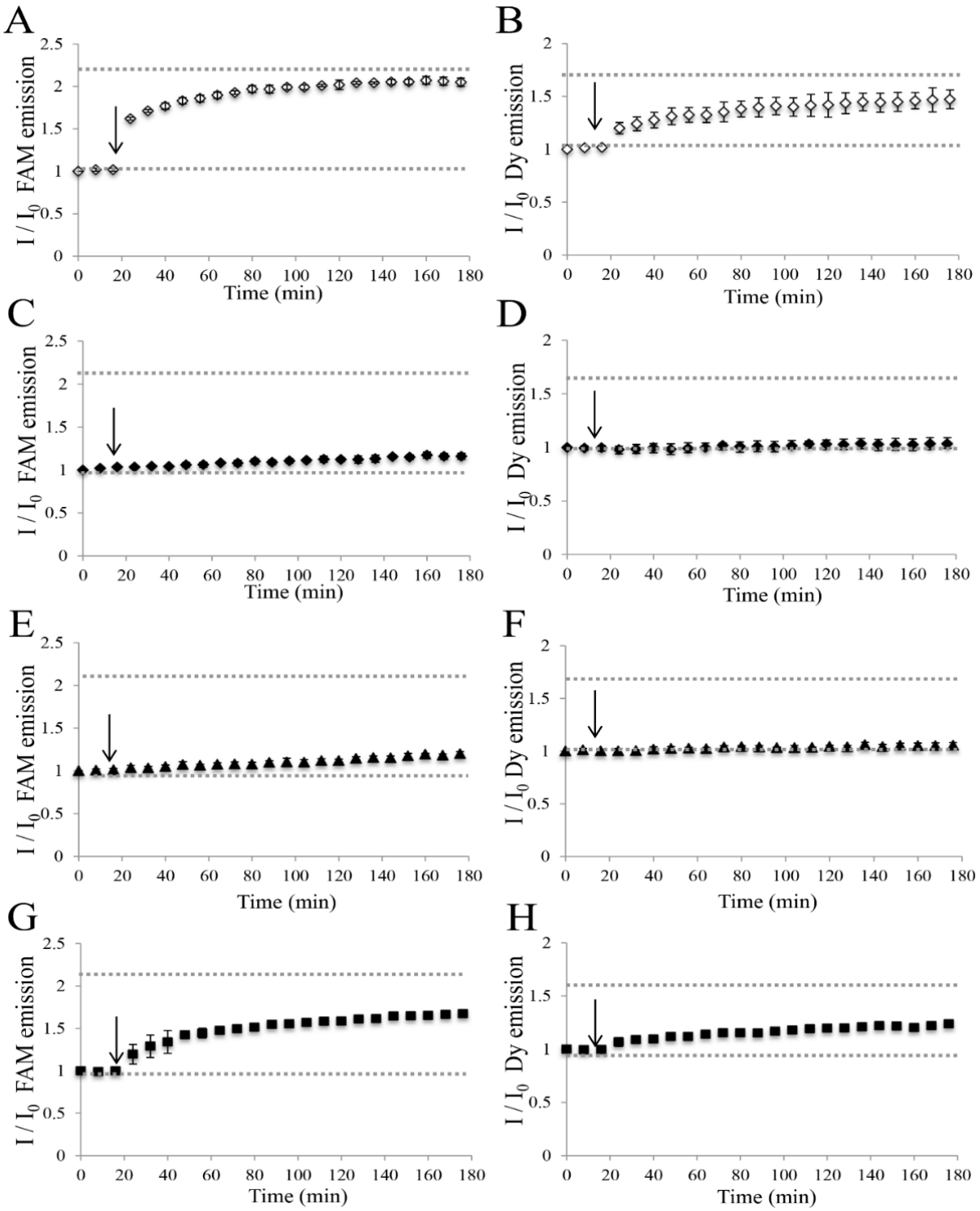

Figure XI.2. Hybridization assays of Biocode-43bp -e14-FAM in presence of different target sequences. A) Biocode-43bp -e14-FAM donor emission in the presence of e14a2 complementary target (white diamonds); B) acceptor-Dy emission in the presence of e14a2 complementary target; C) Biocode-43bp -e14-FAM donor emission in the presence of non-complementary target (black diamonds); D) acceptor-Dy emission in the presence of non-complementary target (black diamonds); E) Biocode-43bp -e14-FAM donor emission in the presence of exon 14 BCR derived target (black squares); F) acceptor-Dy emission in the presence of exon 14 BCR derived target (black squares); G) Biocode-43bp -e14-FAM donor emission in the presence of ABL target (black diamonds); H) acceptor-Dy emission in the presence of ABL target (black diamonds). The black arrow represents the addition of the target sequence.

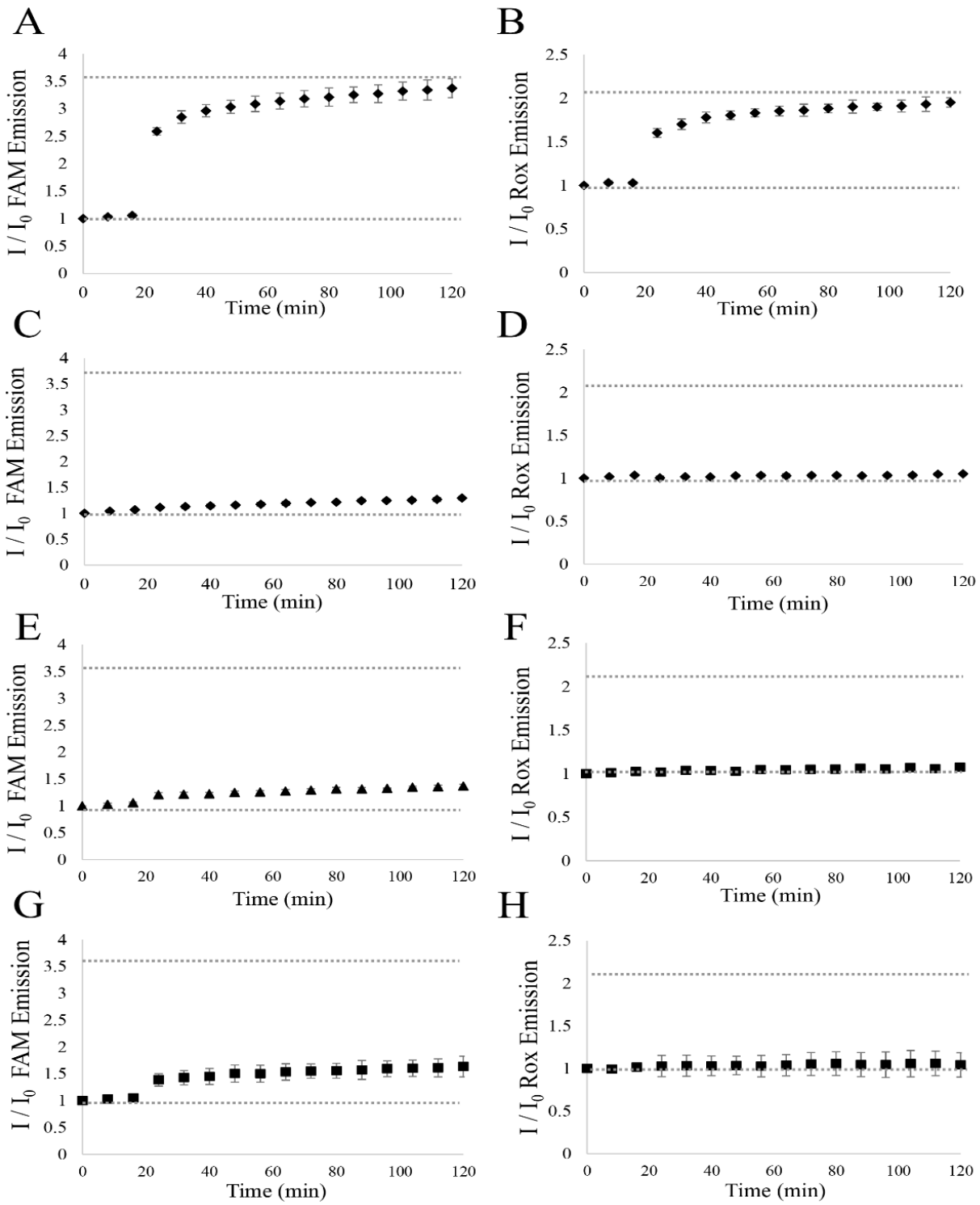

Figure XI.3. Hybridization assays of Biocode-47bp -e13-FAM in presence of different target sequences. A) Biocode-47bp -e13-FAM donor emission in the presence of e13a2 complementary target (white diamonds); B) acceptor-ROX emission in the presence of e13a2 complementary target; C) Biocode-47bp -e13-FAM donor emission in the presence of non-complementary target (black diamonds); D) acceptor-ROX emission in the presence of non-complementary target (black diamonds); E) Biocode-47bp -e13-FAM donor emission in the presence of exon 13 BCR derived target (black squares); F) acceptor-ROX emission in the presence of exon 13 BCR derived target (black squares); G) Biocode-47bp -e13-FAM donor emission in the presence of ABL target (black diamonds); H) acceptor-Dy emission in the presence of ABL target (black diamonds). The black arrow represents the addition of the target sequence.

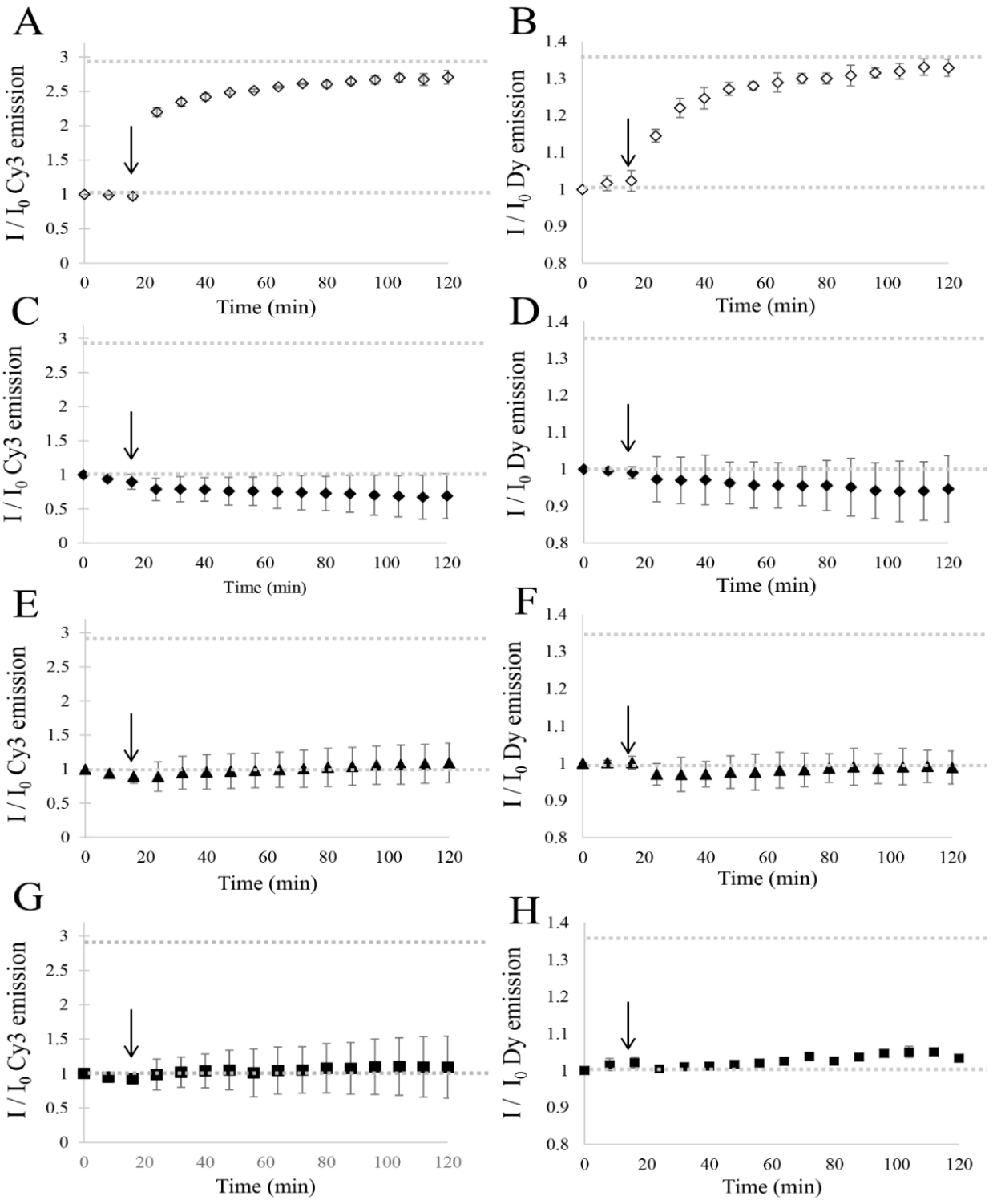

Figure XI.4. Hybridization assays of Biocode-47bp -e14-Cy3 in presence of different target sequences. a Biocode-47bp -e14- Cy3 donor emission in the presence of e14a2 complementary target (white diamonds); b acceptor-Dy emission in the presence of e14a2 complementary target; c Biocode-47bp -e14- Cy3 donor emission in the presence of non-complementary target (black diamonds); d acceptor-Dy emission in the presence of non-complementary target (black diamonds); e Biocode-47bp -e14- Cy3 donor emission in the presence of exon 14 BCR derived target (black squares); f acceptor-Dy emission in the presence of exon 14 BCR derived target (black squares); g Biocode-47bp -e14- Cy3 donor emission in the presence of ABL target (black diamonds); h acceptor-Dy emission in the presence of ABL target (black diamonds). The black arrow represents the addition of the target sequence.

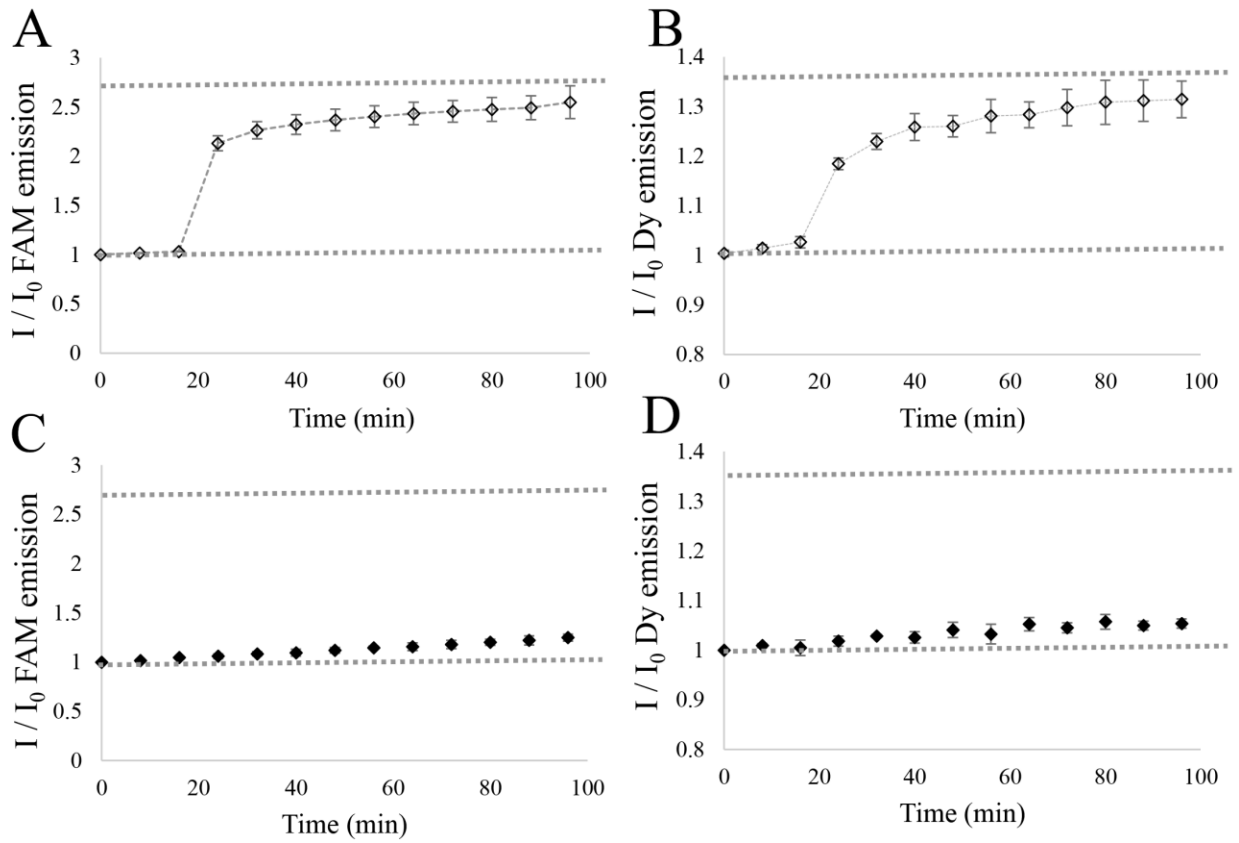

Figure XI.5. Hybridization assays of Biocode-47bp-e14-FAM in presence of different target sequences. A) Biocode-47bp-e14-FAM donor emission in the presence of e14a2 complementary target; B) acceptor-ROX emission in the presence of e14a2 complementary target; C) Biocode-47bp -e14-FAM donor emission in the presence of non-complementary target; D) acceptor-ROX emission in the presence of non-complementary target.

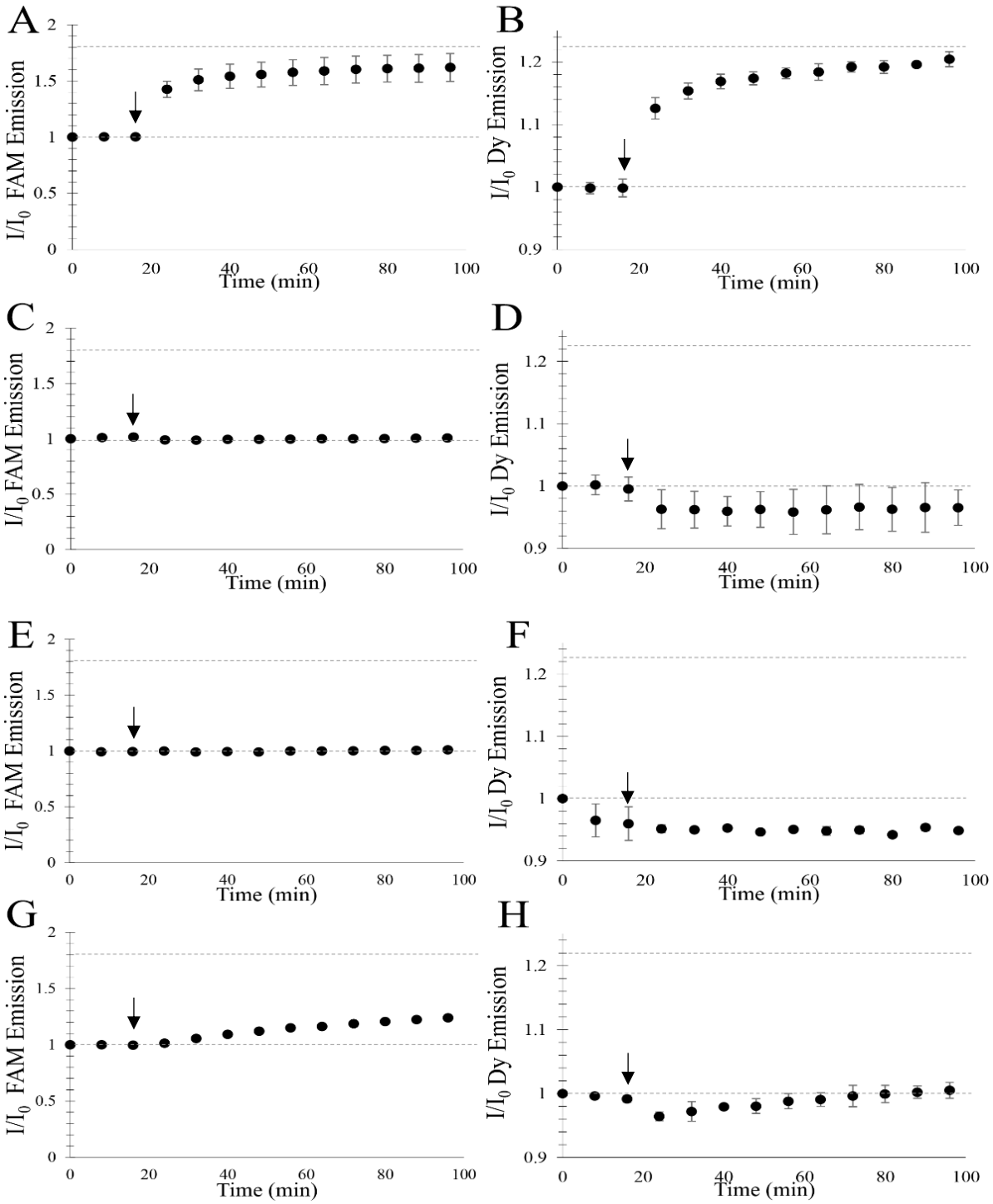

Figure XI.6. Hybridization assays of double-labeled BioCode in presence of different target sequences (e14a2 as a complementary target). A) double-labeled BioCode donor emission in the presence of e14a2 complementary target; B) acceptor-Dy emission in the presence of e14a2 complementary target; C) double-labeled BioCode donor emission in the presence of non-complementary target; D) acceptor-Dy emission in the presence of non-complementary target; E) double-labeled BioCode donor emission in the presence of exon 14 BCR derived target; F) acceptor-Dy emission in the presence of exon 14 BCR derived target; G) double-labeled BioCode donor emission in the presence of ABL target; H) acceptor-Dy emission in the presence of ABL target. The black arrow represents the addition of the target sequence.

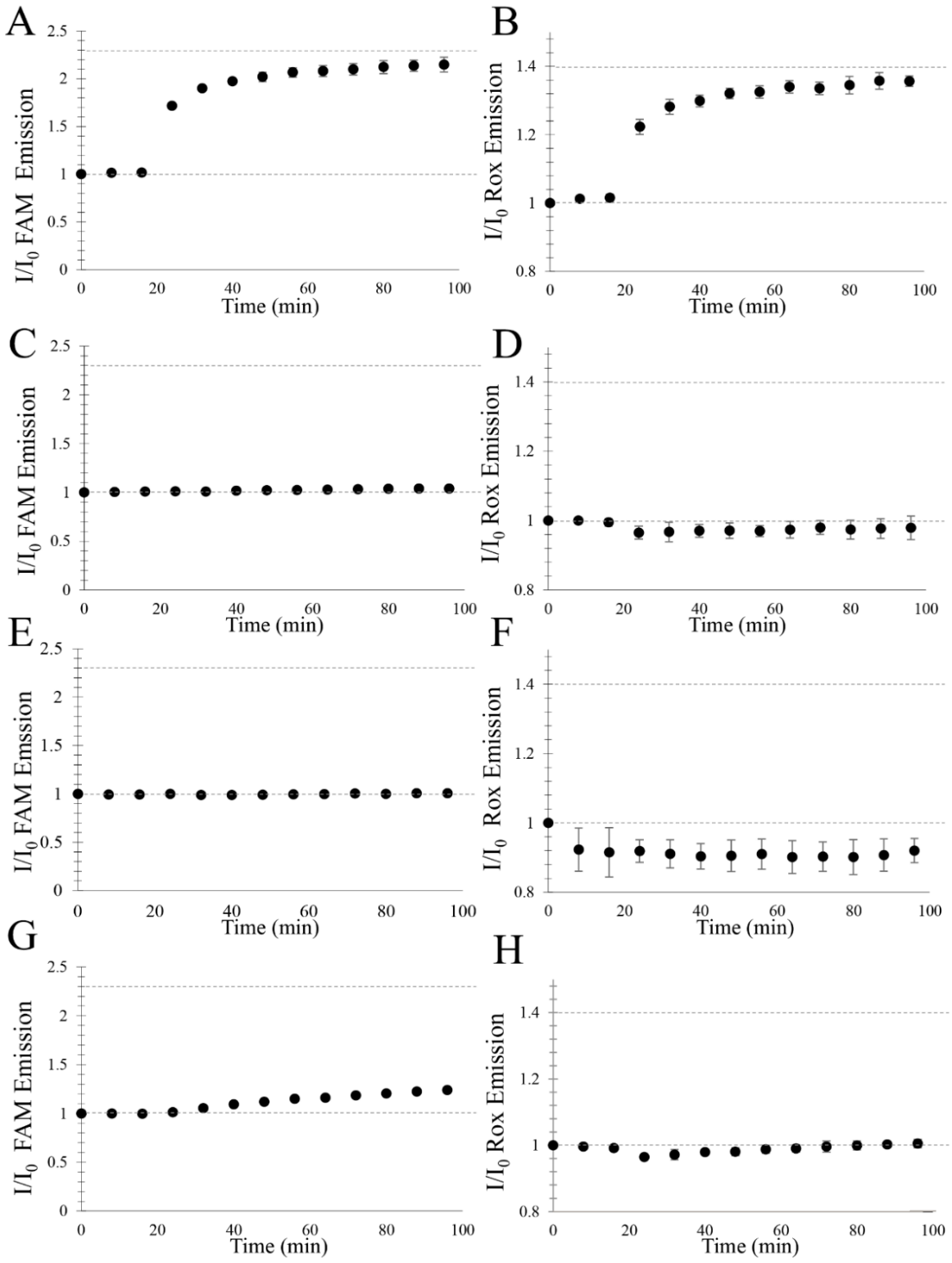

Figure XI.7. Hybridization assays of double-labeled BioCode in presence of different target sequences (e13a2 as a complementary target). A) double-labeled BioCode donor emission in the presence of e13a2 complementary target; B) acceptor-ROX emission in the presence of e13a2 complementary target; C) double-labeled BioCode donor emission in the presence of non-complementary target; D) acceptor-ROX emission in the presence of non-complementary target; E) double-labeled BioCode donor emission in the presence of exon 13 BCR derived target; F) acceptor-ROX emission in the presence of exon 13 BCR derived target; G) double-labeled BioCode donor emission in the presence of ABL target; H) acceptor-ROX emission in the presence of ABL target. The black arrow represents the addition of the target sequence.

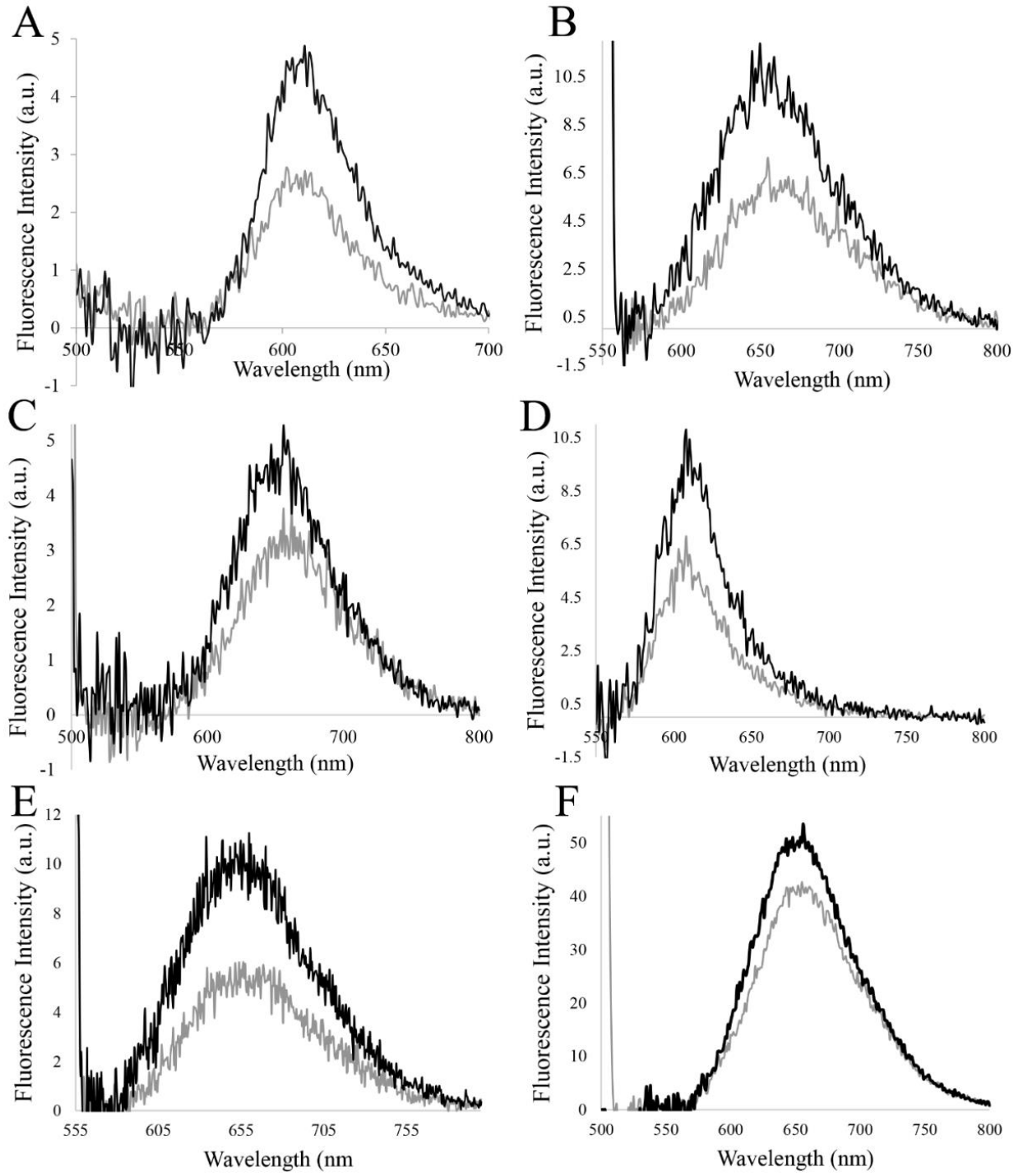

Figure XI.8. Emission spectra of the acceptor in the presence and absence of a fully complementary target, after the subtraction of the donor emission. A) BioCode 43bp_e13_FAM (Acceptor 10bp ROX); B) BioCode 43bp_e13_FAM (Acceptor 10bp dy-520 Xl MegaStockes); C) BioCode 43bp_e14_Dy (Acceptor 10bp dy-520 Xl MegaStockes); D) BioCode 47bp_e13_FAM (12 bp ROX); E) BioCode 47bp_e14_cy3 (Acceptor 12bp dy-520 Xl MegaStockes); F) BioCode 47bp_e14_FAM (12 bp dy-520 Xl MegaStockes); Solid black line – acceptor emission after the incubation with fully complementary target; Solid gray line - acceptor emission after the incubation with fully complementary target.

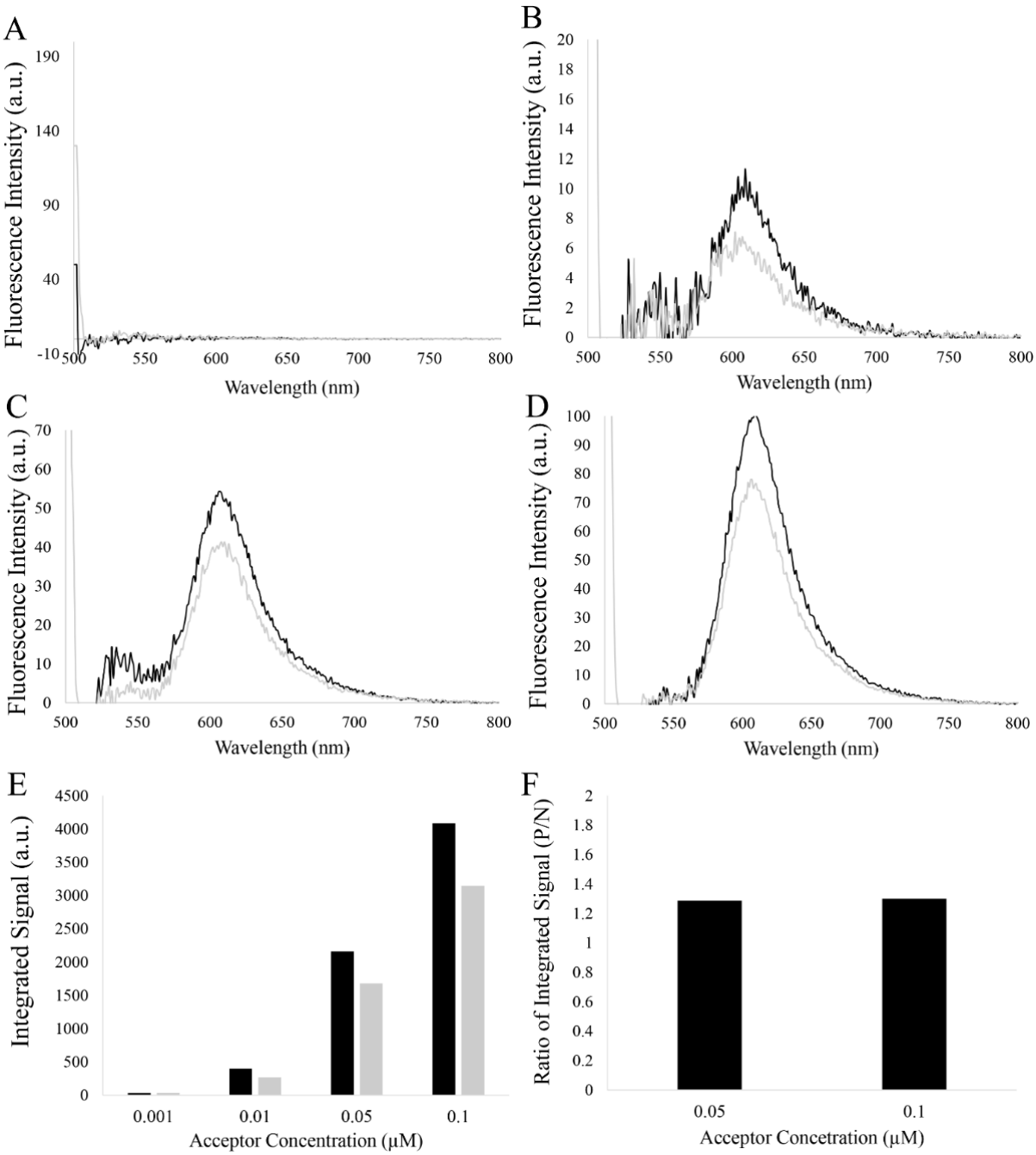

Figure XI. 9. Emission spectra of double-labeled BioCode incubated with an excess of fully complementary target or non-complementary target titrated with ROX-labeled revelator. A) revelator emission band at 0.001 µM in the presence of fully complementary target (black line) and non-complementary target (gray line); B) revelator emission band at 0.01 µM in the presence of fully complementary target (black line) and non-complementary target (gray line); C) revelator emission band at 0.05 µM in the presence of fully complementary target (black line) and non-complementary target (gray line); D) revelator emission band at 0.1 µM in the presence of fully complementary target (black line) and non-complementary target (gray line); The donor emission band was removed mathematically. E) Signal integration of emission band using the tested revelator concentration; F) Ratio of the integrated signal (Positive/negative reaction)

8.12 **Appendix XII**

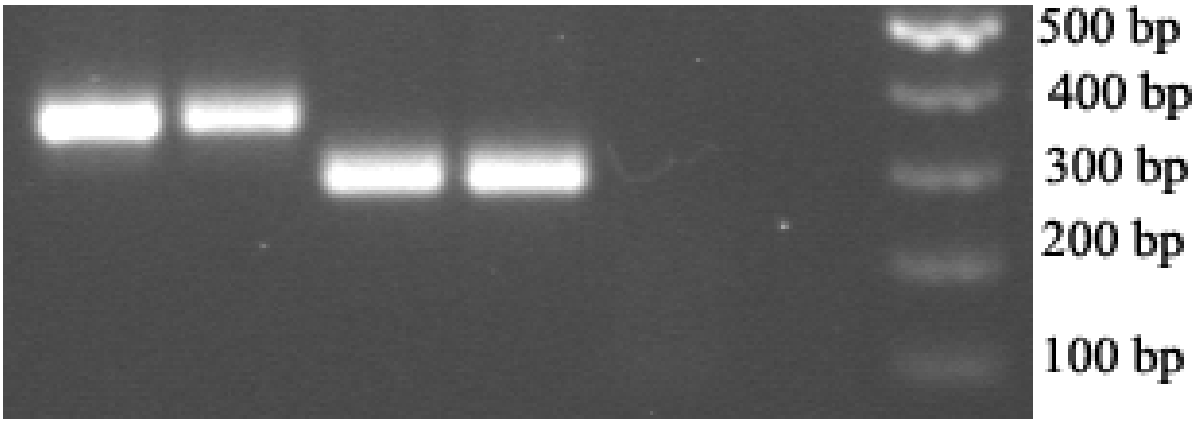

Figure XII.1. Agarose gel electrophoresis of retrotranscript nested-PCR products of the e14a2 (360 bp) and e13a2 (285 bp) fusion transcripts. 1% agarose in 1× TAE, 1 hour at 70 V.

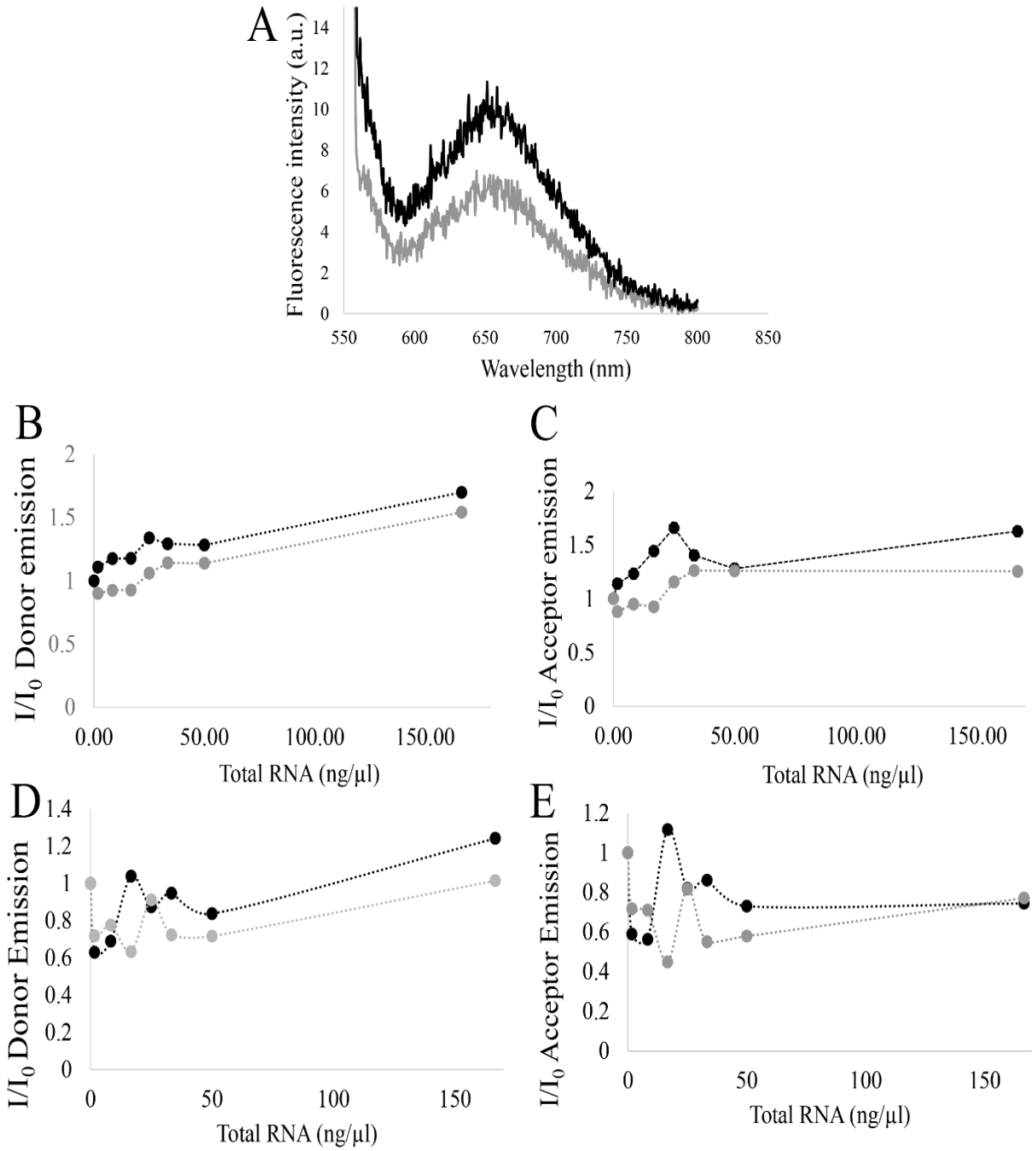

Figure XII.2. Signal variation of BioCode-47bp-e14-Cy3 incubated with RNA derived from k-562. A) Emission spectra of double-labeled BioCode incubated with 166.7 ng/µl of total RNA form K 562 cell line (black line) and no RNA (gray line). B) Donor channel emission variation using different concentration of total RNA of k562 cell line; C) Acceptor channel emission variation using different concentration of total RNA of k562 cell line (black circles) and THP1 (gray circles); D) Donor channel emission variation using different concentration of total RNA of k562 cell line (black circles) and THP1 (gray circles); E) Acceptor channel emission variation using different concentration of total RNA of k562 cell line (black circles) and THP1 (gray circles).

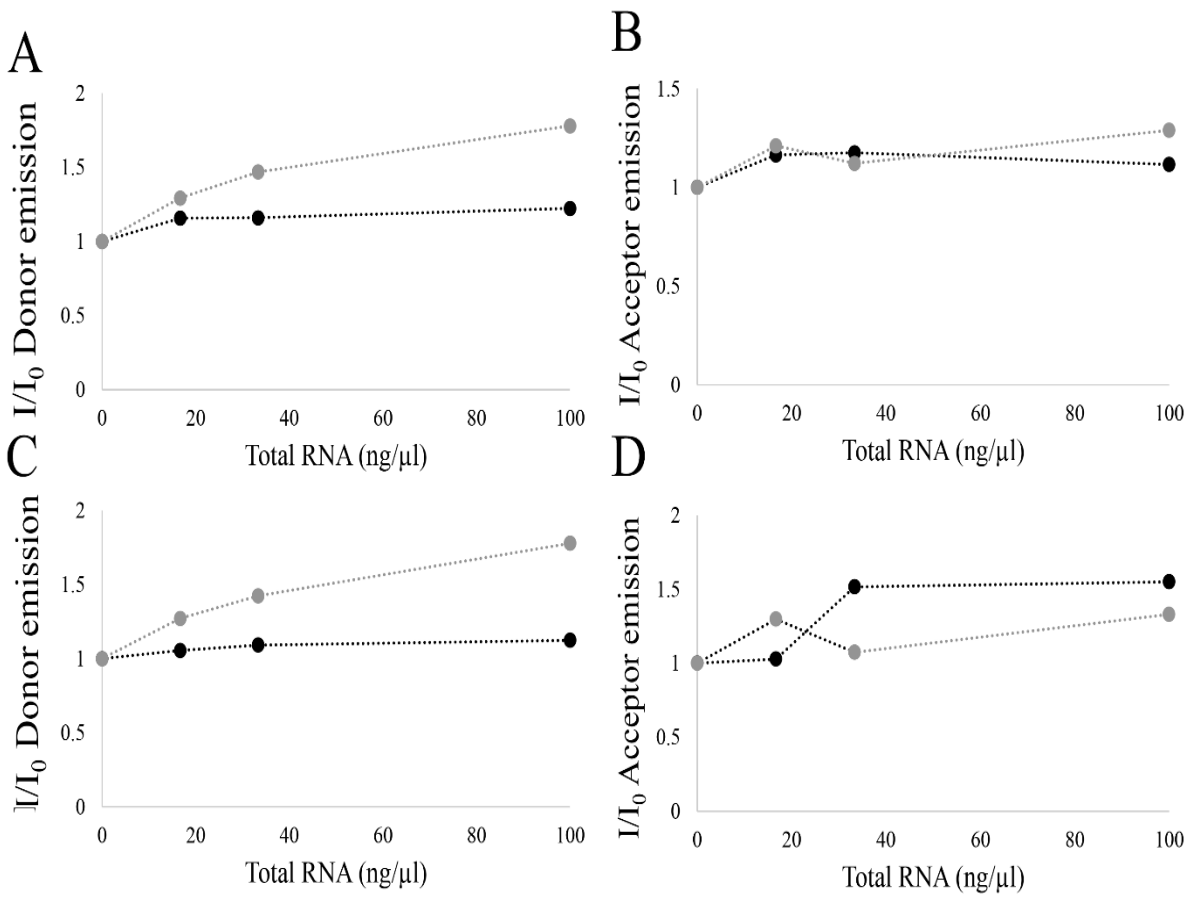

Figure XII.3. Signal variation of double-labeled BioCode incubated with total RNA. A) Donor channel emission variation using different concentration of total RNA of k562 cell line (black circles) and THP1 (gray circles); B) channel emission variation using different concentration of total RNA of k562 cell line (black circles) and THP1 (gray circles); C) Acceptor channel emission variation using different concentration of total RNA of BV173 cell line (black circles) and THP1 (gray circles); D) Acceptor channel emission variation using different concentration of total RNA of BV173 cell line (black circles) and THP1 (gray circles).

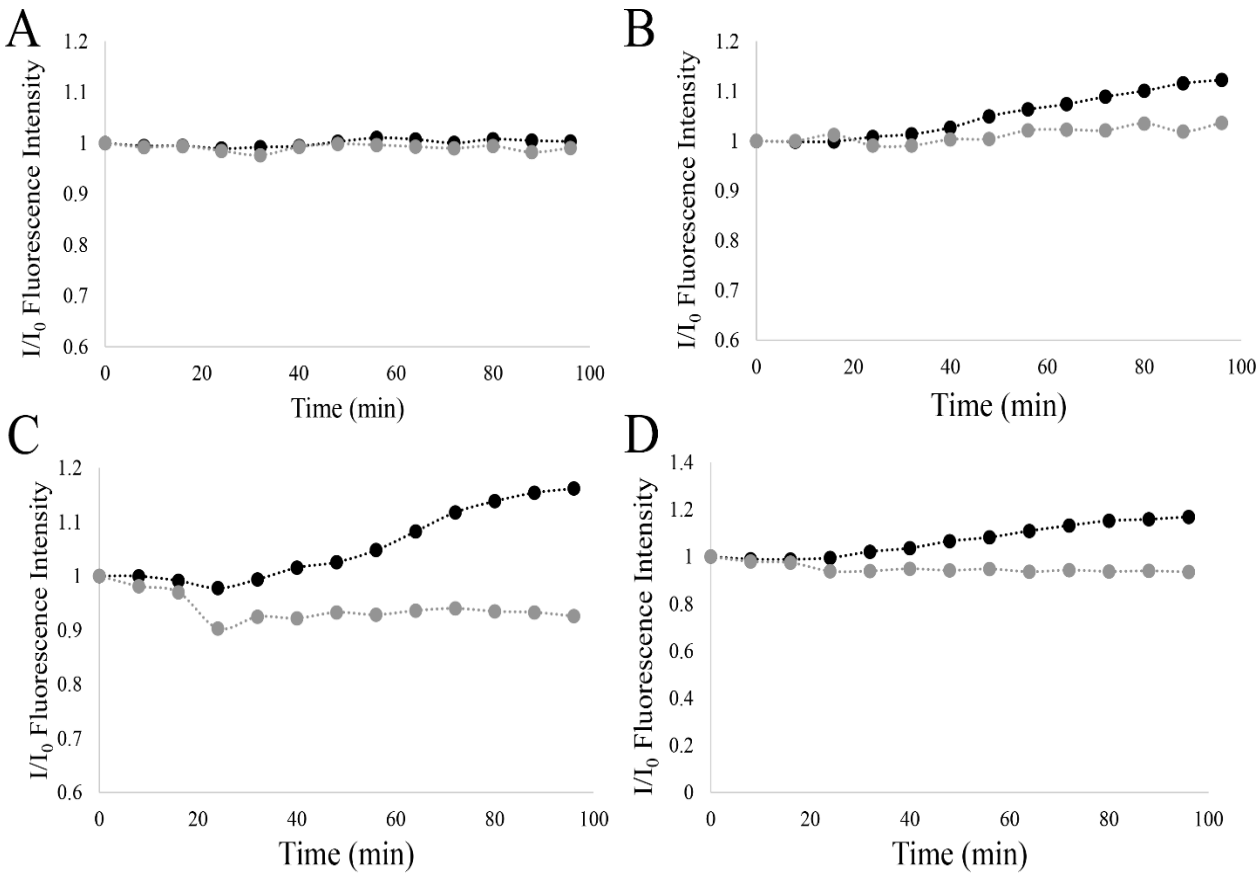

Figure XII.4. Signal variation of double-labeled BioCode incubated with non-purified asymmetric PCR product. A) Emission channel emission variation over time after in the absence of PCR product using cDNA from k562 cell line (black circles – Donor channel; gray circles – Acceptor Channel); B) Emission channel emission variation over time after in the presence of 1 µl of PCR product using cDNA from k562 cell line (black circles – Donor channel; gray circles – Acceptor Channel); C) Emission channel emission variation over time after in the presence of 2 µl of PCR product using cDNA from k562 cell line (black circles – Donor channel; gray circles – Acceptor Channel); D) Emission channel emission variation over time after in the presence of 5 µl of PCR product using cDNA from k562 cell line (black circles – Donor channel; gray circles – Acceptor Channel).

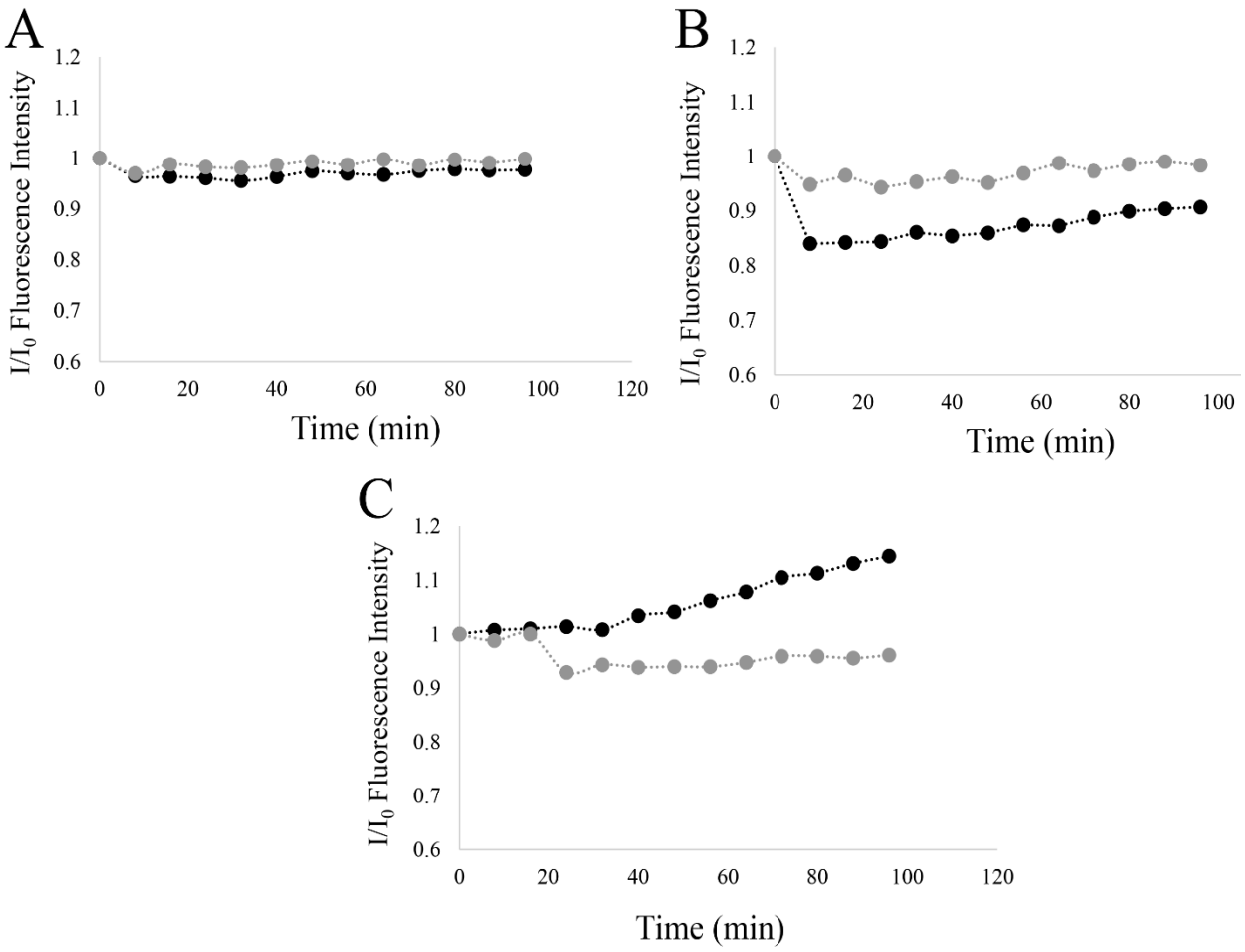

Figure XII.5. Signal variation of double-labeled BioCode incubated with purified asymmetric PCR product. A) Emission channel emission variation over time after in the absence of PCR product using cDNA from k562 cell line (black circles – Donor channel; gray circles – Acceptor Channel); B) Emission channel emission variation over time after in the presence of 2 µl of PCR product using cDNA from k562 cell line (black circles – Donor channel; gray circles – Acceptor Channel); C) Emission channel emission variation over time after in the presence of 5 µl of PCR product using cDNA from k562 cell line (black circles – Donor channel; gray circles – Acceptor Channel).